

-

**MULTISCALE MATHEMATICAL MODELING OF  
THE ABSORPTIVE AND MUCOCILIARY  
PATHOPHYSIOLOGY OF CYSTIC FIBROSIS  
LUNG DISEASE**

by

**Matthew Raymond Markovetz**

B.S., University of Colorado at Boulder, 2012

Submitted to the Graduate Faculty of  
the Swanson School of Engineering in partial fulfillment  
of the requirements for the degree of

**Doctor of Philosophy**

University of Pittsburgh

2017

UNIVERSITY OF PITTSBURGH  
SWANSON SCHOOL OF ENGINEERING

This dissertation was presented

by

Matthew Raymond Markovetz

It was defended on

December 13, 2016

and approved by

Robert S. Parker, Ph.D., Professor, Department of Chemical and Petroleum Engineering

Timothy E. Corcoran, Ph.D., Associate Professor Division of Pulmonary, Allergy, and

Critical Care Medicine

Michael M. Myerburg, M.D., Associate Professor, Div. of Pulmonary, Allergy, and Critical

Care Medicine

Carol A. Bertrand, Ph.D., Research Assistant Professor, Pediatrics

Jason Shoemaker, Ph.D., Assistant Professor, Dept. of Chemical and Petroleum

Engineering

Cheryl A. Bodnar, Assistant Professor, Dept. of Entrepreneurship Education, Rowan

University

Dissertation Advisors: Robert S. Parker, Ph.D., Professor, Department of Chemical and

Petroleum Engineering,

Timothy E. Corcoran, Ph.D., Associate Professor, Div. of Pulmonary, Allergy, and Critical

Care Medicine

Copyright © by Matthew Raymond Markovetz  
2017

# MULTISCALE MATHEMATICAL MODELING OF THE ABSORPTIVE AND MUCOCILIARY PATHOPHYSIOLOGY OF CYSTIC FIBROSIS LUNG DISEASE

Matthew Raymond Markovetz, PhD

University of Pittsburgh, 2017

Airway disease is the primary cause of mortality for the over 70,000 patients with Cystic Fibrosis (CF) worldwide. It is characterized by lung infection, inflammation, and impaired mucociliary clearance (MCC) arising from depletion of the airway surface liquid (ASL) at the organ-scale. Dysfunction in the CF transmembrane conductance regulator protein causes dysregulation in ion and liquid transport alone and via other transport-related proteins. Analysis of cell-system interactions is experimentally complex, however, and motivates the use of mechanistic mathematical models that can also be used to design and optimize treatments for the disease.

Tc99m or In111-labeled DTPA (DTPA) are small-molecule radiological probes that allow for observation of paracellular liquid convection and solute transport at cellular and organ scales, respectively. Previous work has shown that DTPA is hyperabsorbed in CF in a manner that strongly correlates with ASL hyperabsorption. The models of this dissertation describe, in part, the mechanisms that underlie this correlation. At the lung-scale, a physiologically motivated pharmacokinetic model was developed to describe the action of hypertonic saline (HS) as an inhaled therapy in CF. This model predicts that MCC is reduced in patients with CF because they have a reduced fraction of functional ciliated airway – a model parameter – that is increased via HS-induced airway rehydration. This prediction was verified *in vitro* in human bronchial epithelial (HBE) cultures.

A separate, cell-scale model accurately characterizes transcellular liquid transport in HBE cultures using transport parameters that agree well with previously reported values, producing ion flux estimates from the model fit to ASL and DTPA absorption that were similar to known physiological values. It also implicates diminished constitutive Cl<sup>-</sup> secretion in ASL dehydration but suggests that reduced paracellular integrity is the predominant factor leading to hyperabsorption in CF. The cell- and lung-scale models were then used to analyze treatment failure and suggest modifications of a clinical trial, which is the first indication of the utility of airway transport models in designing treatments for patients with CF.

**Keywords:** Cystic Fibrosis, Mathematical Modeling, Epithelial Transport, Mucociliary Clearance, Airway Surface Liquid Absorption.

## TABLE OF CONTENTS

<b>PREFACE</b> . . . . .	xxv■
<b>1.0 INTRODUCTION</b> . . . . .	1
1.1 Multiscalar Transport in Human Airways . . . . .	1
1.1.1 Fundamental Elements of Airway Epithelial Ion and Liquid Transport	2
1.1.2 Airway Epithelial Structure and Function . . . . .	4
1.1.2.1 General Epithelial Structure and Function . . . . .	4
1.1.2.2 Airway Liquid and Solute Transport in Health and CF . . . . .	8
1.1.2.3 The Airway Transport System . . . . .	11
1.2 Modeling Across Biological Scales . . . . .	14
1.2.1 Modeling Epithelial Solute and Liquid Transport at the cellular scale	14
1.2.1.1 Systems Biology Overview . . . . .	14
1.2.2 Systems Biology in Airway Transport at the Cellular Scale . . . . .	18
1.2.3 Systems Biology in Airway Transport at the Organ Scale . . . . .	22
1.2.4 Dissertation Overview . . . . .	24
<b>2.0 PHYSIOLOGICALLY RELEVANT LUNG-SCALE MODELING OF</b>	
<b>MUCOCILIARY AND ABSORPTIVE PULMONARY CLEARANCE</b>	26
2.1 Mucociliary Clearance and Absorption in the Lung . . . . .	26
2.2 Materials and Methods . . . . .	29
2.2.1 Functional Imaging Methods . . . . .	29
2.2.2 Initial Model Structure . . . . .	31
2.2.3 Model Parameter Estimation . . . . .	32
2.2.4 Model Analysis . . . . .	32

2.2.5	<i>In Vitro</i> Assessment of Ciliary Activation . . . . .	33
2.3	Preliminary Analysis . . . . .	34
2.4	Results . . . . .	38
2.4.1	Model Synthesis and Assumptions . . . . .	38
2.4.2	Model Equations . . . . .	41
2.4.3	Model Fit and Predictions . . . . .	41
2.4.4	<i>In Vitro</i> Evaluation of Model Prediction . . . . .	47
2.5	Discussion . . . . .	49
2.5.1	Model Structure Selection and Analysis . . . . .	51
2.5.2	Parametric Considerations . . . . .	55
2.5.3	Study Limitations . . . . .	56
2.5.4	Physiological Implications . . . . .	57
2.5.5	Clinical Relevance . . . . .	58
2.5.6	Summary . . . . .	58
<b>3.0</b>	<b>CELL SCALE MODELING OF LIQUID AND SOLUTE HYPERAB-</b>	
	<b>SORPTION IN CYSTIC FIBROSIS BRONCHIAL EPITHELIA . . . . .</b>	<b>60</b>
3.1	Introduction . . . . .	60
3.2	Materials and Methods . . . . .	62
3.2.1	Model Development . . . . .	62
3.2.2	Model Structure . . . . .	63
3.2.3	Experimental Methods . . . . .	66
3.2.4	Parameter Estimation . . . . .	67
3.3	Experimental and Simulation-based findings . . . . .	68
3.3.1	The mathematical model captures population absorption dynamics in CF and non-CF HBE . . . . .	68
3.3.2	Validation of Model Structure and Dynamic Output . . . . .	69
3.3.3	Effects of Osmotic Agents on ASL and DTPA Absorption in HBE . . . . .	74
3.3.4	Other Considerations Regarding Cell-volume Regulation . . . . .	77
3.3.5	Paracellular Convection of DTPA is Increased in CF Cells . . . . .	82
3.4	Treatment Analysis and Design Using the Cell-scale Model . . . . .	84

3.4.1	Model Analysis of a Clinical Study . . . . .	87
3.5	Summary . . . . .	94
<b>4.0</b>	<b>PARAMETER IDENTIFICATION: METHODS AND MOTIVATING</b>	
	<b>CASES . . . . .</b>	<b>100</b>
4.1	Observability and Identifiability in Systems Models . . . . .	100
4.2	Methods for Parameter Estimation and Identification . . . . .	103
4.3	An Open Source Package for Parameter Likelihood Estimation . . . . .	106
4.3.1	The Pyomo Model Profile Likelihood Estimation (PyMPLE) Package	106
4.4	PyMPLE Example: a Model of the Van de Vusse Reaction in a CSTR . . .	109
4.4.1	Analysis and Model Identification . . . . .	110
4.4.2	Identification of an Unobservable Model . . . . .	113
4.5	Identification of a Lung-scale Mucociliary and Absorptive Clearance Model	117
4.5.1	Problem Formulation . . . . .	118
4.5.1.1	APT-MCMC . . . . .	118
4.5.1.2	PyMPLE . . . . .	119
4.5.2	Model Fit to Data . . . . .	120
4.5.3	Comparison of Likelihood Estimates from APT-MCMC and PyMPLE	122
4.5.4	APT-MCMC and PyMPLE Comparison . . . . .	125
4.6	Summary . . . . .	126
<b>5.0</b>	<b>SUMMARY AND FUTURE WORK . . . . .</b>	<b>127</b>
5.1	Contributions . . . . .	127
5.1.1	Lung-scale Model of MCC, ABS, and Treatment Response . . . . .	127
5.1.2	Cell-scale Model of Airway Liquid and Solute Transport . . . . .	128
5.1.3	Pyomo Model Profile Likelihood Estimation (PyMPLE) Package . .	130
5.2	Future Work . . . . .	131
5.2.1	Updates and Maintenance of PyMPLE . . . . .	131
5.2.2	Additional Components in the Cell-scale Model . . . . .	132
5.2.3	Optimal Treatment Design at the Cell-scale . . . . .	133
5.2.4	Individualized Patient Characterization and Treatment . . . . .	135

<b>6.0 MIXED-METHODS ANALYSIS OF THE EFFECT OF CUSTOMER VOICE ON PRODUCT DESIGN</b>	138
6.1 Introduction	138
6.2 Research Questions:	141
6.3 Methods:	142
6.3.1 Study Design	142
6.3.2 Assessment of Final Membrane Designs	143
6.3.3 Design of Focus Group	144
6.3.4 Assessment of Student Submissions	145
6.3.5 Grounded Theory Framework Development	146
6.3.6 Statistical Analysis	147
6.4 Quantitative Results	148
6.4.0.1 RQ1:	148
6.4.0.2 RQ2:	149
6.4.1 RQ3:	150
6.5 Discussion of Quantitative Findings	151
6.6 Summary of Quantitative Findings	152
6.7 Qualitative Results	152
6.7.1 Results and Discussion	152
6.7.1.1 RQ4:	152
6.7.1.2 RQ5:	155
6.7.2 Study Limitations	160
6.8 Summary	161
<b>APPENDIX A. CODE FOR SIMULATING THE CELL- AND LUNG-SCALE MODELS</b>	163
A.1 Equations of the Cell-scale Model	163
A.2 Addition of Potassium to the Model	164
<b>APPENDIX B. MODEL EQUATIONS</b>	168
B.1 Code for Simulating the Lung-scale Model	168
B.2 Code for Simulating the Cell-scale Model	169

<b>APPENDIX C. PYMPLE CODE AND EXAMPLES</b> . . . . .	173
C.1 Code for PyMPLE . . . . .	173
C.2 Van de Vusse Case Study Code . . . . .	180
<b>APPENDIX D. EXTERNAL STAKEHOLDER QUESTIONS, RESPONSES,</b>	
<b>    AND CATEGORIZATIONS</b> . . . . .	187
<b>BIBLIOGRAPHY</b> . . . . .	197

## LIST OF TABLES

2.1	Abbreviations and constants in this chapter. . . . .	30
2.2	Model parameters in the work presented herein . . . . .	42
2.3	Pharmacokinetic Lung Clearance Parameter Values . . . . .	49
2.4	AIC Values for Various Model Structures . . . . .	53
3.1	Initial conditions for the model compartments immediately following apical Ringer’s addition. Initial apical volumes were determined from data, but solute concentrations were assumed to be similar regardless of post-addition volume. Cellular volume is the total volume of the monolayer. . . . .	66
3.2	Model parameters were set according to values found in the literature (references included) or determined via MCMC search for model training. Nonlinear least-squares search was used under osmotically challenged conditions to account for stress responses that can change transport rates. Abbreviations are transcellular ( $L_{PC}$ ) and paracellular ( $L_{PP}$ ) hydraulic permeabilities, maximum ENaC ( $P_{ENaC}$ ) and CFTR ( $P_{CFTR}$ ) permeabilities, and the respective half-maximal $V_{max}$ and half-minimal $V_{min}$ for those channels. Constitutive chloride permeability ( $P_{ACC}$ ) and basolateral sodium ( $k_{Na}$ ) and chloride ( $k_{Cl}$ ) rate constants were also included in the parameter search. Best-fit values are given in lieu of means due to distributional shape factors. . . . .	71
3.3	Citations are given for comparison of values to *, (52); **, (49), *** (18) . . .	71
4.1	Estimates of reaction rate constants with true values given for comparison to the full and reduced data set examples. . . . .	112

4.2	Kinetic parameter estimates for MCMC and PL (as maximum likelihood) techniques. Deposition parameters were also estimated. Literature values are from Markovetz et al. [1] where trust-region-reflective estimation was used. Time to convergence is given for each method. APT-MCMC is parallelizable, but the estimations for both APT-MCMC and PL occurred on a single 2x Xeon core. . . . .	123
6.1	Thresholds for design outputs . . . . .	144
6.2	Categories and subcategories with their notebook responses. Grammatical errors by students are denoted with [sic]. . . . .	147
6.3	Correlations for each of the four metrics of the final design versus the number of questions asked. . . . .	149
6.4	Comparison of final design metrics between FG and NFG sections. . . . .	150
6.5	Categorized notebook responses . . . . .	153
6.6	Frequency mentions of both customer needs and a design attribute in tandem.	155

## LIST OF FIGURES

1.1	Diagram of the general structure of epithelial monolayers. Epithelial cells adhere to a basement membrane of connective tissue (or coated substrate in tissue cultures). Transcellular transport occurs in all epithelia via channels and pumps in the apical and basolateral membranes. Paracellular transport occurs through the tight junction in “leaky” epithelia, and only to a very small extent in “tight” epithelia. . . . .	5
1.2	Diagram of an Ussing Chamber and the equivalent simplified circuit diagram. A cellular monolayer separates two compartments of electrolyte solution on the apical and basolateral sides. Electrodes on either side of the monolayer measure electrical current, resistance, and potential. . . . .	7
1.3	Known pathways for liquid and ion transport in airway epithelia. CFTR is thought to regulate ENaC and SLC26A9 through intracellular signaling and other domain interactions [2,3]. Other passive $\text{Cl}^-$ and $\text{K}^+$ channels exist in the apical and basolateral membranes (though basolateral $\text{K}^+$ channels are more speculative). Active, dedicated $\text{Cl}^-$ transport also occurs in the basolateral membrane, where $\text{Na}^+$ and $\text{K}^+$ are also actively transported with and without $\text{Cl}^-$ . HBE are “leaky,” thus they also have a high degree of paracellular water and small solute transport [4,5]. . . . .	9
1.4	CFTR in its closed state (left) does not allow $\text{Cl}^-$ or other anions to pass through the apical membrane. Once the R domain is phosphorylated, the NBDs will interact to hydrolyze 2 ATP causing a gating event that allows $\text{Cl}^-$ to move down its electrochemical gradient. Adapted from [6] . . . . .	10

1.5	Normal ASL/PCL (depicted in light blue) homeostasis and MCC are maintained by proper function of CFTR and ENaC at the apical membrane of the airway epithelium (left). In CF (right) the ASL becomes dehydrated due to the absence of CFTR and subsequent dysregulation of Na <sup>+</sup> absorption via ENaC. Mucus becomes viscous and unclearable, leading to chronic infections and subsequent inflammation and scarring. . . . .	12
1.6	<b>Top:</b> Standard-of-care Physician-Patient treatment feedback loop. <b>Bottom:</b> A clinical DSS for treatment design using model-informed physician decisions for patient care. . . . .	18
1.7	Detailed layout of voltage clamp with feedback control loop evident as part of transepithelial impedance measurement hardware (reproduced from [7] with permission). Inputs and set-point (Voffset) illustrate the essential components for biological control in the Ussing Chamber. . . . .	22
2.1	<b>Left panel: schematic of transport routes in the airway epithelium.</b> The black and white horizontal arrows represent mucociliary clearance of TcSC and DTPA, respectively. DTPA (downward white arrow) absorbs across the airway epithelium via the paracellular route. Water (downward blue arrow) also absorbs across the epithelium via the transcellular and paracellular routes. Right panel: normalized TcSC (blue circles) and DTPA (green circles) retention curves with the difference between the respective datasets at each time point shown as absorption (red circles) in CF subject 8. . . . .	27
2.2	Video of recorded ciliary activity with three regions of "hurricane" activity visible. First image is Figure 2.3 superimposed on the video. The superimposition can be recovered by scrolling to the previous page (in the digital format of the dissertation). . . . .	34

2.3	A pseudo-color image of non-CF HBE cells under 10x enhancement is shown. The viewing frame is identical to that in 1. Darker (more blue) regions show areas with lower average change in pixel intensity during 1 whereas lighter (more yellow) regions show areas with higher average change. In combination with 1 it is shown that regions that display little visible movement are more blue, and the regions with visible motion, particularly the “hurricane” regions, are more yellow. . . . .	35
2.4	Model estimated MCC (red) based on functional imaging data (blue) in non-CF subjects, CF subjects without and with HS inhalation, and pediatric patients with CF. C/P was allowed to be fit in this case, allowing for estimation of the deposition pattern that best describes the whole lung clearance curves. . . . .	36
2.5	Model estimated DTPA absorption (red) based on functional imaging data (blue) in non-CF subjects, CF subjects without and with HS inhalation, and pediatric patients with CF. Best fit parameters as well as normalized TcSC and DTPA clearance (TcCL and InCL) and absorption (Abs) are given in each panel for their respective patient group. C/P estimates do not agree with the values obtained directly from imaging data. . . . .	37
2.6	Model estimated MCC (red) based on functional imaging data (blue) in non-CF subjects, CF subjects without and with HS inhalation, and pediatric patients with CF. C/P was allowed to be fit in this case, allowing for variation in deposition pattern that best describes the whole lung clearance curves. . . . .	38
2.7	Model estimated DTPA absorption (red) based on functional imaging data (blue) in non-CF subjects, CF subjects with out and with HS inhalation, and pediatric patients with CF. Best fit parameters as well as normalized TcSC and DTPA clearance (TcCL and InCL) and absorption (Abs) are given in each panel for their respective patient group. C/P estimates do not agree with the values obtained directly from imaging data. . . . .	39
2.8	<b>Schematic model structure describing the clearance of small molecule and particle probes from the lung.</b> Initial depositions: $T_0$ =trachea, $C_0$ =central, $P_0$ =peripheral. See Table 1 for full list of model abbreviations. . . . .	40

2.9	<b>TcSC retention (mean <math>\pm</math> SEM) vs. model fit (black line) for four patient subgroups.</b> (A) Non-CF subjects (n=9) (B) patients with CF (n=12). (C) patients with CF after inhalation of hypertonic saline (n=11). (D) Pediatric patients with CF. Data from [8]. . . . .	43
2.10	<b>DTPA absorption (mean <math>\pm</math> SEM) vs. model fit (line) for four patient subgroups</b> (A) Non-CF subjects (n=9) (B) patients with CF (n=12). (C) patients with CF after inhalation of hypertonic saline (n=11). (D) Pediatric patients with CF. Data from [8]. . . . .	44
2.11	<b>Estimated TcSC retention trajectories for three patient subgroups.</b> Non-CF (red with dashed line), CF IS (green with dotted dashed line), CF HS (blue with line). Shaded envelope characterizes 95% confidence interval (CI) of retention prediction by the model. Pediatric CF subjects not shown due to overlap with adult CF. . . . .	46
2.12	<b>Estimated DTPA absorption trajectories for three groups.</b> Non-CF (red with dashed line), CF IS (green with dotted dashed line), CF HS (blue with line). Shaded envelope characterizes 95% confidence interval (CI) of retention prediction by the model. Pediatric CF subjects not shown due to overlap with adult CF. . . . .	47
2.13	<b>Least-squares solutions for model parameters are shown with 95% confidence intervals for four groups:</b> Non-CF (NCF), CF HS, CF IS, and Pediatric CF (CFP). (A) MCC rate constant ( $k_{LT}$ ) ( $min^{-1}$ ). (B) Fraction (FFCA) of large airway with functional MCC. (C) Peripheral lung absorptive rate constant ( $k_{DB}$ ) ( $min^{-1}$ ). (D) Large airway absorptive rate constant ( $k_{LB}$ ) ( $min^{-1}$ ). . . . .	48
2.14	<b>FFCA determined <i>in vitro</i> in CF HBE cells is shown <math>\pm</math> SEM</b> (A) Activated area is significantly greater between 10 $\mu$ L and baseline (* $p < 0.0005$ ) and 2x10 $\mu$ L and baseline (* $p < 0.0005$ ). Activated area is not significantly greater between hydrated groups ( $p > 0.05$ ). (B) The increase in FFCA after addition of HS in cell cultures is significantly greater than IS (* $p < 0.01$ ). . . . .	50

2.15 Least-squares solutions for model parameters in case 2 of Table ??

are shown for comparison to the selected model with 95% confidence intervals for four patient groups: Non-CF (NCF), CF HS, CF IS, and Pediatric CF (CP). (A) MCC rate constant ( $k_{LT}$ ) (min-1) reiterates that  $k_{LT}$  is the same in all groups. (B) Fraction (FFCA) of large airway with functional MCC. (C) Peripheral lung absorptive rate constant ( $k_{DB}$ ) (min-1) and (D) large airway absorptive rate constant ( $k_{LB}$ ) are nearly identical to their analogs in the selected model. (E) MCC rate constant ( $k_{DL}$ ) (min-1) from D to L is clearly unidentifiable, and the nominal value is much smaller than  $k_{LT}$  in each group. Confidence intervals are also widened in all parameters directly related to MCC. . . . .

54

3.1 Schematic of the contributors to solute and liquid transport across the airway epithelium represented in the model equations. Volumes ( $V_i$ ) of the apical, basolateral, and cellular compartments dynamically respond to changes in osmolarity. Terms describing ENaC and CFTR respond to changes in apical volume according to first and second-order Hill functions, respectively. Basolateral  $\text{Na}^+$  and  $\text{Cl}^-$  fluxes are included to assure conservation of mass. Mannitol (Ml) is included in the model to allow for the description of liquid and DTPA absorption following hyperosmotic challenge. The inclusion of DTPA in the model makes the terms describing paracellular and transcellular water transport mathematically observable and provides a link between the physiological processes measured *in vitro* and *in vivo*. . . . .

65

3.2 Posterior distributions of model parameters are given for base-10 (p) or  $\log_{10}$  transformed values generated from Markov Chain Monte Carlo. Distributions are given along either a linear or logarithmic abscissa. . . . .

68

3.3	Best-fit model trajectories and experimental data after 10 $\mu\text{L}$ apical volume addition to 6 non-CF (NCF)) and 6 CF lines. CF lines demonstrate apical dehydration relative non-CF lines at the start and end points of the experiment (top panel, $p < 5 \times 10^{-10}$ ). Total volume absorbed in the model is 7.25 $\mu\text{L}$ (38.4%) in the non-CF case lines and 6.91 $\mu\text{L}$ (51.0%) in the CF lines. Non-CF cells rapidly return to homeostatic volumes, whereas CF cells exhibit prolonged absorption that results in increased DTPA absorption (bottom panel, $p < 5 \times 10^{-11}$ ). Model-estimated DTPA clearance is 42.7% in non-CF cells compared to 65.0% in CF after 24 hrs. Error bars show experimental data $\pm$ SEM. . . . .	70
3.4	Ensemble distributions of model-predicted non-CF (top) and CF (bottom) $\text{Na}^+$ fluxes. Both primary peaks are well-fit by lognormal distributions. The second peak in the non-CF (NCF) distribution near 7 $\mu\text{eq}/\text{cm}^2/\text{hr}$ only contributes to 2% of the area in the cumulative distribution function. . . . .	72
3.5	The $\text{Cl}^-$ flux ensembles for non-CF (Top) and CF (Bottom) model predictions are approximately normal. Both sets of distributions contain 0. Secretion rates are positive in the apical direction. . . . .	73
3.6	(A, B) Ion flux values from MCMC-generated model ensembles (violins) and ISC measurements (boxes). The model predicts non-CF cells (NCF) have similar but increased $\text{Na}^+$ absorption compared to the data. Model and data are in strong agreement in the CF case for $\text{Na}^+$ absorption. No difference in $\text{Na}^+$ flux is detected experimentally between CF and NCF. (B) $\text{Cl}^-$ secretion is reduced in NCF and reversed (absorption) in CF model ensemble predictions compared to experimentally determined forskolin-induced $I_{\text{Cl}}$ . (C) CF cells have markedly decreased constitutive chloride permeability (D) Paracellular permeability ( $L_{\text{PP}}$ ) is significantly increased in CF. (E) Transepithelial electrical resistance is similar between CF and non-CF cells. . . . .	75

3.7	Model validation against experimental data demonstrates acceptable model agreement in CF (A, C) and non-CF (B, D) HBE cultures. (B) In HBE 1, predicted ASL absorption is too rapid, though the DTPA prediction is in good agreement with the data. HBE 2 demonstrates acceptable agreement between model and data. Both CF lines demonstrate strong agreement between model prediction and data, even in the case of DTPA absorption in CF 2 where initial DTPA concentration is more than double the training set average (note that axis scale is not the same for panels C and D). Error bars experimental data SEM. Error bars are smaller than symbols where not distinguishable. . . . .	76
3.8	(A) by adding 10 $\mu\text{L}$ of either 1.5x concentrated Ringer's or Ringer's and mannitol solution apically to non-CF HBE, ASL volume increase is induced and paracellular DTPA convection stops for approximately the first hour after addition resulting in slow initial DTPA absorption (B). The subsequent decrease in ASL volume induces paracellular liquid absorption and convection of DTPA, which accelerates its absorption. Model estimates are in good agreement with the data. Mannitol reduces overall DTPA absorption ( $p < 0.01$ ) and promotes increased steady state ASL volume ( $p < 0.05$ ) at 24 hours compared to hypertonic Ringer's. (C) and (D) Illustrate that the small disparity in terms of magnitude of initial ASL volume increase was due to differences in initial osmolarities. (E) Cellular height decreases rapidly in response to both hypertonic challenges on the same timescale as that reported by Matsui et al. (2001). . . . .	78
3.9	By only slightly changing the initial height of the monolayer and the hydraulic permeability, the model is able to capture the data of Matsui <i>et al.</i> [9]. Envelope shows region of 95% confidence in model dynamics given the other non-CF parameters from 3.2 . . . . .	79
3.10	Individual (even occluded) cells are detectable by the algorithm. Here four non-CF HBE cells have been identified. Cilia are prominent on one of the cells.	80

<p>3.11 Recordings of normalized cell volume over time are shown for n=3 CF and n=4 non-CF cells. No difference is observed in response between cells, but the performance of the algorithm is verified. . . . .</p>	81
<p>3.12 Figure 3.12 A comparison between model-predicted counts of DTPA either (A) diffused or (B) convected in both CF and non-CF HBE. Diffusion is similar between the two cell types (A), but DTPA convection is dramatically increased in CF (B). Transcellular liquid flow (C) is predicted to be greater than paracellular liquid flow (D) in non-CF cells. In CF cells, flows through both the para- and transcellular pathway are similar, though transcellular flow is nominally increased. The increase in DTPA convection is explained by the correlation between paracellular liquid flow and DTPA absorption (<math>r&gt;0.999</math>, CF and non-CF). CF cultures convect more DTPA because they demonstrate increased paracellular liquid flow as compared to non-CF cultures. The modest increase in diffusion in CF cells is explained by the relative initial hyperconcentration of DTPA in CF cultures due to dehydration present at the beginning of the experiments (E). . . . .</p>	83
<p>3.13 Normalized DTPA retention (mean <math>\pm</math> SEM) in CF (A) cells and non-CF (NCF) cells (B). In A and B DTPA retention was measured in the presence of either an isosmotic or a 450 mOsm (150 mOsm hyperosmotic) basolateral bath. DTPA absorption is increased at 8 hours for CF challenge vs NCF challenge (*, <math>p&lt;0.05</math>) and in CF controls vs. NCF controls and CF challenge vs. NCF challenge at 24 hours (**, <math>p&lt;0.01</math>). The difference between control and challenge is significant (<math>p&lt;0.05</math>) for all CF <math>t&gt;0</math>, and NCF at <math>t=24</math> hours (unmarked). Vertical dotted lines represent differences in retention between control and challenge conditions that are significantly different between CF and NCF. (C) The difference between the control and challenge condition is significantly increased in CF over non-CF at 4 and 8 hours (<math>\Delta</math>, <math>p&lt;0.05</math>) indicating an increased acceleration of DTPA transport in CF due to the osmolarity gradient. . . . .</p>	85

3.14 FFCA is plotted against measurements of ASL volume for n=12 filters following the apical addition of 10 $\mu\text{L}$ of Ringer's. The correlation is significant and consistent with an intermediate volume range below the saturation point in Figure 2.14 . . . . .	86
3.15 Comparison of expected hydration in CF cells using either the surface area of the first 10 airway generations to calculate a 70.1 pL/s or halved (35.1 pL/s) deposition rate. Envelopes are generated from simulating the responses of the entire 8000 parameter set ensemble from model training and give the median ASL volume prediction bounded by its standard deviation. . . . .	88
3.16 Model predicted effects of deposition rate (volumetric rate/surface area) on cell-culture ASL volume using either the total surface area of the first 10 (10G, solid) or 16 (16G, dashed) airway generations are shown alongside the effects of $\text{Na}^+$ absorption rate. Deposition amount in the bronchioles has a large effect on predicted efficacy, and sodium (fast or slow) absorption has a smaller, noticeable, effect. Increased saline concentration (14%) improves hydration. . . . .	90
3.17 Comparison of expected hydration in CF cells using either the ideal 70.1 pL/s or halved (35 pL/s) deposition rate with 14%HS, which is predicted to be successful in restoring hydration. . . . .	91
3.18 The cell-scale, dynamic model (left) predicts similar patterns of ASL height by airway generation to the previously published model by Sood <i>et al.</i> , [10] (right) when considering 7% HS delivery from a Pari LC-Star nebulizer. Heights are reduced overall in the model based on inclusion of terms for liquid and $\text{Na}^+$ absorption that reduce ASL height over the 15 minutes of simulated delivery. Agreement is strong, and reduced heights at left are justifiable given that liquid addition should cause some rapid volume resorption, even in a fifteen minute time-frame. . . . .	92

3.19	Model-predicted hydration of the bronchi where obstruction has been found to begin [11] given anatomically informed deposition rates for either a $1.5 \mu\text{m}$ (tPad, solid) or $4 \mu\text{m}$ orally inhaled aerosol (Pari LC star, dashed, [10]). Acute hydration is predicted for oral inhalation of 7% HS, but not for the tPad. 14% HS (+) provides pronounced hydration at generation 9 beyond that of 7% in the tPad. . . . .	93
3.20	Three ASL volume profiles (median with SD envelope) are shown for cell-culture response to area-normalized deposition rates of either the Pari LC Star alone (magenta) or followed by the tPad at the reduced deposition (RD) rate (yellow). Combination therapy with a rapidly inhaled “priming” dose is able to maintain hydration for an overnight time duration for either HS or mannitol (cyan). However, the absence of cellular transport pathways for mannitol provides sustained hydration. . . . .	94
4.1	The algorithmic flowchart for generating PL analysis via PyMPLE. . . . .	108
4.2	Model fit to full data set is excellent for each of the four model states. . . . .	110
4.3	Profile likelihoods (blue lines) of the kinetic rate constants when all states are measured. Each parameter is identifiable at a 95% confidence level (red line). Optimal values (green dot) are close to the “true” values (purple dot) used in data generation. . . . .	112
4.4	Trajectories for each model are given. The dynamics are similar within each state and to the state behavior in the data across the ensemble of simulations. . . . .	113
4.5	Model fit to A and B is excellent, however, data for C and D were not used in the objective function, and model fit falters accordingly. . . . .	114
4.6	Profile likelihoods (blue lines) of the kinetic rate constants given only data for A and B. Only $k_{AB}$ is identifiable at a 95% confidence level (red line). Optimal values (green dot) are further from the true values (purple dot) than in the observable case. . . . .	115
4.7	Trajectories for each model are given. Trajectories for unobservable states C and D cannot be confidently differentiated from a zero-dynamics case, and span a wide range of possible dynamic forms. . . . .	116

4.8	APT-MCMC ensembles of whole-lung TcSC (top) and DTPA (bottom) clearance. Model estimates capture the data and variance (mean+ SD). Ensembles are a random selection of $10^5$ APT-MCMC simulations of $10^6$ total post-burn-in.	120
4.9	Pyomo estimates of TcSC (top) and DTPA (bottom) clearance. Model agreement with data is strong. Of note is the similarity between data sets, indicating the null result of the clinical trial. . . . .	121
4.10	Large airway clearance parameters and their APT-MCMC distributions (top row) or profile likelihoods for HS (middle) and Sham (bottom) days. Agreement is strong in all cases for both methods except for $k_{LT}$ on the Sham day (bottom left). This difference is likely due to a single anomalous patient that drives underestimation by APT-MCMC on the Sham day on population grounds. A lack of difference between days indicates ineffective treatment for promoting large airway clearance. . . . .	122
4.11	Small airway clearance parameter and initial TcSC central deposition (right column) estimates. Agreement is strong except for $k_{DB}$ on the HS day, which is likely a compensation for the slow MCC brought about by the small values of $k_{LT}$ estimated for HS. Distal MCC constant $k_{DL}$ is identifiable in the Sham case using PyMPLE. Deposition estimates are much less variable using PyMPLE.	124
4.12	Initial TcSC peripheral (left column) and DTPA deposition estimates. Agreement is good in terms of maximum likelihood estimates, but likelihood shape agreement is varied. . . . .	125
5.1	Unoptimized dosing strategy for maintaining CF ASL volumes within the SEM window about the HBE final volume. A bolus is given initially and starting at 8 hours three successive hydrating boli every four hours maintain ASL hydration above the non-CF steady state volume. Other conditions are identical to the training case of Figure 3.3 . . . . .	134
5.2	Volume absorption (left) and DTPA absorption (right) in cell cultures varies across and even within patient genotypes (panel titles as allele 1/allele 2). . .	136
6.1	Schematic of stakeholder/customer and question selection process for the focus group interview. . . . .	145

6.2	Number of cost, BCR, reliability, and flux-related questions asked by each group in FG section. . . . .	149
6.3	The distribution of customers interviewed. Each bar represents the fraction of times each customer was interviewed relative to the other stakeholders. Differences between sections were significant in the case of the nephrologist and hospital administrator ( $p < 0.05$ ). . . . .	156
6.4	Responses that demonstrate significantly different proportions between senior and sophomore students that participated in a focus group. . . . .	158
A1	Model fits to ASL volume and DTPA with added $K^+$ and more detailed transport mechanisms. . . . .	167

## PREFACE

I would be remiss if I did not first express my thanks to God for his goodness in my life and particularly in my time in Pittsburgh. The Lord has been my shelter and providence all my life and that has never been more evident than in the four and a half years I have spent here. There are so many people to thank for their help and goodness to me here as well.

I have to thank my family. To my mom, I miss you always, but I rejoice in the knowledge that you are in Paradise. As my first educator, none of this would be possible without you. I wish you were here to tear up at my defense for no apparent reason. Dad, thank you for always encouraging me. Even though we disagree about the status of civil engineers versus chemical engineers, I thank you for inspiring me to pursue this field. Alexandra, thank you for being the better twin. I don't know that anyone has contributed more to my joy and sanity than you. It was a rough four minutes without you, but I'm thankful that you've been there for me for the rest of them. Faith, you were just a baby when I left, and you're still a baby, just one that is graduating and going to college this year. Honestly, though, I couldn't be prouder of you, your adventurous spirit, and your noble character. The world is your oyster, and you will do incredible things.

There are many friends that I should thank for their support. I promised Charles McCain a shout out in my dissertation, so thank you for moving out here with me when I absolutely needed the support of a friend to do so. Ya heard me. Sunny Salh, it's always good seeing you in the weirdest places to make up for never having crossed paths when we were roommates. Thank you to Scott Owen for keeping it solid and to Kelly for bringing him here a couple times a year, and also Gigi and Randy for their support. Kevin Bell, I'm glad that you're now legally my brother. Really, I couldn't be happier about that. Thank you to the CREW guys in general, and to Ryan Paulson and Dusty Decker. To the Imfelds, especially Gretchen, I

haven't forgotten your request regarding my work in CF. I hope this dissertation is a source of hope for you. Thank you to the many families at the studio that have become second families for us, particularly my sisters, including the Arterburns, the Jenkinses, and the Stulls. Joey, thank you for the always worthy discussions of science, hockey, and faith. To my Pittsburgh friends, thank you. To the East End community, particularly Dr. Bryan McCabe and Rev. Freedom Blackwell, thank you. To Jon Mathieu especially, thank you for the mentorship and many discussions wherever free parking could be found. Everyone from the small group, it has been my great joy to study the Word and pray with you the past few years. You are constantly in my prayers. Allie, thank you for helping me lead that group. Zeke's at 6pm on Tuesdays and the unnecessary text to confirm the meeting have been a highlight of my week for many, many weeks. Eni, thanks for showing up at group and for giving me another thing to look forward to in North Carolina. Sharlee, you are so versatile, and now get to serve as the bridge between small group and department people. Thanks for being the department mom, a Sister in Christ, and always a total bro. There's always a loser's couch waiting for you if you need it. Melissa, thanks for the many hikes and shredding the gnar with me on weekends that we probably should have been working. Michael, you're the coolest Nebraskan I know. Thank you for leading Bible studies with me, bearing with much patience my awful puns the whole way through knowing that more awaited at the apartment.

To my labmates, thank you also for putting up with my terrible jokes with such patience and responding with so much insight. First, thank you to my undergrads, Jasmine, Lauren, Nick, Stacy, Sean, and Joe. You have been of much help, and I hope you were edified by your projects. Thang, thank you for the restaurant suggestions and the high energy when I needed it to start my project. Ari, thank you for the numerous philosophical discussions and the innumerable bits of knowledge (and thank you Natania for being the better half of Natari). Tim, I hope the Bills win the Super Bowl. Thank you so much for all the help and early morning coffee and for the Jurassic Park Melodica video. Christy, thank you for being not only a good labmate, but also a good classmate. I have learned much along the way with you, and I am very glad to have another friend in North Carolina as soon (hopefully very) as you finish your thesis. Megan, thank you for being so faithful in making coffee on the

many mornings when I needed it after Tim left. I think all the lab is grateful that you have left biology and embraced chemical engineering for its many wonders, but I know we are all impressed. Michelle, thank you for picking up the PyMPLE mantle and the encouragement you bring on a daily basis. Florencio, this project is yours now. It couldn't be in more capable hands. I wish that I was able to remain as a fly on wall for the Wednesday meetings. I sense that you are on the cusp of great things. Li Ang, thank you for being one of my best friends in Pittsburgh. I couldn't ask for a better confidant, gym buddy, and snow bro. And as a labmate I don't know that I've learned more from anyone.

Bob, thanks for keeping that very long list of people in line, given that I certainly didn't make it any easier. I cannot fully describe how much I appreciate your willingness to answer my questions, seemingly at every turn. I appreciate your rigor in the face of my occasional reticence and your humor in the face of my sometimes dour outlook; it has turned my desire to be good at what we do into a desire to be excellent at what we do. Tim, thank you for being a constant source of encouragement, wisdom, and humor. I have always left meetings with you feeling better about the state of a paper or project, even in my most frustrated moments when I needed it most. You always improve my work as a consequence. The two of you have been founts of knowledge and advisors in the truest sense.

Cheryl, you have also been a true advisor. Thank you for giving me the opportunity to explore engineering education in a depth that very few graduate students get to experience. It has changed my perspective on pedagogy and, I hope, improved my own ability to teach. Carol, thank you so much for asking questions of that scrub at the CF seminar three years ago. You have been an invaluable resource as a mentor as both a biologist and an engineer, and I'd like to believe that your alma mater had something to do with it. Jason, thank you for the many insights into the world of a professor at the start of their career. Your candidness has been enlightening as I aim for a similar path. Mike, thank you for the serious science and the not-so-serious science. You have been a great mentor, whether at the Tuesday lab meetings or the Friday lab meetings. And thank you to the rest of the PACCM folks: Joe, Ray, Elisa, Matt, Landon, Alison, and especially Stefanie for all the help.

There are many other people who deserve thanks. I apologize I can't thank all of you. I apologize to those who found the length of these acknowledgments obnoxious. I just have so

much to be thankful for. I came here with much uncertainty, but now I have much to look forward to. If hope and a future aren't worth expressions of gratitude I don't what is. You all have given me that, and I thank you for that, and I thank God for the many ways I am blessed by that. I hope that this work provides even a small bit of that hope for a future for those affected by CF. It is an honor to have worked and to continue to work towards treating and even curing those patients.

Then he said to me, "Prophecy to these bones and say to them, 'Dry bones, hear the word of the Lord! This is what the Sovereign Lord says to these bones: I will make breath enter you, and you will come to life.'" – Ezekiel 37:4-5

## 1.0 INTRODUCTION

### 1.1 MULTISCALAR TRANSPORT IN HUMAN AIRWAYS

Cystic Fibrosis (CF) lung disease manifests on multiple in the airway transport system. CF is caused by mutations in the cystic fibrosis transmembrane conductance regulator (CFTR) gene. Disease-causing mutations lead to defects in ion and liquid transport, as well as other cell-structure defects [5, 12, 13, 14]. In health at the molecular scale, proteins such as the epithelial sodium channel (ENaC) serve as a highly specific, single-atom gateway [13, 15], and CFTR provides an anion transport route as well as regulatory control over other transport pathways. At the cell scale, the net effect of the system of ion channels and pumps present at the epithelial surface allows for homeostatic regulation of cell volume and composition [9, 12, 16, 17]. And at the tissue scale, the coordinated efforts of cilia drive a gel-like mucus flow out of the airways taking with it inhaled particles and pathogens [18, 19, 20, 21, 22]. In patients with CF, diminished or absent  $\text{Cl}^-$  transport [4, 23] and dysregulated ion transport in transport proteins other than CFTR [3, 24, 25] lead to airway surface liquid (ASL) dehydration [24]. ASL dehydration collapses the periciliary liquid layer (PCL) beneath hyperviscous mucus, abolishing mucociliary clearance (MCC) [18]. This defect in mucociliary clearance causes patients to be more susceptible to airway infections, and the subsequent inflammation and scarring caused by chronic and recurring infections leads to bronchiectasis and respiratory failure, which is the primary cause of patient mortality in CF.

### 1.1.1 Fundamental Elements of Airway Epithelial Ion and Liquid Transport

Electrochemical potential,  $\hat{\mu}$ , is the primary driving force for epithelial transport at small scales. Gibbs Free Energy,  $\Delta G$ , also provides a thermodynamic driving force during transport against an electrochemical gradient [26]. In the case of the passive flux of a single ion across a membrane, only the membrane potential ( $E_m$ ), described by the Nernst equation (1), and the chemical potential,  $\mu$  (2), need to be considered.  $\Delta\hat{\mu}$  (3), is the sum of the chemical and electrical potential energies:

$$E_m = \frac{RT}{zF} \ln \frac{[Ion_{in}]}{[Ion_{out}]} \quad (1)$$

$$\Delta\mu = RT \ln \frac{[Ion_{in}]}{[Ion_{out}]} \quad (2)$$

$$\Delta\hat{\mu} = \Delta\mu + zFE_m \quad (3)$$

Here  $R$  is the gas constant (J/mol-K),  $T$  is the temperature (K),  $z$  is the valence of the ion, and  $F$  is the Faraday constant. The cell or its external environment, however, are not single-ion solutions. In this circumstance, the electrical potential can be balanced across a membrane (henceforth as  $V_m = 0$ ), while a partial molar driving force remains. As an example, initially equimolar solutions of  $K^+$  and  $Na^+$  could be separated by an ion permeant membrane. There would be no initial electrical driving force as the valence of both ions is the same, but their respective partial molar (*i.e.*  $\mu_i$ ) gradients would cause both species to diffuse across the membrane until electrochemical equilibrium is reached. Thus it is necessary to account for the electrical contributions of all (or the most prevalent) ions in a polyionic system. In the case of biological systems, only the electrical effects due to  $Na^+$ ,  $K^+$  and  $Cl^-$  are usually considered via the three-ion case of the Goldman-Hodgkins-Katz equation (GHK) (4):

$$V_m = \frac{RT}{F} \ln \frac{P_{Na}[Na_{out}^+] + P_K[K_{out}^+] + P_{Cl}[Cl_{in}^-]}{P_{Na}[Na_{in}^+] + P_K[K_{in}^+] + P_{Cl}[Cl_{out}^-]} \quad (4)$$

Where  $P_i$  is the permeability of the ion,  $i$ . From (4) the total electrochemical potential for transport of an ion can be determined, again as the sum of the partial molar energy and the electrical energy [26](5):

$$\Delta\hat{\mu}_i = \Delta\mu_i + zFV_m \quad (5)$$

The two terms on the right-hand-side of (5) can be thought of as diffusive and conductive driving force terms, respectively. If voltage-driven flux is assumed to be dominant, it may be beneficial to treat the system as an electrical circuit subject to Ohm's law,  $J_e = \sigma E$ , where  $J_e$  is the current density (or charge flux), with conductivity  $\sigma$ . Goldman [27] derived the flux relationship (6), assuming that the electromagnetic field is constant, that is nonlinear in terms of conductance:

$$J_e = V_m \frac{\Lambda_+ - \Lambda_- e^{\frac{RT}{F}V_m}}{1 - e^{\frac{RT}{F}V_m}} \quad (6)$$

Where  $\Lambda_+$  and  $\Lambda_-$  are upper and lower bounds on feasible conductivities, given by  $\Lambda_+ = P_i \frac{(zF)^2}{RT} [Ion_{in}]$  and  $\Lambda_- = P_i \frac{(zF)^2}{RT} [Ion_{out}]$ , respectively. Via L'hospital's rule it is evident that (6) predicts that  $\lim_{V_m \rightarrow 0} J_e \neq 0$ , which must hold true if diffusive gradients are present. In that case we have:

$$\lim_{V_m \rightarrow 0} J_e = P_i zF ([Ion_{in}] - [Ion_{out}]) \quad (7)$$

Thus, the charge flux is related to the diffusive flux,  $J_d$  via the equation  $J_d = \frac{J_e}{zF}$ . Indeed, Goldman notes that due to nonlinearities in biological systems, diffusive laws, such as Fick's law (8), may be as useful as Ohm's law relations [27] wherein:

$$J_d = P_i ([Ion_{in}] - [Ion_{out}]) \quad (8)$$

Regardless of the flux equation used, transport dynamics of solutes in biological systems can be studied compartmentally because of the compartmental organization of biology (*e.g.* cell, tissue, organ, etc.). Thus, using molar dynamics of the  $n_i$  solutes in a cell as an example,

modelers can derive systems of ordinary differential equations to describe solute influx and efflux through  $k = 1, \dots, K$  transport pathways over time as shown in (9):

$$\frac{dn_i}{dt} = A_C \sum_k^K (J_{i,k}) \quad (9)$$

Where  $A_C$  is the area of the surface (*e.g.* apical membrane) through which flux occurs. From this form, all models of epithelial solute and transport at the cellular scale relevant to this work are derived. However, it is prudent to first discuss the structure and pathways involved in the epithelial transport system.

## 1.1.2 Airway Epithelial Structure and Function

### 1.1.2.1 General Epithelial Structure and Function

Epithelial tissues are, regardless of context, interfacial tissues. The skin and the cornea are manifest examples of the interfacial function of epithelia, as they protect body systems from external threats. Internally, epithelia primarily occupy the interface between organ systems and facilitate transport between these organ systems. Intestinal epithelia serves to transport nutrients from the digestive tract to the bloodstream while also serving as a barrier to external threats; the proximal tubules in the kidney transports sodium from the bloodstream, drawing water with it; lung epithelia secrete liquid and surfactants to keep airways hydrated and alveoli open for gas exchange.

In general, epithelia have the following structural elements in common: an apical interfacial membrane, a junctional space that facilitates intercellular communication and paracellular liquid and solute transport, and a basement membrane where the epithelium attaches to connective tissues in the body. This is illustrated for a generalized epithelial monolayer in Figure 1.1.

Transport in epithelial tissues occurs through either the transcellular route - via molecular channels and pumps - or the paracellular route - via the tight junction. The tight junction is more permeant in “leaky” tissue types (*e.g.* cornea, airway, intestine) than “tight” tissues (*e.g.* kidney, bladder) where almost no paracellular liquid or solute transport occurs [28]. Although lacking information for human (or any species) bronchial epithelial cells, Table 9.3 of Charles House’s book [29] demonstrates well the order-of-magnitude differences in

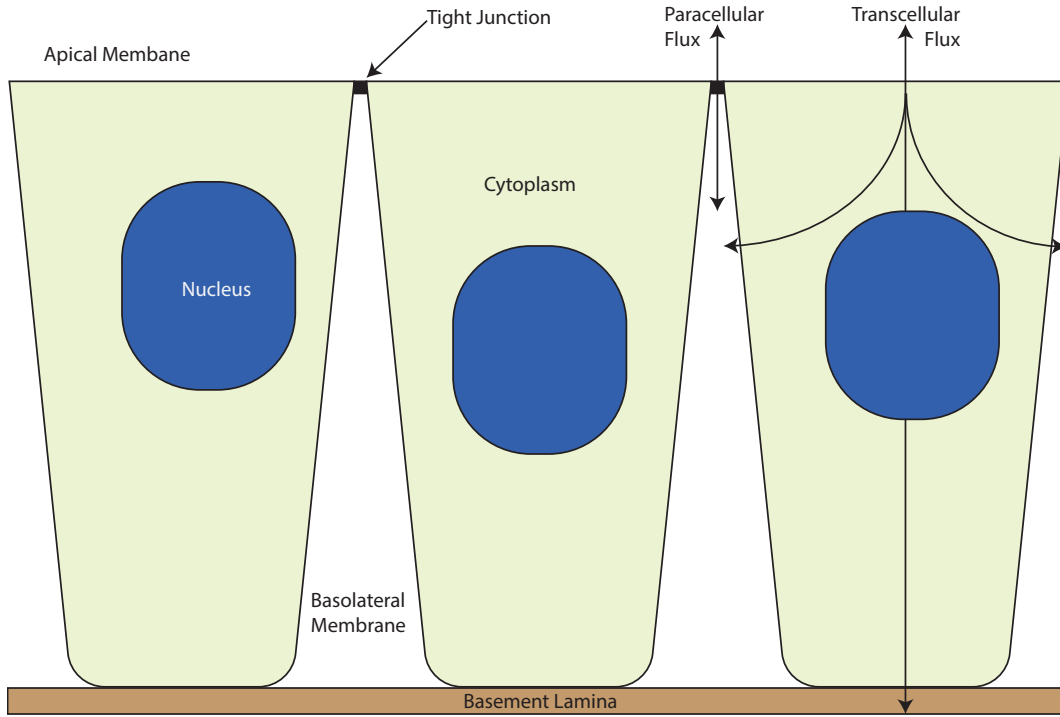


Figure 1.1: Diagram of the general structure of epithelial monolayers. Epithelial cells adhere to a basement membrane of connective tissue (or coated substrate in tissue cultures). Transcellular transport occurs in all epithelia via channels and pumps in the apical and basolateral membranes. Paracellular transport occurs through the tight junction in “leaky” epithelia, and only to a very small extent in “tight” epithelia.

hydraulic permeability ( $L_p$ ), electrical resistance and potential difference, and ion transport rate that distinguish “leaky” from “tight” epithelia.

Characterization of a tissue type as either “leaky” or “tight” has traditionally been based on electrophysiological measurements of junctional resistance. Indeed, electrophysiology has been fundamental in the development nearly all current knowledge regarding ion transport in biology. Hans Ussing’s development of the chamber that now bears his name opened the doors to investigating transport at the cell and tissue scale [30]. In that work,  $\text{Na}^+$  absorption was identified as the source of the electrical conductivity of frog skin.  $\text{Na}^+$  was considered as a possible source of the current due to previous work from Ussing that showed

net  $\text{Na}^+$  absorption across frog skin [31] where  $\text{Na}^+$  influx and efflux were measured using identical concentrations of  $\text{Na}^{22}$  and  $\text{Na}^{24}$  isotopes via the relation given in (10) [31]:

$$\log_{10} \frac{J_{in}}{J_{out}} = \frac{V_m}{58} \quad (10)$$

Thus, the electrical potential can be determined across the membrane in such a way as to assess net ion transport. As an aside, [31] also introduces the utility of radiological methods to study epithelial transport, which are discussed in detail in the subsequent chapter of this dissertation.

The Ussing chamber has improved with the advance of electronics since its invention, but its form and concept remain the same. As depicted in Figure 1.2 an Ussing Chamber consists of two large ( $\approx 3$  mL) electrolyte-containing fluid compartments separated by an epithelial monolayer.

Operation of the Ussing Chamber entails placing electrodes near the monolayer (improving the quality of the constant-field assumption) and measuring the current of the epithelia under either short- or, less-frequently, open-circuit conditions. Short-circuit current ( $I_{SC}$ ) calculations conditions require that the voltage across the monolayer be “clamped” (*i.e.* held constant at 0), which is convenient for computing net ion flux according to the Goldman equation (6). Li and colleagues provided a brief but detailed overview of the modern Ussing Chamber [32].

The Ussing Chamber can also be applied to study individual membrane potentials. Figure 1.2 shows the simplest equivalent circuit diagram of the epithelial ion transport system [33]. From this representation it is easily observed that the three general transport pathways (apical and basolateral membranes and the paracellular junction) are individual resistors that provide a measurable electrical effect and can be studied individually or together depending on experimental design. The values for apical and basolateral membrane potentials ( $V_a$  and  $V_b$ ) can be calculated using (11) and (12), respectively:

$$V_A = \frac{E_A(R_B + R_P) + E_B R_A}{R_A + R_B + R_p} \quad (11)$$

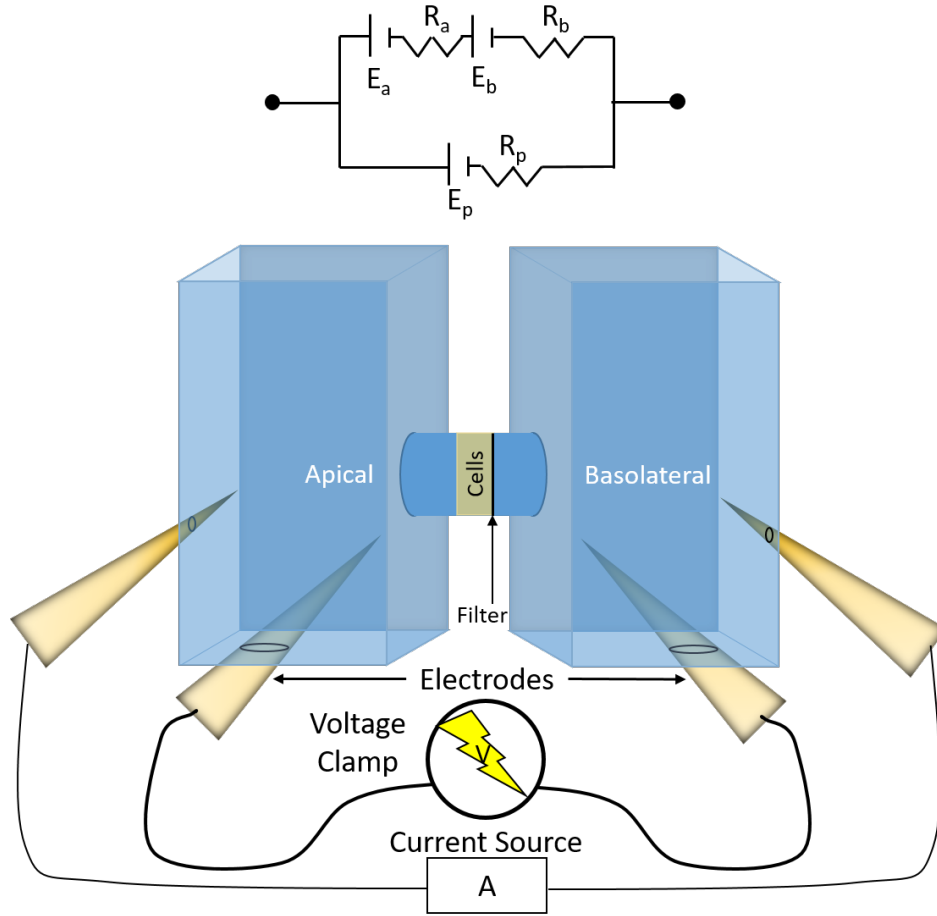


Figure 1.2: Diagram of an Ussing Chamber and the equivalent simplified circuit diagram. A cellular monolayer separates two compartments of electrolyte solution on the apical and basolateral sides. Electrodes on either side of the monolayer measure electrical current, resistance, and potential.

$$V_B = \frac{E_B(R_A + R_P) + E_A R_B}{R_a + R_B + R_P} \quad (12)$$

Here  $E_a$  and  $E_b$  are the electromotive potentials across the apical and basolateral membranes, respectively. The paracellular resistance,  $R_P$ , is due to the occluding effect of junction proteins like actin, claudins, connexins, and zonula occludens proteins [34]. The density and structure of these proteins is what largely determines the “tightness” of an epithelial

tissue type, where tighter epithelia have increased electrical resistance. The apical ( $R_A$ ) and basolateral ( $R_B$ ) resistances are related to the density of channels and transporters in the apical and basolateral membranes. Higher densities and turnover rates correlate with lower resistances. In general, the apical membrane is transport limiting and  $R_A > R_B$  due to the rapid homeostatic action of basolateral transporters like the  $\text{Na}^+/\text{K}^+$ -ATPase (NaKP), and the Na-K-Cl-Cl (NKCC) cotransporter [35].

**1.1.2.2 Airway Liquid and Solute Transport in Health and CF** The diagram in Figure 1.3 illustrates the well-described channels and transporters in the airway epithelium.

Of most importance to this dissertation is CFTR, and how its absence or dysfunction contribute to CF lung disease. CFTR has 5 protein regions [6]: two transmembrane regions that together form the anion channel, and three cytosolic regions: two nucleotide binding domains (NBD1 and 2) and a regulatory (R) domain that work in concert for channel gating. Its structure is depicted in Figure 1.4.

For gating to occur, CFTR requires phosphorylation by protein kinase A (PKA) in its R domain, which serves as “gatekeeper.” The phosphorylation in R domain causes a conformational change that allows NBD1 and NBD2 to interact and hydrolyze ATP, thus opening the gate [6]. Mutations in the NBD1 coding region are the most common sources of CFTR dysfunction leading to disease, but location is not considered a primary factor in disease classification. Currently, there are six classes of disease-causing CFTR mutations [36]:

1. No full length CFTR produced due to a nonsense mutation near the C-terminus
2. Little or no CFTR trafficked to the membrane. The most common mutation,  $\Delta\text{F508}$ , is of this class.
3. The gating of the ion channel of CFTR is affected. Ivacaftor [37] is approved to treat many mutations of this class.
4. The conductance of CFTR is reduced.
5. The synthesis amount of CFTR is insufficient.
6. CFTR is less stable in the membrane.

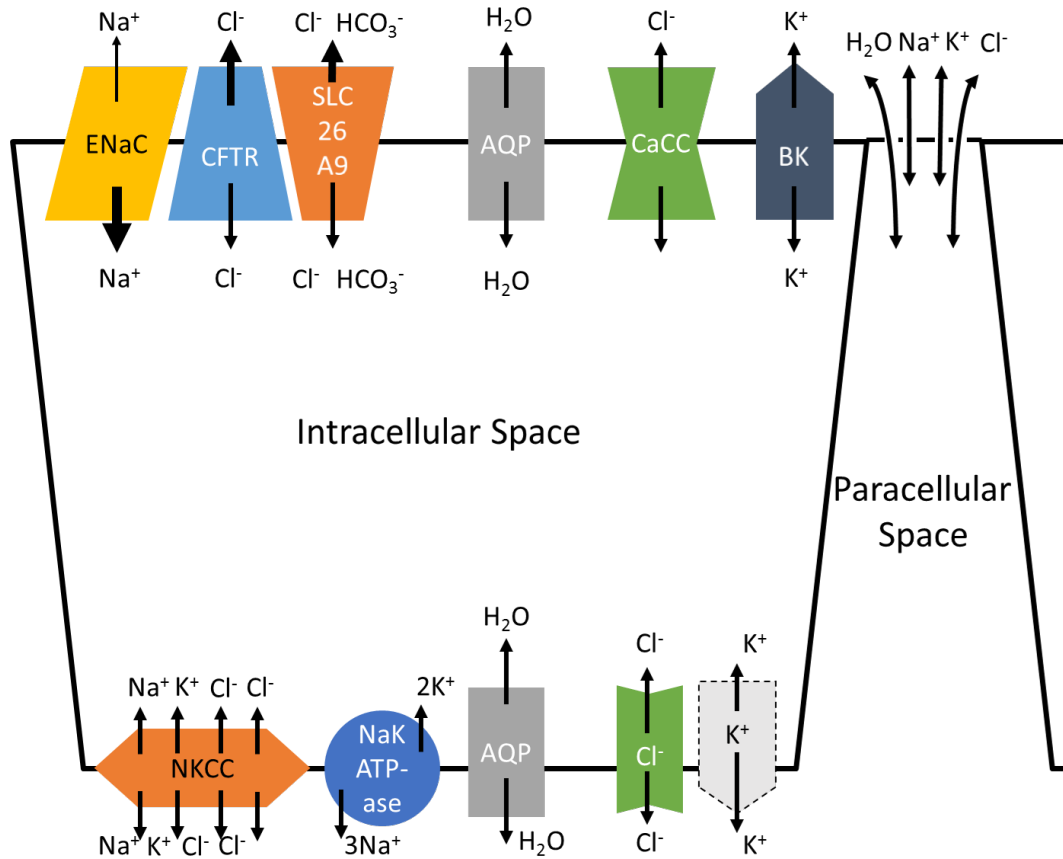


Figure 1.3: Known pathways for liquid and ion transport in airway epithelia. CFTR is thought to regulate ENaC and SLC26A9 through intracellular signaling and other domain interactions [2, 3]. Other passive  $\text{Cl}^-$  and  $\text{K}^+$  channels exist in the apical and basolateral membranes (though basolateral  $\text{K}^+$  channels are more speculative). Active, dedicated  $\text{Cl}^-$  transport also occurs in the basolateral membrane, where  $\text{Na}^+$  and  $\text{K}^+$  are also actively transported with and without  $\text{Cl}^-$ . HBE are “leaky,” thus they also have a high degree of paracellular water and small solute transport [4, 5].

Type 1 mutations are usually very brief truncations of CFTR due to a mutated stop codon in the gene. They make up roughly 10% of the patient population [38]. The type 2 deletion of the phenylalanine at position 508 (part of NBD1) in CFTR ( $\Delta\text{F508}$  as a genotype) is the most common CF-causing mutation, present in  $\approx 85\%$  of patients with

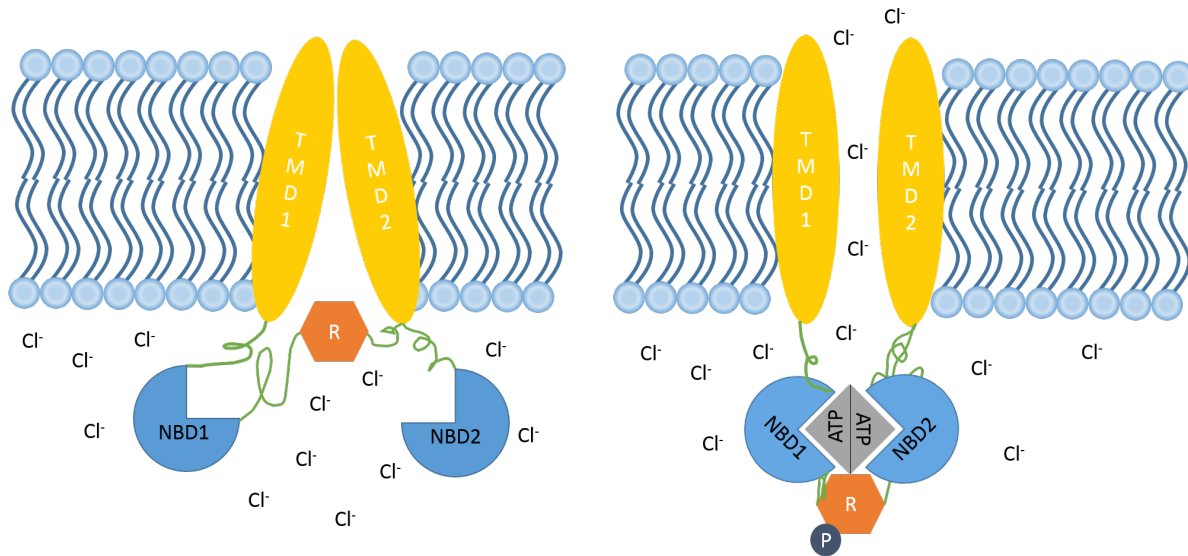


Figure 1.4: CFTR in its closed state (left) does not allow  $\text{Cl}^-$  or other anions to pass through the apical membrane. Once the R domain is phosphorylated, the NBDs will interact to hydrolyze 2 ATP causing a gating event that allows  $\text{Cl}^-$  to move down its electrochemical gradient. Adapted from [6]

CF [39] and  $\approx 45\%$  are homozygous for the  $\Delta\text{F508}$  allele [40]. Roughly another 5% of patients bear a type 3 disease causing mutation (*e.g.* G551D or G551S) in the NBD1 encoding region of their genome [41]. These type 2 and 3 mutations prevent proper gating of CFTR, and thus show no electrochemical sensitivity to stimulation by forskolin, which stimulates PKA [37]. This has been useful in the identification of pharmaceuticals to treat defective CFTR directly, as evidenced by the fact that the only currently approved CFTR modulators are the "potentiator" ivacaftor [37,41] in type 3 mutations and the "corrector" lumacaftor [40,42] for  $\Delta\text{F508}$  homozygote patients in combination with ivacaftor. These two drugs cover roughly 50% of the patient population, which is a promising advance in the field of treating CF. Investigation into these types of targeted therapies will continue [43] and no doubt should. However individual patient response to treatment is varied, particularly in the case of the lumacaftor-ivacaftor combination therapy [40,44]. With more than 2,000

different disease causing mutations [45] and interpatient variability even within genotypes there is still a need for better generalized therapies that can treat 100% of patients effectively and also affordably. Therapies like hypertonic saline and ibuprofen can accomplish similar improvements in lung function as the combination therapy [40], but cost 2 to 4 orders of magnitude less per year [46]. The promise of systems medicine in this case of generalized therapies is that mathematical models can provide optimized and personalized dose and treatment scheduling for every individual patient, which is a primary motivating factor for this thesis. To do so requires a systems understanding that studies disease effects at a much broader systems scope than CFTR alone.

**1.1.2.3 The Airway Transport System** At the cell scale, the primary effects of absence or dysfunction in CFTR occur in the apical membrane and result in airway surface liquid (ASL) dehydration. ASL dehydration, in turn, causes mucociliary clearance failure due to the increased viscosity of the mucus. Inhaled pathogens and particles become entrapped in the static mucus and leading to infection, inflammation and fibrosis. This process is detailed in Figure 1.5

CFTR is both a chloride channel and a transport regulator; it regulates ENaC through PKA [2, 47] and members of the solute carrier 26 (SLC26) family through its R domain [48], in some cases forming a  $\text{Cl}^-$ - $\text{HCO}_3^-$  exchange complex [3]. Obviously, these pathways are directly affected by the absence or dysfunction of CFTR that is the cause of CF. Intuitively, the severity of CF as a disease is an indicator of the relative importance of these apical pathways for transport in health. The role of ENaC in  $\text{Na}^+$  transport has already been discussed, but its importance is further highlighted in CF where absence of CFTR leads to increased  $\text{Na}^+$  (thus, also liquid) absorption [2, 49]. SLC26A9 has constitutive  $\text{Cl}^-$  transport activity that is significantly decreased in CF cells [3].  $\text{Ca}^{2+}$ -activated  $\text{Cl}^-$  channels (CaCC) in the lungs, particularly transmembrane protein 16A (TMEM16A), are thought to be the only remaining  $\text{Cl}^-$  secretion route in CF [24, 50]. Apical  $\text{K}^+$  conductance through the large conductance  $\text{Ca}^{2+}$ -activated  $\text{K}^+$  (BK) channel has also been postulated to assist in the maintenance of ASL volume [51]. Any net flux of ions through the apical membrane will also cause osmotic water transport through aquaporins (AQP) in the same direction; AQPs also

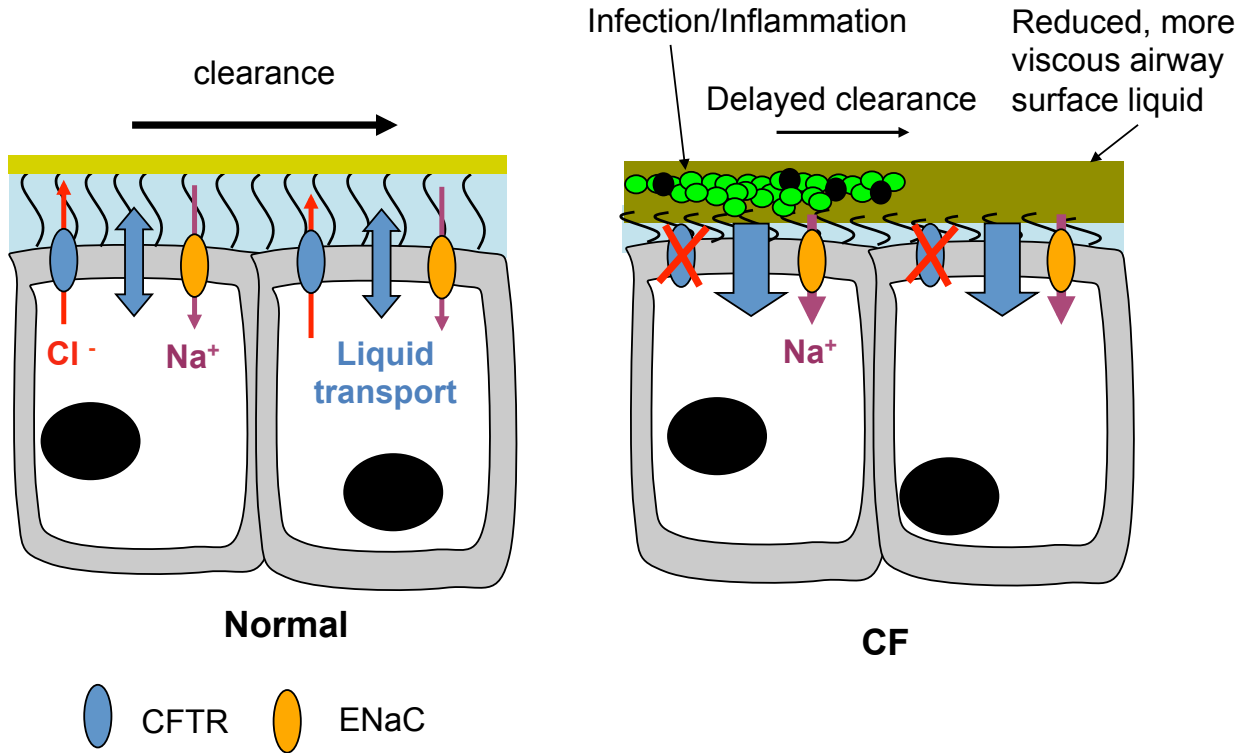


Figure 1.5: Normal ASL/PCL (depicted in light blue) homeostasis and MCC are maintained by proper function of CFTR and ENaC at the apical membrane of the airway epithelium (left). In CF (right) the ASL becomes dehydrated due to the absence of CFTR and subsequent dysregulation of  $\text{Na}^+$  absorption via ENaC. Mucus becomes viscous and unclearable, leading to chronic infections and subsequent inflammation and scarring.

facilitate water transport in the basolateral membrane. Schreiber and colleagues suggested that CFTR also regulates AQP-3 in the airways, in addition to its regulation of other ion channels [52].

Basolateral transport primarily maintains cellular homeostasis in terms of volume and electrochemical properties, including pH. The primary transporters involved are NKCC, which transports a  $\text{Na}^+$  and  $\text{K}^+$  with two  $\text{Cl}^-$  electroneutrally [53], and NaKP, which maintains the high intracellular  $\text{K}^+$  concentration through ATP-driven pumping in an electrogenic exchange of 2  $\text{K}^+$  for an efflux of 3  $\text{Na}^+$  [54,55]. There are other anion channels that transport

$\text{Cl}^-$ , including volume sensitive outward rectifying channels (BORC) and inward rectifying channels (BIRC) [55]. The presence of a basolateral  $\text{K}^+$  channel has been reported [56]. The contribution of non-transporter routes for  $\text{K}^+$  is likely small and negligible for  $\text{Na}^+$ .

As discussed previously, HBE are leaky. There is little question whether ions move paracellularly through the junctional space, and most solutes with hydrodynamic radius  $<3.8$  nm will also traverse the junction [57]. However, there is a large divide in the field about whether water primarily traverses the junctions or even does so at all. Hill and Shachar-Hill [57, 58] and Fischbarg [59, 60] advocate a predominantly paracellular route for liquid transport. Ruess [61], along with MacLaren and colleagues [62], have stated that paracellular water transport is unnecessary to explain the transport behavior observed in leaky epithelia. Spring and his students have published strong evidence against paracellular transport in Madin-Darby canine kidney (MDCK) cells [63], but Spring was less inclined to make a claim in favor of either side of the debate [64].

Recent work has sought to address at least part of question in human bronchial epithelia. Using a two-probe functional imaging method wherein inhaled non-absorbable large molecule  $\text{Tc}^{99\text{m}}$ -labeled sulfur colloid (TcSC) and absorbable small-molecule  $\text{In}^{111}$ -labeled DTPA (DTPA), it has been determined that DTPA is hyperabsorbed in the airways of patients with CF [8, 21]. It has also been observed that there is an *in vitro* correlation between the absorption of DTPA and liquid absorption in HBE cell culture [65]. DTPA can only traverse the paracellular space of the epithelium. Paracellular liquid transport likely influences DTPA transport via convection. Identifying the convective effects requires an understanding of the other primary driving mechanism for paracellular transport of DTPA: diffusion. This is facilitated by the use of a mathematical model as stated in [59].

## 1.2 MODELING ACROSS BIOLOGICAL SCALES

### 1.2.1 Modeling Epithelial Solute and Liquid Transport at the cellular scale

**1.2.1.1 Systems Biology Overview** Systems biology is an expansive field. In one sense it is the application of systems analysis and engineering tools to study of biology. In another, more philosophical, sense it is an alternative to the traditionally reductionist approach in biology. Whereas biological research often studies the components of life as individual elements, systems biology focuses on the synergistic interactions of those elements and the systems processes they drive. The interactions of operations within a system can be formally modeled; those interactions in biological systems are no exception. The interactions of molecules and cell and organ processes in biology are what give rise to life and health or disease. In his seminal review [66] Hiroaki Kitano cited four primary areas that could be elucidated through the use of a systems approach: systems structures, dynamics, control, and design methods. Systems structure concerns the network of elements that comprise a system while dynamics concern the time-dependent behavior of those elements and the subsequent evolution of the network. Understanding the structure and dynamics allows for the application of control over states in the system through external inputs (*e.g.* therapeutics) and design of favorable interactions or interventions to affect system output in a desired manner. Jonathan Bard [67] describes the aims of systems biology from the perspective of a biologist as two-fold: the narrow aim focuses on protein network interactions (but not the reductionist understanding of protein functionality); the broader aim seeks to relate molecular interactions in the cell to phenotypic outputs.

Indeed, the equations from Section 1.1.1 fit into the first two categories proposed by Kitano. The GHK equation 6 is built upon the structure of an electrochemical system, and it describes the dynamic, passive movement of ions across a membrane. The often complicated tasks that are accomplished by enzymes and other proteins can also be viewed as chemical

reaction sequences that are well-described by mass-action kinetics. As an example of mass action kinetics, the Langmuir-Hinshelwood mechanism of catalysis on a surface is:



Takes a reactant  $A$  that associates and dissociates in an elementary way with catalysis site  $S$  given kinetic rate constants  $k_1$  and  $k_2$ , respectively, to form reaction intermediate  $AS$ . This intermediate is converted into product  $B$  with constant  $k_3$  and the catalysis site is unchanged. If  $S$  is imagined to be the binding pocket of an enzyme or transport protein it could be assumed that the mathematical form that governs enzymatic conversion or transport of  $A$  over time should be the same as the Langmuir-Hinshelwood expression:

$$\frac{dA}{dt} = -\frac{k_3 A}{\frac{k_2}{k_1} + A} \quad (1.2)$$

And this is indeed the case with the modification that because the enzymatic reaction occurs in the aqueous phase, the right hand side should be multiplied by initial enzyme concentration,  $S_0$ . Then by observation, when  $A \gg \frac{k_2}{k_1}$  the rate  $\nu = \frac{dA}{dt} \approx k_3 S_0$  is at its maximum, hence  $\nu_{max} = k_3 S_0$ . By defining  $K_M = \frac{k_2}{k_1}$  and calling it the Michaelis constant, the ubiquitous Michaelis-Menten equation of systems biology is obtained:

$$\frac{dA}{dt} = -\frac{\nu_{max} A}{K_M + A} \quad (1.3)$$

Equation forms for active transport through NaKP [54,68] and NKCC [53,69] stem from the mass-action kinetic descriptions of the reaction network structure of each transporter. As examples, the rate equation of Lindenmayer and colleagues [54]:

$$\nu_{pump} = \nu_{pump,max} \left( \frac{Na_C}{Na_C + K_{int,Na}(1 + K_C/K_{int,K})} \right)^3 \left( \frac{K_B}{Na_B + K_{ext,K}(1 + Na_B/K_{ext,Na})} \right)^2 \quad (1.4)$$

Reflects the stoichiometry of NaKP in its exponents as well as an inhibitory terms in the denominator for pumping against concentration gradients in the cell interior (*int*) or exterior

(*ext*), but the Michaelis-Menten components of their mass action derivation are recognizable. More obvious still are these elements in the NKCC equations of Miyamoto and colleagues [53]:

$$\begin{aligned} \nu_{NKCC} = & \nu_{NKCC,max} \left( \frac{Na_B}{Na_B + K_{Na}^{CO}} \right) \left( \frac{K_B}{K_B + K_K^{CO}} \right) \left( \frac{Cl_B}{Cl_B + K_{Cl,1}^{CO}} \right) \left( \frac{Cl_B}{Cl_B + K_{Cl,2}^{CO}} \right) \\ & - \nu_{NKCC,max} \left( \frac{Na_C}{Na_C + K_{Na}^{CO}} \right) \left( \frac{K_C}{K_C + K_K^{CO}} \right) \left( \frac{Cl_C}{Cl_C + K_{Cl,1}^{CO}} \right) \left( \frac{Cl_C}{Cl_C + K_{Cl,2}^{CO}} \right) \end{aligned} \quad (1.5)$$

Where the basolateral ( $B$ , inward) and cellular ( $C$ , outward) rate terms are the product of a Michaelis-Menten term for each transported ion. While somewhat reductionist, these rigorous studies on molecular function have found utility in a number of undeniably systems-focused models [16, 17, 70] of epithelial physiology.

An example of systems biology in the broader sense at work in epithelial transport would be that of Bertrand and colleagues [7]. They employed a model of exocytosis based on membrane electrical characteristics. Using standard parameter estimation techniques with 5 parameters they were able to characterize exocytosis events in goblet-like cells based on an increase in monolayer capacitance and resistance. This simpler model, self-described as "lumped", makes good on one of the promises of systems biology: emergent biological behavior can be characterized by simple, physically grounded models [71].

An extension of model prediction and analysis is the use of models for process control and design, which are more relevant from an engineering and clinical applications perspective. The primary goal of process control is to maintain desired process operation conditions (setpoint tracking) in light of external perturbations (disturbances). In medicine, good patient health is the desired operating condition and disease can be viewed as a disturbance to that process. Traditionally, medicine has operated solely under physician control (under the strong assumption of patient compliance), as illustrated in Figure 1.6. This comprises both the obvious feedback regime wherein a doctor makes treatment decisions based on patient charts, as well as feedforward control (*i.e.* prophylactics). However, biological nonlinearities produce synergisms that often obfuscate underlying causes of disease and lead to unexpected side-effects. The fundamental assumption of this dissertation is that physician decisions are most often good, but usually based on linear disease-treatment expectations that could be improved if personalized, model-based predictions of patient response to treatment are given to support clinical actions. This clinical decision support system (DSS) or treatment design scheme is given Figure 1.6.

In this paradigm, final treatment decisions are solely in the hands of the physician, but they are informed by rigorous, quantitative predictions of a course of therapy that is optimal within measurement error and timing. This paradigm has been explored in a number of fields: in cancer chemotherapy [72, 73, 74, 75] and neutropenia [76]; in glucose

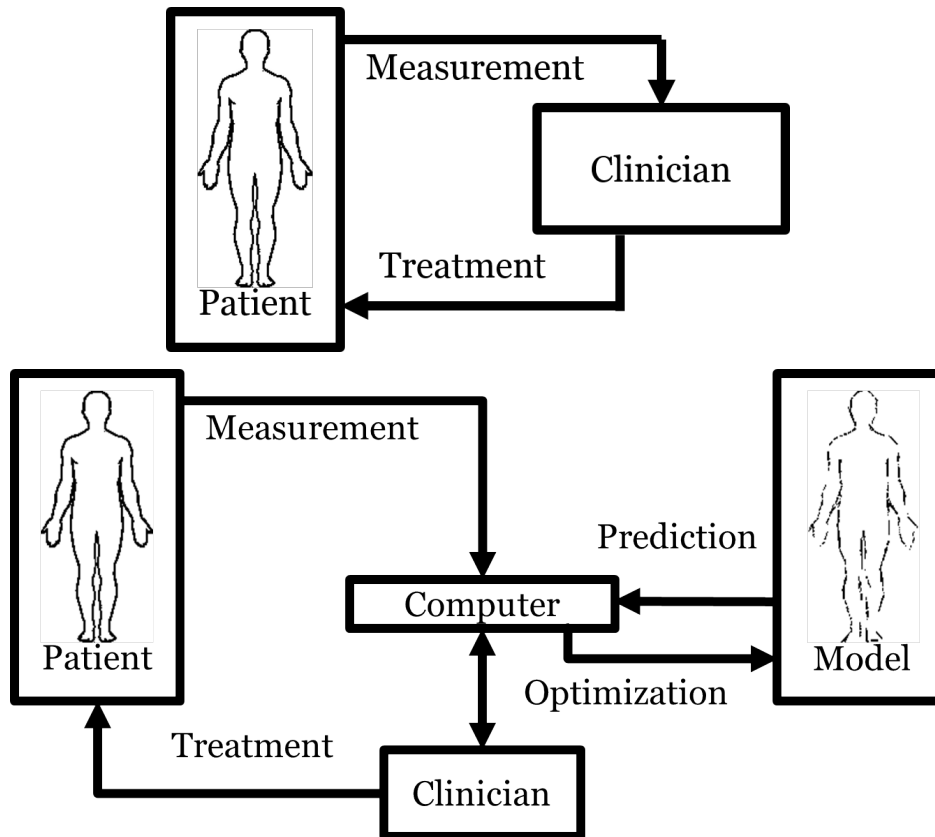


Figure 1.6: **Top:** Standard-of-care Physician-Patient treatment feedback loop. **Bottom:** A clinical DSS for treatment design using model-informed physician decisions for patient care.

control in diabetes [77, 78, 79, 80] and critical care [81, 82]; in sepsis [83, 84] and many other diseases [85, 86].

### 1.2.2 Systems Biology in Airway Transport at the Cellular Scale

Most of the mathematical models used in the the study of epithelial liquid and ion transport have been utilized for their structural and dynamical insight. Beginning with Hartmann and Verkman [87], differential algebraic equation (DAE) models have been used to predict ion fluxes in airway epithelia. Their work was able to roughly match experimental data from the Ussing Chamber in dog trachea, but they did not account for dynamic cell volumes due

to water flux, nor did they evaluate paracellular transport. Novotny and Jakobssen [88, 89] made a significant step forward in airway modeling by accounting for liquid and ion transport in the paracellular space while also modeling cell volume regulation in the thin-film environment of native airway. They also considered how CF might effect transport [89]. The structure of their model is physiologically detailed and produces accurate estimates of homeostatic liquid volumes and transport processes over the minutes-length time scale of Ussing Chamber experiments. However, their numerical integration method - Euler integration with algebraic electrical constraints solved via Newton's method at every step - is unstable over time periods of simulated hours. Falkenberg and Jakobssen [55] translated the Novotny model from Fortran into Matlab and added pH regulation. Despite the change of programming language - and the more advanced DAE solution capabilities of the Matlab program - the Euler-Newton differential algebraic equation solution approach from [88] was preserved. Thus, modifications to the integration approach used for their model would need to be made to provide long-term model stability. Fischbarg and Diecke [90] developed a similar model of fluid and electrolyte transport that accounted for paracellular water and flux in the corneal epithelium that calculates similar flux values to those of [87]. Also in the eye, Zhu and Chauhan [91] developed a model of tear dynamics that accounted for the electroosmotic effects involved in liquid and ion transport. Terashima and colleagues developed a model that described volume regulation of cardiac cells that accounted for many similar transport mechanisms to those in the airway epithelium [92].

In 2013, two ODE models of airway liquid and transport in nasal epithelia were presented by different groups that were very similar structurally and parametrically. The first model, by Garcia and colleagues [16], differs in terms of pathways represented in the second model, by O'Donoghue and colleagues [17], only by the addition of apical  $K^+$  transport. Both models used Monte Carlo methods to estimate model parameters and used Ussing Chamber data from the same experiments performed by Willumsen and Boucher [56, 93]. In terms of scope, Garcia and colleagues demonstrated that nasal epithelial transport parameters could be readily identified using a mathematical model [16]. O'Donoghue and colleagues extended that finding by also asserting their model prediction that CF cells demonstrate increased  $Na^+$  permeability, which has been reported experimentally in human bronchial epithelia [2, 49].

The primary utility of both studies is stated as the rapid prediction of HNE culture transport behavior in Ussing Chamber experiments.

The Ussing Chamber is not, however, representative of the *in vivo* environment of the airway epithelial tissues. HNE and HBE have a semi-infinite basolateral fluid reservoir in the bloodstream, but they exist at a "thin-film" air-liquid interface (ALI). Airway cells homeostatically regulate the ASL volume and composition [12, 94] while also maintaining their own internal volume and composition [9]. It is known that ENaC and CFTR are regulated by the ASL volume [13, 49]. The characteristic "ramp-up" behavior of  $I_{SC}$  observed in Ussing Chamber experiments using airway epithelia is due to the effect of ASL flooding on ENaC permeability [13], and is a clear visualization of the switch between thin-film and flooded transport paradigms. Other transport effects such as fluid secretion due to phasic shear stress acting on purinergic signaling pathways is only observable in the thin-film environment [24, 49, 95]. The thinness of the thin-film makes ion transport difficult to measure - though it can be done with more specialized electrodes [12] - since the electrodes used in Ussing Chamber experiments cannot be sufficiently submerged in the native ASL, which also hinders comparison of ion transport in the two regimes. These discrepancies motivate developing measurement methods and models that can describe liquid and solute transport in the physiological thin-film setting.

The most readily accessible dynamic observable in the thin-film is ASL height (at the center of the cell culture) [5, 9, 12, 70, 96]. Height does not correlate with measurements of volume [65, 97], which are usable in the thin-film or otherwise. Therefore, it may be more useful to inform thin-film models using ASL volume data.  $\text{Na}^+$  and  $\text{Cl}^-$  concentrations are easy to obtain as they can be measured in the thin film using flame emission or small electrodes [12, 94]. Intracellular volume can be measured as well via fluorescence microscopy, which useful in informing homeostatic mechanisms present in homeostatic models. ATP and  $\text{Ca}^{2+}$  concentrations have also been measured over time [24, 95, 98]. Each of the aforementioned thin-film measurements could be useful for modeling the liquid and solute transport process involved in maintaining homeostasis in the cell and ASL. To date, however, thin-film models have only used ASL and cellular height/volume [70, 96] and ATP [96] to inform or test their predictions. The model of Warren and colleagues [70] is similar in structure to

many of the electrophysiological models of liquid and solute transport processes in the literature (that of O'Donoghue and colleagues [17] is modeled after it) with full treatment of ion fluxes using the GHK equation 6. It also considers the effect of a step change in intracellular  $\text{Ca}^{2+}$  (due to osmotic or other stress) on  $\text{Cl}^-$  secretion via CaCCs. The step change is a somewhat arbitrary simplification of the  $\text{Ca}^{2+}$  response seen in physiological cell stress, but serves to improve model fit. The model by Warren *et al.* does not account for paracellular liquid transport or the known ASL regulation effects on ion transport, providing a clear path forward for future models. The other thin-film model by Herschlag and colleagues [96] is interesting in its parsimony. They take an ion-agnostic perspective, accounting for only the general effect of cation and anion transport and purinergic signaling on ASL volume regulation. Their successful incorporation of a phasic shear stress model of ASL regulation is a novel notion in the modeling literature as well.

The stated research scope of these aforementioned models is directed toward the benchtop study of airway liquid and solute transport and the identification of new therapies. Currently none of these models have been used in a manner considering disease control and therapeutic design possibilities. This presents an opportunity to use systems biology tools in a novel way within a field where so much of the experimental data is generated from devices meant for experimental control and design. As a motivating point, regardless of the epithelial transport process studied, the Ussing Chamber is an important engineering tool because it allows for the control of an entire physiological transport system using only voltage and current measurements. Furthermore, it allows for input design that can elucidate model parameters [7]. This was illustrated by Bertrand and colleagues wherein the control aspect was addressed in the first figure of [7] (reproduced with permission in Figure 1.7), and design was one of the featured results of that work.

One of the takeaways from Figure 1.7 should be that the concepts of control have been generally introduced to the field of epithelial biology through the Ussing Chamber. If adopted and applied more widely in the field, control and also design of epithelial response to external inputs (*i.e.* therapies) could be used to effect better patient care in CF and other diseases of epithelial origin. This notion is one of the essential motivations for this thesis. Ultimately, though, any design that does not account for returning mucociliary clearance in patients

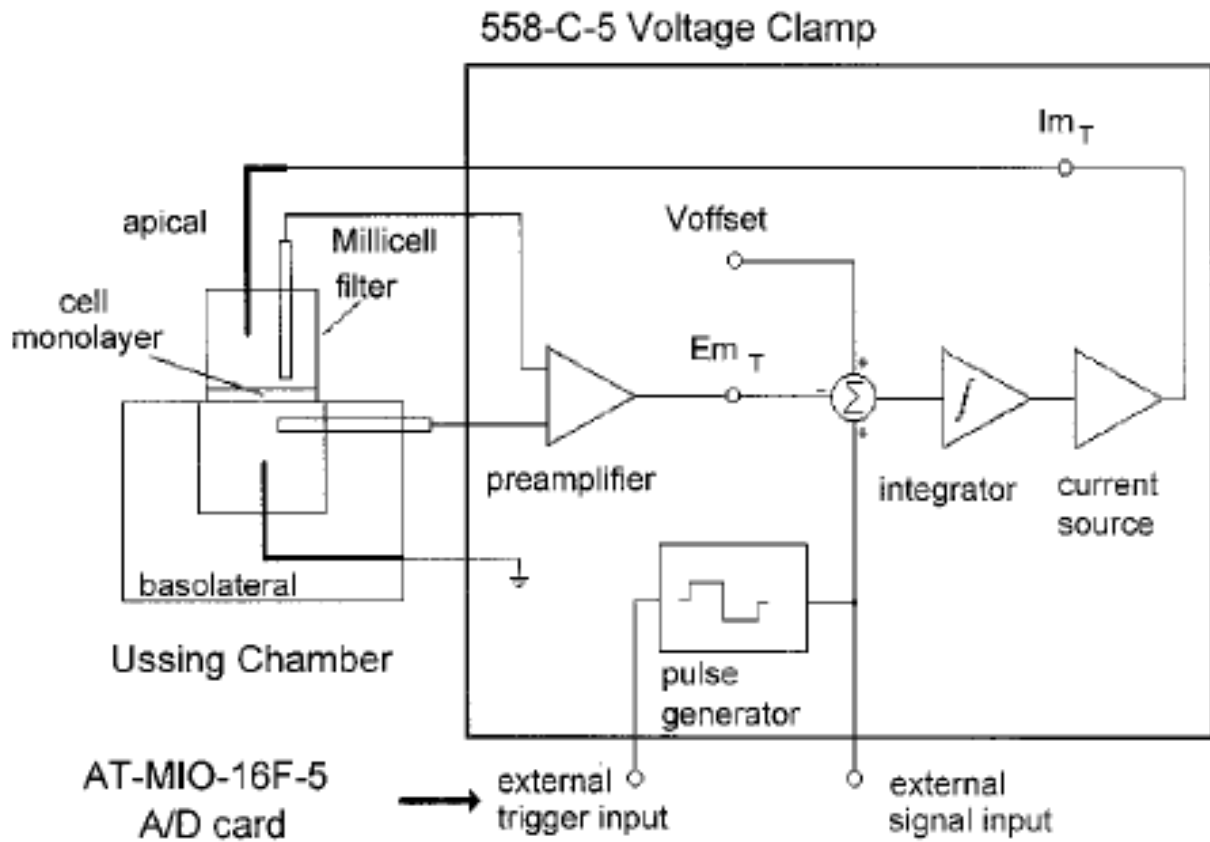


Figure 1.7: Detailed layout of voltage clamp with feedback control loop evident as part of transepithelial impedance measurement hardware (reproduced from [7] with permission). Inputs and set-point ( $V_{offset}$ ) illustrate the essential components for biological control in the Ussing Chamber.

with CF will fail to account for what is a key setpoint maintaining patient lung function. This must be accomplished by also modeling airway transport on the whole-lung scale.

### 1.2.3 Systems Biology in Airway Transport at the Organ Scale

Measurements of MCC have long been used to gauge treatment response in patients with cystic fibrosis and are now an accepted biomarker to that end [99]. The recently developed

method of measuring DTPA absorption in the lung has also shown utility for indicating therapeutic benefit [1,8]. These studies usually produce data-dense time-series measurements of particle clearance, which are well-suited for model-based analysis.

Incidentally the field of pharmacokinetic (PK) modeling focuses on the routes by and the rates at which compounds of interest are cleared from the body. At the most basic level, PK models can be empirical statistical estimates of residence time in the body given as an area under a clearance curve (AUC) [8,100]. Added detail is provided with the use of "compartments" that partition drug disposition in the body into model states that interact with other compartments via specific clearance rates. These model compartments can be purely mathematical constructs [101,102] or represent the transport that occurs between organs and tissue in the body [103] or more often a combination of the two [1,80] with varying degrees of detail.

Most of the literature on PK studies in CF focuses on antibiotics and antifungals [101,104,105,106,107,108,109,110,111,112]. While some of these studies involve oral or intravenous administration of the therapeutic of interest, none of the existing inhaled compounds for CF lung infections - tobramycin [101,105], colistin [108,113], aztreonam [114], and levofloxacin [115] - utilize mechanistic compartment-based PK models.

In fact, few compartment based models of lung clearance exist that account for the effect of MCC on an inhaled drug [116]. One such model has been used to characterized insulin delivery in isolated perfused rat trachea [117], and another described the PK characteristics of inhaled corticosteroids [118]. In the aforementioned studies, pharmacodynamics (*i.e.* the description of drug efficacy over time) are also relevant, but may be considered separately. PK descriptions of radiopharmaceutical lung clearance are odd in that the probes used to measure MCC and absorption have no pharmacodynamic effect [8,21]. However, in the case of treating patients with CF PK models of probe MCC can be used to directly gauge the PD of mucociliary-targeted therapies. The addition of probe absorption to PK models of MCC can then also assess the PD of absorption-targeted therapies through the strong correlation between probe absorption and liquid absorption [65]. Moreover, describing the causality of this correlation requires a detailed mechanistic focus on airway epithelial solute transport. Such a multi-scalar understanding of airway transport would not only allow

for PK-PD characterization of therapies. Rather, this description could be used to design optimal treatment schedules for patients with CF.

#### 1.2.4 Dissertation Overview

Lung disease is the primary cause of mortality for patients with Cystic Fibrosis. Failure in the mucociliary apparatus due to airway dehydration prevents inhaled particles and pathogens from being cleared out of the lung, leading to infection, inflammation, and bronchiectasis. Rescue of mucociliary clearance, either via direct hydration or restoration of CFTR function and/or correction of the concomitant ion transport defects should improve respiratory function in patients with CF. Therefore, a robust, physiologically motivated mathematical description of mucociliary clearance in the lung could be useful as predictor of therapeutic benefit. The addition of a model of solute absorption in the lung could provide additional understanding about therapeutic effect and provide a link to the *in vitro* observations of correlation between ASL liquid and solute absorption. This is the focus of [chapter 2](#). The resultant model described [Chapter chapter 2](#) has simple kinetic parameter descriptions of TcSC and DTPA clearance with an added physiological parameter, the fraction of functional ciliated area/airway (FFCA), that is decreased in patients with CF and in CF cells *in vitro*. FFCA is increased both *in vivo* and *in vitro* via hydration, particularly by way of inhaled hypertonic saline, a therapy in CF. FFCA is therefore a trans-scalar parameter that relates CF lung disease at the organ scale down to a cell-scale defect.

The lung-scale description of DTPA absorption in [chapter 2](#) is useful in demonstrating clinical benefit of therapies with physiological grounding. However, it does not explain the mechanisms that lead to increased MCC through increased FFCA, nor does explain the DTPA hyperabsorption present in the lungs of patients and its abrogation via osmotic therapy. [chapter 3](#) begins to address these shortcomings through development and analysis of a detailed mathematical model of cell-scale liquid and solute transport. The resultant model accurately captures liquid and DTPA transport behavior from data, and the coincident ion fluxes are within reported values despite being an emergent property of the model state and parameter values. The model structure is robust and physiologically reasonable vari-

ations in the parameter values allow for the identifiability of individual patient transport characteristics. Also presented is a detailed analysis of treatment failure in an investigative hypertonic saline delivery device. Identification of most-likely failure modes informs the design of theoretically more effective treatment formulations or dose schedules.

[chapter 4](#) presents a newly developed parameter identification tool that assesses practical identifiability via the profile likelihood in the Pyomo modeling environment. A series of case studies focuses on the interrelation of model observability and identifiability through a canonical chemical engineering reaction system and the Chapter 2 lung-clearance model. [chapter 5](#) will provide perspective and prospective insight regarding future improvements in modeling airway epithelia and treatment design in Cystic Fibrosis, including a proposed optimal treatment formulation.

The final chapter, ([chapter 6](#)) details a research project performed in parallel with the main topic of this thesis. The academy is not only responsible for the collection of knowledge but also its dissemination and the optimization thereof. Accordingly, this thesis also contains research on the effect of external stakeholder input on engineering product design. This work was performed using data recorded from the notebook responses of undergraduate chemical engineering students. Primary focus was directed toward understanding how customer and external stakeholder voice could affect final product performance and economics for the benefit of product users. Within that investigation, considerations were made regarding both quantitative and qualitative student outputs as well as for student experience level.

## 2.0 PHYSIOLOGICALLY RELEVANT LUNG-SCALE MODELING OF MUCOCILIARY AND ABSORPTIVE PULMONARY CLEARANCE

### 2.1 MUCOCILIARY CLEARANCE AND ABSORPTION IN THE LUNG

Cystic Fibrosis (CF) is an autosomal recessive disease that arises from a defect in the Cystic Fibrosis Transmembrane Conductance Regulator (CFTR) gene. CF affects multiple organ systems, with the most detrimental effects occurring in the lungs [119]. CFTR encodes an anion channel on epithelial surfaces, that is dysfunctional or absent from the CF epithelium. The associated loss of  $Cl^-$  and  $HCO_3^-$  secretion along with a tendency to hyperabsorb  $Na^+$  through the epithelial sodium channel (ENaC) results in osmotic gradients that favor rapid absorption of the airway surface liquid (ASL) layer, leading to dehydrated airway mucus and impaired mucociliary clearance (MCC) [120], [21]. The inability to clear pathogens via MCC leads to chronic infection, inflammation, airway damage, and premature respiratory failure.

Inhaled agents that reverse osmotic gradients in the airways are used to treat the ASL dehydration defect associated with CF. Hypertonic saline (HS) is one such osmotic agent that has been shown to increase both MCC and lung function in patients with CF [22], [121]. More recently CFTR modulators have been developed that substantially improve lung function in individuals with specific CFTR mutations [41].

Outcome measures and biomarkers that quantify the basic pathophysiology of CF lung disease are needed to allow for the rapid screening of new therapeutics for CF. Ideally, these screening methods seek to quantify the basic pathophysiology of CF lung disease. Mucociliary clearance scans, which quantify the clearance of a radiopharmaceuticals from the lungs, are one such functional imaging method for studying outcomes in CF.

This method was expanded herein to include measuring the clearance of a radiolabeled small-molecule that can be absorbed as well as cleared via MCC. Similar techniques have been used in the past to resolve the individual components of lung clearance [122], [123]. The *in vivo* method utilizes Technetium 99m sulfur colloid (TcSC) a non-absorbable particle probe and Indium 111-DTPA (DTPA) an absorbable small molecule probe. The probes are delivered together in a liquid aerosol. Figure 2.1 presents a schematic for pharmaceutical clearance from the airway epithelium. Shown at left in Figure 2.1, the small molecule probe (green) clears more rapidly than the particle probe (blue). It assume that MCC clears the probes at similar rates and that the difference in their clearance rates is therefore associated with the absorption of the small molecule (red).

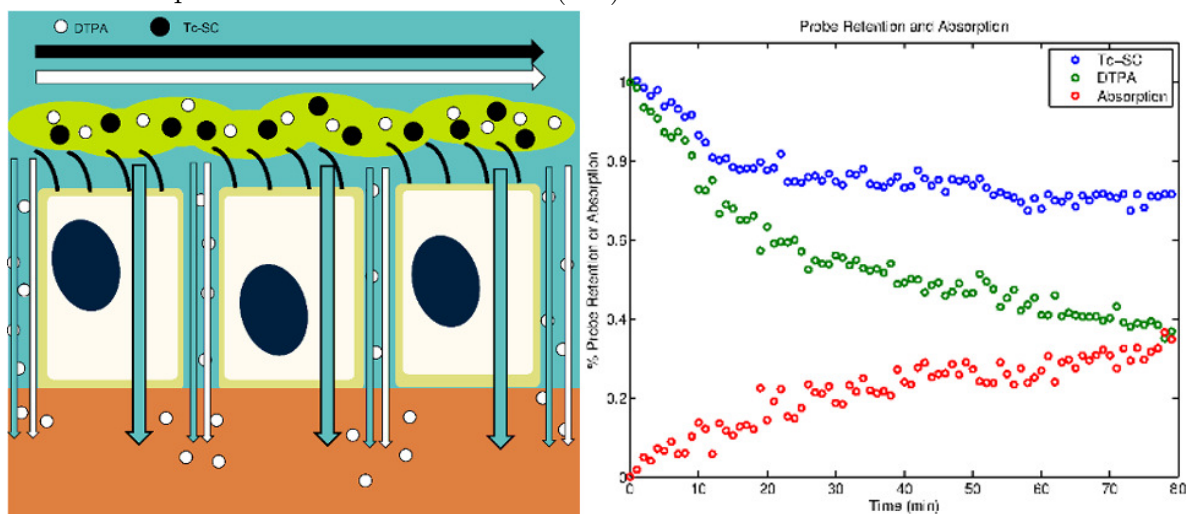


Figure 2.1: **Left panel: schematic of transport routes in the airway epithelium.** The black and white horizontal arrows represent mucociliary clearance of TcSC and DTPA, respectively. DTPA (downward white arrow) absorbs across the airway epithelium via the paracellular route. Water (downward blue arrow) also absorbs across the epithelium via the transcellular and paracellular routes. Right panel: normalized TcSC (blue circles) and DTPA (green circles) retention curves with the difference between the respective datasets at each time point shown as absorption (red circles) in CF subject 8.

Previous *in vitro* studies have demonstrated a relationship between DTPA and airway surface liquid absorption rates [65]. DTPA absorption is increased both *in vivo* in CF

airways and *in vitro* in CF airway cell cultures [8,65]. Decreases in DTPA absorption after osmotic therapies have also been demonstrated *in vitro* and *in vivo* [8,65]. Thus, multi-probe methods offer a potential means of measuring of both MCC and ASL absorption rates [8]. Successful CF therapies should restore ASL volume by correcting defective airway epithelial ion transport [42,124]. The restoration of airway hydration should be rapidly detectable through these multi-probe imaging methods as decreased liquid absorption rates are reflected through slower absorption of DTPA and improvements in MCC cause increased TcSC clearance.

While many medications are given via inhalation, few mechanistic PK descriptions of inhaled drug clearance out of the lung exist. The PK models that do exist are generally one (systemic) or two (lung and blood) compartment models [101,105,108,113,114,115,125] and generally do not consider MCC. The information gained from an at least partially physiological description of the mucociliary and absorptive clearance of pharmaceuticals in the lungs could provide insight toward improving drug efficacy. Furthermore, in the case of functional imaging, PK models stand to provide a more detailed description of airway diseases (e.g. CF) that cause changes in the MCC and absorptive properties of the airways.

This chapter begins by evaluating the utility of a previous, semi-physiological PK model for inhaled insulin by applying its structure to the functional imaging data of particle and small molecule clearance from the human respiratory tract. Presented after that is an extended compartment-based model that better allows an informed physiologically motivated model structure and identifiable parameter values. The goal in developing this model is to better resolve the specific physiological mechanisms that contribute to the composite functional imaging result. While used to gauge response to HS inhalation, the PK aspect of these models measures the clearance of the probes and not the clearance of HS. However, these mechanism-specific measurements may provide more sensitive and detailed evaluations of therapeutic efficacy than the currently used image-derived metrics. The challenge is to construct a mathematical representation of the physiology that can resolve the underlying mechanisms and their interactions.

There have been a number of mechanistic compartment-based PK models for inhaled pharmaceuticals [116,117,118,126,127], but none have considered the PK behavior of the

radiopharmaceuticals used for functional imaging from which the data originates, nor has anyone assessed absorption kinetics with the methodology employed here. It is hypothesized that by dividing the lung into a solely absorptive peripheral lung region and separate central lung region that has both absorption and MCC capability, and by subdividing this central lung region into fractions with and without functional ciliated airway, the dynamics of simultaneous particle and small molecule probe clearance from the lung are reproducible. Further hypothesized is that (i) functional ciliated airway clears at the same rate in patients with CF and non-CF subjects; (ii) the fraction of functional ciliated airway (FFCA) is decreased in CF (*i.e.* a binary distinction between clearing and non-clearing regions); and (iii) FFCA can be increased through inhalation of HS. The models provide estimates of FFCA, MCC, and lung absorption, the latter of which is believed to be related to liquid hyper-absorption in CF small airways. These measured parameters may substantially expand the utility of the functional imaging measurement by providing more mechanistic insight into lung physiology and response to therapeutic agents (a list of all abbreviations and their definition used in this work can be found in Table 2.1).

## 2.2 MATERIALS AND METHODS

### 2.2.1 Functional Imaging Methods

Data from previously reported clinical imaging studies were utilized [8]. These studies included both adult (n=12) and pediatric (n=9) patients with CF and healthy controls (n=9). Raw imaging data from this study can be found in the supplement in Table S1 pf [1]. An aerosol based functional imaging technique that measures the clearance of two different radiopharmaceutical probes from the lungs over 80 minutes was used. Indium-111-labeled diethylene triamine pentaacetic acid (DTPA) is a small molecule probe ( $\approx 500$  Da) that is cleared from the lung through both absorption and MCC while Technetium-99m-labeled sulfur colloid (TcSC) is a particle probe ( $\approx 300$ nm) that is cleared only by MCC. DTPA absorption is calculated by subtracting the TcSC clearance rate (MCC) from the total In-DTPA

Table 2.1: **Abbreviations and constants in this chapter.**

<b>Abbreviation</b>	<b>Description</b>
AIC	Akaike Information Criterion; a Metric of Model Appropriateness
ASL	Airway Surface Liquid Layer
C	Imaging Region of Interest About the Central Lung; Analogous to $L$ in Model
CF	Cystic Fibrosis
CFTR	Cystic Fibrosis Transmembrane Conductance Regulator
CI	Confidence Interval
DMEM	Dulbecco's Modified Eagle Medium
DTPA	Indium-111 Diethylene Triamine Pentaacetic Acid
ENaC	Epithelial Sodium Channel
FFCA	Fraction of Functional Ciliated Airway
HBE	Human Bronchial Epithelial (cell)
HS	Hypertonic Saline
IS	Isotonic Saline
k	Number of Free Parameters in Model
MCC	Mucociliary Clearance
N	Number of Data Points Analyzed for Model Fit
ODE	Ordinary Differential Equation
PK	Pharmacokinetic
Tc-SC	Technetium-99m Sulfur Colloid
$W_i$	Weighting Factor of the $i^{th}$ Element of the Dataset for AIC
$y_i$	$i^{th}$ Value of Dataset
$\hat{y}_i$	$i^{th}$ Value of Model Fit

clearance rate. Both probes were mixed and delivered together via nebulizer in the same liquid aerosol. All patient studies were approved by the University of Pittsburgh Institutional Review Board (clinicaltrials.gov numbers NCT01223183 and NCT01486199).

The aerosolized probes were delivered simultaneously by nebulizer using a technique that deposited aerosol primarily in the airways [8]. Their clearance (normalized decrease in radioactive counts over time) was then independently assessed over 80 minutes using dynamic planar scintigraphy. Images were corrected for background, decay, and spillover in the emission spectra of the probes prior to analysis [8]. Whole, peripheral and central lung zones were considered, where the central zone was defined as a rectangle with  $\frac{1}{2}$  the height and width of the whole lung region of interest positioned along the medial lung border and centered vertically. At  $t=10$  minutes (11th imaging frame) subjects inhaled nebulized saline treatments for 10 minutes. Adult patients with CF inhaled 7% hypertonic saline (HS,  $n=11$ ) on one testing day and isotonic saline (IS) on the other. Control and pediatric CF subjects performed a single testing day with isotonic saline. Changes in DTPA absorption in response to osmotic therapies have previously been demonstrated both *in vitro* [65] and *in vivo* [8]. Analysis of the TcSC and DTPA retention curves as well as DTPA absorption (ex: Figure 2.1) plotted with a logarithmic ordinate showed that the data did not follow a monoexponential profile, which guided selection of the model structure and kinetics necessary to accurately reproduce the data.

### 2.2.2 Initial Model Structure

Sakagami [116] proposed a robust modeling scaffold for inhaled pharmaceuticals that takes into account the regional pharmacokinetic (i.e. MCC and ABS) differences between the large conducting airways ( $L$ ) and the distal lung ( $D$ ), consisting of smaller airways and alveoli. Analysis of the corresponding system of compartment-based ordinary differential equations (ODEs) yielded a bi-exponential retention curve for TcSC as proposed by Byron [117]. However, this model structure could not be reconciled with the whole of the data used herein (see **Discussion**).

### 2.2.3 Model Parameter Estimation

Regression of model parameters, regardless of model structure, was performed sequentially as follows. Model parameters were estimated using nonlinear least-squares regression (via *lsqnonlin* in MATLAB, ©2013, The MathWorks, Natick, MA) between model predictions and experimental data. The experimental design allowed for sequential estimation of the MCC and absorption rate parameters as follows:

1. The parameters that govern MCC ( $k_{LT}$  and FFCA) were fit to the TcSC retention data.
2. The regressed MCC parameters were then fixed, and the absorption rate parameters ( $k_{DB}$  and  $k_{LB}$ ) were fit to the absorption curve.
3. Parameter uncertainty was calculated using the *nlparci* function in MATLAB (©2013, The MathWorks, Natick, MA) to obtain confidence intervals on all model parameters.

### 2.2.4 Model Analysis

The assumptions above were tested individually, and in combination, for appropriateness using the Akaike Information Criterion (AIC). Akaike [128] originally proposed that model appropriateness could be assessed according to the equation:

$$AIC = (-2)\ln(\text{maximum likelihood}) + 2k \quad (2.1)$$

Where a Gaussian distribution represents the maximum likelihood of the data and  $k$  is the number of free parameters in the model. Thus, the model with the least value of AIC is deemed most appropriate in terms of model fit and parsimony. Yamaoka and colleagues [129] further elaborated on this information criterion by proposing that for a process with Gaussian error the AIC can be found from the equation:

$$AIC = N\ln\left(\sum_{i=1}^N ((\hat{y}_i) - y_i)^2 / N\right) + 2k \quad (2.2)$$

Where  $\hat{y}_i$  is the model fit and  $y_i$  is the data value at the  $i^{th}$  image of the  $N=80n$  set because there are 80 images per patient and  $n$  patients per study group.

### 2.2.5 *In Vitro* Assessment of Ciliary Activation

We developed an *in vitro* imaging assay to measure the fraction of the epithelium that has functional MCC in order to test the hypotheses that FFCA is decreased in CF and that hydration can recruit areas of otherwise non-functional cilia. Fully differentiated human bronchial epithelial (HBE) cell cultures were viewed using a phase-contrast objective (Nikon Eclipse TI). These cultures were derived from lungs removed at the time of lung transplantation and prepared using previously described methods approved by the University of Pittsburgh IRB [13]. A series of 10 images was taken of each culture that allowed for the determination of the change in pixel intensity between successive images in the stack, as shown and Video 1. Ciliary beat can be observed under these conditions and is characterized by a change in light intensity measured by the camera. This change in light intensity can be translated to a change in pixel intensity in the images obtained when placed in sequence to form a movie of ciliary motion (see Figure 2.3).

The average change in pixel intensity of all cultures was determined in both CF lines (n=6) and a non-CF line. Average changes in the intensity of each pixel from 12 untreated cultures from the non-CF line were measured and the average change in intensity over all pixels was used as a baseline measurement of functional ciliary movement. Pixels in each stack with average change in intensity greater than the non-CF baseline were said to have functional ciliary movement. To test the effect of osmotic agents, 5  $\mu\text{L}$  of either isotonic (300 mOsm) or hypertonic (600 mOsm) saline was added to the apical surface of cells prior to imaging. To test for saturating effects of hydration, Dulbecco's Modified Eagle Medium (DMEM) was sequentially added from the basolateral bath to the apical surface of the cultures as follows: 10  $\mu\text{L}$  of DMEM was added to the apical surface of the cells from the basolateral bath before the cells were imaged, and an additional 10  $\mu\text{L}$  of basolateral DMEM was added to the apical surface prior to a second, identical, imaging routine.

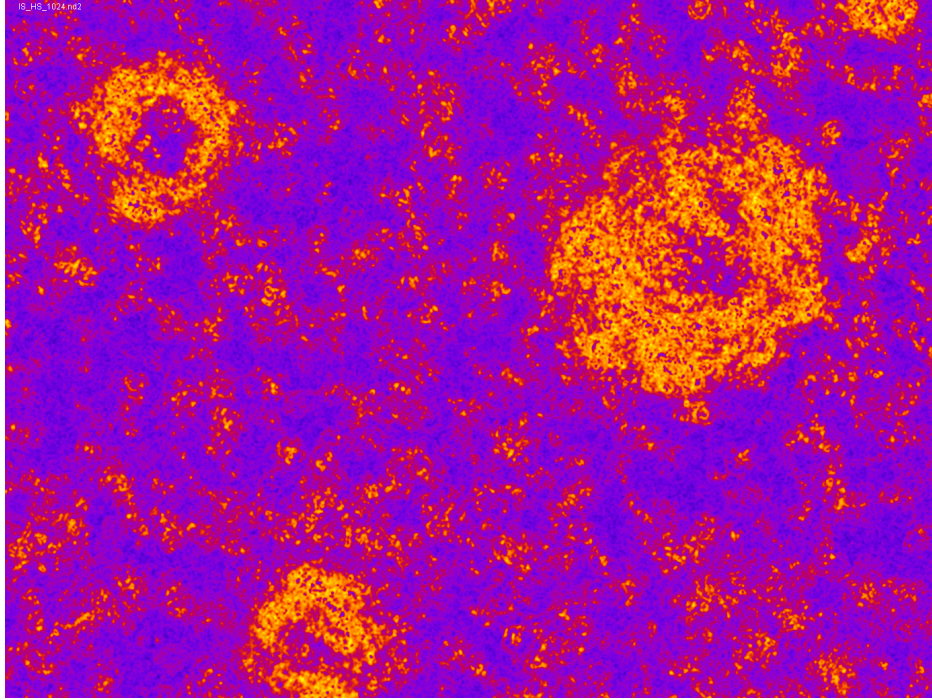


Figure 2.2: Video of recorded ciliary activity with three regions of "hurricane" activity visible. First image is Figure 2.3 superimposed on the video. The superimposition can be recovered by scrolling to the previous page (in the digital format of the dissertation).

### 2.3 PRELIMINARY ANALYSIS

This section presents and analyze an example of a flexible compartmental PK model of MCC and absorption-based drug clearance from the lung developed by Sakagami and colleagues [116]. This model structure takes into account the regional PK differences between the large conducting airways (L) and the distal lung (D) consisting of smaller airways and alveoli [9]. This model had four kinetic parameters to be solved for by regression:  $k_{DL}$  and  $k_{LT}$  as MCC rate constants, and  $k_{AP}$  and  $k_{AL}$  as absorption rate constants. The model also has a dosing parameter (C/P) that represents the ratio of radiopharmaceuticals delivered to the large airways as compared to the distal lungs. Using this as a starting point, the case of first order clearance kinetics via both absorption and MCC in both L and D was

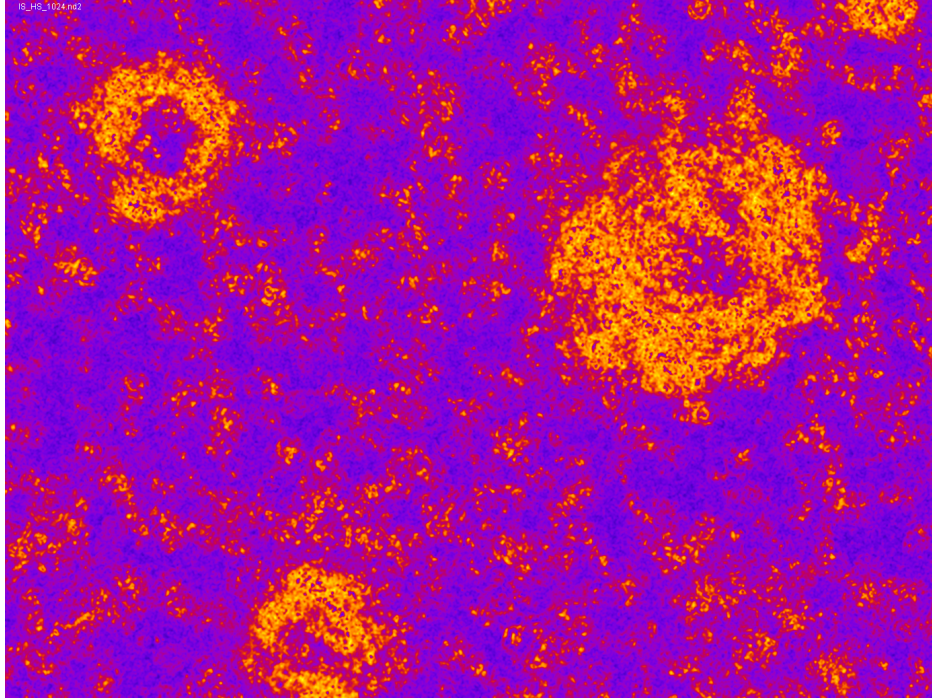


Figure 2.3: A pseudo-color image of non-CF HBE cells under 10x enhancement is shown. The viewing frame is identical to that in 1. Darker (more blue) regions show areas with lower average change in pixel intensity during 1 whereas lighter (more yellow) regions show areas with higher average change. In combination with 1 it is shown that regions that display little visible movement are more blue, and the regions with visible motion, particularly the “hurricane” regions, are more yellow.

considered. Under the assumption that TcSC is not absorbed in any lung region, analysis of the corresponding system of compartment-based ordinary differential equations (ODEs) yielded a bi-exponential retention curve for TcSC as proposed by Byron [126]. Regression of the model parameters was performed sequentially. First, the MCC rate parameters were fit to the TcSC retention data. Those values were then fixed and the absorption rate parameters were fit via the same functions to the absorption curve for DTPA. In the case where C/P was allowed to vary model fit was excellent, as illustrated in Figure 2.4 for MCC and Figure 2.5

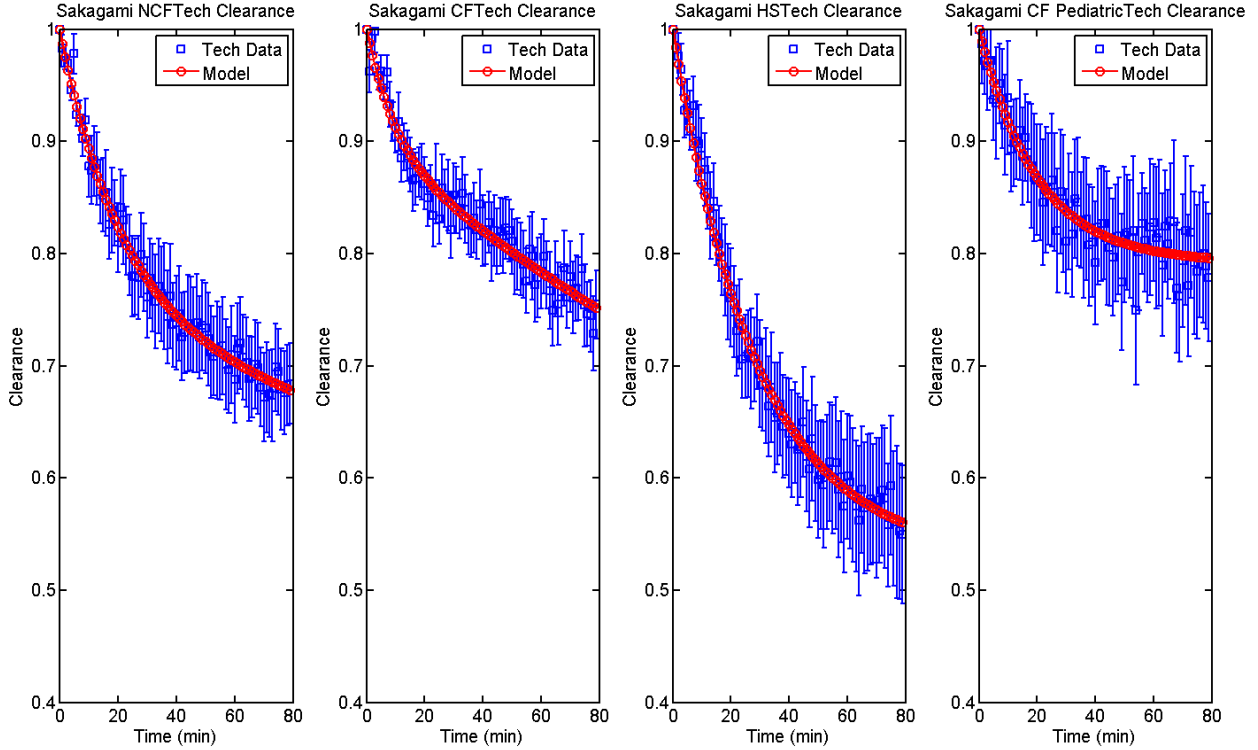


Figure 2.4: Model estimated MCC (red) based on functional imaging data (blue) in non-CF subjects, CF subjects without and with HS inhalation, and pediatric patients with CF. C/P was allowed to be fit in this case, allowing for estimation of the deposition pattern that best describes the whole lung clearance curves.

However, interrogation of model parameters revealed that while  $k_{LT}$  values were on the same order of magnitude as reported in [116] C/P values were below unity. This does not agree with measured C/P values that were in excess of 2 for all subjects as would be anticipated based on the use of a breathing pattern designed to promote airways deposition [8]. In an attempt to reconcile the model structure with the imaging metric, the model was refit with a C/P lower bound of 1.5. As illustrated in Figure 2.6, the model fit of MCC suffered from extreme heteroskedasticity. The text and data in Figure 2.7 provide evidence that bounding the C/P model parameter facilitated agreement with the imaging metric in terms of its estimation but at the expense of model fit, particularly in terms of MCC.

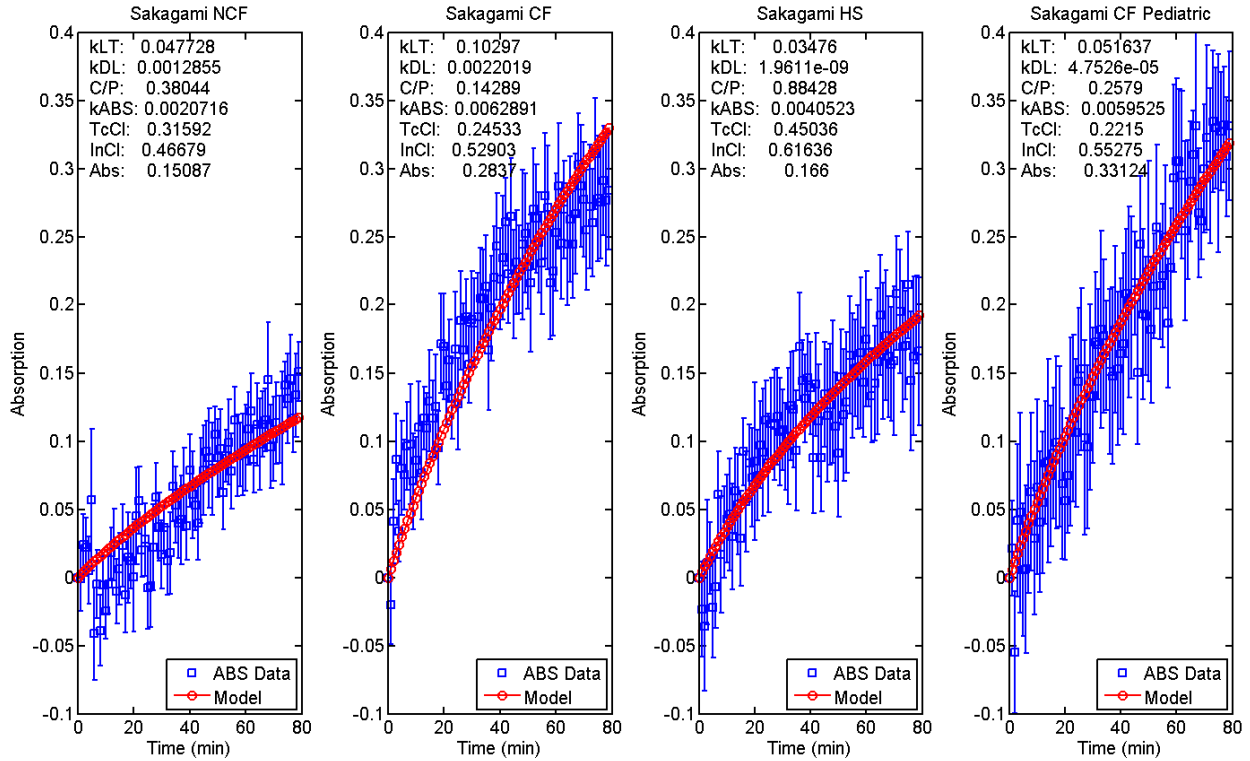


Figure 2.5: Model estimated DTPA absorption (red) based on functional imaging data (blue) in non-CF subjects, CF subjects without and with HS inhalation, and pediatric patients with CF. Best fit parameters as well as normalized TcSC and DTPA clearance (TcCL and InCL) and absorption (Abs) are given in each panel for their respective patient group. C/P estimates do not agree with the values obtained directly from imaging data.

Furthermore, analysis of the model parameters via the asymptotic method from a numerically approximated Jacobian yielded wide confidence intervals. These intervals were in excess of  $\pm 10$  times the nominal parameter value indicating poor model parameter identifiability.

C/P determines the deposition fractions in compartments with assigned physiological clearance types: fast MCC in central lung, slow MCC in the periphery. C/P was too small in the better fitting case, and MCC was too slow in the constrained case. This indicated that a good fit required a lower contribution of large airway clearance behavior than could be justified by the deposition data. This understanding is the basis of the concept that in

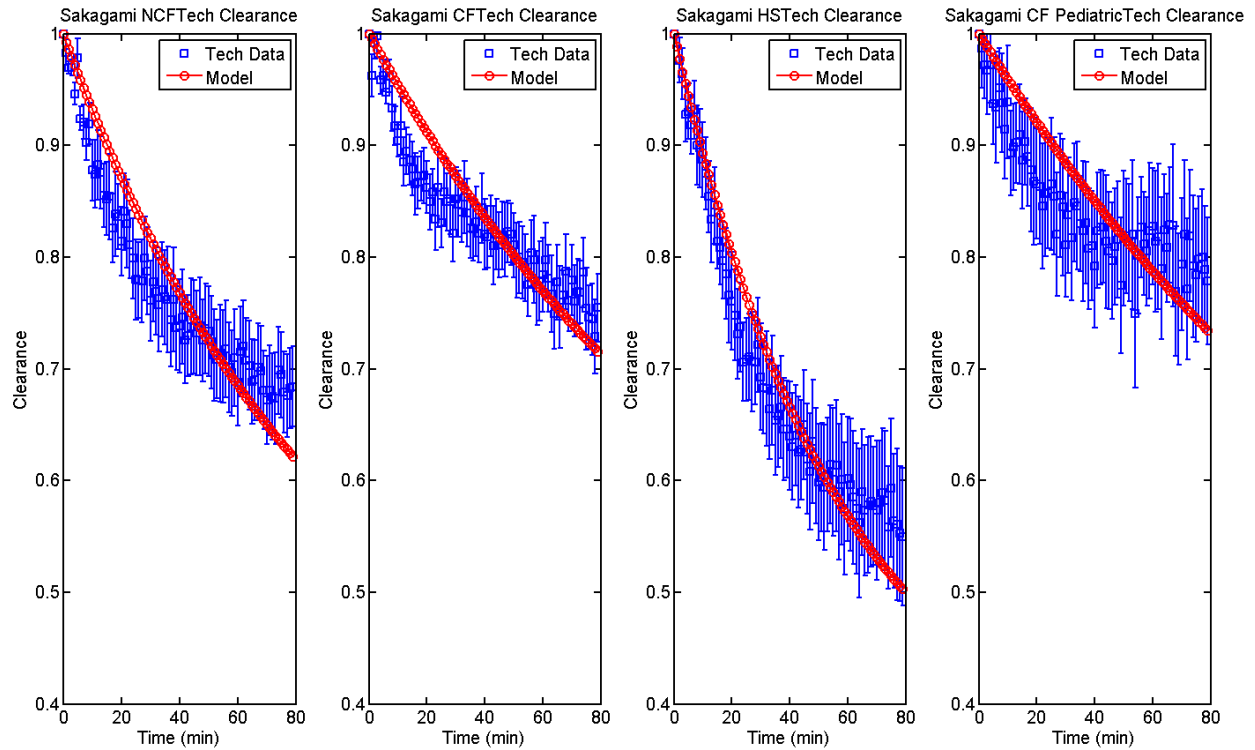


Figure 2.6: Model estimated MCC (red) based on functional imaging data (blue) in non-CF subjects, CF subjects without and with HS inhalation, and pediatric patients with CF. C/P was allowed to be fit in this case, allowing for variation in deposition pattern that best describes the whole lung clearance curves.

the large airways only a fraction of area with working ciliary clearance exists. The resultant model structure and analysis of its behavior are the focus of the rest of this chapter.

## 2.4 RESULTS

### 2.4.1 Model Synthesis and Assumptions

The original model of Sakagami [116] was extended structurally to account for the dynamics and deposition observed in the clinical data set. Founded on a basic understanding of lung

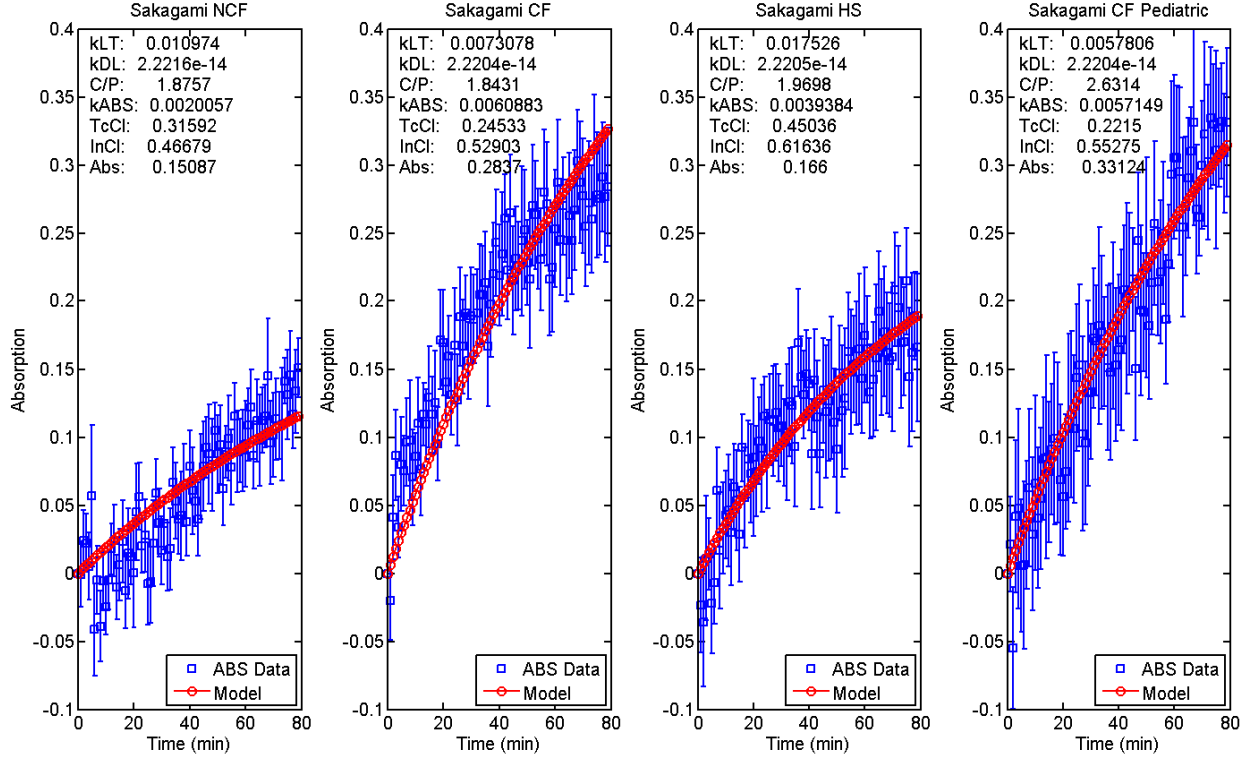


Figure 2.7: Model estimated DTPA absorption (red) based on functional imaging data (blue) in non-CF subjects, CF subjects with out and with HS inhalation, and pediatric patients with CF. Best fit parameters as well as normalized TcSC and DTPA clearance (TcCL and InCL) and absorption (Abs) are given in each panel for their respective patient group. C/P estimates do not agree with the values obtained directly from imaging data.

anatomy and physiology, the lung structure can be lumped into two key dynamical structures as shown in Figure 2.8.

Additional assumptions made in synthesizing this model are as follows:

- A fraction of the large airways ( $L$ ), which are represented in the central ( $C$ ) lung region of interest (ROI) [130], has functional MCC, with MCC in the remainder of  $L$  being non-functional. This allows the subdivision of  $L$  into two sub-compartments:  $L_F$ , which has functional MCC, and  $L_N$ , which has no functional MCC.

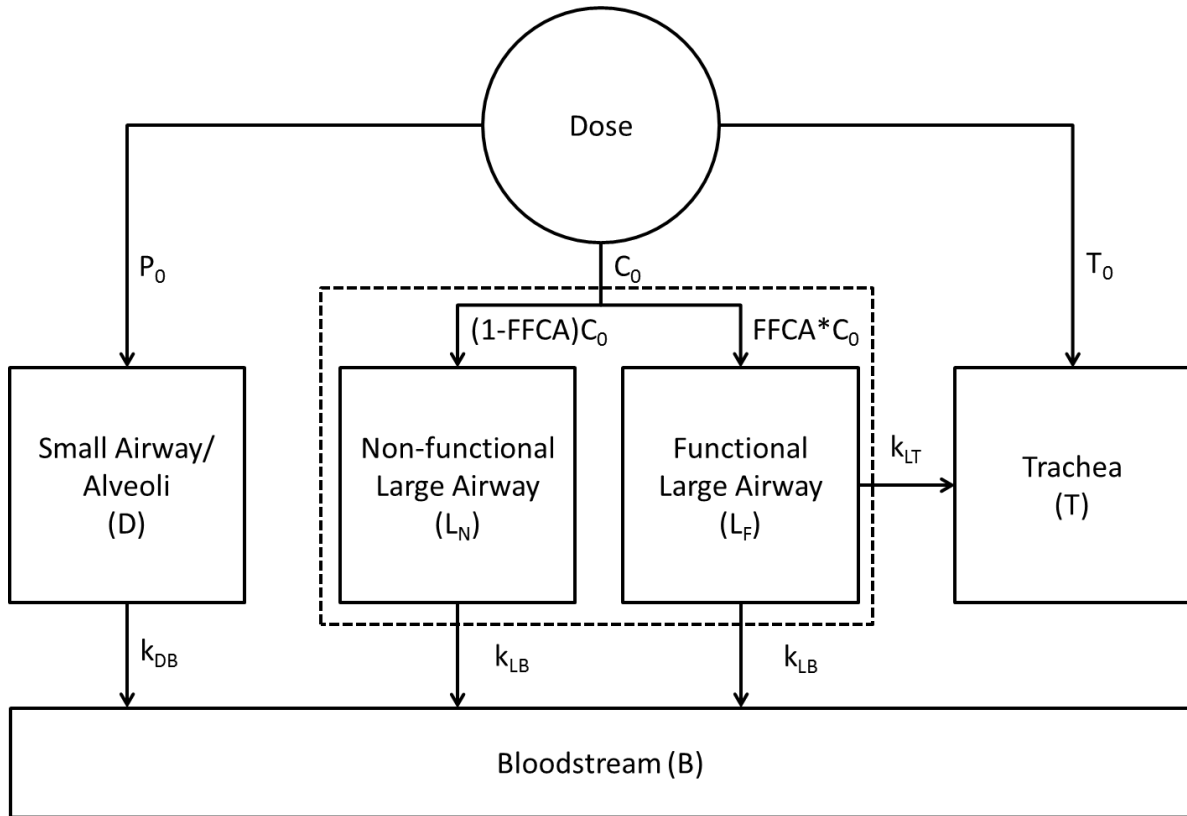


Figure 2.8: **Schematic model structure describing the clearance of small molecule and particle probes from the lung.** Initial depositions:  $T_0$ =trachea,  $C_0$ =central,  $P_0$ =peripheral. See Table 1 for full list of model abbreviations.

- The initial doses of the radiopharmaceuticals delivered to either the central ( $C_0$ ) or peripheral ( $P_0$ ) lung regions are described as the number of counts within  $C$  or in the area outside of  $C$  but within the whole lung ROI in the first image, respectively [8] (Figure S1 provides a visual representation of the C and P ROIs).
- 10% of inhaled radiopharmaceuticals were assumed to deposit in the trachea ( $T_0$ ) [116]. However, neither counts in  $T$  nor the bloodstream ( $B$ ) have a unique impact on the clearance of the TcSC and DTPA.
- MCC in the distal lung  $D$ , which contains small and intermediate-sized airways in addition to alveoli [130], is a slow process; given the 80-min timescale of the data this rate

cannot be resolved with confidence. As a result, the MCC term from D to L,  $k_{DL}$ , is neglected.

The result of these assumptions is a three-compartment model for MCC in the lung wherein two compartments ( $D$  and  $L_N$ ) are absorptive and one compartment ( $L_F$ ) has MCC in addition to absorptive clearance, as shown in Figure 2.

### 2.4.2 Model Equations

Equations modeling the transport of both of the probes are outlined below. The model parameters  $k_{LT}$ ,  $k_{DB}$ ,  $k_{LB}$  and FFCA, the fraction of  $L$  with functional MCC, were determined by nonlinear least-squares regression as described in **Methods**. For TcSC clearance,  $k_{DB}$  and  $k_{LB}$  are set equal to 0. The mathematical description of this model, written as ODEs representing the change in counts in each model compartment, is as follows (see Table 2.2 for full list of model abbreviations and [Appendix B](#) for code to simulate the equations):

$$\frac{dD}{dt} = -k_{DB}D \quad (2.3)$$

$$\frac{dL_N}{dt} = -k_{LB}L_N \quad (2.4)$$

$$\frac{dL_F}{dt} = -k_{LB}L_F - k_{LT}L_F \quad (2.5)$$

$$\frac{dT}{dt} = k_{LT}L_F \quad (2.6)$$

$$\frac{dB}{dt} = k_{DB}D + k_{LB}(L_N + L_F) \quad (2.7)$$

### 2.4.3 Model Fit and Predictions

The ability of the model to reproduce therapeutic response after the inhalation of hypertonic saline was studied using imaging data from patients with CF who inhaled isotonic saline (IS)

Table 2.2: **Model parameters in the work presented herein**

<b>Parameter</b>	<b>Description</b>
$B$	Bloodstream Model Compartment (units counts)
$C_0$	Initial Counts in $L$ (units counts)
$D$	Distal Lung Model Compartment (units counts)
FFCA	Free Parameter; Fraction of $C_0$ in $L_F$ (units counts)
$L$	Large Airway Model Super-Compartment (units counts)
$L_F$	Sub-compartment of $L$ with Functional MCC (units counts)
$L_N$	Sub-compartment of $L$ without Functional MCC (units counts)
$k_{DB}$	Free Parameter; Rate Constant of Absorption in $D$ (units $min^{-1}$ )
$k_{DL}$	Free Parameter (Unused in Final Model); Rate Constant of MCC from $D$ to $L$ (units $min^{-1}$ )
$k_{LB}$	Free Parameter; Rate Constant of Absorption in $L$ (units $min^{-1}$ )
$k_{LT}$	Free Parameter; Rate Constant of MCC from $L$ to $T$ (units $min^{-1}$ )
$P_0$	Initial Counts in $D$ (units counts)
$T$	Trachea Model Compartment (units counts)

and hypertonic saline on alternating study days [8]. Retention of TcSC, which is a metric of MCC, is shown with model fit for each patient group in Figure 3 [21]. Data from pediatric patients with CF and healthy controls who inhaled isotonic saline is also shown. The model captured the dynamics of MCC in all patient groups. The previously described increases in MCC associated with HS inhalation are apparent in the image-derived data and the model fits. However, as previously reported, no statistical differences in baseline MCC were detected between the CF IS, pediatric CF, and control groups [8].

DTPA is assumed to deposit in the same regions and clear by MCC at the same rate as TcSC; DTPA absorption is then captured by regressing the parameters  $k_{DB}$  and  $k_{LB}$ . Additionally, the previous studies have shown that the absorption of DTPA is proportional

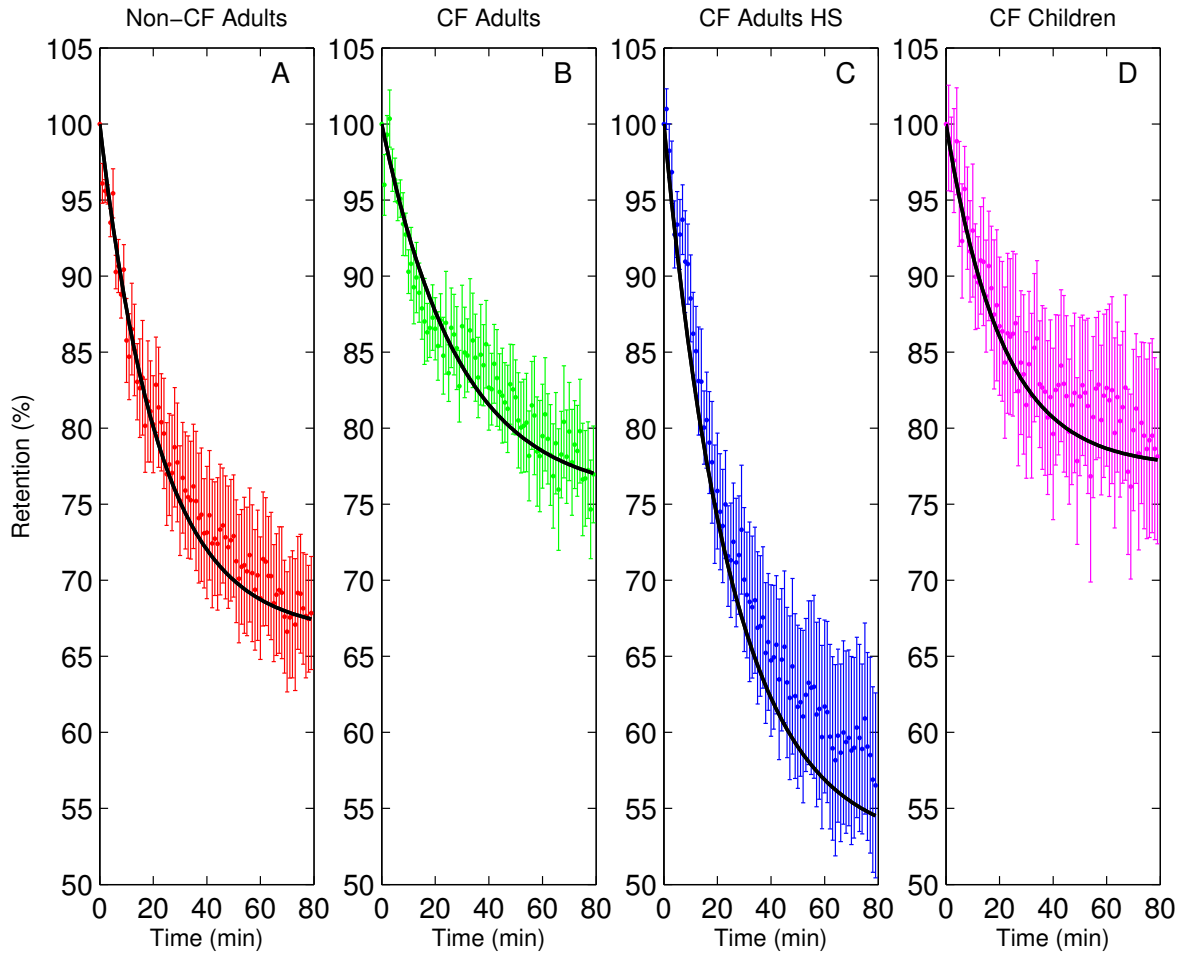


Figure 2.9: **TcSC retention (mean  $\pm$  SEM) vs. model fit (black line) for four patient subgroups.** (A) Non-CF subjects ( $n=9$ ) (B) patients with CF ( $n=12$ ). (C) patients with CF after inhalation of hypertonic saline ( $n=11$ ). (D) Pediatric patients with CF. Data from [8].

to the absorption of airway surface liquid in vitro [65]. As such, the effect of hypertonic saline on liquid absorption, using DTPA as an analog, is shown in Figure 4, along with the model fit for each group [8]. The model again captured the dynamics of absorption in all groups. Increased baseline rates of DTPA absorption are apparent in both adult and pediatric CF groups, as previously described [8].

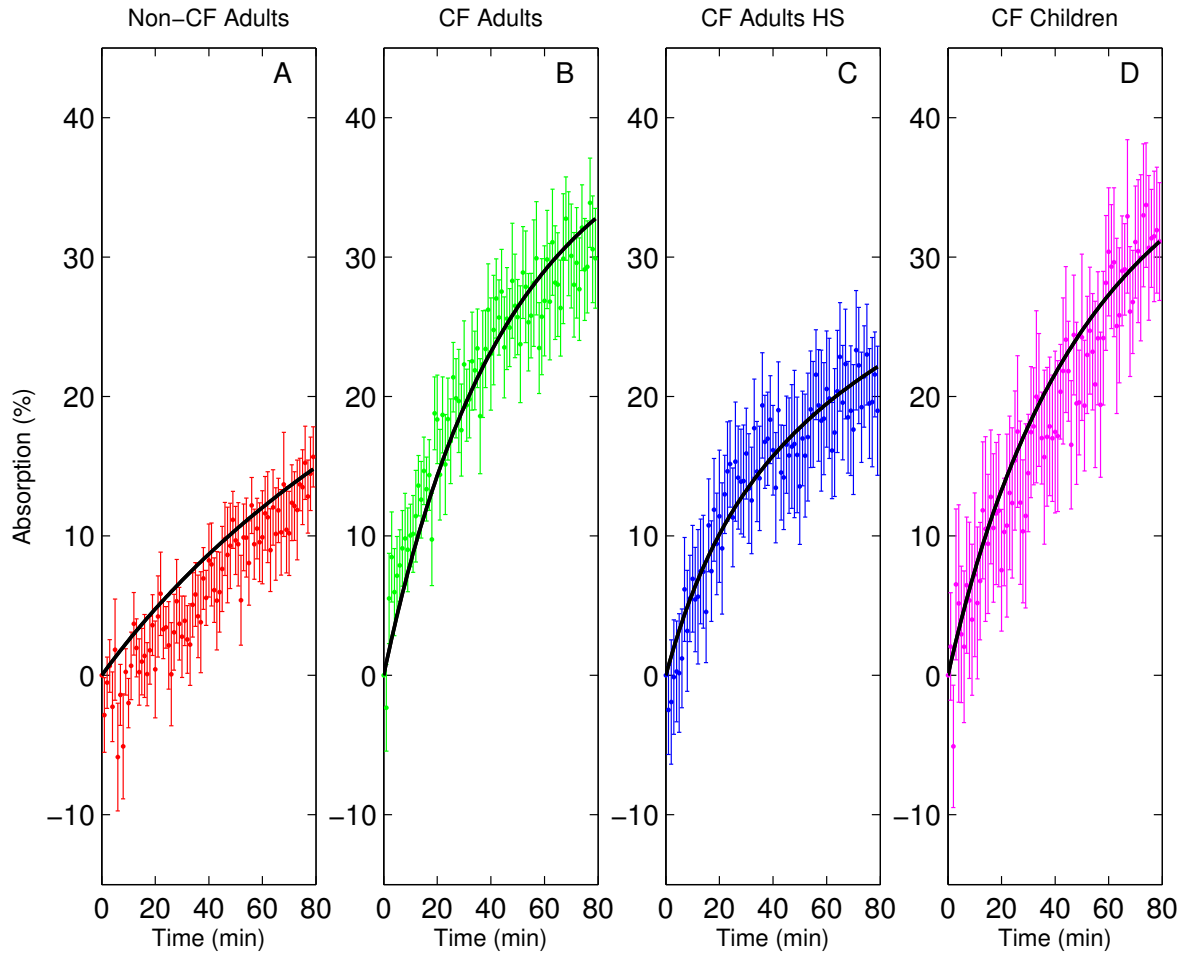


Figure 2.10: **DTPA absorption (mean  $\pm$  SEM) vs. model fit (line) for four patient subgroups** (A) Non-CF subjects (n=9) (B) patients with CF (n=12). (C) patients with CF after inhalation of hypertonic saline (n=11). (D) Pediatric patients with CF. Data from [8].

The model predicts that both TcSC retention and liquid absorption will follow trajectories within narrow envelopes based on the predicted upper and lower 95% confidence intervals (CIs) of the model parameters. These CI envelopes are derived using all possible combinations of the upper and lower 95% CIs and nominal values of the model parameters to generate the extreme values of model predictions. Figure 5 shows that predicted model trajectories lead to different final values of TcSC retention for all adult patient groups, with

no overlap in trajectory envelopes of CF IS and non-CF groups for  $t > 18$  min and no overlap between non-CF and HS trajectories for  $t > 27$  min. In other words, the three adult patient subgroups have characteristically different total MCC behavior. Pediatric CF clearance trajectories closely resemble those of adult patients with CF, but are not shown for ease of interpretation. Patients with CF display less MCC than non-CF subjects, which appears to contradict the finding in [8]. However, the present work evaluates the entire time course of clearance, while the end of study value ( $t = 80$  min) was used as the evaluation time point in [8]. By using the entire data sequence, particularly the dynamic response at short times, it is possible to parametrically estimate and differentiate - with confidence - the MCC and absorption dynamics between patients with CF and non-CF subjects. These analyses also indicate that MCC function in patients with CF can be rescued by HS treatment, which caused total MCC to exceed that of non-CF subjects.

Figure 6 shows that the model-predicted trajectories for liquid absorption have no overlap for all  $t > 0$ . Pediatric CF trajectories again resemble those of adult patients with CF, but are not shown. Patients with CF have higher absorption than non-CF subjects, which can be partially remediated by HS treatment. Combined, the results in Figures 5 and 6 indicate that HS has two distinct mechanisms of action, both rescuing MCC and ameliorating liquid hyperabsorption [22].

It has been proposed that the apparent increase of MCC following HS treatment occurs by increasing the rate at which MCC occurs [22], [131]. The model suggests that the intrinsic rate of MCC is the same in all patient groups, and the rescue of MCC can be attributed to the recruitment of inactive portions of the airway. Figure 7A shows that the rate of MCC,  $k_{LT}$ , is not significantly different between all patient groups ( $p > 0.05$ ). However, the parameter FFCA (Figure 7B), which describes the fractional area of large airways with functional MCC, is significantly lower in patients with CF versus non-CF subjects ( $p < 0.05$ ). Patients with CF given HS, however, show a significantly increased FFCA ( $p < 0.05$ ). This would support the concept of increased MCC, not through an intrinsic rate increase, but through an increase in the overall epithelial area contributing to MCC.

The model also agrees with previous reports that absorption, represented by  $k_{DB}$  and  $k_{LB}$  in the model, is increased in patients with CF vs. non-CF subjects ( $p < 0.001$  both

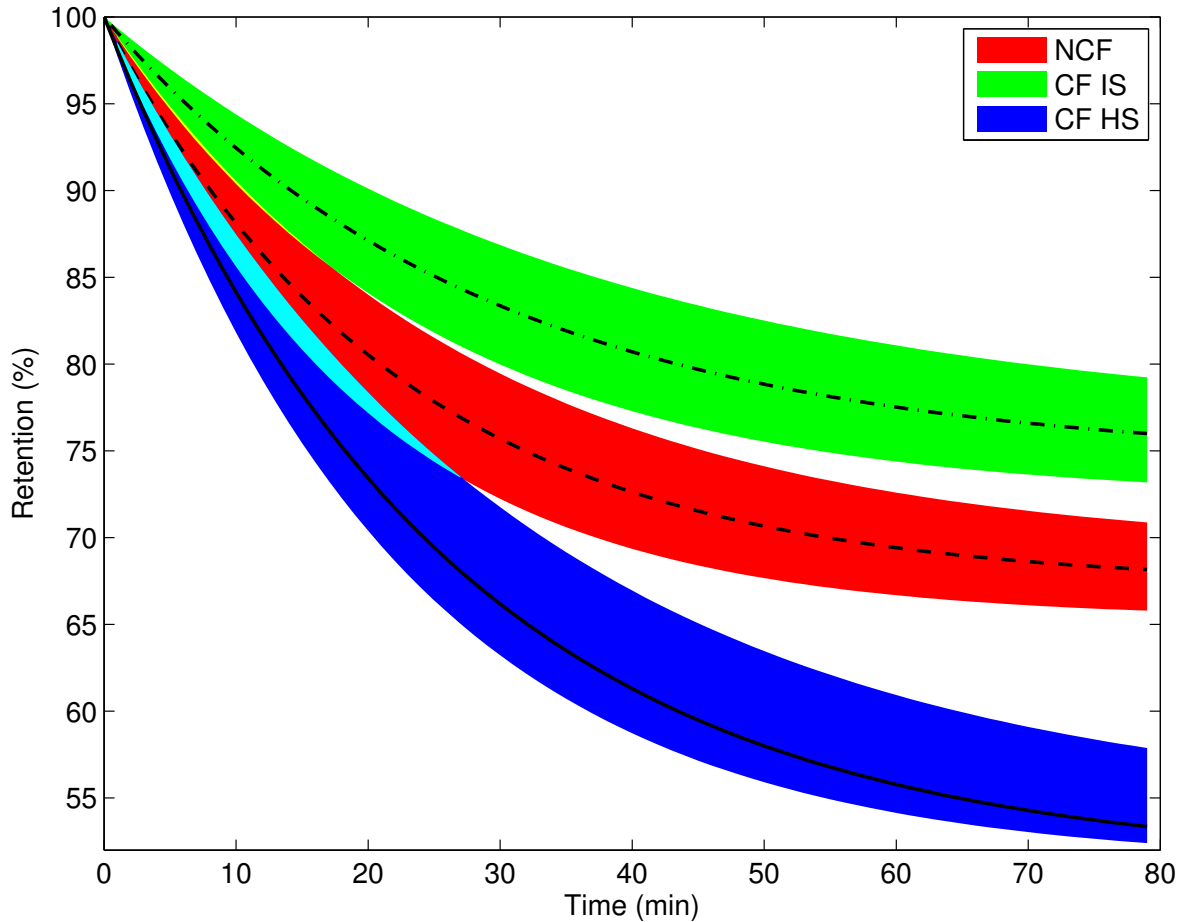


Figure 2.11: **Estimated TcSC retention trajectories for three patient subgroups.** Non-CF (red with dashed line), CF IS (green with dotted dashed line), CF HS (blue with line). Shaded envelope characterizes 95% confidence interval (CI) of retention prediction by the model. Pediatric CF subjects not shown due to overlap with adult CF.

parameters) [8, 132]. The model demonstrates that HS inhalation decreases absorption in the peripheral lung ( $k_{DB}$ ), which includes both small and intermediate sized airways and alveolar regions, more than IS inhalation ( $p < 0.001$ ). All model parameters are similar when comparing baseline measurements in the pediatric and adult CF IS groups ( $p = \text{NS}$ ). The parameters, as well as those of similar studies, are shown in Table 2.3.

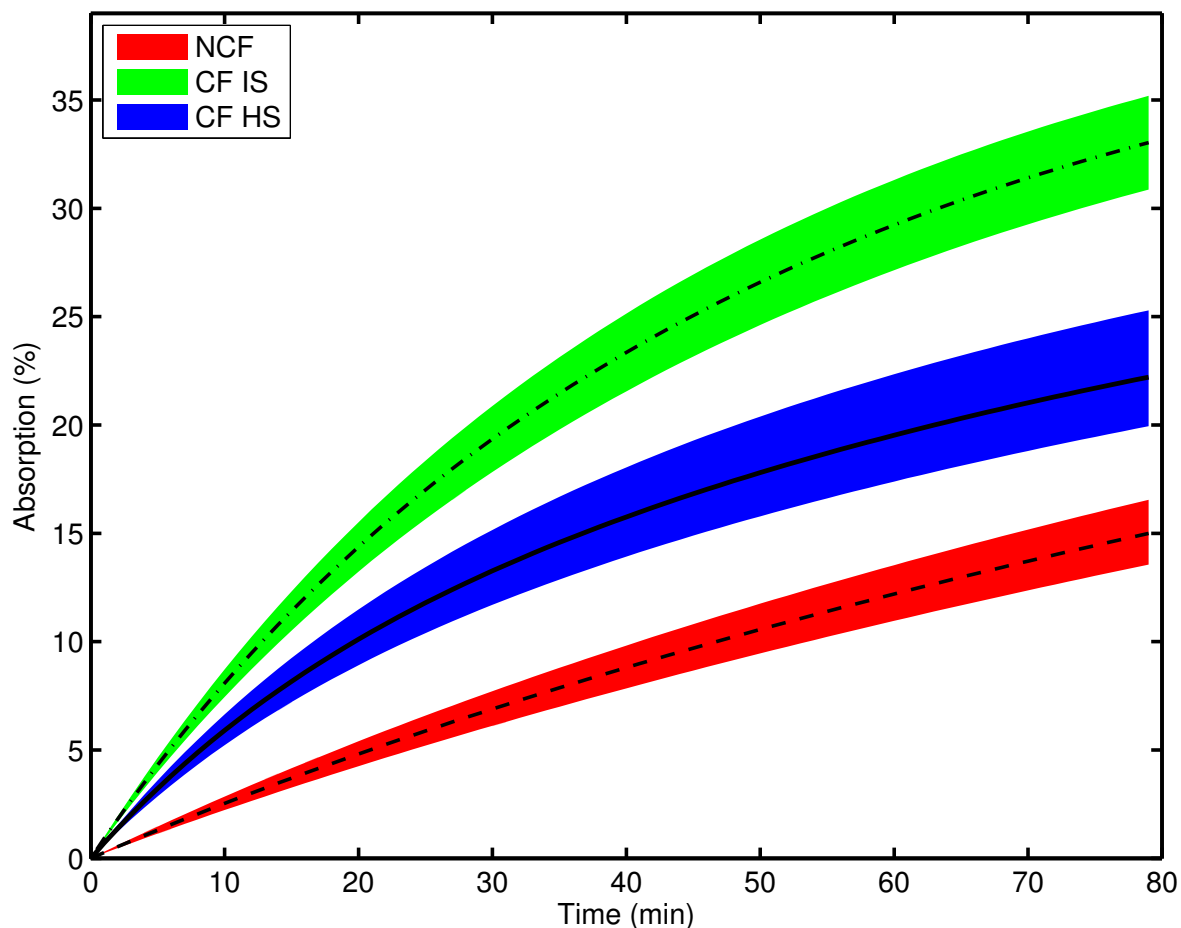


Figure 2.12: **Estimated DTPA absorption trajectories for three groups.** Non-CF (red with dashed line), CF IS (green with dotted dashed line), CF HS (blue with line). Shaded envelope characterizes 95% confidence interval (CI) of retention prediction by the model. Pediatric CF subjects not shown due to overlap with adult CF.

#### 2.4.4 *In Vitro* Evaluation of Model Prediction

In order to verify that hydration increases the fraction of functional ciliated area, CF HBE cultures were imaged (6 lines, n=12 filters) before and after addition of 10  $\mu\text{L}$  of Dulbecco's Modified Eagle Media (DMEM) (Sigma-Aldrich, St. Louis, MO, USA), a liquid cell culture media, to the apical surface and again after a second addition of 10  $\mu\text{L}$  of DMEM. It was

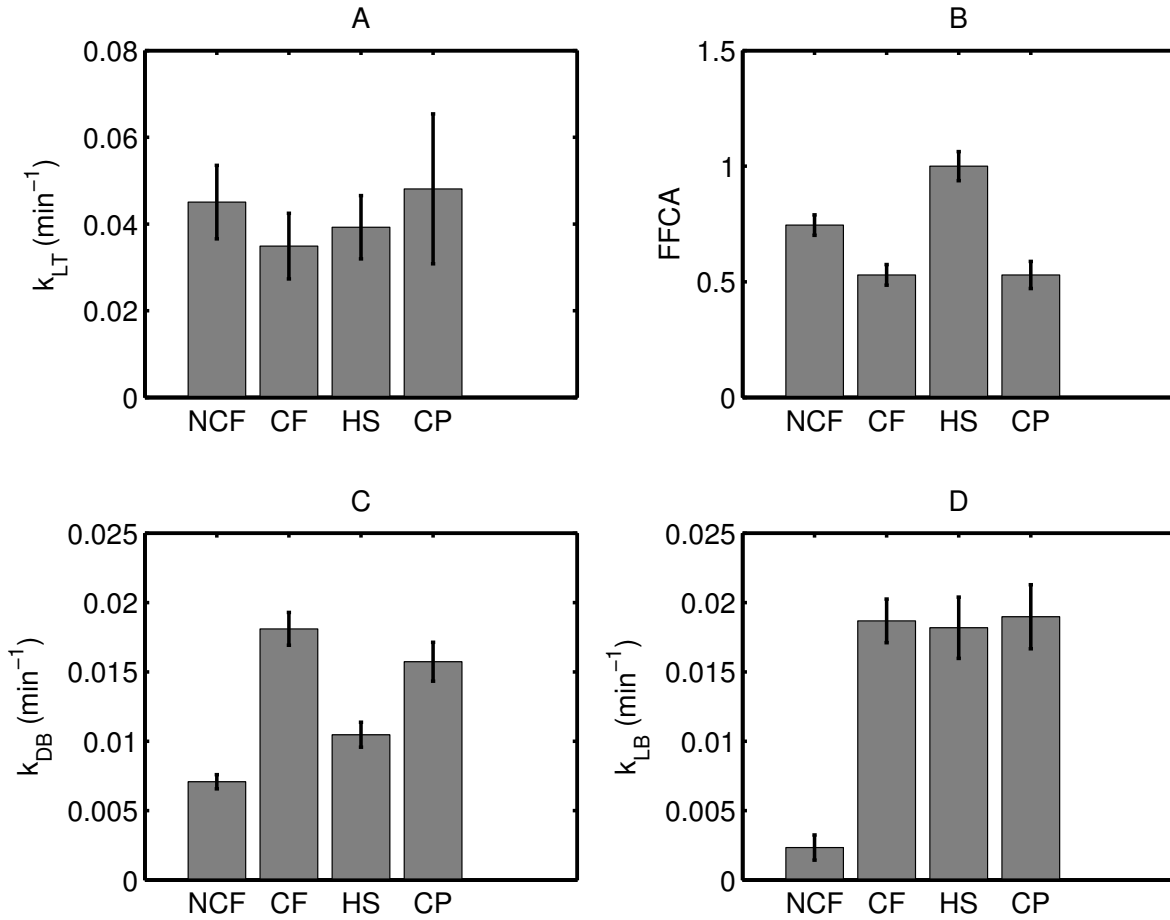


Figure 2.13: **Least-squares solutions for model parameters are shown with 95% confidence intervals for four groups:** Non-CF (NCF), CF HS, CF IS, and Pediatric CF (CFP). (A) MCC rate constant ( $k_{LT}$ ) ( $\text{min}^{-1}$ ). (B) Fraction (FFCA) of large airway with functional MCC. (C) Peripheral lung absorptive rate constant ( $k_{DB}$ ) ( $\text{min}^{-1}$ ). (D) Large airway absorptive rate constant ( $k_{LB}$ ) ( $\text{min}^{-1}$ ).

determined that hydration of HBE cells by addition of 10  $\mu\text{L}$  significantly increases the fraction of functional ciliated area ( $p < 0.0005$ ) above baseline. No further increase in FFCA was observed following a second addition of 10  $\mu\text{L}$  DMEM ( $p = \text{NS}$ ), as shown in Figure 8A. CF HBE cells were imaged following apical addition of either 5  $\mu\text{L}$  IS ( $n=6$ ) or HS ( $n=6$ ). A comparison of relative effect of IS and HS in CF HBE cells is shown in Figure 8B. Both

Table 2.3: **Pharmacokinetic Lung Clearance Parameter Values**

<b>Study</b>	$k_{LT}(min^{-1})$	$k_{DB}(min^{-1})$
NCF	0.0450±0.0085	0.0071±0.0005
CF HS	0.0393±0.0073	0.0105±0.0009
CF IS	0.0349±0.0076	0.0181±0.0012
CF Pediatric	0.0481±0.0173	0.0157±0.0014
Sakagami* [117]	0.022 ± 0.002	0.048 ± 0.003

Values from this study are shown with  $\pm$  95% confidence interval.

\* PK model in isolated perfused rat lung. Three fluorescent markers used, but only the parameter values for sodium fluorescein (F-Na) are shown since  $MW_{F-Na} = 376 \text{ Da} \approx MW_{DTPA}$ .

IS and HS additions increase functional area ( $p < 0.05$  and  $p < 0.001$ , respectively). However, HS increases functional area significantly more than IS ( $p < 0.01$ ).

## 2.5 DISCUSSION

The failure of the CF airway epithelium to secrete  $Cl^-$  and absorb  $Na^+$  in a normal manner results in a net osmotic gradient that favors rapid absorption of liquid from the ASL, resulting in diminished MCC and an accumulation of dehydrated mucus in the airways. Nuclear imaging methods have been developed to measure MCC and have been used as biomarkers of therapeutic efficacy. A novel method that measures both MCC and ASL absorption has been explored more recently [8]. This method involves the inhalation of radiolabeled particle and small molecule probes (TcSC and  $In^{111}$ -DTPA, respectively). The difference between total DTPA clearance and TcSC clearance can be used to estimate the absorption of DTPA,

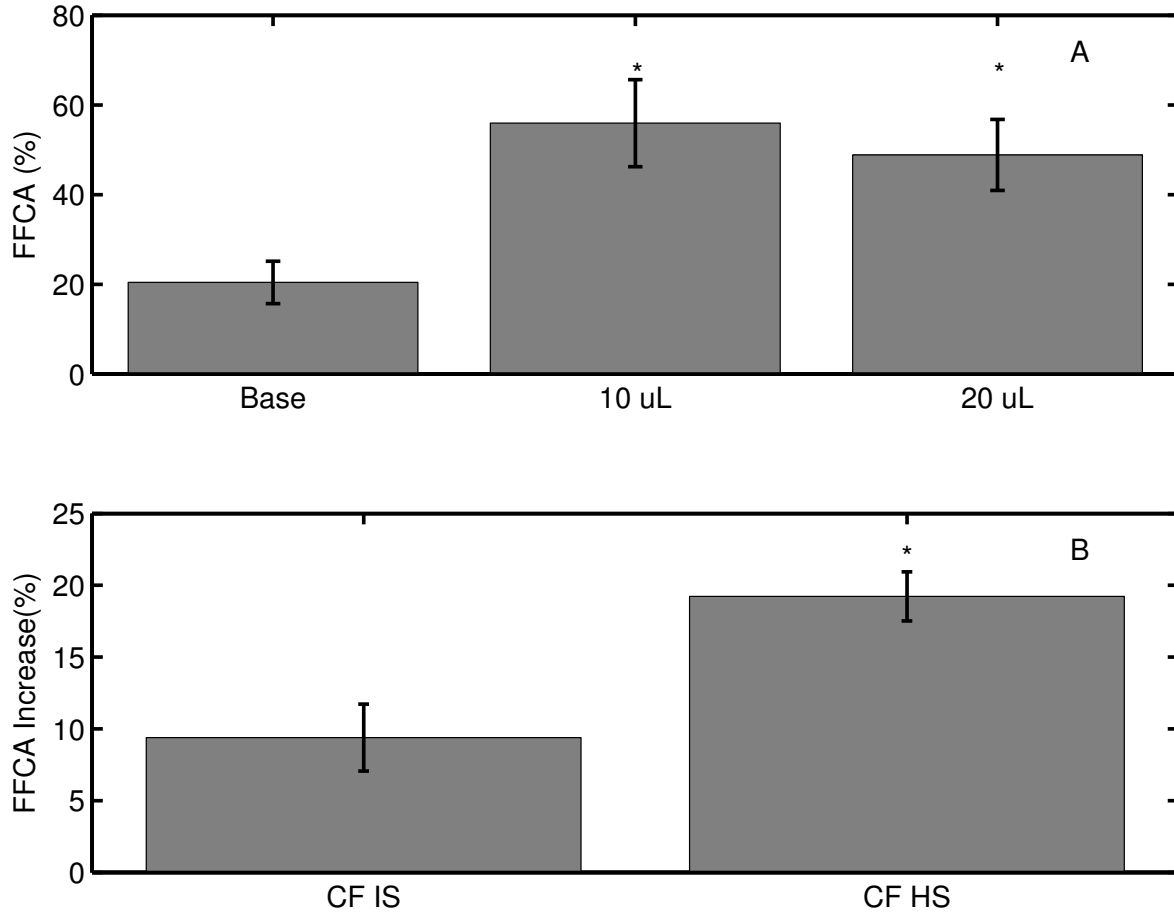


Figure 2.14: **FFCA determined *in vitro* in CF HBE cells is shown  $\pm$  SEM (A)** Activated area is significantly greater between 10  $\mu$ L and baseline (\*  $p < 0.0005$ ) and 2x10  $\mu$ L and baseline (\*  $p < 0.0005$ ). Activated area is not significantly greater between hydrated groups ( $p > 0.05$ ). (B) The increase in FFCA after addition of HS in cell cultures is significantly greater than IS (\*  $p < 0.01$ ).

and previous studies have demonstrated: (i) a positive and significant correlation between DTPA and ASL absorption rates [65]; (ii) DTPA absorption response to the use of osmotic therapies both *in vivo* and *in vitro* [8,65].

This work describes a model developed to consider the basic mechanisms governing small molecule and particle probe clearance from physiologically distinct compartments of the lung.

The combination of these mechanisms is reflected in the imaging result. Compartment or mechanism specific results provide additional insight into CF lung pathophysiology and therapeutic mechanisms of action. They may also provide more sensitive and accurate predictions of therapeutic efficacy than analyses of the composite imaging data as the compartmental description incorporates the inherent time-correlation of mass transport within the model structure.

### 2.5.1 Model Structure Selection and Analysis

The physically descriptive model includes central and peripheral lung compartments. The central zone includes large airways, intermediate and small airways, and alveoli while the peripheral zone includes only intermediate and small airways and alveoli [130], [133]. The peripheral zone includes both smaller airways and alveoli in a single compartment. The model also includes compartments for the trachea and blood. As determined by Akaike Information Criterion (AIC) [128] analysis, a quantitative metric that weights the model accuracy (as measured by sum-squared error) against the cost of model complexity (quantified by the number of parameters in a model), the most appropriate model given the timeframe of the data assumed zero MCC from the peripheral compartment. Model rate constants describing MCC from the functional large airway compartment ( $k_{LT}$ ), absorption from the small airway/alveolar compartment ( $k_{DB}$ ), large airway absorption ( $k_{LB}$ ), and FFCA were fit to the data. The fixed mathematical structure of the model is able to capture the dynamics of both MCC and the absorption of DTPA in the lungs of all patient groups.

An alternative, and more highly parameterized, model than that shown in Figure 2 would include parameter  $k_{DL}$  as an MCC rate constant from compartment  $D$  to compartment  $L$ , in addition to MCC rate constant  $k_{LT}$  and absorption rate constants  $k_{DB}$  and  $k_{LB}$ . All kinetics were assumed to be first order. Furthermore, the initial dosing of probes was included using a free dosing parameter (C/P), representing the ratio of radiopharmaceutical doses delivered to the large airways and peripheral lung. Under the assumption that TcSC is not absorbed in any lung region, the MCC curve was found to be bi-exponential, as suggested previously [116]. However, regression and analysis of the model parameters via the MAT-

LAB functions *lsqnonlin* (a nonlinear least-squares regression algorithm) and *nlparci* (an algorithm that computes confidence intervals on estimated parameters from the covariance matrix) yielded wide parameter confidence intervals, approximately  $\pm 10$  times the nominal parameter value. By eliminating  $k_{DL}$  the confidence intervals on parameter estimates are tightened dramatically (the worst case parameter CI from the model herein is  $k_{LB}$  in non-CF subjects which has CI's that are  $\pm 39\%$  of the nominal value).

While a two-compartment model, like that proposed by Sakagami in [116], may be used to describe clearance, the parameters may not be able to be estimated with confidence if a physiological rate process captured by a parameter in the model is on the timescale of the experiment, or longer. The 80-minute functional imaging session inherently limits the confidence that can be derived for slower physiological processes. Therefore it is hypothesized that the departure from monoexponential clearance seen in the retention curves could be explained by a non-zero steady state value for pharmaceutical retention. While this is aphysiologic over a period of days, an apparent non-zero baseline would manifest if a slow clearance process was occurring and data collection was short by comparison to the half-life of the clearance. This behavior can be realized in a number of ways in a kinetic model. In the present study, it is most easily incorporated by adding a new compartment that has no apparent MCC mechanism over the experimental timescale. Thus, while it is believed that MCC in D can be observed on a longer timescale, its mechanism is considered to be practically unidentifiable (i.e. there is insufficient data to inform this parameter) over the timescale examined in this chapter [134]. The numerical and experimental efforts used to identify this clearance effect are detailed in [chapter 4](#).

The model structure presented in Figure 2, and its grounding assumptions discussed in the **Results** section may fail to include mechanisms that could manifest on timescales longer than the 80 minute imaging period. To address the question of model appropriateness on the timescales of the data, the model was compared to the following alternative model structures with AIC as the basis for quantitative comparison:

Case 1. Exclude  $k_{LB}$ : DTPA absorption in  $L$ , represented by rate constant  $k_{LB}$ , is not appreciable over the 80-minute functional imaging timescale and should not be regressed to achieve model fit

Case 2. Include  $k_{DL}$ : MCC in  $D$ , represented by rate constant  $k_{DL}$ , is significant over the 80-minute functional imaging study timescale

The AIC values of each case above, in comparison to the model in Figure 2, are given in Table 2.4.

Table 2.4: **AIC Values for Various Model Structures**

	<b>Model</b>	<b>Case 1</b>	<b>Case 2</b>
NCF	-2546.28	-2535.65	-2543.38
CF HS	-2430.25	-2227.60	-2426.25
CF IS	-2775.62	-2287.07	-2775.57
CF Pediatric	-1858.37	-1597.47	-1854.37

The Akaike Information Criterion (AIC) is a metric for determining the most appropriate model for a system, where better fit is balanced against a penalty for overparameterization, such that more negative values are better. Total AIC is shown as calculated from Equation 7 for all cases: 1) exclude  $k_{LB}$  from model structure; 2) include  $k_{PL}$  in model structure.

These values demonstrate that the Figure 2 model displays the best combination of model fit and parsimony for the data set from [8]. Parsimony was especially important for model selection between the nominal case and Case 2, where the difference between AIC of the two cases was less than  $\pm 1\%$ . However, it is important to again note that there may in fact be clearance mechanisms from  $D$ ,  $L_N$ , and  $L_F$  that are not accounted for in this model because of constraints on the ability to quantitatively resolve their effects with confidence over the timescale of imaging. This is illustrated graphically in Figure 9, where it is clear that the parameter  $k_{DL}$  cannot be confidently identified as employed in Case 2 above. The experimental and mathematical methodologies that can be used to identify  $k_{DL}$  are discussed in [chapter 4](#).

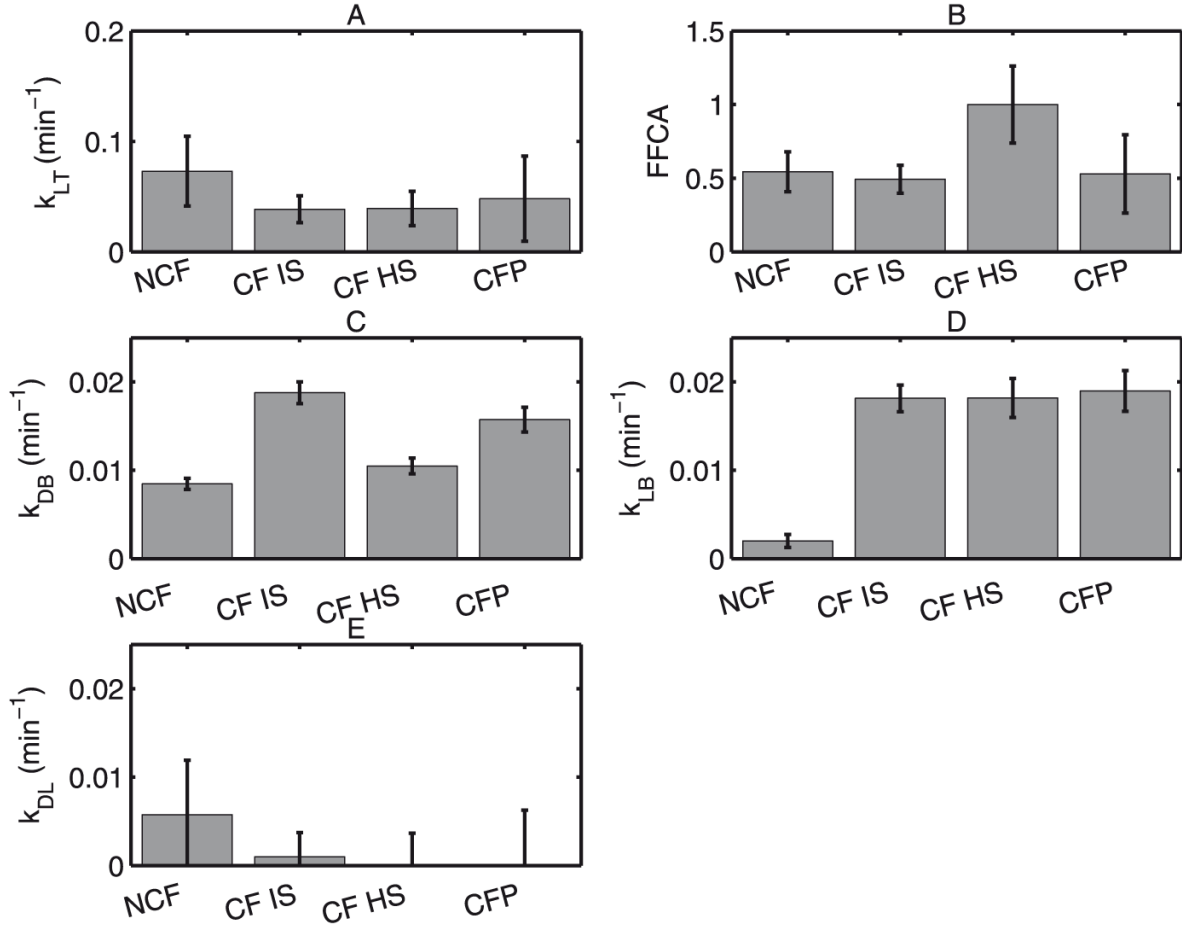


Figure 2.15: Least-squares solutions for model parameters in case 2 of Table ?? are shown for comparison to the selected model with 95% confidence intervals for four patient groups: Non-CF (NCF), CF HS, CF IS, and Pediatric CF (CP). (A) MCC rate constant ( $k_{LT}$ ) ( $\text{min}^{-1}$ ) reiterates that  $k_{LT}$  is the same in all groups. (B) Fraction (FFCA) of large airway with functional MCC. (C) Peripheral lung absorptive rate constant ( $k_{DB}$ ) ( $\text{min}^{-1}$ ) and (D) large airway absorptive rate constant ( $k_{LB}$ ) are nearly identical to their analogs in the selected model. (E) MCC rate constant ( $k_{DL}$ ) ( $\text{min}^{-1}$ ) from D to L is clearly unidentifiable, and the nominal value is much smaller than  $k_{LT}$  in each group. Confidence intervals are also widened in all parameters directly related to MCC.

### 2.5.2 Parametric Considerations

In non-CF subjects, FFCA is found to be  $< 1$ . The notion that not all of the surface of the conducting airways has functional cilia is a novel finding in humans. Hoegger *et al.* [135] recently report that even in the trachea, the most conductive airway, of newborn pigs without CF  $\approx 70\%$  of particles clear in ten minutes and that those same particles are only actively moving  $\approx 80\%$  of the time. While this timeframe is considerably shorter than the one in the study, it has been established that particles can be retained in the conducting airways of non-CF animals for a potentially significant amount of time. It would be reasonable to assume that particles deposited deeper in the airways, like those in this study, would be retained longer. This provides further reason to believe, in addition to the *in vitro* findings presented here, that the estimation of FFCA as a model parameter is grounded in realistic physiology.

Our model asserts that the rate of DTPA absorption ( $k_{DB}$ ) is increased in the peripheral lung (small airway and alveoli) compartment of patients with CF as compared to non-CF subjects. Hypertonic saline slows this rate to nearly non-CF levels. Previous *in vitro* studies have related DTPA hyperabsorption to liquid hyperabsorption [65]. It is assumed that DTPA hyperabsorption occurs via a paracellular mechanism, driven by increased paracellular liquid absorption, as DTPA has no known transcellular route by which to absorb. Therefore, it is likely that these current results reflect the basic liquid absorption defect associated with CF. The aerosol delivery techniques utilized to deliver the radiopharmaceuticals targeted large and small airways through a specialized breathing pattern both MCC and absorption were observed, indicating airway - as opposed to alveolar - involvement. Additionally, transient correction of the absorption defect would be expected after administration of an inhaled osmotic therapy based on most current hypotheses of airway disease in CF [120]. However, the possibility of alveolar effects cannot be completely excluded that may be related to yet undocumented physiological differences between the alveolar regions of CF and non-CF lungs.

The rate at which DTPA absorbs in the large airways ( $k_{LB}$ ) is similar to  $k_{DB}$  in the CF IS, CF pediatric and non-CF groups. However, while hypertonic saline decreases the

value of  $k_{DB}$  in patients with CF, it has no significant effect on  $k_{LB}$ . MCC is the dominant clearance mode in the large airways in both IS and HS cases. It has been shown *in vitro* that HS modulates the FFCA of the airway epithelium and have shown *in vivo* that increased MCC can be attained by modulating FFCA without requiring change in MCC rate. The two rate constants in the central region ( $k_{LT}$  and  $k_{LB}$ ) describe competing and correlated processes, whereas FFCA describes a more macroscopic phenomenon. Therefore, it would be expected that a change in one rate constant in L would induce a corresponding change in the other. Between IS and HS days there is no change in  $k_{LT}$  (the dominant process), so it would not be expected a change in  $k_{LB}$  either. However, due to the increase in FFCA, total MCC increases in the central lung after HS inhalation, which results in less DTPA being present and able to absorb in accordance with its unchanged rate constant. In effect, the underlying rate of DTPA absorption is unchanged, but an increase in total MCC as a result of increased FFCA leads to less DTPA being available for absorption and a smaller total quantity of DTPA absorbed in the CF HS case. In the case of D, however, it is assumed that there is no competing, certainly no governing, MCC term in D. Thus, conditions affecting D must result changes in  $k_{DB}$ .

### 2.5.3 Study Limitations

A primary limitation of the functional imaging method utilized is its inability to uniquely discern airways and alveoli. Given the three dimensional nature of the lung architecture, small airways and alveoli are likely to be included in any zone analyzed via 2D imaging. The small sizes of these structures make them impossible to differentiate from each other through direct imaging, though other physiological measurements (such as 24 hr MCC) may help to differentiate their functional effects. The limited time scale of imaging (80 minutes) in the current study may have also limited assessment of small airway mucociliary clearance. Extended-duration imaging studies may yield additional data that can inform processes with slower rates and model parameters such as  $k_{DL}$ , which was excluded from the Figure 2 model on AIC grounds.

#### 2.5.4 Physiological Implications

Our original study (see [8]) described significant differences in baseline whole lung DTPA absorption when comparing CF and healthy subjects. MCC was decreased in the CF groups, but not at statistically significant levels. This study finds that MCC is decreased (in a statistically significant way) in the CF IS group for  $t > 18$  minutes. The difference between these two findings arises from differences in the analysis tools used in this work versus the endpoint analysis performed in [8]. The confidence intervals presented here are around the parameters of the model, as opposed to being derived from statistical analysis of a final retention value, as in [8]. The model parameters govern the entire time-course of clearance, and thus are informed by the entire dynamic of the data given in [8]. The resulting confidence-interval-derived envelopes in Figures 5 and 6 capture the uncertainty of each physiologically descriptive parameter in the model. This is achieved by simulating the model at all possible combinations of upper and lower CIs for each parameter and determining the extreme values of model prediction at every time point. Hence, the CIs about the parameters are used to generate physiologically, as opposed to empirically, informed predictions of clearance behavior in each subject group population. The narrowness of the parameter CIs indicates confidence in the model parameter estimates (in that they are well informed from the dynamic data in [8]) and generates narrow prediction envelopes in each case, indicating a physiological difference in MCC dynamics between patients with CF and non-CF subjects that is not found via the previous endpoint-analysis methods.

Response to HS inhalation was apparent in terms of both decreased absorption and increased MCC as compared to IS inhalation. These trends are reflected in the modeled result. The model suggests that the observed increase in MCC following HS inhalation is due to an increase in FFCA rather than an increase in MCC rate, and a detailed analysis of this hypothesis using the *in vivo* imaging data is ongoing. The model also predicts that FFCA is reduced in patients with CF as compared to the healthy population. This prediction was used as a hypothesis about inducing a functional change *in vivo* that can be tested *in vitro*. To further elucidate this phenomenon, and validate that such behavior is possible, *in vitro* studies were performed with HBE cell cultures. A quantitative visual assay of ciliary

movement demonstrated that a larger fraction of the cell culture surface was activated after the addition of hypertonic saline vs. isotonic saline.

### **2.5.5 Clinical Relevance**

Some previous imaging studies have shown significant differences in whole lung MCC between CF and non-CF subjects [19, 136] while others have not [22]. By ascribing a fixed mathematical structure to the model, the clearance curves were constrained to a single family of dynamical forms, which allows for more sensitive comparisons between the dynamical, and also endpoint, behavior present from one patient group to another. This ultimately increases the confidence in the model assertion that MCC is decreased in patients with CF and can be increased by hypertonic saline inhalation and, subsequently, that the model offers a better tool than statistical models for use in clinically gauging MCC.

Applications of this model may include the design of dosing regimens for agents targeting changes in MCC and/or absorption. For example, the timeline of the effects associated with an osmotic therapy (correction of liquid absorption defects) could be assessed independently of the resulting secondary effects (recruitment of functional ciliated airway, large and small airway clearance). Dosing timed in accordance with the duration of the counter-absorptive effect may provide more continuous clearance from the lungs and patient benefit, though outcome assessment is beyond the scope of the model at present. The model could also be used to resolve the pharmacodynamics of medications with subtle, complex, or multiple therapeutic effects, to the degree that these agents impact MCC and absorption.

### **2.5.6 Summary**

Our physiologically motivated compartmental model is able to reproduce the clearance behavior of both large particle (TcSC) and small molecule (DTPA) radiolabeled probes as informed by functional imaging data. The model asserts that liquid absorption rate is increased in the peripheral lung of patients with CF as compared to non-CF subjects, and that hypertonic saline will decrease the rate of absorption in patients with CF to near non-CF levels. The model also attributes increased MCC induced by hypertonic saline treatment

to an increase in airway surface area with functional ciliary clearance, as opposed to an increased rate of clearance. The physiology inherent to the model structure and parameterization allow for increased sensitivity in gauging the effects of hypertonic saline *in vivo* in a real-time manner. This model should, therefore, be extendable to other treatments, both present and future, that target the liquid hyperabsorption and MCC deficiency present in cystic fibrosis.

### 3.0 CELL SCALE MODELING OF LIQUID AND SOLUTE HYPERABSORPTION IN CYSTIC FIBROSIS BRONCHIAL EPITHELIA

#### 3.1 INTRODUCTION

Liquid volume regulation by human bronchial epithelia (HBE) is essential to maintaining cell, tissue, and organ-level function in the lung [22]. In patients with cystic fibrosis (CF), the most common life-shortening autosomal recessive disorder in caucasians, the Cystic Fibrosis Transmembrane Conductance Regulator (CFTR) protein is absent or dysfunctional. This causes dysregulation of ion transport at the airway surface, which leads to airway surface liquid (ASL) depletion, mucus accumulation, and impaired mucociliary clearance (MCC) [12]. Impaired MCC allows pathogens to establish chronic opportunistic infections in the airways. Concomitant inflammation leads to airway damage and bronchiectasis resulting in premature respiratory failure. Despite these multi-scale effects, however, at the most basic level CF is a disease caused by abnormal cellular transport of ions and water.

In healthy epithelia, water, ions, and other solutes are transported in and out of cells via a number of passive and active mechanisms [49]. In CF, deficient or absent  $\text{Cl}^-$  and  $\text{HCO}_3^-$  secretion via CFTR have been identified as the primary anion transport defects [135, 137].  $\text{Na}^+$  hyperabsorption via dysregulation of the epithelial sodium channel (ENaC) has been considered the primary cation transport defect [49], though recent studies have called this into question [25]. Passive basolateral  $\text{K}^+$  transport is also affected [138]. Water transport and volume regulation are also likely affected through failed CFTR interaction with aquaporin-3 (AQP3) [52]. Passive water and solute transport occurs in the paracellular space and is regulated by tight junction integrity, which may be diminished in CF airways [139, 140, 141].

Historically, the active ion transport properties of HBE have been studied experimentally in the Ussing chamber [32]. A number of mathematical models have characterized the ion transport that occurs in the Ussing chamber: without liquid transport [87], in CF [55, 88, 89], and comparing differences between CF and non-CF cells [16, 17]. In the Ussing Chamber, current is only measurable when electrodes on the apical and basolateral sides of a cell culture sample are submerged, which requires flooding the apical membrane of cultured HBE [32]. There is evidence that both CFTR and ENaC currents are sensitive to ASL volume [13, 88], implying that the function of these channels is not a true representation of *in vivo* physiology in the flooded environment of an Ussing chamber and that it may be more relevant to model HBE cell cultures under “thin-film” conditions. A model of thin-film culture conditions was developed by Herschlag and colleagues [96] to capture purinergic effects on ASL homeostasis, but it does not distinguish between types of ions. Warren et al. [70] developed a thin-film model of  $\text{Ca}^{2+}$  effects on ion and liquid transport that does not account for finite basolateral volumes, the auto-regulatory effects of the ASL volume, or paracellular water transport.

Our model adds to those presently in the literature by accounting for the cellular components of liquid and solute transport most relevant to CF. This includes apical chloride transport through both CFTR and alternate channels such as calcium-activated chloride channels (CaCCs) and members of the solute carrier family (e.g. SLC26A9) [3], apical sodium transport through ENaC, and a linear description of basolateral  $\text{Na}^+$  and  $\text{Cl}^-$  transport. Paracellular transport of all components is also included to reflect the leakiness of HBE, the extent of which is still debated [59, 61, 64]. The model incorporates the transport of the radiopharmaceutical  $\text{Tc}^{99\text{m}}$ -DTPA (DTPA), an *in vivo* functional imaging probe that is representative of small molecule absorption. DTPA absorption is increased in the lungs of patients with CF [8, 21] and in CF HBE where it is strongly correlated with ASL absorption [65]. DTPA can only move through the paracellular pathway, and its absorption rate characterizes paracellular flows and tight junction integrity [65]. DTPA transport across the epithelium occurs through two mechanisms: (i) concentration driven diffusion; and (ii) convection or “solvent drag” due to water flow through the tight junction [57].

Presented here are the derivation and validation of a mathematical model of airway epithelial ion and liquid transport considering the case of volume addition under thin film conditions. Model-determined and channel-specific permeability coefficients are compared for Cl<sup>-</sup> and Na<sup>+</sup>, trans- and paracellular liquid transport using DTPA as a surrogate, and cell volume response in CF and non-CF epithelia. Treatment-relevant responses to hyperosmotic solutions are also modeled. It is sought to parameterize disease-relevant components of liquid volume regulation in CF. Furthermore, this model could provide insight into the mechanisms by which airway depletion leads to reduced fractions of functionally ciliated airway, as has been previously modeled and reported [1, 8]. It could then be mathematically coupled to an airway scale model [1] by using disease-based parameterization to study the mucociliary transport effects of CF that manifest from the cellular-scale processes.

## 3.2 MATERIALS AND METHODS

### 3.2.1 Model Development

The parameters defining model geometry are based on the assumption that cultures were composed of a single layer of cells and that these cells were in the shape of rectangular prisms.

Apparent apical surface areas of all the tight junctions ( $A_{TJ}$ ) and cells ( $A_C$ ) on the filter ( $A_F$ ) are related mathematically. For a grid of rectangles  $m$ -by- $n$  in dimension there are  $2mn-m-n$  interior borders (*i.e.*, junctions). Thus, the expression for relative abundance of junctions to cells is  $\frac{2mn-m-n}{mn} \frac{(junctions)}{(cells)}$  which reduces to  $2 \frac{(junctions)}{(cell)}$  when  $mn$  is large. Therefore, when there are a large number of cells on the filter it can be shown that  $A_{TJ}$  can be approximated by the following relationship:

$$A_{TJ} = A_F \frac{2A_{TJ,1}}{A_{C,1}} = A_F \frac{2D_{TJ}D_C}{(D_{TJ}+D_C)^2} \quad (3.1)$$

Here  $A_{TJ,1}$  and  $A_{C,1}$  are the areas of a single tight junction and cell for TJ ( $D_{TJ}=60$  nm) and cell ( $D_C=8$   $\mu$ m) diameter, respectively.  $A_C$  can then be determined as the difference

between  $A_{TJ}$  and  $A_F$  ( $A_F=0.33 \text{ cm}^2$ ). Dynamic cell-volume behavior was captured solely by allowing the cell height to change in response to osmotic influx or efflux of water, as would be expected in columnar bronchial epithelia [9].

The transport of water from compartment  $i$  to  $j$  is driven solely by osmotic pressure difference  $\Delta\pi_{i,j}$ :

$$\Delta\pi_{i,j} = \sum_k \gamma_k \frac{n_{k,i}}{V_{k,i}} - \sum_k \gamma_k \frac{n_{k,j}}{V_{k,j}} \quad (3.2)$$

Here  $n_{k,i}$  is the number of moles of solute,  $k$ , which is divided by the volume of compartment  $i$  and multiplied by osmotic coefficient  $\gamma_k$ . Because  $A_C$  is assumed to be constant, the height of the epithelium may be determined at any given time from the volume of the cell compartment as  $h_C(t)=V_C(t)/A_C$ . Initial cell height was specified to be  $30.2 \mu\text{m}$  based on values from the literature [16] but varies in response to osmotic and volumetric effects in the system and accounts for the ability of the cells to change internal volume during simulation. This allows us to determine the paracellular permeability of a solute  $k$  at any instance in time as:

$$P_{k_{A,B}}(t) = \frac{\mathcal{D}_k}{h_C(t)} \quad (3.3)$$

Paracellular permeability,  $P_{k_{A,B}}$ , is taken to be the diffusion coefficient ( $\mathcal{D}_k$ ) of species  $k$  divided by the length of the paracellular pathway (*i.e.* cell height), which changes with time. The absorption of DTPA is modeled based on its use as an *in vivo* analog for measuring transepithelial liquid transport. DTPA absorption occurs through the paracellular pathway and characterizes paracellular flows and tight junction integrity. Our experiments have also shown that DTPA absorption is proportional to overall apical liquid absorption [65].

### 3.2.2 Model Structure

Based on the model schematic given in Figure 3.1, the equations governing liquid and solute transport in HBE were established, defining mass balances for ASL (A), basolateral (B), and cellular (C) compartments. Transport of water from compartment  $i$  to  $j$  is driven solely by osmotic pressure difference,  $\Delta\pi_{i,j}$ , as described in Equation 3.2.

The volumetric flux from any compartment to another is:

$$\frac{dV_i}{dt} = L_{P_{i,j}} V_w \sum_j (\Delta\pi_{i,j}) \quad (3.4)$$

Here,  $L_P$  is the hydraulic permeability of the membrane separating compartments  $i$  and  $j$ , and  $V_w$  is the molar volume of water (0.018 L/mol). By assuming that the cells in the culture are neighboring rectangular prisms, it is also assumed that the apical and basolateral membrane areas are identical. In reality the basolateral membrane area is at least 10-fold larger than the apical membrane area (16-fold in the resting geometry of the model). This is because basolateral transport proteins begin to appear in the membrane immediately adjacent to tight junctions in the lateral intercellular space (LIS). Hence, the entire membrane area across the tight junction away from the apical membrane is basolateral. As such, hydraulic permeabilities of the apical and basolateral membranes are allowed to be equal ( $L_{PA}=L_{PB}$ , thus it is denoted as  $L_{PC}$ ), though previous studies have found [9], and some [16] have applied, order of magnitude differences between the membrane permeabilities.

Solute transport occurs via diffusion down a concentration gradient (given as a concentration difference,  $\Delta C_{k_{i,j}} = C_{k_i} - C_{k_j}$ ) between compartments, via active transport into and out of the cell ( $J_{act}$ ) and by bulk fluid convection in the paracellular space ( $J_{conv}$ ). Thus, overall solute transport in a given compartment is given by:

$$\frac{dn_{k,i}}{dt} = \sum_j P'_{k_{i,j}} \Delta C_{k_{i,j}} + J_{k,act_{i,j}} + J_{k,conv_{i,j}} \quad (3.5)$$

Here,  $P'_{k_{i,j}}$  is the modified permeability (if volume-regulated; the true permeability,  $P_{k_{i,j}}$ , is used if not) of a membrane to a solute. These equations are applied to the appropriate transport pathways illustrated in Figure 3.1 for  $\text{Na}^+$ ,  $\text{Cl}^-$ , DTPA, and mannitol. A full list of model state equations can be found in Appendix A and code to simulate the equations in in Appendix B, but their function is summarized briefly below.

ENaC is the apical channel for transcellular  $\text{Na}^+$  transport, and is represented mathematically by an ASL-volume-regulated Michaelis-Menten expression that is maximally permeable at high volumes. A linear regulator in the basolateral membrane drives intracellular  $\text{Na}^+$  concentration towards a homeostatic value of 23 mM.  $\text{Cl}^-$  homeostasis is maintained at 44

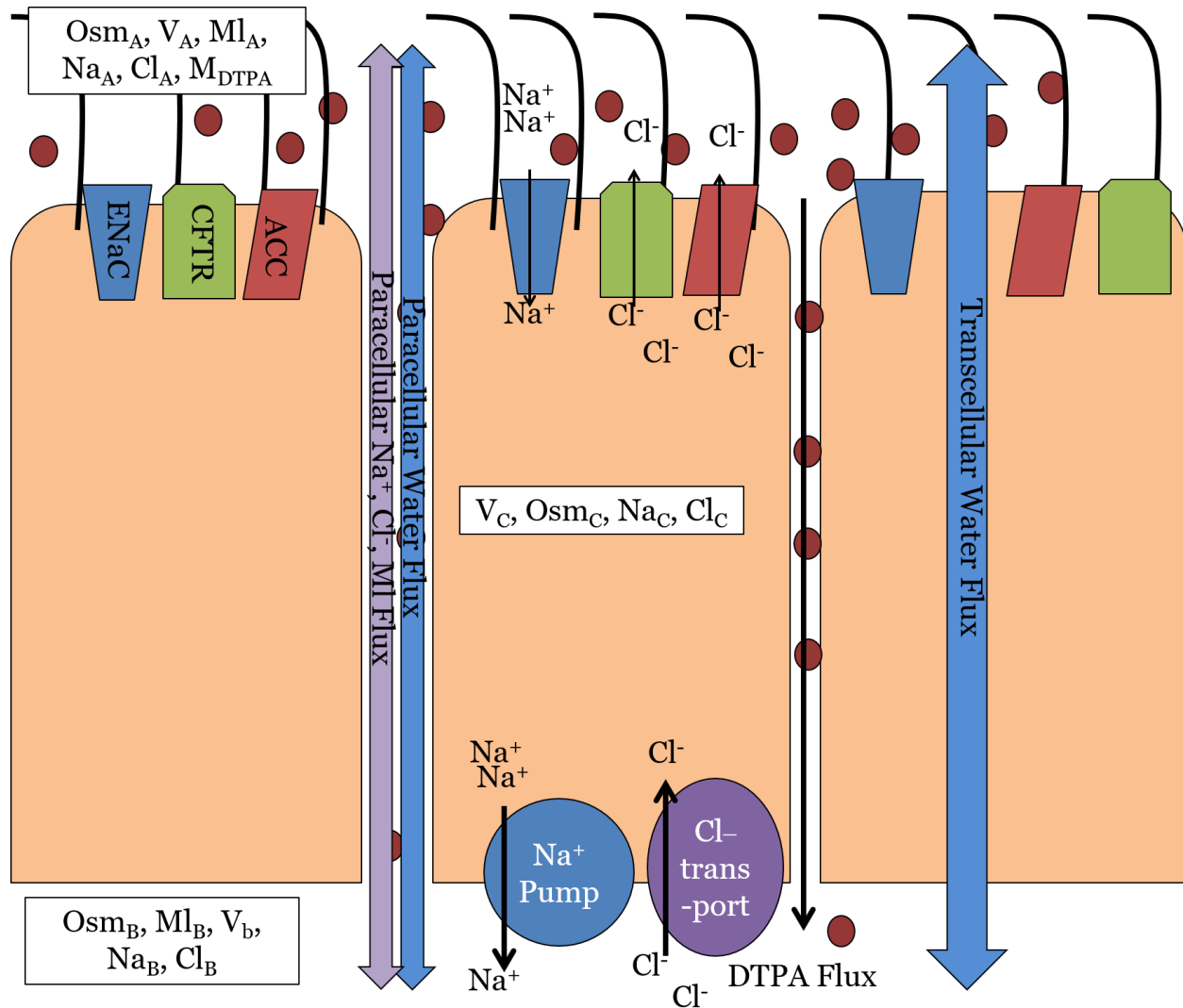


Figure 3.1: Schematic of the contributors to solute and liquid transport across the airway epithelium represented in the model equations. Volumes ( $V_i$ ) of the apical, basolateral, and cellular compartments dynamically respond to changes in osmolarity. Terms describing ENaC and CFTR respond to changes in apical volume according to first and second-order Hill functions, respectively. Basolateral Na<sup>+</sup> and Cl<sup>-</sup> fluxes are included to assure conservation of mass. Mannitol (MI) is included in the model to allow for the description of liquid and DTPA absorption following hyperosmotic challenge. The inclusion of DTPA in the model makes the terms describing paracellular and transcellular water transport mathematically observable and provides a link between the physiological processes measured *in vitro* and *in vivo*.

Table 3.1: Initial conditions for the model compartments immediately following apical Ringer’s addition. Initial apical volumes were determined from data, but solute concentrations were assumed to be similar regardless of post-addition volume. Cellular volume is the total volume of the monolayer.

	Apical	Basolateral	Cellular
Na <sup>+</sup> (mM)	140	140	23
Cl <sup>-</sup> (mM)	119.6	119.6	44
Other Solutes (mM)	40.4	40.4	233
Water ( $\mu$ L)	Measured	400	0.98

mM via action of a linear regulator in the basolateral membrane. These linear regulators are surrogates for the homeostatic regulation that is accomplished by the Na-K-ATPase and NKCC-cotransporter in biology [16, 17]. CFTR is an apical volume-regulated Cl<sup>-</sup> channel modeled with a second-order Hill functionality that is maximally permeable at zero ASL volume. ACC is an alternate, linear, constitutively active Cl<sup>-</sup> channel also in the apical membrane of the model. DTPA and mannitol, another osmotic agent used in therapy, are restricted to diffusion and convection through the paracellular space. Initial conditions for Na<sup>+</sup> and Cl<sup>-</sup> concentration and liquid volume in each compartment are given in Table 3.1.

### 3.2.3 Experimental Methods

CF and non-CF HBE cultures will absorb ASL following an apical volume challenge in order to restore homeostasis [97]. It is also known that CF HBE hyperabsorb ASL and DTPA relative to non-CF HBE when similarly challenged [49, 65, 97]. Experimental training data for the model was obtained by observing the dynamics of liquid and DTPA absorption in HBE cell cultures after a 10 $\mu$ L apical addition of Ringers solution and Technetium 99m-labeled DTPA. Apical volume was determined over the course of the experiments using an optical method described by Harvey and colleagues [97]. DTPA absorption was determined

according to the methods of Corcoran and colleagues [65] concurrently with the volume measurements. Primary HBE cultures from CF (11 donors, n=102 filters, > 6 filters per donor) and non-CF (12 donors, n=93 filters, > 6 filters per donor) lungs removed at the time of transplant were used for this model training data set. Estimates of net Na<sup>+</sup> and Cl<sup>-</sup> flux were determined from Ussing Chamber measurements of Na<sup>+</sup> and Cl<sup>-</sup> currents ( $I_{Na}$  and  $I_{Cl}$ , respectively) obtained according to the procedure in [65].  $I_{Na}$  is calculated as the amiloride sensitive short-circuit current ( $I_{SC}$ ).  $I_{Cl}$  is measured as the difference between forskolin-stimulated and bumetanide-inhibited  $I_{SC}$  under amiloride block. Transepithelial electrical resistance (TER) exceeded 250  $\Omega\text{cm}^2$  for all cultures used. These cultures were prepared using previously described methods and obtained through a protocol approved by the University of Pittsburgh IRB [8].

### 3.2.4 Parameter Estimation

Model training was performed via Markov Chain Monte Carlo (MCMC) search for 9 free parameters that best fit the dynamics of liquid and DTPA absorption in HBE cells. The MCMC algorithm used is that developed by Hogg: parallel tempering for estimation (ptempest) [142]. The ptempest algorithm is freely available online (<https://github.com/RuleWorld/ptempest>). In the simulations, least sum-squared-error (SSE) was the objective function between simulation predictions and ASL volume (in  $\mu\text{L}$ ) and DTPA absorption data (fitted as retention in thousands of counts to scale it suitably versus ASL volume). The SSE can be used as an estimate of the  $-\log(\text{likelihood})$  under the assumption of normal variance in the data [129]. The resultant posterior parameter distributions for 8,000 swaps across 4 chains are presented in Figure 3.2. Constrained parameter refitting was performed in the characterization of model-predicted responses to osmotic challenges in order to account for the physiological changes that occur under such stresses. This was accomplished using the Matlab (© 2015, The MathWorks, Natick, MA) function *lsqnonlin*.

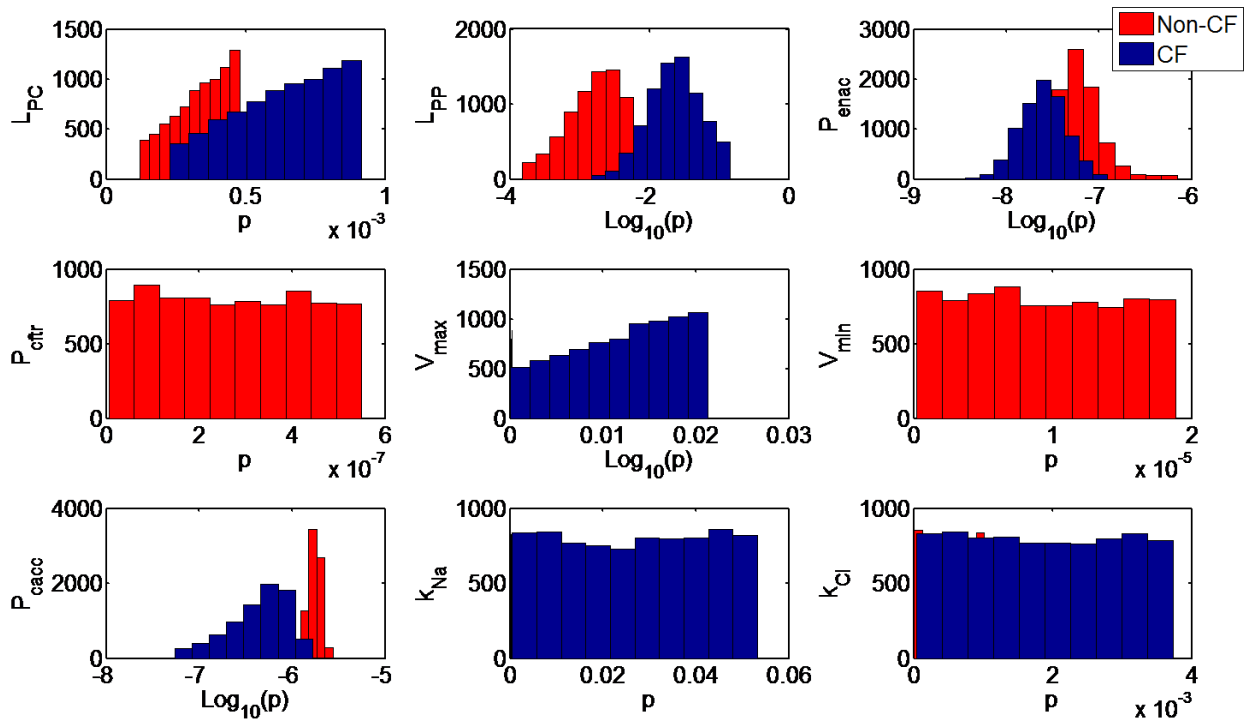


Figure 3.2: Posterior distributions of model parameters are given for base-10 ( $p$ ) or  $\log_{10}$  transformed values generated from Markov Chain Monte Carlo. Distributions are given along either a linear or logarithmic abscissa.

### 3.3 EXPERIMENTAL AND SIMULATION-BASED FINDINGS

#### 3.3.1 The mathematical model captures population absorption dynamics in CF and non-CF HBE

We first examined whether model simulations were able to predict the absorption dynamics of the ASL and DTPA. A  $10 \mu\text{L}$  bolus of Ringers solution and DTPA was added to the apical side of HBE cell cultures as described in **Materials and Methods**. Data demonstrated that CF cells had decreased ASL volumes immediately after volume addition and all time points through the 24 hours of the experiment (t-test,  $p < 5 \times 10^{-10}$ ), indicative of the characteristic depletion of CF ASL. DTPA absorption was also significantly increased in the CF cells

( $p < 5 \times 10^{-10}$ ), which has been previously reported in *in vitro* experiments and in *in vivo* functional imaging studies [21,65]. The distributions of all model parameters were generated from model training via MCMC. Model simulations, using the best-fit parameter sets given in Table 3.2, were able to capture the absorption dynamics of the ASL and DTPA as shown in Figure 3.3. The model-predicted apical volume and DTPA trajectories were within the standard error about the mean for all time points. Non-CF cells rapidly reabsorbed liquid to return to homeostasis whereas CF cells demonstrated a slower but continued absorption of liquid that exceeded that of non-CF cells over time.

In addition to good dynamic agreement between model output and experimental data, the best-fit parameters determined via Monte Carlo search agreed well with those found in the literature and are detailed in Table 3.2. The mean hydraulic permeabilities of the cell in both CF ( $6.1 \times 10^{-4}$  m/s) and non-CF ( $3.2 \times 10^{-4}$  m/s) were similar to those reported by Matsui and colleagues ( $2.4 \times 10^{-4}$ , CF;  $0.96 \times 10^{-4}$ , non-CF) [9]. Additionally, the mean maximum permeability of ENaC ( $6.3 \times 10^{-8}$  m/s, non-CF;  $2.5 \times 10^{-8}$  m/s, CF) is of similar magnitude to what has been reported in Ussing chamber experiments [56,93] ( $2.3 \times 10^{-8}$ , non-CF;  $6.3 \times 10^{-8}$ , CF), which occur in flooded conditions where the Michaelis-Menten-type switch governing ENaC in the model is nearly saturated. The thin-film model demonstrated an opposite trend in ENaC permeability to the Ussing chamber experiment comparing CF and non-CF cells. Paracellular water permeability was ten-fold greater in CF cells compared to non-CF cells, which may indicate a defect in the barrier integrity of CF cells.

### 3.3.2 Validation of Model Structure and Dynamic Output

As validation of the estimates of liquid and DTPA absorption, it was sought to determine whether the ion transport rates predicted by the model were similar to relevant physiological measurements. The change in the amount of either  $\text{Na}^+$  or  $\text{Cl}^-$  in the apical compartment in the first hour after the liquid and DTPA addition was determined and the model-predicted flux ( $\mu\text{eq}/\text{cm}^2/\text{hr}$ ) of each ion was computed. These flux estimates were compared to those calculated from short circuit estimates in the Ussing Chamber, as shown in Figure 3.6A for  $\text{Na}^+$  absorption and Figure 3.6B for  $\text{Cl}^-$  secretion.

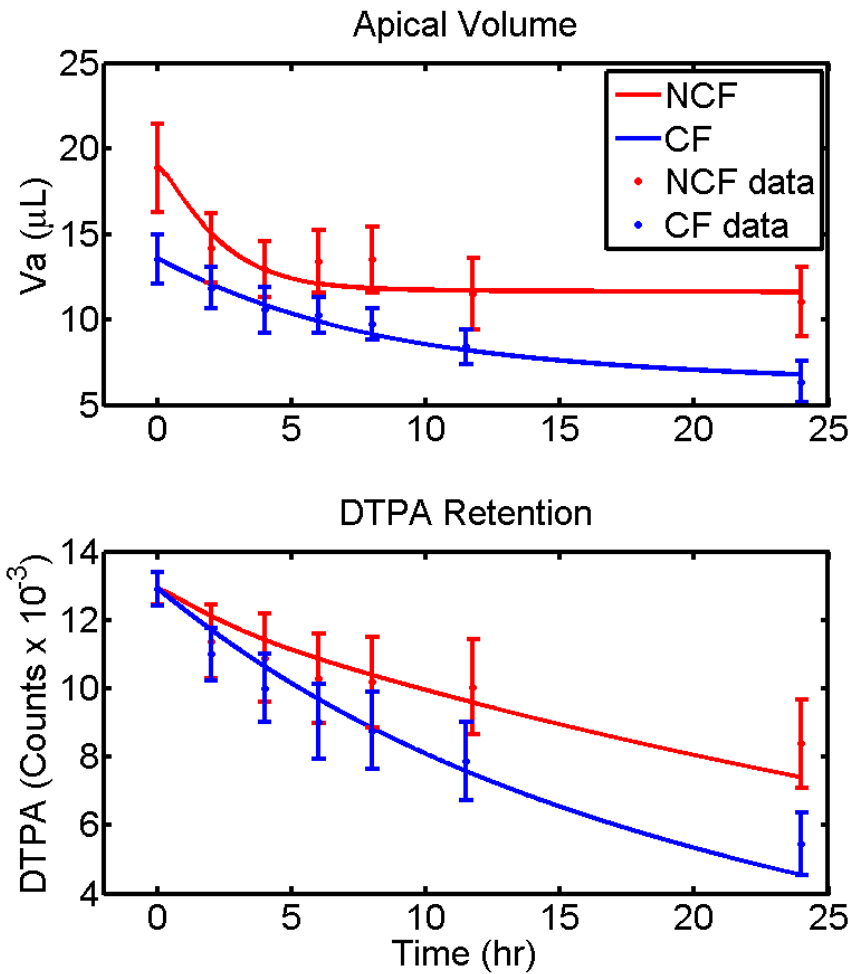


Figure 3.3: Best-fit model trajectories and experimental data after 10  $\mu\text{L}$  apical volume addition to 6 non-CF (NCF) and 6 CF lines. CF lines demonstrate apical dehydration relative non-CF lines at the start and end points of the experiment (top panel,  $p < 5 \times 10^{-10}$ ). Total volume absorbed in the model is 7.25  $\mu\text{L}$  (38.4%) in the non-CF case lines and 6.91  $\mu\text{L}$  (51.0%) in the CF lines. Non-CF cells rapidly return to homeostatic volumes, whereas CF cells exhibit prolonged absorption that results in increased DTPA absorption (bottom panel,  $p < 5 \times 10^{-11}$ ). Model-estimated DTPA clearance is 42.7% in non-CF cells compared to 65.0% in CF after 24 hrs. Error bars show experimental data  $\pm$  SEM.

Table 3.2: Model parameters were set according to values found in the literature (references included) or determined via MCMC search for model training. Nonlinear least-squares search was used under osmotically challenged conditions to account for stress responses that can change transport rates. Abbreviations are transcellular ( $L_{PC}$ ) and paracellular ( $L_{PP}$ ) hydraulic permeabilities, maximum ENaC ( $P_{ENaC}$ ) and CFTR ( $P_{CFTR}$ ) permeabilities, and the respective half-maximal  $V_{max}$  and half-minimal  $V_{min}$  for those channels. Constitutive chloride permeability ( $P_{ACC}$ ) and basolateral sodium ( $k_{Na}$ ) and chloride ( $k_{Cl}$ ) rate constants were also included in the parameter search. Best-fit values are given in lieu of means due to distributional shape factors.

	$L_{PC}$ (m/s) $\times 10^{-4}$	$L_{PP}$ (m/s) $\times 10^{-3}$	$P_{ENaC}$ (m/s) $\times 10^{-8}$	$P_{CFTR}$ (m/s) $\times 10^{-8}$	$V_{max}$ (L) $\times 10^{-6}$	$V_{min}$ (L) $\times 10^{-6}$	$P_{ACC}$ (m/s) $\times 10^{-8}$	$k_{Na}$ ( $s^{-1}$ ) $\times 10^{-5}$	$k_{Cl}$ ( $s^{-1}$ ) $\times 10^{-5}$
CF	4.57 *2.43	14.6	1.23 **6.3	-	214	-	0.554	107	7.47
Non-CF	2.40 *2.40	1.50	7.00 **2.3	5.50 **4.3, ***6.6	2.30	1.88	1.89	1.39	2.27
Ringers	2.76	11.4	1.94	5.50	2.30	1.88	1.25	1.39	2.27
Mannitol	6.34	5.64	4.54	5.50	2.30	1.88	7.35	1.39	2.27

Table 3.3: Citations are given for comparison of values to \*, (52); \*\*, (49), \*\*\* (18)

Maximum likelihood estimation functions were generated for  $\text{Na}^+$  fluxes by fitting the means and standard deviations of a lognormal and normal distribution summed together with a fitted weighting factor to isolate and characterize the small secondary peak near  $7 \mu\text{eq}/\text{cm}^2/\text{hr}$  in the non-CF ensemble Figure 3.6A. The weighting factor was 0.98 in the non-CF case and 1.00 in the CF case indicating that the primary peak in the non-CF case and the only visible peak in the CF case are lognormally distributed as shown in Figure 3.4. The large peak in the non-CF case is used as the basis of all further interrogation.

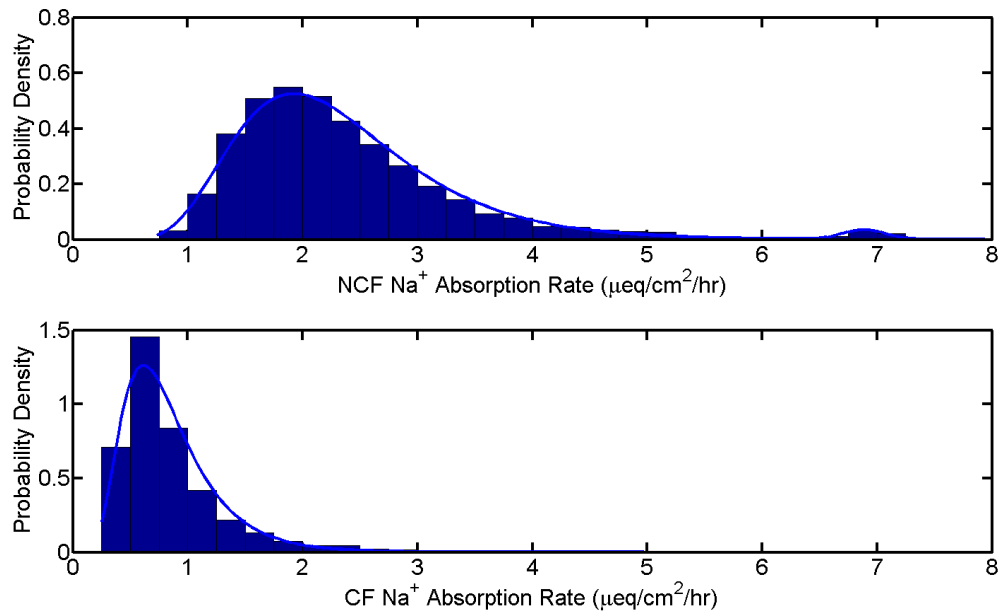


Figure 3.4: Ensemble distributions of model-predicted non-CF (top) and CF (bottom)  $\text{Na}^+$  fluxes. Both primary peaks are well-fit by lognormal distributions. The second peak in the non-CF (NCF) distribution near  $7 \mu\text{eq}/\text{cm}^2/\text{hr}$  only contributes to 2% of the area in the cumulative distribution function.

Figure 3.5 demonstrates that the  $\text{Cl}^-$  flux distributions are approximately normal. The non-CF case has a minor left skew, but is approximately normal. The CF distribution is well-approximated by a normal distribution. Both distributions include 0, and the CF distribution includes 0 within a standard deviation of the mean. This quantitatively recapitulates

the representation of the CF absorptive phenotype given by Goralski and colleagues [23]. Comparisons of these flux values to data are presented in Figure 3.6.

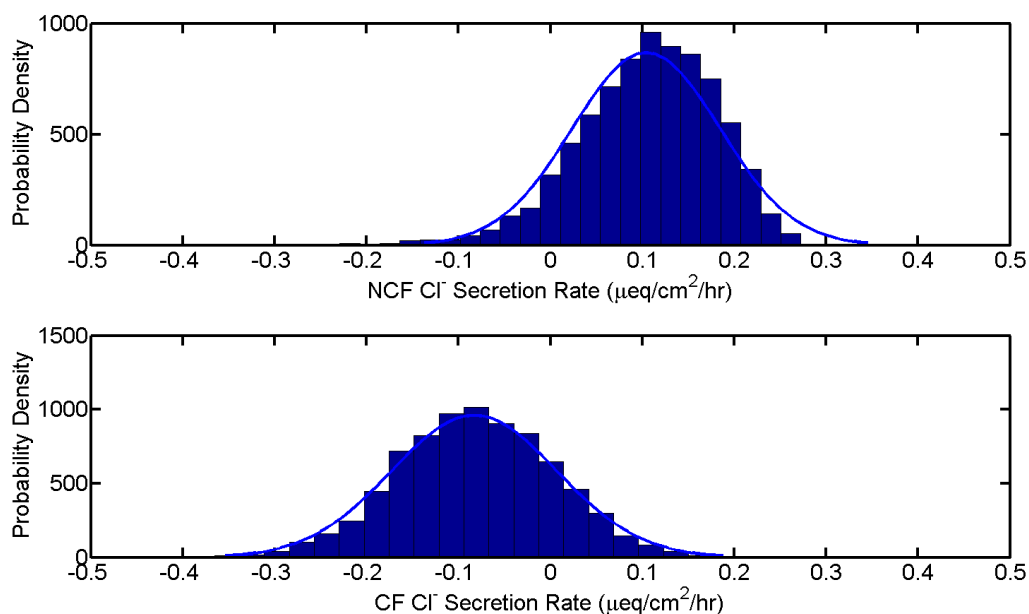


Figure 3.5: The  $\text{Cl}^-$  flux ensembles for non-CF (Top) and CF (Bottom) model predictions are approximately normal. Both sets of distributions contain 0. Secretion rates are positive in the apical direction.

These distributions are compared in the split violin plots of Figure 3.6A and B. Model estimates for  $\text{Na}^+$  flux are similar to experimental values and those that have been reported for airway epithelia [4,143].  $\text{Cl}^-$  secretion (Figure 3.6B) determined from forskolin-stimulated  $I_{\text{Cl}}$  is significantly decreased in CF cells ( $p < 0.05$ ), as would be expected. While due in part to absent  $\text{Cl}^-$  transport through CFTR, the predicted permeability of the constitutively active alternate chloride channel (ACC) is also decreased in CF in the model (Figure 3.6C).  $\text{Cl}^-$  fluxes in CF as estimated by the model are also reduced and suggest that net  $\text{Cl}^-$  absorption occurs alongside liquid absorption in this open-circuit condition. That  $\text{Cl}^-$  flux is either small in terms of secretion (NCF) or absorption (CF) has been reported [23,136,143], particularly under open-circuit conditions for CF [4]. Parameter ensembles for  $L_{\text{PP}}$  were logarithmically distributed for both CF and NCF model simulations, but CF paracellular hydraulic perme-

ability is increased by an order of magnitude (Figure 3.6D). Mean transepithelial electrical resistance (TER) was indicative of full differentiation for all cultures used in model training and was statistically indistinguishable between CF and NCF (Figure 3.6E).

We next validated the model in cells from additional CF and non-CF airways. Model response to volume addition in these 2 CF and NCF lines (n=4 filters per line) was compared to experimental data without adjusting any parameter values that were previously derived from the model training data. Only initial apical volume and DTPA counts were changed as model inputs for these validations. Model predictions for both CF cell lines overestimate liquid absorption at 24 hours (Figure 3.7A). It may be that there is a late-stage homeostasis mechanism present in these lines that is diminished or unaccounted for in the model parameterization or structure. However, the CF lines chosen for validation were selected at their earliest availability and displayed an unusually high starting volume for CF cells. As such, the model should overpredict absorption because the model structure favors a return to near homeostatic volumes as the mass balance allows. Model estimates for DTPA absorption are accurate in both CF cases (Figure 3.7C). Model agreement with non-CF data is acceptable ASL volume (Figure 3.7B), and the general strength of agreement between model and DTPA data (Figure 3.7D) in the time points preceding the last indicates that the model is well-suited to represent the bulk of behaviors present in the cellular system.

### 3.3.3 Effects of Osmotic Agents on ASL and DTPA Absorption in HBE

Because DTPA is only known to traverse the epithelial layer through the paracellular space, its transport is only due to diffusive and convective flux. Paracellular convection of DTPA was delayed experimentally by applying 10  $\mu$ L of hypertonic fluid to the apical surface of non-CF HBE. Two different hypertonic fluids, concentrated Ringer's and mannitol in Ringer's, were selected because mannitol is not transported transcellularly like the ions in Ringer's, which we hypothesized would change the nature of the liquid transport dynamics observed. Concentrated Ringer's may be thought of as a surrogate for hypertonic saline, which is a standard therapy in CF [22]. Inhaled powdered mannitol has also been shown to be therapeutic in CF [136]. As shown in Figure 3.8A and B, addition of either concentrated Ringer's

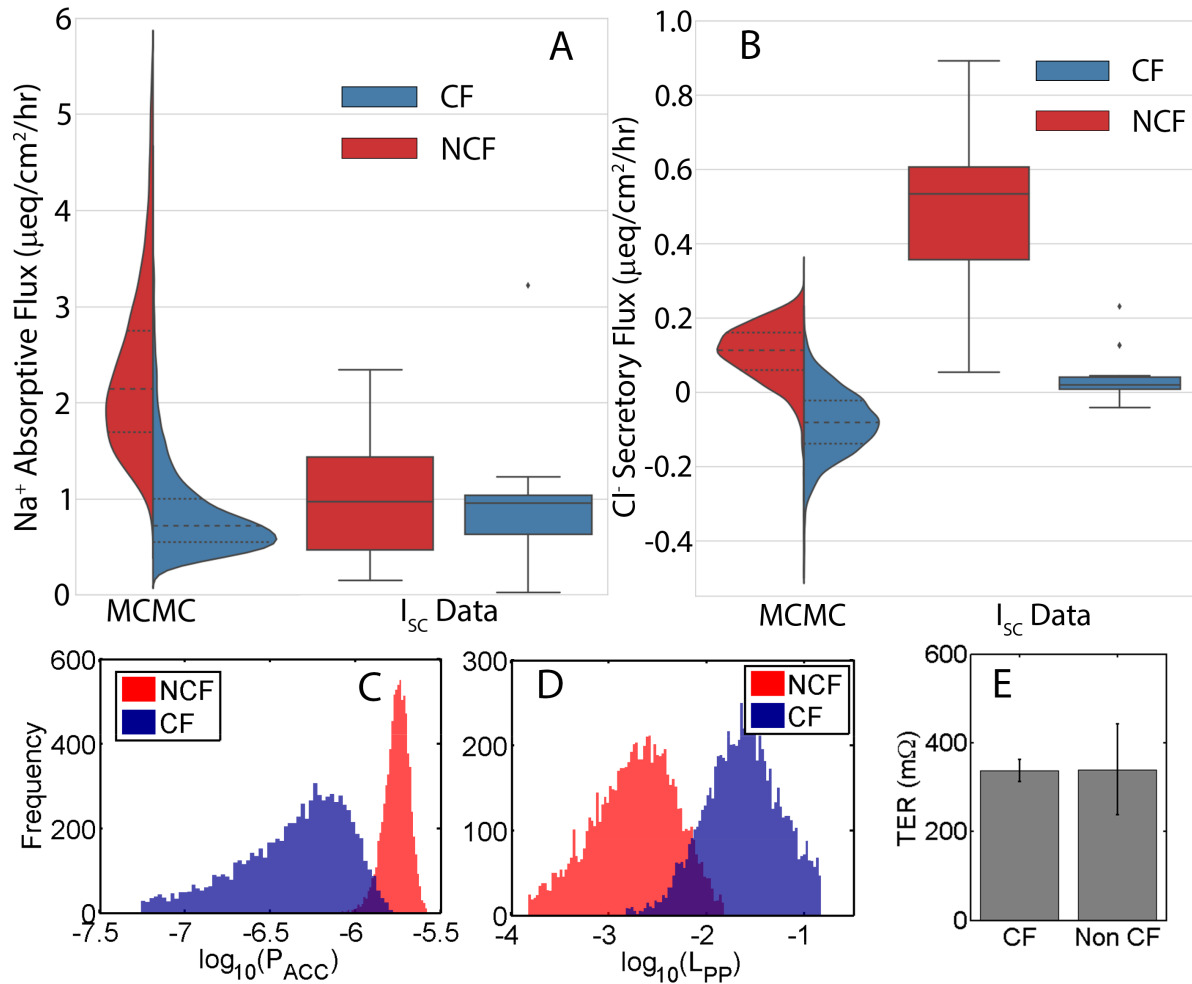


Figure 3.6: (A, B) Ion flux values from MCMC-generated model ensembles (violins) and ISC measurements (boxes). The model predicts non-CF cells (NCF) have similar but increased Na<sup>+</sup> absorption compared to the data. Model and data are in strong agreement in the CF case for Na<sup>+</sup> absorption. No difference in Na<sup>+</sup> flux is detected experimentally between CF and NCF. (B) Cl<sup>-</sup> secretion is reduced in NCF and reversed (absorption) in CF model ensemble predictions compared to experimentally determined forskolin-induced I<sub>Cl</sub>. (C) CF cells have markedly decreased constitutive chloride permeability (D) Paracellular permeability (L<sub>PP</sub>) is significantly increased in CF. (E) Transepithelial electrical resistance is similar between CF and non-CF cells.

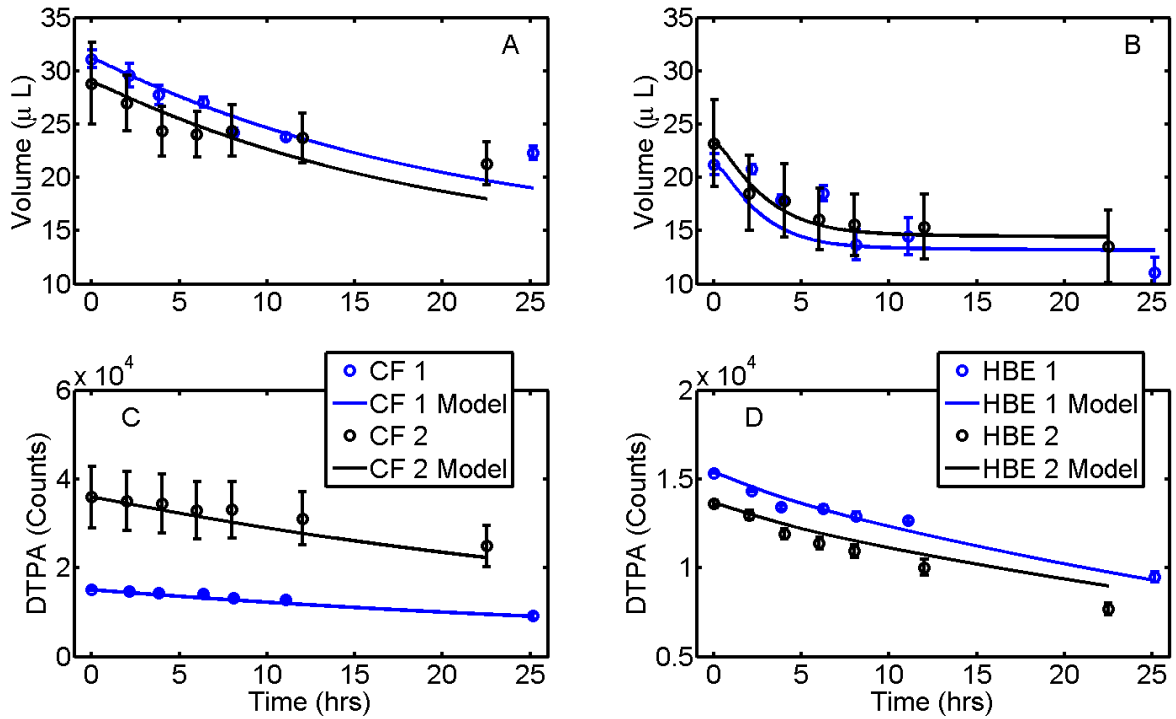


Figure 3.7: Model validation against experimental data demonstrates acceptable model agreement in CF (A, C) and non-CF (B, D) HBE cultures. (B) In HBE 1, predicted ASL absorption is too rapid, though the DTPA prediction is in good agreement with the data. HBE 2 demonstrates acceptable agreement between model and data. Both CF lines demonstrate strong agreement between model prediction and data, even in the case of DTPA absorption in CF 2 where initial DTPA concentration is more than double the training set average (note that axis scale is not the same for panels C and D). Error bars experimental data SEM. Error bars are smaller than symbols where not distinguishable.

solution (450 mOsm) or 150 mOsm of mannitol to standard Ringer's induced ASL swelling and arrested paracellular convection of DTPA. Osmotically induced ASL expansion reached a maximum after approximately 1 hour, at which point absorption began, introducing paracellular convection. This is illustrated in Figure 3.8B in the Ringer's curve by an acceleration of DTPA absorption. As osmolarities in all compartments are predicted to stabilize in less than 1 hour (Figure 3.8C and D), convection decreased towards a solely diffusive regime.

Cell volume dynamics (Figure 3.8E) were extremely fast (order  $<1$  minute) compared to the ASL dynamics, which agrees with the findings of Matsui and colleagues [9]. Cell volume ultimately recovers due to the homeostatic feedback mechanisms built into the model, though at a slower rate than the initial volume response, which has been reported by Okada and colleagues [95].

Model trajectories for the osmotic challenge conditions were generated from refitting the model parameters via constrained nonlinear least-squares regression. Up to a five-fold [144] change in model transport parameters from their baseline was allowed to result from the cellular stress response after either addition of concentrated Ringer’s or mannitol (see Table 3.2). Refitting is justified under this new case of hypertonic challenge because the cell must act rapidly in order to preserve its volume and osmotic environment [144]. This will necessarily change ion and water transport behavior through a combination of  $\text{Ca}^{2+}$  release and channel trafficking [13, 95] and osmotically activated water channels [144]. Particularly, ENaC permeability should decrease [13, 95] and transcellular water permeability should increase [144], which can be observed in Table 3.2. Simulated responses in Figure 3.8A and B agree well with the data and also illustrate the different convective and diffusive mechanisms present after osmotic challenge. Additionally, mannitol decreased the absorption of DTPA more than concentrated Ringer’s ( $p < 0.01$ ) and increased the steady state ASL volume ( $p < 0.05$ ). Furthermore, model agreement with volume and DTPA profiles under a previously untrained condition demonstrates the structural robustness of the model and its ability to capture the underlying physics of the experimental system.

### 3.3.4 Other Considerations Regarding Cell-volume Regulation

Figure 3.8E demonstrated that cell-volume response occurs on a time-scale similar to that reported by Matsui *et al.* [9]. A 150 mOsm hypertonic apical solution (of raffinose instead of mannitol) was also applied to the lumen of cells in that study. Figure 3.9 shows that the model can be refit to non-CF cell-volume data collected from that same study [9] by increasing the initial “monolayer” height and varying  $L_{PP}$ . Regression of the model over

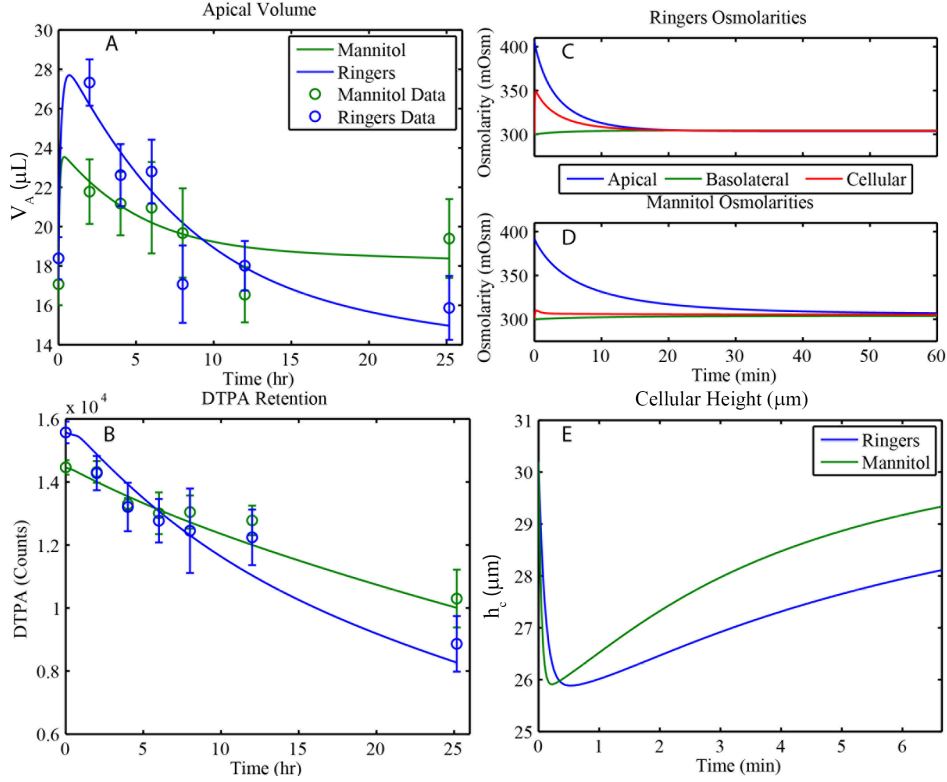


Figure 3.8: (A) by adding 10  $\mu\text{L}$  of either 1.5x concentrated Ringer's or Ringer's and mannitol solution apically to non-CF HBE, ASL volume increase is induced and paracellular DTPA convection stops for approximately the first hour after addition resulting in slow initial DTPA absorption (B). The subsequent decrease in ASL volume induces paracellular liquid absorption and convection of DTPA, which accelerates its absorption. Model estimates are in good agreement with the data. Mannitol reduces overall DTPA absorption ( $p < 0.01$ ) and promotes increased steady state ASL volume ( $p < 0.05$ ) at 24 hours compared to hypertonic Ringer's. (C) and (D) Illustrate that the small disparity in terms of magnitude of initial ASL volume increase was due to differences in initial osmolarities. (E) Cellular height decreases rapidly in response to both hypertonic challenges on the same timescale as that reported by Matsui et al. (2001).

these two parameters yielded a 95% confidence interval on monolayer height  $h_c = [35.55, 37.58] \mu\text{m}$  and  $L_{PP} = [1.576, 2.744] \times 10^{-4} \text{ m/s}$ .

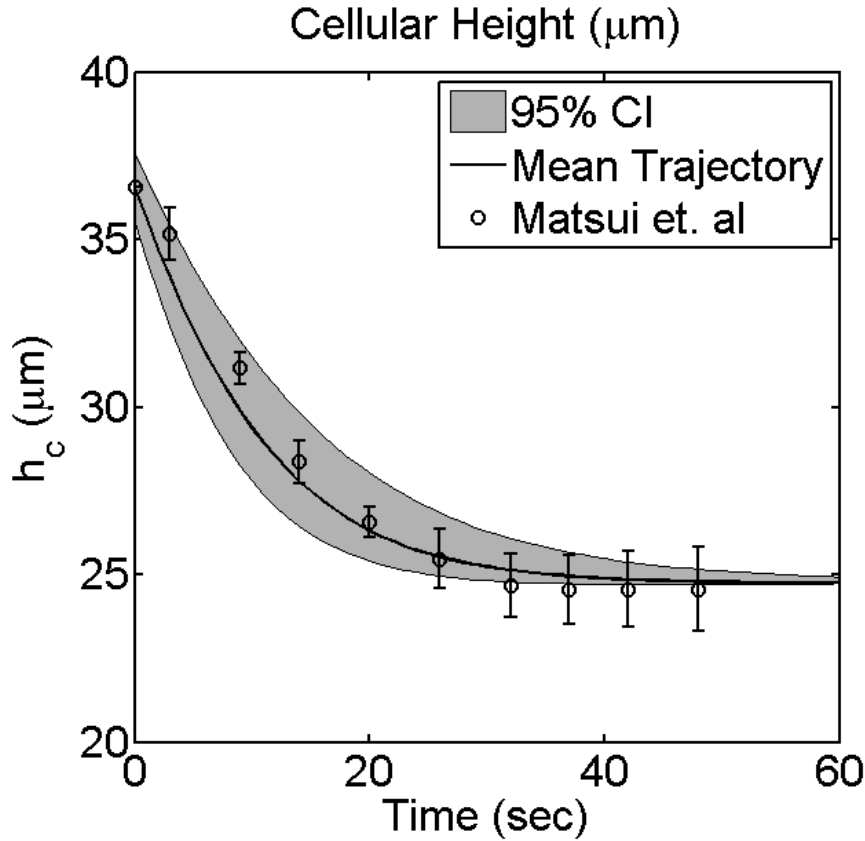


Figure 3.9: By only slightly changing the initial height of the monolayer and the hydraulic permeability, the model is able to capture the data of Matsui *et al.* [9]. Envelope shows region of 95% confidence in model dynamics given the other non-CF parameters from 3.2

The confidence envelope was generated from combinatorial selection of cell-height and permeability 95% confidence bounds. The nominal initial value for height of  $36.56 \mu\text{m}$  is a reasonable value for the monolayer [9]. The absence of CF volume-response data motivated the development of a simple, rapid method (as opposed to confocal microscopy or other more involved methods [145, 146]) to measure cellular volume response. This method involved detaching fully differentiated HBE cells from the transwell filters they are grown on and plating them on a glass slide for video capture via bright-field microscopy. As a consequence of detachment the cells become spherical, which minimizes their surface area to volume ratio.

This allows for recognition via the circular Hough Transform in Matlab [147] as shown in Figure 3.10.

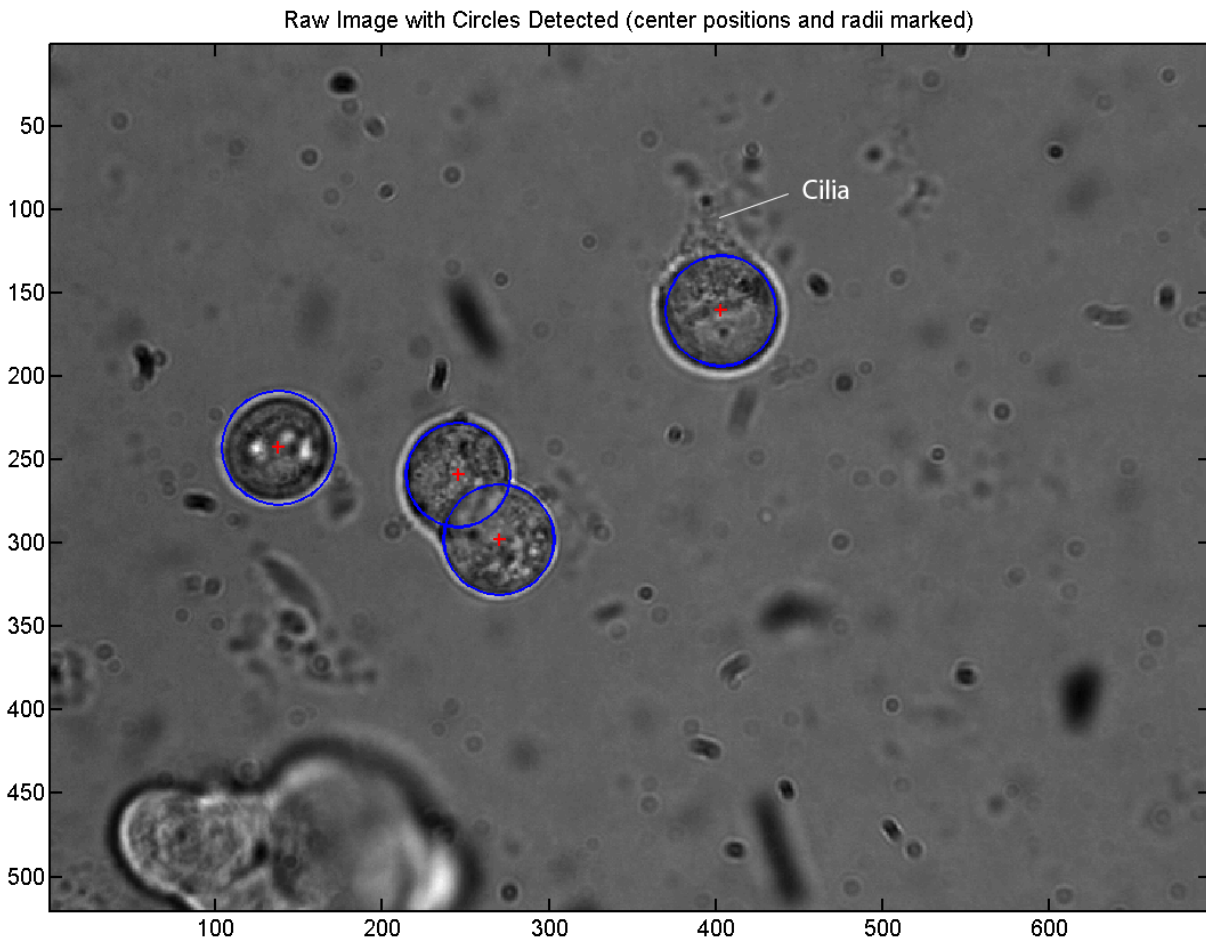


Figure 3.10: Individual (even occluded) cells are detectable by the algorithm. Here four non-CF HBE cells have been identified. Cilia are prominent on one of the cells.

The microscope used has the ability to perfuse various solutions over the surface of the slide. In the case of a perfused anisosmotic solution, any change in cell volume can be recorded over time and the resulting video can be analyzed frame-by-frame for each cell. This is demonstrated for a normalized cellular volume-response comparison between CF and non-CF cells in Figure 3.11, where cell-volume decrease was induced via perfusion with a 450 mOsm mannitol solution.

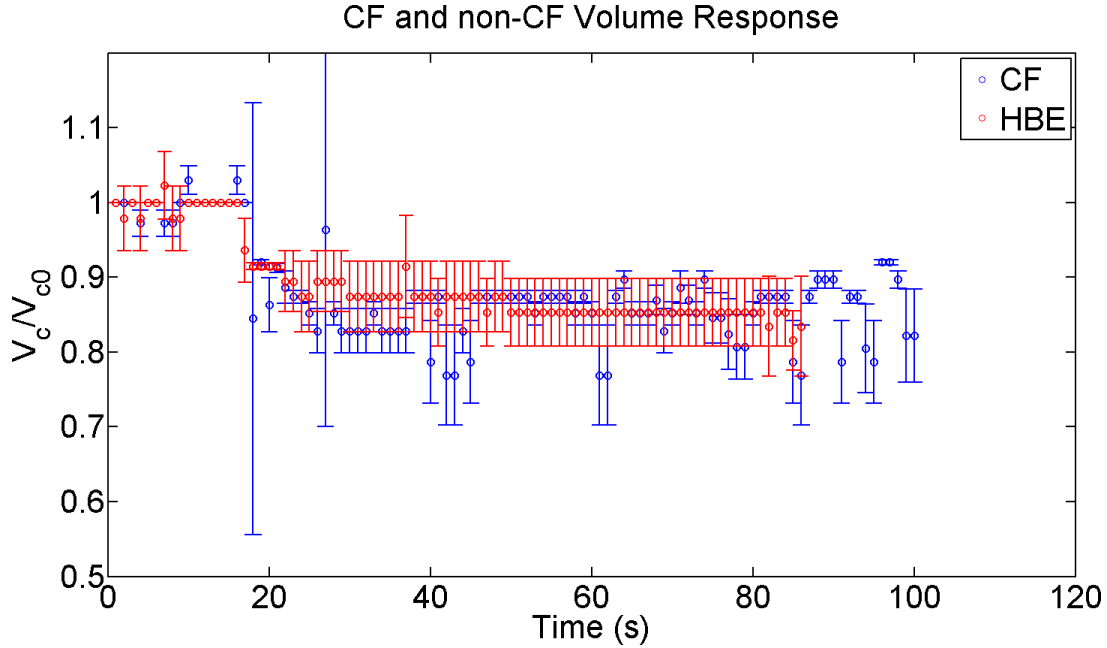


Figure 3.11: Recordings of normalized cell volume over time are shown for  $n=3$  CF and  $n=4$  non-CF cells. No difference is observed in response between cells, but the performance of the algorithm is verified.

No difference was observed between the CF and non-CF cells in terms of dynamics or magnitude of response. This is to be expected for two reasons. The first, from the modeling result, is that  $L_{PC}$  of CF and non-CF cells are not expected to be different (see Table 3.2). This also makes sense in terms of evolutionary fitness; cell-volume response must be tightly regulated for survival, so even diseased cells would not be expected to have a noticeably different volume regulatory response. Solely focusing on the validity of the model, similarities in  $L_{PC}$  between CF and non-CF cells should result in the similarities in cell-volume regulation that we report here.

### 3.3.5 Paracellular Convection of DTPA is Increased in CF Cells

Equation 3.5, when written for DTPA in the apical compartment, has no active or passive flux terms into or out of the cell. Thus, the DTPA transport equation reduces to a two-term form yielding the contributions of diffusion or convection to its transport at any instant:

$$\begin{aligned} \frac{dDTPA_A(t)}{dt} &= J_{diff} + J_{conv} \\ &= -P_{DTPA_{A,B}} A_{TJ} \left( \frac{DTPA_A(t)}{V_A(t)} - \frac{DTPA_B(t)}{V_B(t)} \right) + \frac{DTPA_A(t)}{V_A(t)} \frac{dV_A(t)}{dt} \end{aligned} \quad (3.6)$$

Equation 3.6 structurally matches the description of drug absorption in the intestine given by Lennernas [148]. From equation 3.6 the contributions of diffusion and convection to DTPA transport can be estimated individually. Model estimates for concentration driven diffusive flux between CF and non-CF cells were similar despite the higher DTPA concentrations in the CF cells that were associated with lower ASL volumes (Figure 3.12A). Differences in convection between CF and non-CF were more apparent. The model predicted a threefold difference in paracellular convection of DTPA between CF and non-CF cell cultures (3,179 vs. 913 counts, CF vs. non-CF in Figure 3.12B). Furthermore, approximately 38% of DTPA absorption was estimated to be due to convection in CF cells, which is similar to experimental values that we have previously reported [8]. It follows that total DTPA absorption was increased in CF, implicating abnormal convective transport due to increased paracellular water transport as the primary cause (i.e. solvent drag).

The equation governing water transport, Equation 3.7, between the ASL and the cell or basolateral compartments can be split into separate terms in a manner similar to the treatment of Equation 3.6:

$$\frac{dV_A}{dt} = J_{trans} + J_{para} = -L_{P_{A,B}} A_{TJ} V_w (\pi_A - \pi_B) - L_{P_{A,C}} A_C V_w (\pi_A - \pi_C) \quad (3.7)$$

Upon integration of the individual terms, illustrated in Figure 3.12C and D, model-estimated transcellular water flux exceeded paracellular flux in the non-CF case, which has been experimentally reported [63, 149], and nominally so in CF. Paracellular liquid flux was increased threefold in CF. Diffusive driving force (Figure 3.12E) was initially increased in CF cells due to the lower initial ASL volume present in those cultures, but decreased convection in the

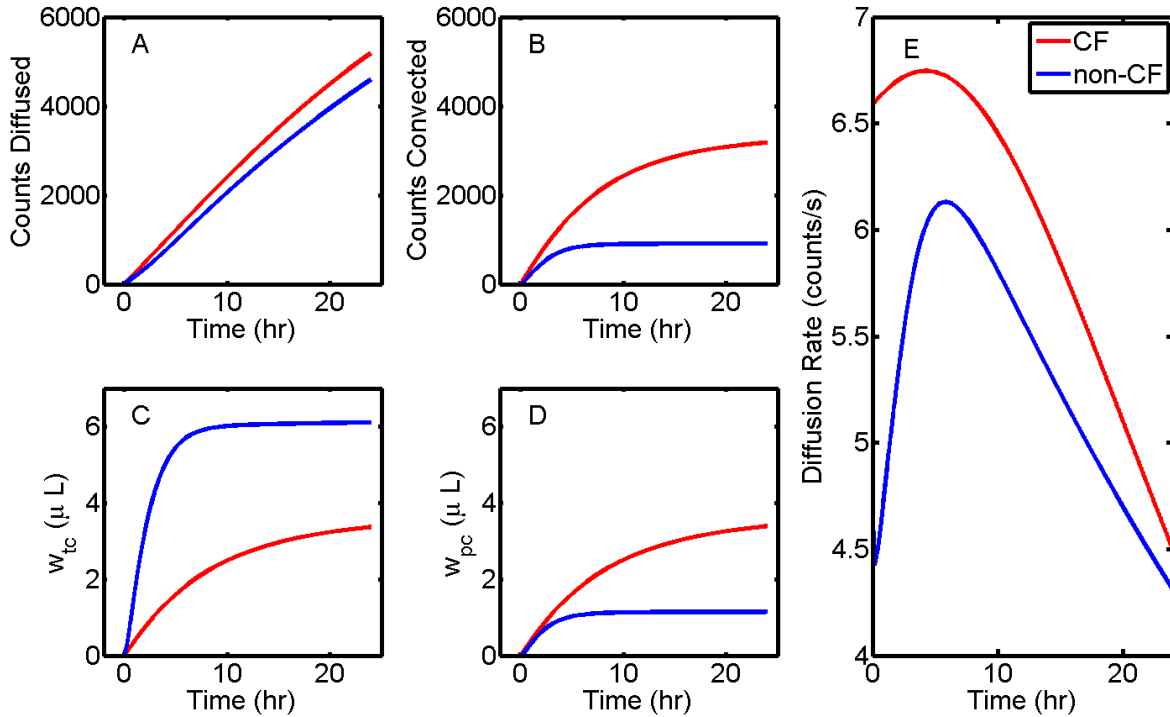


Figure 3.12: Figure 3.12 A comparison between model-predicted counts of DTPA either (A) diffused or (B) convected in both CF and non-CF HBE. Diffusion is similar between the two cell types (A), but DTPA convection is dramatically increased in CF (B). Transcellular liquid flow (C) is predicted to be greater than paracellular liquid flow (D) in non-CF cells. In CF cells, flows through both the para- and transcellular pathway are similar, though transcellular flow is nominally increased. The increase in DTPA convection is explained by the correlation between paracellular liquid flow and DTPA absorption ( $r > 0.999$ , CF and non-CF). CF cultures convect more DTPA because they demonstrate increased paracellular liquid flow as compared to non-CF cultures. The modest increase in diffusion in CF cells is explained by the relative initial hyperconcentration of DTPA in CF cultures due to dehydration present at the beginning of the experiments (E).

non-CF cells caused this disparity to diminish over time as DTPA in the non-CF ASL was concentrated due to predominantly transcellular water absorption.

In order to test whether paracellular integrity may be compromised in CF, a 10  $\mu$ L bolus of DTPA and Ringer’s was added apically and reversed the osmotic gradient of the mannitol experiments in Figure 3.8 (*i.e.*  $Osm_{B,0}=450$  mOsm) in an additional 3 CF (n=6+4+6 filters) and non-CF (n=6+4+5 filters) lines (TER > 250  $cm^2$  for all lines). This osmotic gradient drives rapid ASL absorption [9, 65], through both the trans- and paracellular pathways and caused increased DTPA absorption in CF cells for all  $t>0$  and in non-CF cells at  $t=24$  hours. DTPA absorption was again increased in CF cells without basolateral mannitol (Figure 3.13A,  $p<0.01$ ) at 24 hours compared to non-CF control cells (Figure 3.13B) and in CF cells exposed to basolateral mannitol at 8 and 24 hours ( $p<0.05$ , 0.01, respectively). Acceleration of DTPA absorption due to the imposed gradient was measured as the difference in apical DTPA retention between the control and gradient conditions at every time point (Figure 3.13C). The difference in absorption in the CF cells (control vs. basolateral mannitol) was greater than that of the non-CF cells (control vs. basolateral mannitol) at 4 and 8 hours ( $p<0.05$ ), indicating that CF cells are more susceptible to further increased paracellular absorption, congruent with the model-predicted barrier defect.

### 3.4 TREATMENT ANALYSIS AND DESIGN USING THE CELL-SCALE MODEL

Up to this point, results relating only to the structure and dynamics of the airway epithelium have been presented. As previously discussed in chapter 1, however, this knowledge regarding structure and dynamics can also be used to control biological processes and design desired responses [66]. In the context of disease treatment, control and design are similar in concept: halt and reverse the progression of a disease using some treatment as an actuator. They tend to differ in terms of actuation frequency, with control theory implementations for acute and some chronic illnesses that require intensive or frequent care [77, 82] and optimal design implementations for diseases where long-term treatment outcomes are the primary goal [76].

Airway dehydration in CF following rehydration is generally thought to occur on a time-scale of 2-6 hours when ASL height (not volume) is measured *in vitro* [24, 49, 97]. Such

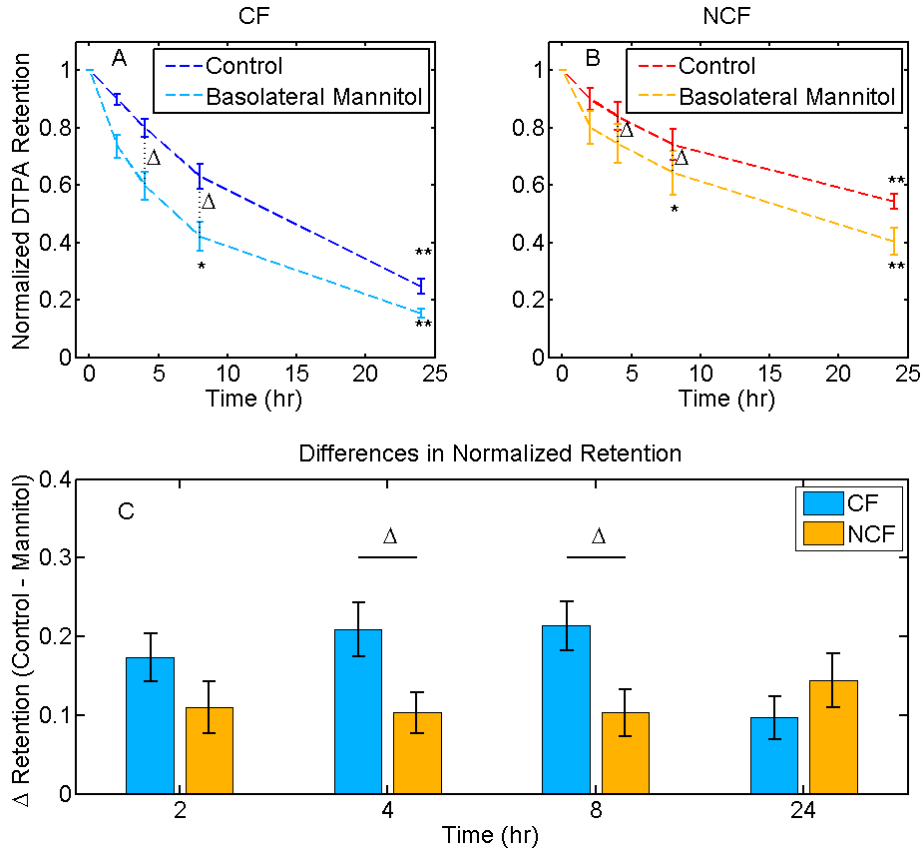


Figure 3.13: Normalized DTPA retention (mean  $\pm$  SEM) in CF (A) cells and non-CF (NCF) cells (B). In A and B DTPA retention was measured in the presence of either an isosmotic or a 450 mOsm (150 mOsm hyperosmotic) basolateral bath. DTPA absorption is increased at 8 hours for CF challenge vs NCF challenge (\*,  $p < 0.05$ ) and in CF controls vs. NCF controls and CF challenge vs. NCF challenge at 24 hours (\*\*,  $p < 0.01$ ). The difference between control and challenge is significant ( $p < 0.05$ ) for all CF  $t > 0$ , and NCF at  $t = 24$  hours (unmarked). Vertical dotted lines represent differences in retention between control and challenge conditions that are significantly different between CF and NCF. (C) The difference between the control and challenge condition is significantly increased in CF over non-CF at 4 and 8 hours ( $\Delta$ ,  $p < 0.05$ ) indicating an increased acceleration of DTPA transport in CF due to the osmolarity gradient.

time scales do not necessitate intensive monitoring and frequent (multiple per hour) treatments. Furthermore, current hydrating therapies in CF like inhaled hypertonic saline require cumbersome equipment and periods of time longer than taking a pill or using an asthma inhaler. Thus, it is better to formulate model-based treatment as a long-term treatment design problem instead of a control problem.

To begin, Tarran and colleagues have shown that there is a correlation between ASL height and mucociliary transport velocity [49], and Figure 3.14 demonstrates that there is also a positive correlation between ASL volume and FFCA.

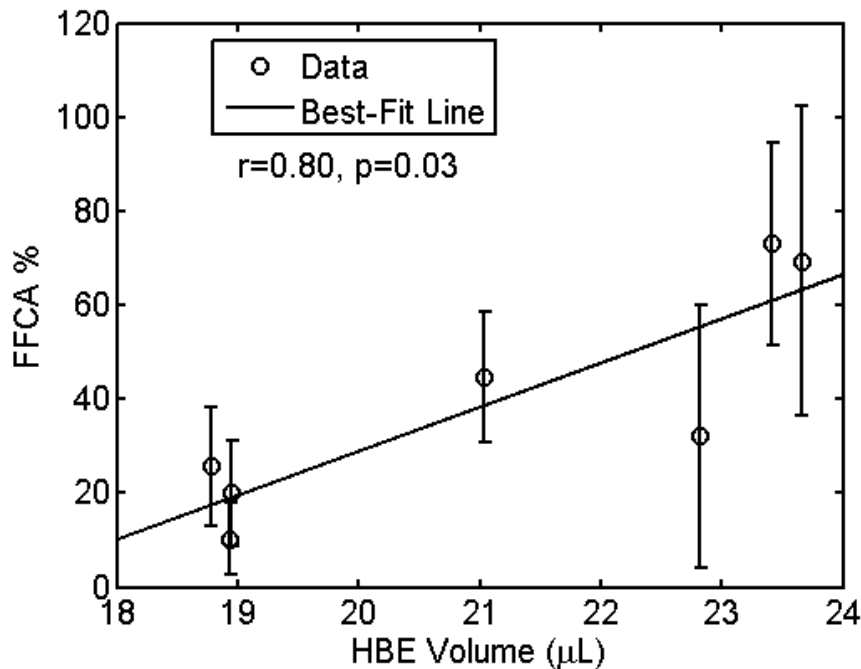


Figure 3.14: FFCA is plotted against measurements of ASL volume for  $n=12$  filters following the apical addition of  $10 \mu\text{L}$  of Ringer’s. The correlation is significant and consistent with an intermediate volume range below the saturation point in Figure 2.14

While not mechanistic, this relationship underscores the idea that increasing airway hydration (up to saturation) will improve MCC and thus patient health. So while a mechanistic study of how FFCA, MCC, and hydration interrelate should be performed, a treatment de-

sign that targets ASL volume should also be effective in improving MCC. Conversely, the model should also be able to provide reasons for treatment failure to improve MCC.

### 3.4.1 Model Analysis of a Clinical Study

Goralski and Button [150] developed a cell-scale experimental model of aerosol deposition on cultured HBEs. Using a nano-nebulizer they were able to provide a scaled down dose of hypertonic saline with a deposition rate equivalent on a per surface area basis to that of the standard Pari LC-star nebulizer. They reported that slower deposition rates induced less cell-volume reduction while improving duration of hydration. They also noted that 4 hours was the minimum interval that allowed for repeated dosing with equivalent rehydration as the first dose. These findings provide two starting points for treatment design. The first, that slow dosing might improve airway hydration and, thus, mucociliary clearance was tested in a clinical study of nebulized HS given overnight (for 8 hours) via a nasal cannula and trans-nasal pulmonary aerosol delivery (tPad) device designed by Parion Sciences Inc. The trial and analysis were performed at the University of Pittsburgh to avoid conflicts of interest. Results for that trial in terms of patient MCC and DTPA absorption are presented in the next chapter ([chapter 4](#)). In brief, the study no difference in MCC or DTPA absorption in HS vs. a sham treatment control day.

This study provided an opportunity to use the cell-scale model described above to identify possible failure modes given that previous cell-scale experiments suggested the trial would be successful. Patton and colleagues identified aerosol generation and particle deposition as the primary challenges for inhalation therapy [151]. The aerosol generation of the tPad is well characterized so the first focus was on the effect of deposition rate on airway hydration [152]. The simplest means of approximating deposition in the lung, which has enormous surface area and heterogeneous topology [153], is to assume a uniform deposition rate throughout similar lung regions. Based on the morphometry described by Weibel [153], functional imaging scans, and known tPad output, a surface area normalized deposition rate was calculated for HS in the bronchi (i.e. airway generations 1-10) of 70.1 pL/s. For 7% HS, this is equivalent to 0.92  $\mu\text{mol}/\text{cm}^2/\text{s}$  of  $\text{Na}^+$ , which is in excess of the model best-fit and median estimate for

Na<sup>+</sup> fluxes of 0.65 and 0.74  $\mu\text{mol}/\text{cm}^2/\text{s}$ , respectively. Since net Na<sup>+</sup> absorption is required for liquid absorption, it is expected that this rate to produce a hydrating effect over time. Indeed, model predictions for this rate indicate as much across the ensemble of parameters generated from ptempest, as seen in Figure 3.15.

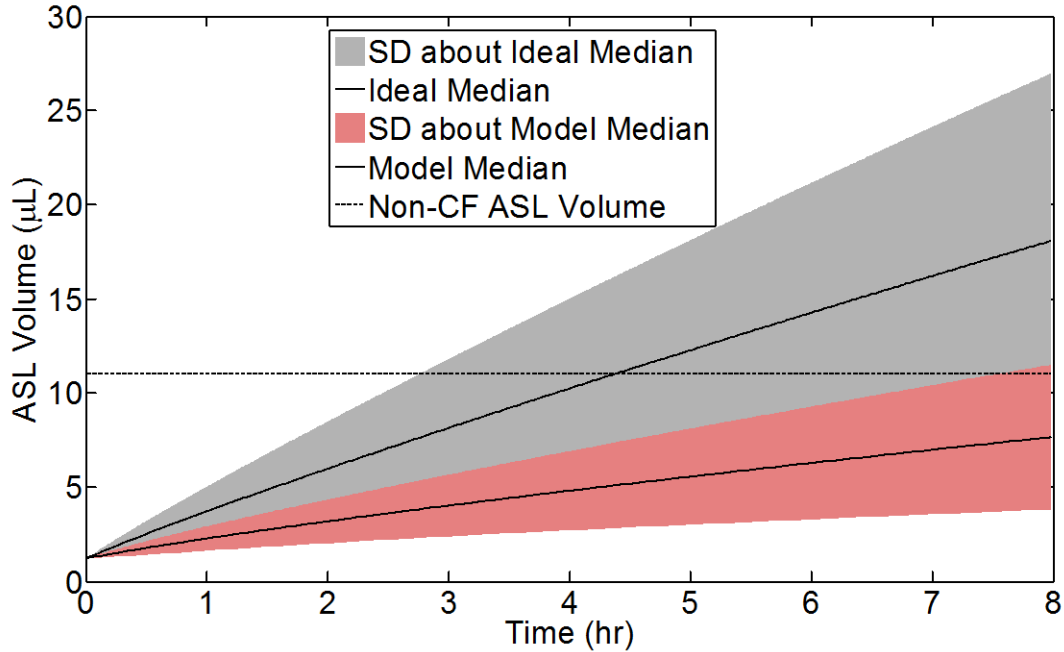


Figure 3.15: Comparison of expected hydration in CF cells using either the surface area of the first 10 airway generations to calculate a 70.1 pL/s or halved (35.1 pL/s) deposition rate. Envelopes are generated from simulating the responses of the entire 8000 parameter set ensemble from model training and give the median ASL volume prediction bounded by its standard deviation.

But as seen from the other modeled case in Figure 3.15, halving the deposition rate does not restore CF ASL volumes to resting levels seen in non-CF cells. This halving could easily fit into the uncertainty about the total surface area where deposition occurred. Therefore, it may simply be that not enough aerosol was delivered to the airway surface to induce hydration.

Inherent to the assumptions is that half the total dose was deposited on an area equal in size to the first 10 airway generations given estimates of a central to peripheral dosing ratio

(C/P see [8]) of  $\approx 1$ . It is possible that a larger proportion of bronchioles is represented in the central region, however. If that were the case it would be expected that deposition rate per surface area would decrease up to 10-fold in the extreme case that the first 16 generations (Weibel limit of “conducting” airways) were used for the area estimate.

Furthermore, there is some uncertainty in terms of  $\text{Na}^+$  absorption rates. Some groups have found  $\text{Na}^+$  absorption to be increased in CF [12, 13] while others report values closer non-CF rates [25]. The variability of  $\text{Na}^+$  flux is also apparent in the model predictions and data given above in Figure 3.6. Because of that, model-predicted sensitivity to  $\text{Na}^+$  absorption rates was also evaluated.

Ionic concentration in the aerosol and not the liquid volume carrying it is the primary source of rehydration for osmotic therapies. Thus, whether or not increased (14%) saline concentration could ameliorate these issues was tested as well. Each of these sources of possible variation in therapeutic effect were tested via simulation using the model best-fit parameter set for CF. The results of these simulations are shown in Figure 3.16.

A uniform deposition profile involving the first 16 airway generations is untenable for successful hydration as no scenario with this assumption exceeds non-CF baseline hydration. Sodium absorption rates ranging between the values and those of Boucher [4] have a smaller, but observable effect on hydration. While 14% HS does substantially improve predicted hydration, it is not able to counteract such a poor deposition profile, though it would be able to counteract the reduced deposition case of Figure 3.15 as seen in Figure 3.17.

The uniform deposition assumption is not, however, the best means of informing the model. Many computational fluid dynamics models (CFD) exist that describe the deposition patterns of aerosols as a function of size, flow condition, and lung geometry. That of Martonen and colleagues [154] was chosen because it predicted the deposition pattern of the tPad and that of Gerrity and colleagues [155] was selected as another point of comparison for an airway generation-specific model of deposition and hydration. These CFD models provide estimates of aerosol dose for each airway generation based on aerosol size.

These deposition models were utilized in a set of simulations of the cell-scale model and assume that the dose deposited in each airway generation is uniformly distributed over the area of all branches in that generation [154]. For the following simulations ASL initial height

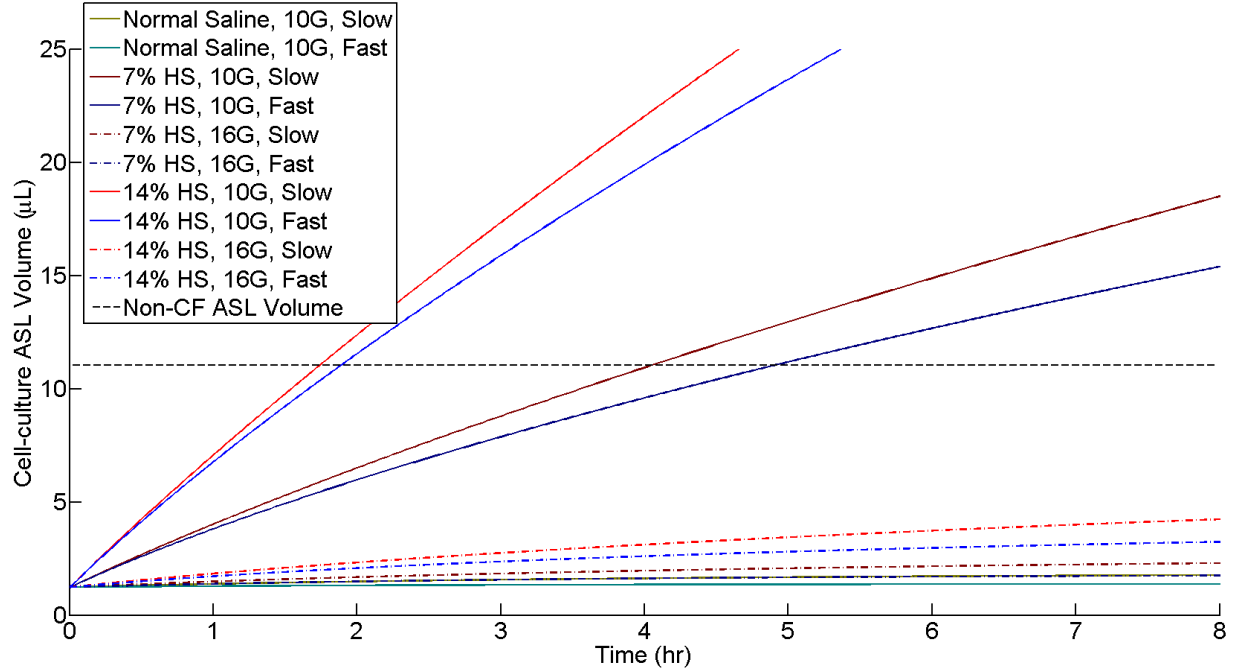


Figure 3.16: Model predicted effects of deposition rate (volumetric rate/surface area) on cell-culture ASL volume using either the total surface area of the first 10 (10G, solid) or 16 (16G, dashed) airway generations are shown alongside the effects of  $\text{Na}^+$  absorption rate. Deposition amount in the bronchioles has a large effect on predicted efficacy, and sodium (fast or slow) absorption has a smaller, noticeable, effect. Increased saline concentration (14%) improves hydration.

was set to be  $7 \mu\text{m}$  according to the literature [24, 97]. The analysis begins in Figure 3.18 by comparing the dynamic estimate of generational hydration to the static estimate of Sood *et al.* [10] for ASL height added following fifteen minutes of inhaling isotonic saline via the Pari LC-star ( $4 \mu\text{m}$  particle size).

Since the model includes the active liquid and ion transport occurring in the model and the Sood *et al.* [10] prediction does not, ASL height added is decreased in every airway generation in the model. However the profiles of ASL height vs. generation are similar between models. This provides evidence that the model is suitable for making predictions

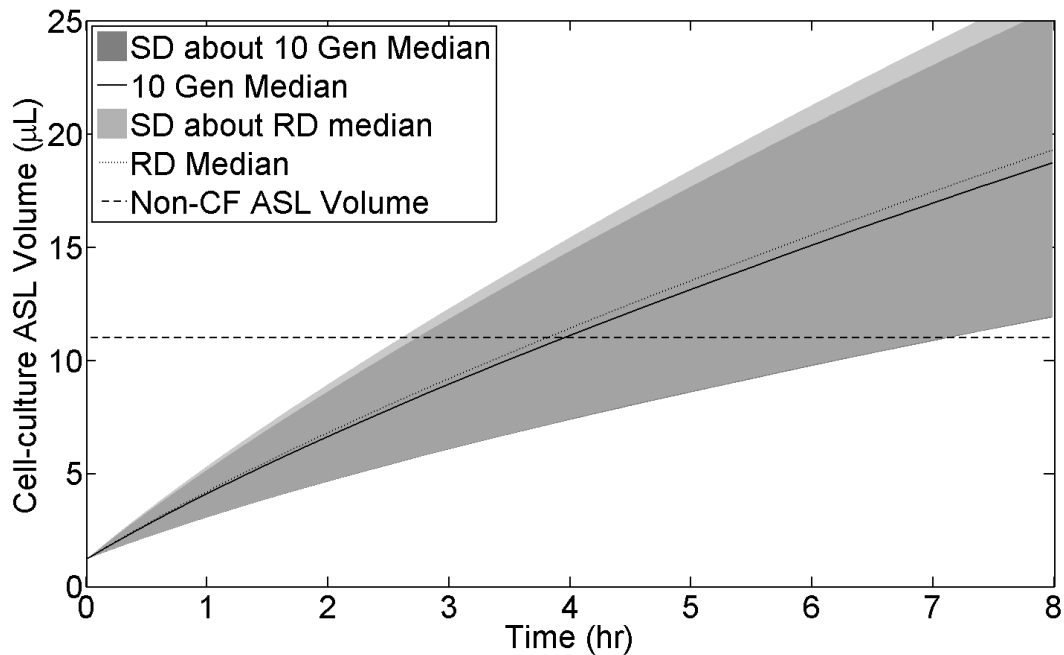


Figure 3.17: Comparison of expected hydration in CF cells using either the ideal 70.1 pL/s or halved (35 pL/s) deposition rate with 14%HS, which is predicted to be successful in restoring hydration.

across airway generations and their specific deposition rates. Accordingly height response was predicted at each generation for each deposition rate and particle size associated with the Pari LC-star and extended analysis to the tPad with its reduced aerosol size and deposition rate. Hydration profiles are given for each nebulizer at the airway generations most susceptible to mucus accumulation and obstruction [11] for their respective treatment durations in Figure 3.19.

While hydration levels may seem high, it should be noted that this model does not account for mucociliary clearance between generations that would be induced by upon airway rehydration. The known acute action of HS after oral inhalation [150, 156] is evident in the model prediction. For well hydrated generations like generation 7, the tPad is expected to slow ASL resorption by about 30%. Generation 8 has sustained moderate hydration but

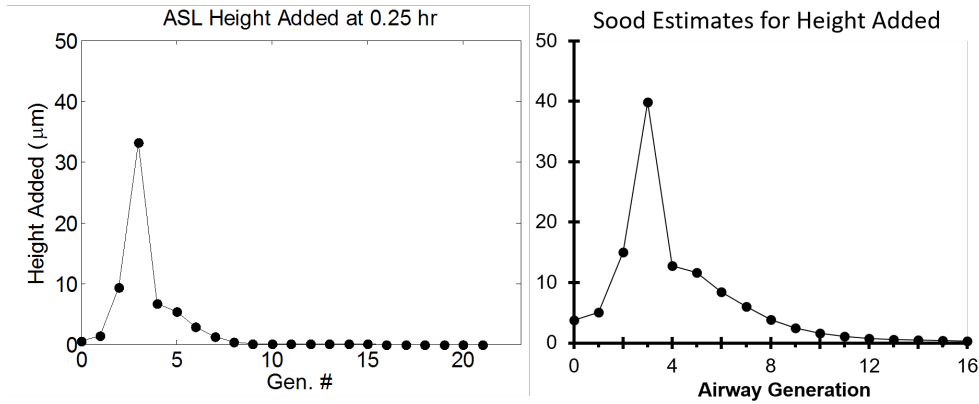


Figure 3.18: The cell-scale, dynamic model (left) predicts similar patterns of ASL height by airway generation to the previously published model by Sood *et al.*, [10] (right) when considering 7% HS delivery from a Pari LC-Star nebulizer. Heights are reduced overall in the model based on inclusion of terms for liquid and  $\text{Na}^+$  absorption that reduce ASL height over the 15 minutes of simulated delivery. Agreement is strong, and reduced heights at left are justifiable given that liquid addition should cause some rapid volume resorption, even in a fifteen minute time-frame.

the predicted deposition pattern for the tPad is such that generations beyond it are not substantially hydrated. This issue is predicted to be solvable by using 14% HS instead 7%, where the added osmotic drawing power overcomes the inherent ability of the lower airways to absorb added  $\text{Na}^+$ . This is one possible design suggestion posed by the generational modeling result.

However, the uniform deposition assumption can be reapplied to a sequential treatment involving both the Pari LC-star and the tPad. Orally inhaled HS provides an acute treatment effect that the long-term deposition period of the tPad is meant to fix. By “priming” the lungs with a quick, hydrating dose of HS with an oral nebulizer, the tPad operates on airways in a pre-hydrated state and can be thought of as a hydration maintenance device in the same way an IV drip might be used instead of a bolus. This concept is not limited to HS alone. It was noted in Figure 3.8 that mannitol has a longer residence time in the ASL due a lack

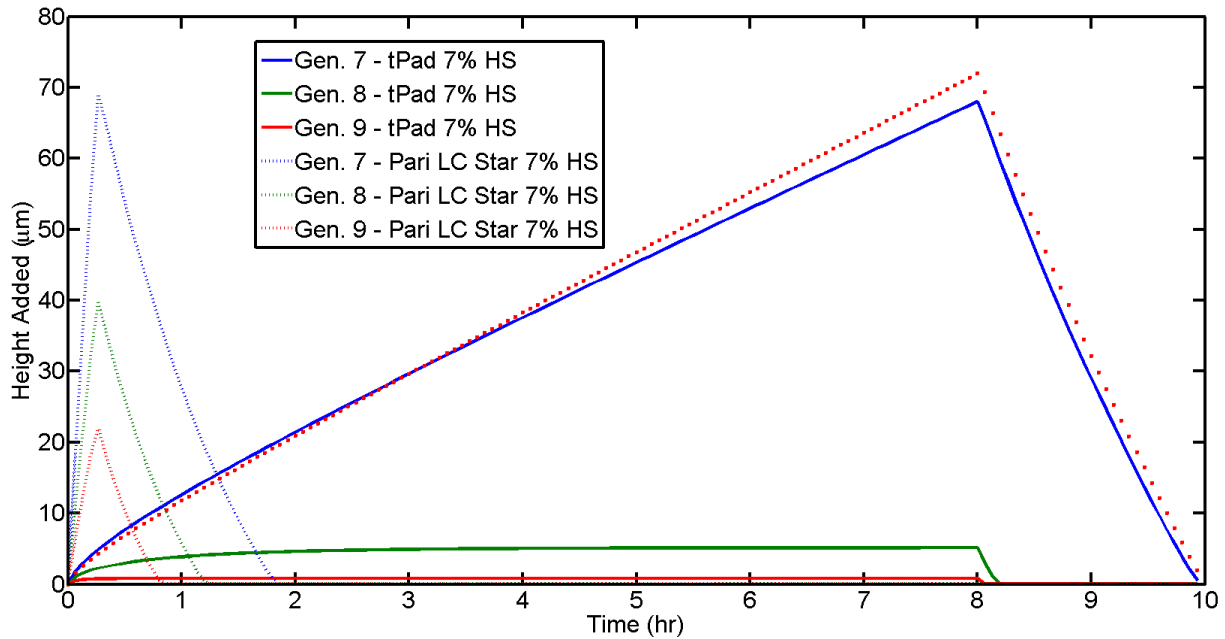


Figure 3.19: Model-predicted hydration of the bronchi where obstruction has been found to begin [11] given anatomically informed deposition rates for either a  $1.5 \mu\text{m}$  (tPad, solid) or  $4 \mu\text{m}$  orally inhaled aerosol (Pari LC star, dashed, [10]). Acute hydration is predicted for oral inhalation of 7% HS, but not for the tPad. 14% HS (+) provides pronounced hydration at generation 9 beyond that of 7% in the tPad.

of cellular transport pathways that translated to more long-term and robust hydration and reduced solute absorption. Figure 3.20 compares the efficacy of 7% HS alone to oral HS and either extended delivery 7% HS or 20% mannitol at half of the ideal tPad deposition rate.

Figure 3.20 illustrates priming the airways with a proven, though acute, inhaled osmotic therapy may allow for extended therapeutic benefit via the tPad or a similar extended delivery device. The benefit may be extended even further using more durable osmotics, like mannitol, or by reducing  $\text{Na}^+$  absorption with ENaC blockers.

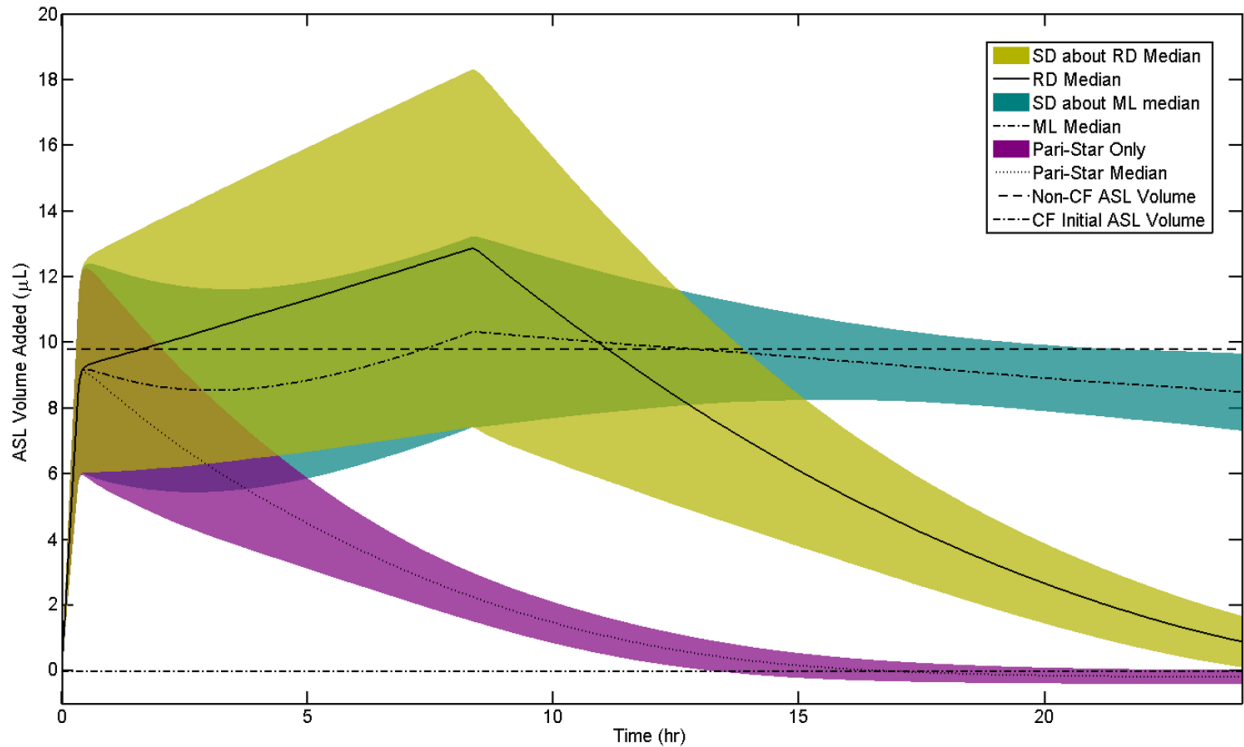


Figure 3.20: Three ASL volume profiles (median with SD envelope) are shown for cell-culture response to area-normalized deposition rates of either the Pari LC Star alone (magenta) or followed by the tPad at the reduced deposition (RD) rate (yellow). Combination therapy with a rapidly inhaled “priming” dose is able to maintain hydration for an overnight time duration for either HS or mannitol (cyan). However, the absence of cellular transport pathways for mannitol provides sustained hydration.

### 3.5 SUMMARY

Previous mathematical models of airway epithelia have considered liquid and solute transport in varying degrees of mechanistic detail. Typically models have been designed around Ussing chamber conditions [16,17,55,88,89], which are flooded in comparison to physiological (thin-film) conditions. The model represents an advancement in that it accounts for paracellular transport and includes dynamic apical, basolateral, and cellular compartments under thin-film conditions. These conditions recreate the conditions in the human airway, allowing

the model epithelium to establish a homeostatic ASL at an air-liquid interface. By considering the effects that ASL and cell volume have in terms of regulating solute and liquid flux in an HBE culture system, a structurally robust model that recapitulates experimental findings has been constructed. Previous models also typically solve the algebraic electrophysiological transport relationships involving Kirchhoff's laws ([55, 88]) and/or use high-order representations of ion transporters, particularly in the basolateral membrane [16, 70]. Instead, lumped kinetics were used for basolateral transport and apical transport terms that preserve physiological phenomena (e.g. volume regulation) in the equation structure. The result is a simplified model of epithelial solute and liquid transport that captures ASL and DTPA absorption dynamics with model parameter and species flux values that reflect those found in the literature. Furthermore, the model also explains physiological observations regarding the routes of water transport in non-CF and CF HBE, namely that there is more paracellular transport in CF epithelia than non-CF epithelia.

Using an identical model equation structure for both populations, we were able to identify different parameterizations for CF and non-CF cell cultures that give rise to different ASL and DTPA absorption dynamics. It was estimated that  $\text{Na}^+$  flux (thus, ENaC permeability) is similar between CF and non-CF cells (Figure 3.6A), which is in agreement with some experimental studies that have found that ENaC is not necessarily hyperabsorptive in CF [25, 157] but contradicts the findings of some previous experimental and modeling studies [17, 93] conducted under Ussing chamber conditions. Ussing chamber measurements from cell lines used for the training set indicate transepithelial  $\text{Na}^+$  flux as calculated from  $I_{\text{Na}}$  values are similar in CF and non-CF. Ussing Chamber experiments, where ENaC transport kinetics are essentially saturated, are difficult to extend to thin film conditions. However, the model is structured such that  $P_{\text{ENaC}}$  represents the saturated permeability of ENaC. It is shown in Table 3.2 that the estimates for  $P_{\text{ENaC}}$  are similar to those in the flooded conditions of Ussing Chamber studies [56, 93]. The model calculations for mean  $\text{Na}^+$  flux in both CF and non-CF cells are between the lower ( $0.74 \mu\text{eq}/\text{cm}^2/\text{hr}$ , [87]) and upper ( $2.15 \mu\text{eq}/\text{cm}^2/\text{hr}$ , [4]) bounds found in the literature. In the case of CF in particular, the model-predicted  $\text{Na}^+$  flux demonstrates excellent agreement with the value calculated from the data, which is evidence of the physiological relevance of the model.

We also calculated via the model that  $\text{Cl}^-$  flux is decreased in CF to the point of inversion from secretion in the non-CF case to absorption in the CF case. Indeed, the model estimates for  $\text{Cl}^-$  flux are reduced in comparison to values calculated from the Ussing Chamber data. However, the Ussing Chamber estimates of  $\text{Cl}^-$  flux are based on the difference between  $I_{\text{SC}}$  under bumetanide inhibition and the  $I_{\text{SC}}$  of forced  $\text{Cl}^-$  secretion following forskolin stimulation. Resting  $\text{Cl}^-$  fluxes must be smaller than the forskolin stimulated values, and open-circuit studies have shown that low secretive or even absorptive  $\text{Cl}^-$  flux may occur [4, 23]. The model-estimated permeability of the constitutively active (*i.e.* not volume-regulated) chloride channel was also analyzed in the model,  $P_{\text{ACC}}$ . We found that  $P_{\text{ACC}}$  is decreased in CF HBE in addition to the absence of CFTR function (Figure 3.6C). This agrees with findings from Ussing Chamber experiments that  $I_{\text{Cl}}$  is decreased in CF HBE, which may be in line with the findings of Bertrand and colleagues [3], who suggest that SLC26A9 is a constitutively active  $\text{Cl}^-$  channel whose function is diminished by dysfunction in CFTR. Accordingly, it may be that the model demonstrates that the hyperabsorptive dynamics that arise in CF are due, at least in part, to the absence of constitutive  $\text{Cl}^-$  transport brought on by the absence of CFTR regulatory presence in addition to the loss of its chloride channel function.

The major factor contributing to differences in absorption dynamics between CF and non-CF epithelia is hydraulic permeability (Figure 3.6D, Table 3.2), which the model describes as being 10 fold higher in CF. The model cellular hydraulic permeabilities in non-CF and CF cells are close to literature values [9] derived from similar thin-film experiments. They indicate that CF cultures are more permeable to both trans- (only  $\sim 2x$ ) and paracellular ( $\sim 10x$ ) water flows. TER is a metric of epithelial junction integrity, in terms of permeability of ions through the paracellular space that is measured in the Ussing Chamber. There was no difference in TER between CF and non-CF cells (Figure 3.6E). However, this does not necessarily speak to the permeability of water through the cellular junctions in an open-circuit, thin-film experiment like that on which the model was trained. It could be that water transport kinetics vary greatly between the Ussing Chamber and thin-film conditions, which more closely mimic the airway environment. It is also possible that a decrease in

paracellular resistance was balanced by an increase in transcellular resistance due to the lack of  $\text{Cl}^-$  conductance through CFTR.

We also validated the model using four additional cell lines (2 CF and 2 non-CF, Figure 3.7). The effective use of the best-fit parameters generated by MCMC during model training demonstrates that these parameters and their distributions are representative of the respective CF and non-CF cell populations, implying that cell parameters from a “new” subject would fall within these ranges.

In order to demonstrate appropriate model response to osmotic challenges, 10  $\mu\text{L}$  of either 450 mOsm concentrated Ringer’s or mannitol+Ringer’s solutions was added with DTPA to the ASL of non-CF HBE. Model parameters were refit, resulting in the best-fit values given in Table 3.2. The subsequent apical hyperosmolarity induced ASL swelling (Figure 3.8A) as the ASL volume increased (up to  $t \approx 1$  hour). DTPA transport was slowed due to abrogated convection, as illustrated by the visible downward deflection in the slope of the concentrated Ringer’s curve (Figure 3.8B). Dilution and experimental variability caused small differences in initial ASL osmolarity (Figure 3.8C and 5D), resulting in more swelling in the Ringer’s-only condition. Model-predicted changes occur rapidly, and maximum cell shrinkage occurs on a similar time-scale as reported by Matsui and colleagues [9] (Figure 3.8E). Mannitol increased steady-state ASL volume and reduced DTPA absorption as compared to concentrated Ringer’s. Mannitol is not actively transported through cells; it can only diffuse through the paracellular pathway, which is comparatively slow. The residence time for mannitol and therefore its osmotic effect in the ASL was longer than the residence time of the ions of Ringer’s solution, which are actively transported by epithelial cells. There was also no appreciable difference in osmotic volume response between CF and non-CF cells (Figure 3.11).

Our training data corroborates previous reports, both *in vitro* [65] and *in vivo* [8], that DTPA absorption is increased in the CF airway. Using the mathematical description of DTPA absorption from the ASL, it is possible to probe the relative contributions of diffusion (Figure 3.12A) and convection (Figure 3.12B) that lead to this increased DTPA absorption in CF. Concentration driven diffusion differences diminish during the experiment as the larger transcellular liquid absorption in non-CF cells “concentrates” DTPA in the ASL relative

to CF cells (Figure 3.12E). The model predicts that convective transport explains approximately 80% of the increase in DTPA absorption seen in CF vs. non-CF cells. Furthermore, convection accounts for 20% of total DTPA absorption in non-CF cells, increasing to nearly 40% in CF cells, which is close to experimentally observed values [8]. The model also suggests that the majority of liquid absorption occurs through the transcellular pathway in both CF and, particularly, non-CF cells (Figure 3.12C). This agrees with previous reports [149] that transcellular, namely aquaporin-mediated, water transport exceeds the volume of transport that occurs in the paracellular space.

In order to test the model prediction that paracellular permeability is increased in CF cells, a basolateral osmolarity gradient was imposed favoring increased ASL absorption. In so doing, this accelerated DTPA absorption at all time points (2-24 hours) in CF cells and at 24 hours in non-CF cells. CF cells in both the control and challenge conditions absorbed DTPA faster than non-CF cells (Figure 3.13A and B). Moreover, the acceleration induced by the gradient was greater in CF cells than non-CF, verifying the model predictions that paracellular permeability is increased (*i.e.* barrier integrity is diminished) in CF cells.

There are two disease-relevant implications of this work to CF:

1. According to the MCMC-estimated ion fluxes and related Ussing Chamber measurements (Figure 3.6), the depletion of CF ASL originates in dysfunctional ion transport and subsequent dysregulation of liquid transport through epithelial cells.
2. Paracellular liquid transport is increased in CF vs. non-CF HBE, leading to the increased convective and total absorption of DTPA observed in CF (Figures 3.12 and 3.13). Paracellular transport does not exceed that of the transcellular route, but possible structural deficiencies indicated by the model paracellular permeability (Figure 3.6C) suggest its contribution is significant in terms of overall liquid absorption.

CFTR has been shown to regulate not only ion transport but also liquid transport via interactions with AQP3 in airway epithelial cells [52]. This could explain the parametric and dynamic transport differences observed in this work. It has also been reported that structural and functional defects (*e.g.* connexin 43 mistrafficking or impaired cytoskeletal interactions) exist in the tight junction of CF cells [139,140,141], which would further explain

the aforementioned threefold increase observed in paracellular transport. This abnormality is distinguishable from transcellular transport through the model, which describes these transport mechanisms independently, in concert with the experimentally known cellular ion and liquid transport defects in CF.

Because the model is able to distinguish between paracellular and transcellular liquid and solute transport in HBE cells, it follows that transport in the airways *in vivo* could be described by the physiological equations developed herein. MCC and DTPA absorption in the lungs of subjects with and without CF [1,8] has been previously observed and modeled. That model provided a physiological explanation for the deficient MCC observed in patients with CF and a mechanistic description of DTPA absorption. It also demonstrated the therapeutic effect of hypertonic saline on both MCC and DTPA absorption

This work represents a mechanistic description of DTPA and liquid transport. Furthermore, it is a system of ordinary differential equations that are less computationally expensive to solve than the differential algebraic equation-based models in the literature. The reduced complexity of the model in terms of active ion transport, particularly that of  $\text{Na}^+$ , is also useful for more rapidly identifying patient-specific parameters and designing patient treatment and dosing strategies in real time on its own or merged with a lung-scale model.

We have shown the utility of the model in diagnosing possible causes of treatment failure for the tPad system for overnight HS delivery via nasal cannula. It was determined that insufficient saline deposition is the most likely explanation for why the study was negative (see Figures 3.15 and 3.16). Simulations presented in Figure 3.17 and Figure 3.19 suggest that 14% hypertonic saline may hydrate intermediate airways more effectively than 7%. However, they also suggest that priming the airways with a short (20 min) pre-hydrating dose of HS via the Pari LC-star or similar device may allow the tPad maintain ASL hydration for the duration of overnight treatment. Figure 3.20 illustrates this point as well suggesting that mannitol may be a more durable therapeutic than HS, which is similar to the result presented in 3.8. Ultimately, these results demonstrate that the cell-scale model is a useful explanatory and predictive tool that is well-positioned for rigorous optimal treatment design.

## 4.0 PARAMETER IDENTIFICATION: METHODS AND MOTIVATING CASES

### 4.1 OBSERVABILITY AND IDENTIFIABILITY IN SYSTEMS MODELS

Parameter identification is one of the most important problems in systems modeling, and is only complicated by the complexities and nonlinearities present in biological models. Cobelli and DiStefano [158] describe the concept of identifiability as one primarily focused on the uniqueness of solutions to the problem of parameter estimation. They define a “structurally identifiable” model as a model with a unique solution to the parameter estimation problem [158]. As evidenced by the models presented in previous chapters, this estimation problem is often ill-posed with many more unknown parameters in the vector  $\underline{\theta}$  than model equations, and the observables,  $y(t)$ , often come in the form of noisy data. In this case, the estimation problem can be posed as an optimization problem. In the case of modeling dynamic data, the objective function,  $F$ , is usually a variant of minimizing the sum squared error (SSE) between model fit and data. A standard variance-weighted form of the SSE is given in (4.1):

$$\min_{\underline{\theta}} F = \sum_i^m \sum_k^n \frac{1}{\sigma^2(t_k)} (\hat{y}(t_k, \underline{\theta}) - y(t_k))^2 \quad (4.1)$$

The variance,  $\sigma(t_k)^2$ , of the data is used to weight the squared difference between the model value of the  $i = 1, \dots, m$  states,  $\hat{y}(t_k, \underline{\theta})$ , and the value of the observable given data at  $k = 1, \dots, n$  points in time,  $t$ . The most standard means of optimization using this objective function is regression [134, 159, 160]. For a linear optimization problem the solution and the confidence in that solution is exact [134]. Solutions for nonlinear models or even nonlinear optimization problems (*i.e.* the final model of chapter 2) are rarely guaranteed

to be in closed form, and characterizing the confidence in those estimates introduces the subject of “practical identifiability” [134, 160]. Raue and colleagues [160] define a model parameter  $\theta_i$  as practically identifiable if finite confidence intervals can be placed on the optimal estimate,  $\theta_i^*$ . A parameter is said to be “structurally unidentifiable” if it has infinite confidence intervals [158, 160, 161]. The parameter  $k_{DL}$  from the lung-scale model of chapter 2 is a relevant example of a “practically unidentifiable” parameter (see Figure 2.15). It has finite confidence intervals, but there is insufficient information to map mucociliary clearance in the model state D to observable data (either distal or whole-lung counts) in a way that provides confidence intervals that exclude 0 and negative values. That is, even though the data is such that the lung-scale model structure is observable, the data for D are not sufficient to say that  $k_{DL}$  is different from 0 (*i.e.* ineffectual).

This concept of observability is also important in modeling. Cobelli and DiStefano [158] provided a detailed review of the concepts of identifiability and structural identifiability in the face of model observability questions. They borrow the definition of observability in the linear case from Kalman [162]:

$$\begin{aligned}\frac{dx^1}{dt} &= A^{11}(t)x^1(t) + B^1(t)u(t) \\ \frac{dx^2}{dt} &= A^{21}(t)x^1(t) + A^{22}(t)x^2(t) + B^2(t)u(t) \\ y(t) &= C^1(t)x^1(t)\end{aligned}$$

Where  $x^1$  is an  $m_1$ -vector and  $x^2$  is an  $m - m_1$  vector,  $u$  is the control input, and  $A^{11}$ ,  $A^{21}$ , and  $A^{22}$  are the submatrices representing the state effects on state dynamics. Note that the  $y$  outputs  $x^1$  dynamics are affected by the  $x^1$  states but not the  $x^2$  states. Thus, a system is observable if a system of equations can be specified from its state equations that relates each state to either another state or an output. Restated, a system is completely observable if its state variables,  $x$ , are not split into two groups wherein one group (*i.e.*  $x^2$ ) has no effect on either the other states or the outputs. Thus, for a linear system of  $m$  states, if the *Linear Observability Matrix*  $\mathcal{O} = [C, CA, CA^2, \dots, CA^{m-1}]'$  is of rank  $m$ , the system is observable.

In the nonlinear case, the observability matrix is developed from higher order Lie derivatives of  $y(x)$ ,  $\mathcal{L}^n(y(x))$  [163]. If we let  $f = A(x) * x$ , and  $y = C(x) * x$ , and assume  $Bu = 0$ ,

the *Nonlinear Observability Matrix*,  $\mathcal{O}_{NL}$  is determined as follows [164] from the Lie bracket sequence:

$$\begin{aligned}\mathcal{L}^0(y) &= y \\ \mathcal{L}^1(y) &= \nabla(y)f \\ \mathcal{L}^2(y) &= \mathcal{L}^1(y)f \\ &\vdots \\ \mathcal{L}^n(y) &= \mathcal{L}^{n-1}(y)f\end{aligned}$$

Where  $\mathcal{O}_{NL}$  is ultimately:

$$\mathcal{O}_{NL} = \nabla \begin{bmatrix} \mathcal{L}^0(y) \\ \mathcal{L}^1(y) \\ \vdots \\ \mathcal{L}^{m-1}(y) \end{bmatrix}$$

And  $\nabla$  is the Jacobian with respect to the states,  $x$ .

As an example, the lung clearance model of [chapter 2](#) can be shown to satisfy the observability criteria. Note that for the Tc-SC model the absorption parameters are  $k_{LB} = k_{DB} = 0$ , thus the change in the whole-lung count output is due only to MCC from  $L_F$ , so we have one relationship. The change in D is also observable via its own measurement as defined by the P box from imaging, so we have another.  $L_N$  is observable due to the observability of  $L_F$  and D to which  $L_N$  is related algebraically in Laplace space. As such, the model is observable. Conveniently, the same model structure when applied to DTPA is also observable but only because of the observability of the Tc-SC model. Since we can set the values for the MCC rate constants at the values obtained in estimated Tc-SC clearance, absorption is strictly observable based on data from D and also L since FFCA is known.

It is interesting to note that this model, while completely observable, is not totally identifiable. This possibility is discussed by Cobelli and DiStefano [158] and is another way of defining the case of practical unidentifiability [160]. Specifically, while MCC in D is technically observable in the mathematical sense, the rate constant that governs its dynamics,

$k_{DL}$ , is ill-informed by the data. In the case of  $k_{DL}$ , selection of time points for gathering data is the primary issue with identifiability; MCC in D is known to be detectable on the order of hours [116], but there are only 80 minutes of data to inform the clearance constant. Data sparseness can also be a cause of unidentifiability [134], but we show this is not the case - and that it is the former point discussed - later in this chapter. However, it is useful to first discuss the available methods of parameter estimation and identification including those used in this dissertation.

## 4.2 METHODS FOR PARAMETER ESTIMATION AND IDENTIFICATION

Parameter identification is commonly performed via regression, which can be applied in linear and nonlinear models using gradient-based methods. Newton-Raphson methods are the simplest of this class of search. Most common to this dissertation, however, is the trust-region-reflective method that is built in to the Matlab function *lsqnonlin* (©2013, The MathWorks, Natick, MA). These methods require the computation of the Jacobian  $J = \frac{dF}{d\theta}$  of the model states at every iteration, which is computationally expensive for large systems. So-called quasi-Newton methods approximate the Jacobian or Hessian  $H = \frac{d^2F}{d\theta^2}$  in order to improve computational performance. An example of this type of solver that is used in this dissertation is the interior point optimizer *ipopt*, which employs the the Broyden-Fletcher-Goldfarb-Schano (BFGS) algorithm [165].

The general assumption of (4.1) is that the minimum solution set in all of parameter space, called the global optimum, is the true solution to the estimation problem. While there is some debate regarding whether true global optimality is essential in the identification problem in biology [166], it is useful to explain how it can be obtained. Gradient-based methods on their own can only guarantee that the solution achieved is globally optimal if the optimization is formulated as a linear program (LP) or quadratic program (QP). In part, this is because gradient-based methods require a convex objective surface for convergence, which are guaranteed in these formulations. Gradient-based solvers tend to fail for nonlinear

programs (NLPs) because NLPs are rarely globally convex, but they require an initial guess in order to determine an optimal value for a given parameter. Thus, the goodness of the solution provided by these methods for NLPs is heavily reliant upon the quality of the initial guess. With an infinite number of guesses any algorithm achieve global optimality [167]. For most models with any degree of physiological detail, such methods are only useful for verification of nonconvexity. As a next step, Raue and colleagues propose that the sparseness afforded by Latin Hypercube sampling (LHS) is a strong method for generating an ensemble of initial guesses for an optimization algorithm [168]. An additional benefit of LHS is that it is highly parallelizable; a single guess and subsequent optimization routine can be assigned to a dedicated computational core or thread for independent simulation in parallel with other optimizations in the hyperspace. There is still no guarantee that any solution is globally optimal, but this method has the benefit that deterministic assignment of initial conditions is computationally cheap and good solutions can generally be found [168]. Deterministic programs that solve NLPs to global optimality (if needed) also exist (e.g. BARON [169] and KNITRO [170]), but may still struggle in optimizing the systems of highly nonlinear differential equations that often arise in biology.

In many cases, particularly those with a high degree of nonlinearity, stochastic methods for parameter identification may be useful [166] and some can be shown to provide guaranteed convergence in finite time [142]. In a similar manner to LHS, these methods can randomly sample values in parameter hyperspace for determination of the objective function value, but they iteratively improve fit through statistical biasing instead of a gradient-based search - be it through evolutionary “fitness” [171], simulated annealing [172], parallel tempering [142] or otherwise. Papers by Moles, Mendes, and Banga [166] and by Raue *et al.* [168] provide a broad survey of such algorithms for the interested. Another such method that is used in the second case study of this chapter is the Affine Parallel Tempering Markov Chain Monte Carlo (APT-MCMC) method developed by Zhang and colleagues [173]. This is a Markov Chain Monte Carlo variation of the Metropolis-Hastings algorithm that applies an affine transformation during likelihood calculations for improved performance. Stochastic and deterministic methods both rely on the assumption that the global solution is the best (*i.e.* “real”) solution. In the stochastic sense, however, the “real” solution is the most

likely solution. As stochastic simulations progress, the history of objective function values at sampled locations in parameter space preserves an estimate of the likelihood function  $\mathcal{L}$ . Confidence intervals on parameters can be calculated directly from this likelihood estimate. Thus, it is a benefit of stochastic simulations that the parameter estimation algorithm itself simultaneously provides information regarding the practical identifiability of the model.

An estimate of the likelihood can be obtained for deterministic cases as well using  $F$  from 4.1 as the measure of  $\mathcal{L}$ . The Fisher information matrix is one methodology that is commonly used in systems biology [174]. Rooney and Biegler [159] provided an outline for developing a joint confidence region between two model parameters that was exploited for one and two parameters by Word and colleagues [175]. The confidence regions or intervals for  $p$  parameters are generated by finding  $\theta^*$  that satisfies the optimization problem 4.1 and then solving for each of the  $\theta_i$  that provide the maximal distance from  $\theta_i^*$  that does not exceed the given confidence value  $\alpha$  from the likelihood ratio (LR) test [176], as formulated in 4.2.

$$\begin{aligned} & \text{maximize} && \sum_i (\theta_i - \theta_i^*)^2 \\ & \text{s.t.} && LR = 2[\log(\mathcal{L}^*) - \log(\mathcal{L})] \leq \chi_{1-\alpha,p}^2 \end{aligned} \tag{4.2}$$

$\chi_{1-\alpha,p}^2$  is the  $\chi^2$  value for confidence at the  $1 - \alpha$  level for  $p$  number of parameters. If the solution to 4.2 is found iteratively for a single parameter,  $\theta_i$ , by increasing the distance  $(\theta_i - \theta_i^*)^2$  in a stepwise manner until the LR constraint is violated, the contour generated in the objective space of 4.1 over all examined  $\theta_i$  is equivalent the Profile Likelihood (PL) described by Raue and colleagues [134]. Profiling the likelihood in this manner provides the confidence intervals of 4.2 for all practically identifiable parameters while also revealing structural unidentifiabilities and nonlinearities in the objective space [134, 160]. PL methods have been shown to be more computationally efficient than stochastic Monte Carlo methods in general [168]. Even so, the lack of guarantee or even detail with regard to global optimality in the former case may justify the use of stochastic analysis. Specifically, stochastic algorithms like MCMC provide not only the likelihood estimate for each parameter but also allow for analysis of parameter-parameter correlations from the marginal distributions gen-

erated. A comparison between PL and a Markov-Chain Monte Carlo (MCMC) method in identifying the parameters of the model from [chapter 2](#) will be the focus of a case study in the fourth section of this chapter. Before that, however, the generation of the PL algorithm used for that purpose within the open source optimization package Pyomo, will be discussed.

### 4.3 AN OPEN SOURCE PACKAGE FOR PARAMETER LIKELIHOOD ESTIMATION

#### 4.3.1 The Pyomo Model Profile Likelihood Estimation (PyMPLE) Package

Pyomo [\[177\]](#) is an algebraic modeling language (AML) that is designed to exploit the benefits of the programming language Python, namely its high-level, object-oriented nature and expanse of available open source packages and libraries. Pyomo is itself open source and available to anyone with a Python installation, making it more accessible than most other licensed AMLs, including AMPL [\[178\]](#) and its solvers, with which Pyomo can also interface. As their name might suggest, AMLs are not well-suited for the solution of differential equations, though it is generally possible through tedious effort [\[179\]](#). Others have developed their own methods for optimizing certain classes of dynamic systems [\[180\]](#). For this reason, Pyomo has recently become more appealing to dynamicists with the advent of the `pyomo.dae` package [\[179\]](#). This package automates the discretization of Pyomo `Var()` type variables and their dependent `DerivativeVar()` type variables into an algebraic approximation of each differential equation. It supports standard and backward finite difference transformations, collocation on finite elements, and custom discretization schemes for integration. The `pyomo.dae` package is capable of solving partial differential equations (PDEs) and differential algebraic equations (DAEs), and the same methods can be used to solve systems of ordinary differential equations (ODEs), like those presented previously in this dissertation. This combination of easy-to-generate solutions to dynamical systems within a powerful optimization framework makes `pyomo.dae` an ideal platform for high-performance identification in systems engineering and systems biology.

Currently, `pyomo.dae` will only optimize a model parameter or parameter set without generating direct information about practical identifiability. Asymptotic confidence intervals can quickly be calculated from the covariance,  $C$ , and the Hessian,  $H$ , since  $C = 2H^{-1}$ , according to 5.3.

$$CI_{\theta_i} = \theta_i^* \pm \sqrt{\chi^2(\alpha, p) C_{i,i}} \quad (5.3)$$

For most quasi-Newton methods such as `ipopt` [165], the Hessian is already approximated by the algorithm. While fast, this approximation of the CIs is not always good, and can be improved by calculating parameter likelihoods [134, 159]. Word and colleagues [175] set a precedent for using likelihood-based techniques within the Pyomo framework using a dynamic model of the seasonality of infectious diseases. That work was performed prior to the release of the `pyomo.dae` package. Consequently all of their discretization and estimation techniques were developed in a custom implementation for their model. Since `pyomo.dae` is now available to automate the discretization transformations of differential equations, the goal of the work that follows in this chapter is to also automate the analysis of parameter identification via profile likelihood.

Described herein is the Pyomo Model Profile Likelihood Estimation (PyMPLE) package. PyMPLE works in concert with `pyomo.dae` as a standalone module and class in Python. Instantiation and execution of the PyMPLE class and its methods and attributes is accomplished via a `run_file.py` script that imports the module and provides requisite arguments for PyMPLE and the `pyomo.dae` model. An example of a run file and the `pyomo.dae` model it runs are given in Appendix C, as is the full code of PyMPLE itself. The outline of the process by which profile likelihoods are obtained is presented in Figure 4.1

The PyMPLE class has six methods:

1. `PyMPLE.__init__` is the initialization method for an instance of the class
2. `PyMPLE.get_CI` is the method that sequentially calculates the profile likelihood and confidence intervals of model parameters for a given  $\alpha$  value.
3. `PyMPLE.ebarplots` generates a matplotlib bar plot with errorbars at the upper and lower CI for each model parameter.

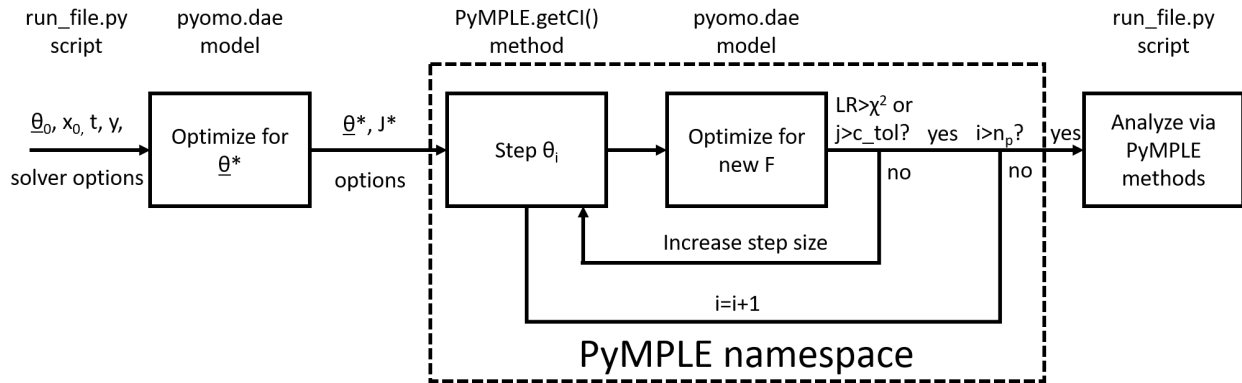


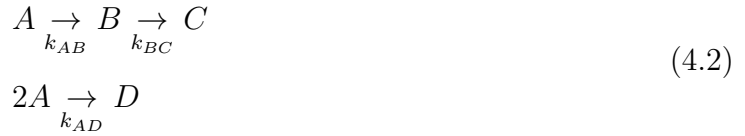
Figure 4.1: The algorithmic flowchart for generating PL analysis via PyMPL.

4. `PyMPL.plot_PL` Plots the profile likelihoods of each profiled parameter in  $\theta$  and returns the figure handle containing the graphs.
5. `PyMPL.plot_trajectories` generates graphs of the dynamic state trajectories for each solution instance from the profiling algorithm and returns the figure handle containing the graphs.
6. `PyMPL.pop` pays homage to the built-in Python method of the same name that returns and deletes the final element of a list by returning the final elements of the upper and lower profile arrays (*i.e.* the upper and lower bounds) of one or more requested parameters.

Each of the methods except for `PyMPL.pop` uses the numpy numerical package, and the graphing methods use the Seaborn and matplotlib graphing packages. Methods 3-6 can only be used upon completion of the `PyMPL.get_CI` method execution. A detailed description of the argument structure of these methods is contained in the code provided in [Appendix C](#).

#### 4.4 PYMPLE EXAMPLE: A MODEL OF THE VAN DE VUSSE REACTION IN A CSTR

The Van de Vusse reaction scheme [181] is a widely used [182, 183, 184] chemical engineering model for the study of nonlinear reaction systems. It has the following structure:



Where cyclopentadiene (A) is converted to the desired product cyclopentanol (B) with byproducts of cyclopentanediol (C) and dicyclopentadiene (D). Under the assumption that the reaction is carried out in an isothermal CSTR with only A in the feed, there is no need for an energy balance and the mass balances for the system become:

$$\begin{aligned}
 V \frac{dC_A}{dt} &= F(C_{Af} - C_A) - V k_{AB} C_A - V k_{AD} C_A^2 \\
 V \frac{dC_B}{dt} &= -F C_B + V k_{AB} C_A - V k_{BC} C_B \\
 V \frac{dC_C}{dt} &= -F C_C + V k_{BC} C_B \\
 V \frac{dC_D}{dt} &= -F C_D - \frac{1}{2} V k_{AD} C_A^2
 \end{aligned} \tag{4.3}$$

We set the inputs  $\frac{F}{V} = 4/7 \text{min}^{-1}$  and  $C_{Af} = 10 \frac{\text{mol}}{\text{L}}$  and the rate constants  $k_{AB} = 5/6 \text{min}^{-1}$ ,  $k_{BC} = 5/3 \text{min}^{-1}$ , and  $k_{AD} = 1/6 \frac{\text{mol}}{\text{L-min}}$ . This served as a numerical basis for demonstrating the functionality of PyMPLE as well as some key concepts regarding identifiability, observability, and their relationship to experimental design. We simulated the system of equations over 10 minutes of dynamics using ode15s in Matlab, so that a clear steady state was achieved in the data following start-up. Normal random error ( $\mu = 0$ ,  $\sigma = 0.1$ ) was added to each of the state-value vectors in time. This noisy data was preserved for re-optimizing the parameters under a number of observability and data-richness conditions as follows in the next section.

#### 4.4.1 Analysis and Model Identification

We generated a model of the system using the `pyomo.dae` package to discretize the differential equations of our model. As a first example we fit the concentrations of all model states over time while attempting to identify  $\theta^*$  as the set of model rate constants given the initial guesses  $\{k_{AB,0}, k_{BC,0}, k_{AD,0}\} = \{1/2, 5/2, 1/3\}$ . Using 110 finite elements per state - one for each time-point - and a backwards finite difference transformation we fit the model parameters to the data using the `ipopt` solver. The state trajectories given the optimal parameter set are plotted over time in Figure 4.2.

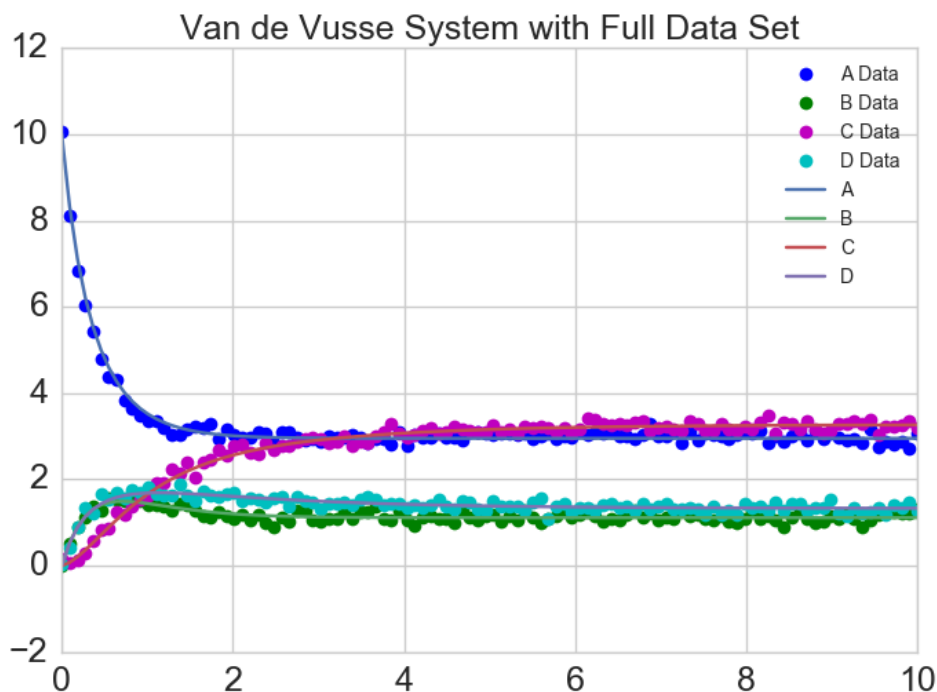


Figure 4.2: Model fit to full data set is excellent for each of the four model states.

In this case, the model is fully observable.

$$f = A(x)x = \begin{bmatrix} -\frac{F}{V}C_A - k_{AB}C_A - k_{AD}C_A^2 \\ -\frac{F}{V}C_B + k_{AB}C_A - k_{BC}C_B \\ -\frac{F}{V}C_C + k_{BC}C_B \\ -\frac{F}{V}C_D - \frac{1}{2}Vk_{AD}C_A^2 \end{bmatrix}$$

$$y = Cx = \begin{bmatrix} C_A \\ C_B \\ C_C \\ C_D \end{bmatrix}$$

Its nonlinear observability matrix is:

$$\mathcal{O}_{NL} = \nabla \begin{bmatrix} \mathcal{L}^0(y) \\ \mathcal{L}^1(y) \\ \mathcal{L}^2(y) \\ \mathcal{L}^3(y) \end{bmatrix} = \begin{pmatrix} 1 & 0 & 0 & 0 \\ 0 & 1 & 0 & 0 \\ 0 & 0 & 1 & 0 \\ 0 & 0 & 0 & 1 \\ -k_{AB} - 2A k_{AD} & 0 & 0 & 0 \\ k_{AB} & -\frac{F}{V} - k_{BC} & 0 & 0 \\ 0 & k_{BC} & -\frac{F}{V} & 0 \\ A k_{AD} & 0 & 0 & -\frac{F}{V} \\ (k_{AB} + 2A k_{AD})^2 + 2k_{AD} \left( k_{AD} A^2 + k_{AB} A - \frac{F}{V} \right) & 0 & 0 & 0 \\ -k_{AB} (k_{AB} + 2A k_{AD}) - k_{AB} \left( \frac{F}{V} + k_{BC} \right) & \left( \frac{F}{V} + k_{BC} \right)^2 & 0 & 0 \\ 0 & -\frac{F}{V} k_{BC} - k_{BC} \left( \frac{F}{V} + k_{BC} \right) & \frac{F}{V}^2 & 0 \\ -k_{AD} \left( k_{AD} A^2 + k_{AB} A - \frac{F}{V} \right) - A \frac{F}{V} k_{AD} - A k_{AD} (k_{AB} + 2A k_{AD}) & 0 & 0 & \frac{F}{V}^2 \end{pmatrix}$$

Which is rank  $m = 4$ . Thus the system is observable.

This is an intuitive result because each state is directly informed by data, and the problem is well-posed with a rich dataset. It is not surprising that under these conditions the rate constants are all practically identifiable as demonstrated in the profile likelihoods of Figure 4.3.  $\theta^*$  is similar to the known values of the parameters (see Table 4.1).

The observability of the model given the full data set translates, in this case, to full identifiability of the kinetic rate constants. It also has an effect on the quality of the estimation of state dynamics. To account for this, when the PyMPLE algorithm solves the model dynamics for each parameter set during profiling it also stores the trajectory values as a dictionary of arrays that represent the entire ensemble of model simulations which can be plotted. In this first case, each model state has data to inform its dynamics, and the narrow range of state trajectories in Figure 4.4 reflects this.

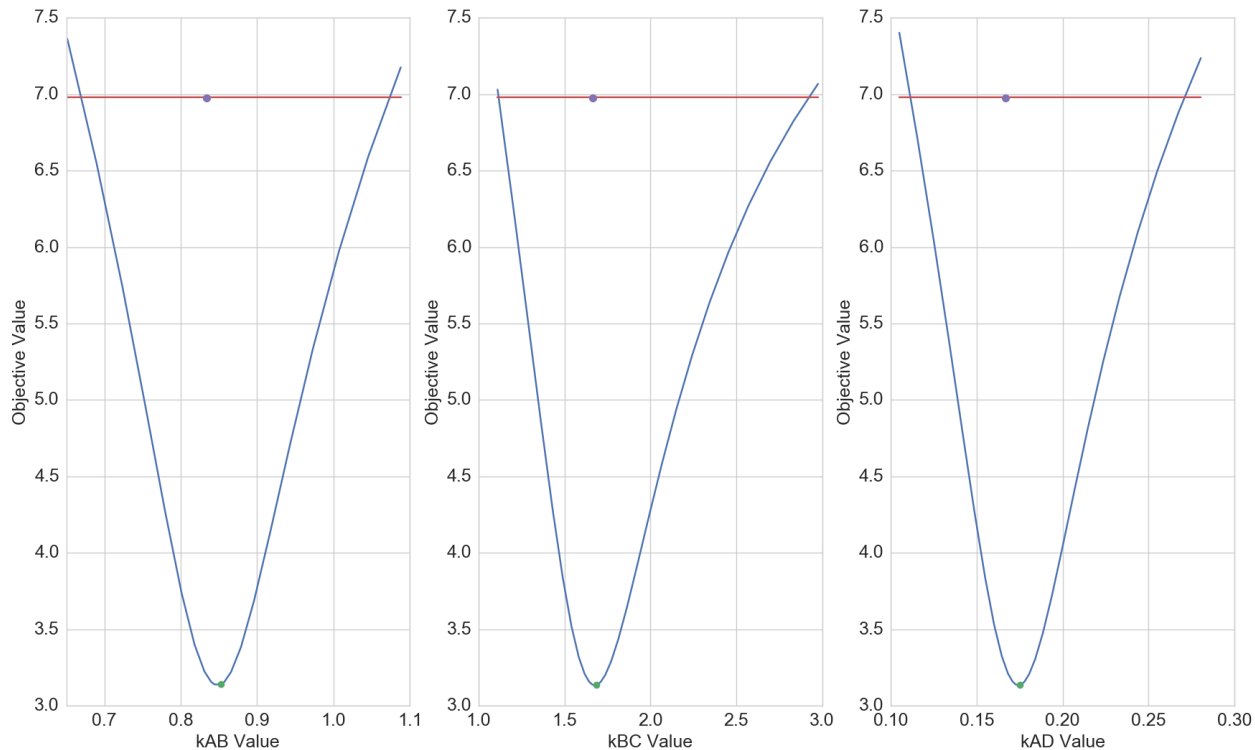


Figure 4.3: Profile likelihoods (blue lines) of the kinetic rate constants when all states are measured. Each parameter is identifiable at a 95% confidence level (red line). Optimal values (green dot) are close to the “true” values (purple dot) used in data generation.

Table 4.1: Estimates of reaction rate constants with true values given for comparison to the full and reduced data set examples.

Parameter	Full Data	No C or D	True Values
$k_{AB} \text{ (min}^{-1}\text{)}$	0.848	0.749	0.833
$k_{BC} \text{ (min}^{-1}\text{)}$	1.677	1.401	1.667
$k_{AD} \text{ (}\frac{\text{mol}}{\text{L-min}}\text{)}$	0.174	0.202	0.167

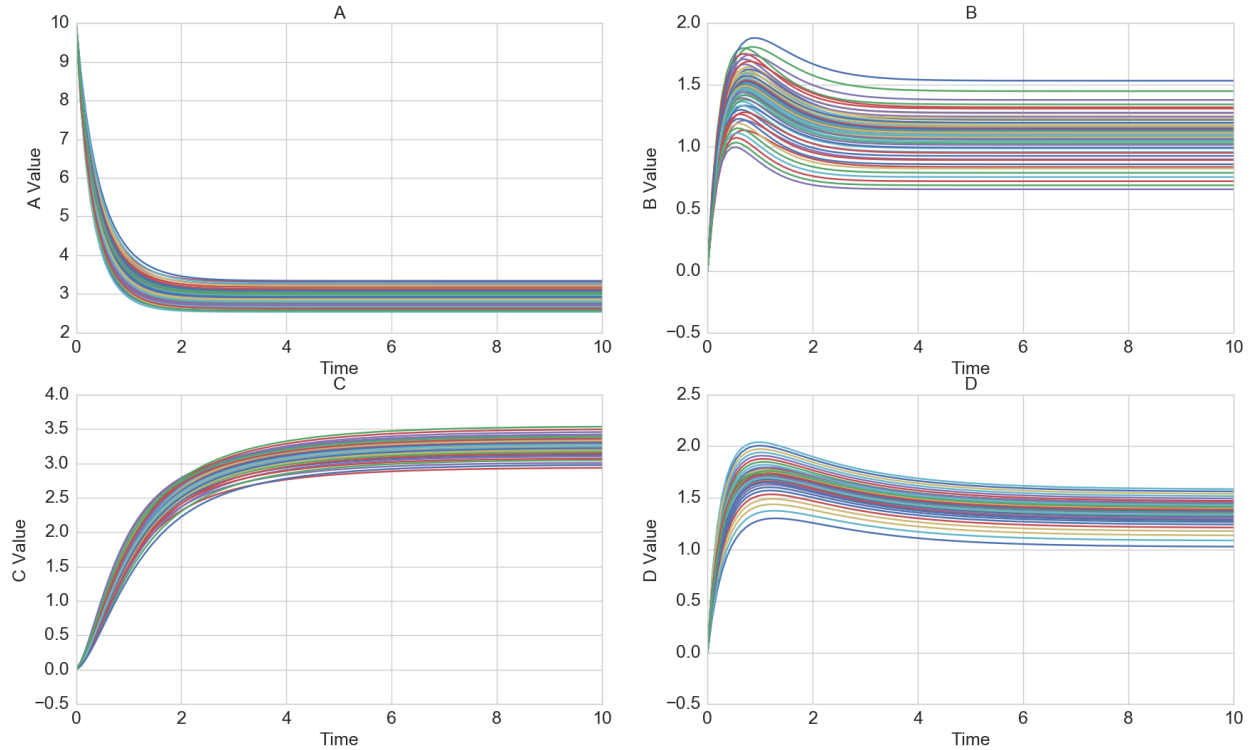


Figure 4.4: Trajectories for each model are given. The dynamics are similar within each state and to the state behavior in the data across the ensemble of simulations.

#### 4.4.2 Identification of an Unobservable Model

All of the components of the Van de Vusse process are chemically similar, which may pose multiple difficulties including sensor detection of individual component concentrations. In the hypothetical case that measurements of only A and the desired product B are taken, the model states C and D become unobservable. Thus, the new vector field  $y$  is:

$$y = Cx = \begin{bmatrix} C_A \\ C_B \\ 0 \\ 0 \end{bmatrix}$$

This has multiple effects in terms of model performance. The first is demonstrated in Figure 4.5, where values for C are underestimated while the values for D are overestimated.

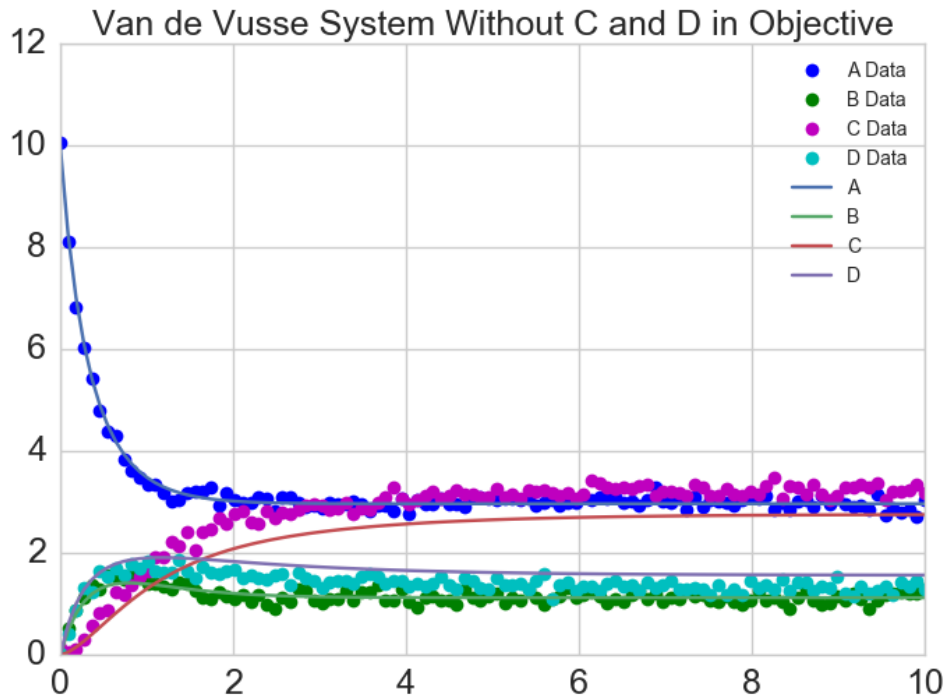


Figure 4.5: Model fit to A and B is excellent, however, data for C and D were not used in the objective function, and model fit falters accordingly.

The nonlinear observability matrix is:

$$\mathcal{O}_{NL} = \nabla \begin{bmatrix} \mathcal{L}^0(y) \\ \mathcal{L}^1(y) \\ \mathcal{L}^2(y) \\ \mathcal{L}^3(y) \end{bmatrix} =$$

$$\begin{pmatrix} 1 & 0 & 0 & 0 & 0 \\ 0 & 1 & 0 & 0 & 0 \\ 0 & 0 & 0 & 0 & 0 \\ 0 & 0 & 0 & 0 & 0 \\ -k_{AB} - 2A k_{AD} & 0 & 0 & 0 & 0 \\ k_{AB} & -\frac{F}{V} - k_{BC} & 0 & 0 & 0 \\ 0 & 0 & 0 & 0 & 0 \\ 0 & 0 & 0 & 0 & 0 \\ (k_{AB} + 2A k_{AD})^2 + 2k_{AD} (k_{AD} A^2 + k_{AB} A - \frac{F}{V}) & 0 & 0 & 0 & 0 \\ -k_{AB} (k_{AB} + 2A k_{AD}) - k_{AB} (\frac{F}{V} + k_{BC}) & (\frac{F}{V} + k_{BC})^2 & 0 & 0 & 0 \\ 0 & 0 & 0 & 0 & 0 \\ 0 & 0 & 0 & 0 & 0 \end{pmatrix}$$

Is rank  $m = 2$ , proving the system is non-observable.

That C and D are unmeasured also affects parameter identifiability. As illustrated in in Figure 4.6, parameters  $k_{BC}$  and  $k_{AD}$  are unidentifiable from zero. Furthermore,  $\theta^*$  estimates are worse than the full data case, as shown in Table 4.1. Confidence intervals on the estimates are substantially wider in the unobservable case as well.

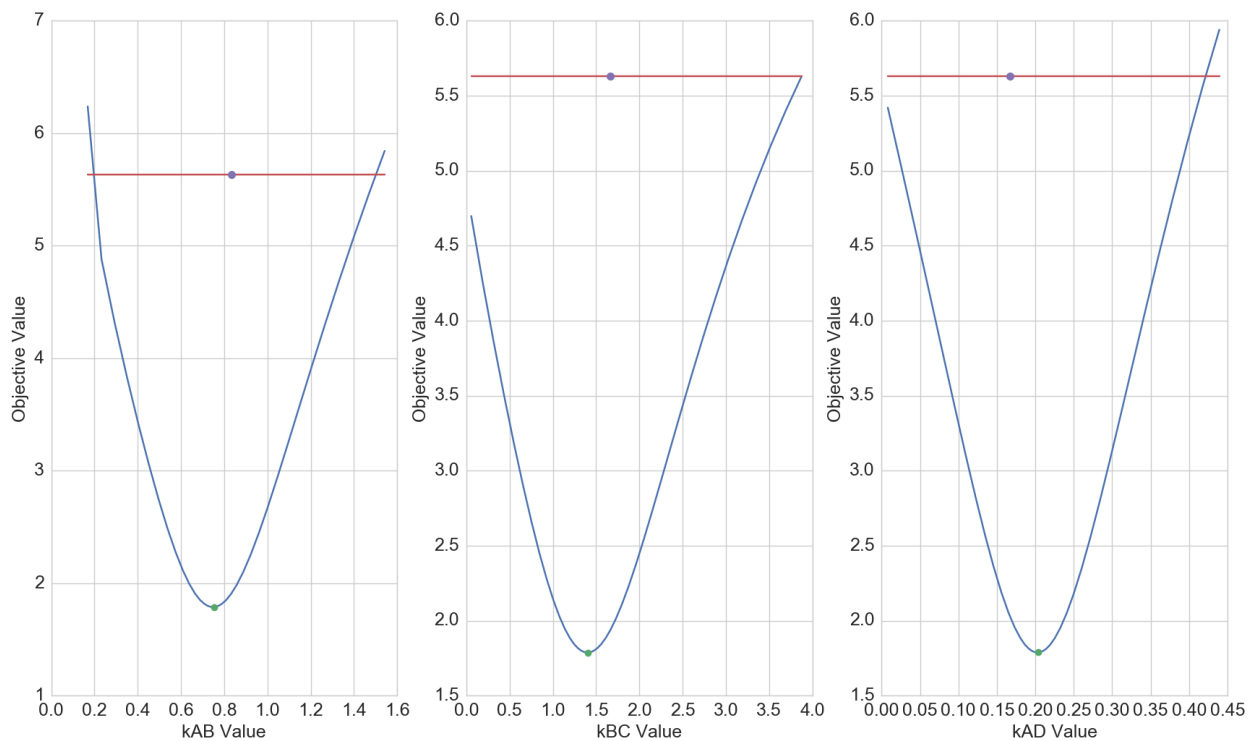


Figure 4.6: Profile likelihoods (blue lines) of the kinetic rate constants given only data for A and B. Only  $k_{AB}$  is identifiable at a 95% confidence level (red line). Optimal values (green dot) are further from the true values (purple dot) than in the observable case.

These results demonstrate that observability affects identifiability in a meaningful way, but its effect on state estimation may be even more meaningful. This is demonstrated in Figure 4.7 in the trajectories for C and D. As a direct consequence of not being able to identify  $k_{BC}$  and  $k_{AD}$  as different from 0, there is no ability to estimate the concentrations of C and as being different from 0 at any point in time. Furthermore, the range of possible concentrations generated during profiling precludes the possibility of accurate state estimation.

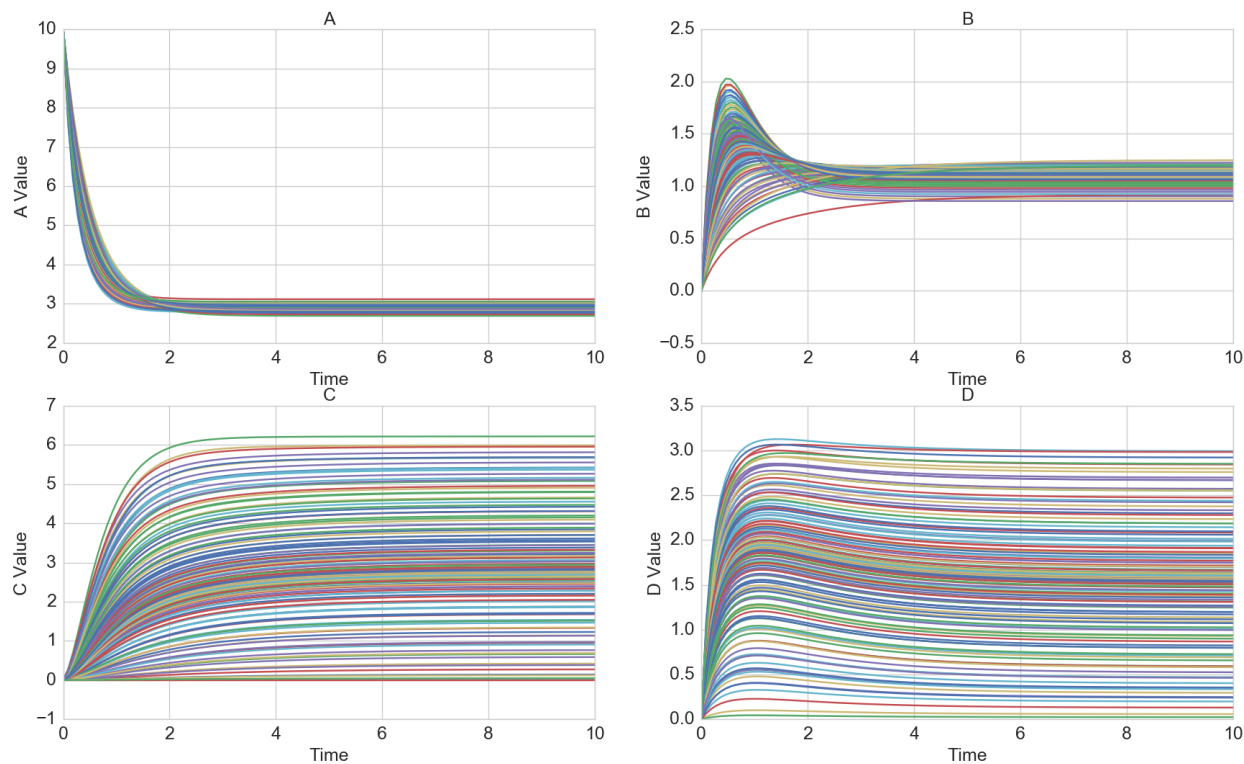


Figure 4.7: Trajectories for each model are given. Trajectories for unobservable states C and D cannot be confidently differentiated from a zero-dynamics case, and span a wide range of possible dynamic forms.

These findings motivate the following conclusions. The first is that observability and identifiability are interrelated despite the fact that neither is a necessary condition for the other [158]. Stemming from that concept is the notion that an ill-posed optimization problem can lead to poor performance if insufficient thought is given to data collection during experimental or process design [185]. This may be even more important for biological systems

where scale, complexity, and ethics greatly constrain the type and frequency of measurements. To that end, this example shows that PyMPLE is useful in providing analysis of process identifiability and observability. However, it should also be demonstrated that PyMPLE can serve the same function in biological models.

#### 4.5 IDENTIFICATION OF A LUNG-SCALE MUCOCILIARY AND ABSORPTIVE CLEARANCE MODEL

We continue the study of identifiability and observability in systems with a case study of *in vivo* clearance model of [chapter 2](#). Data for the model comes from a more recent clinical trial involving patients with Cystic Fibrosis (CF). The trial involved determining the efficacy of slow (as opposed to orally inhaled), continuous, overnight delivery of nebulized hypertonic saline (HS) through a nasal cannula. This follows from unpublished findings that reducing the deposition rate of HS can prolong airway surface liquid (ASL) hydration in human bronchial epithelial cell cultures. HS has been shown to be effective in treating the mucociliary clearance (MCC) and ASL hyperabsorptive defects that bring about CF lung disease [1, 8, 22].

The trial examined clearance every 2 minutes for the first 90 minutes following the inhalation of Tc<sup>99m</sup>-Sulfur Colloid (TcSC) and In<sup>111</sup>-DTPA (DTPA) as described in [8]. Additional images were obtained at 180 and 360 minutes to assess whether MCC in the distal lung, which is known to be slow [1] could be determined from later data points. The result is an extended-duration, though more sparsely measured, data set than that of [1]. MCC was determined from functional imaging of Tc-SC clearance, as it is a large particle that is not absorbable into the bloodstream. Absorption (ABS) was determined as the normalized difference between Tc-SC and DTPA retention. Initial counts in the central ( $C_0$ ) and peripheral ( $P_0$ ) lung were also estimated for both TcSC and DTPA.

Parameter identification was performed via two methods. The first utilized APT-MCMC [173]. This approach requires simultaneous optimization of the MCC and ABS parameters, making the model unobservable for DTPA. The second employed a variation of the PyM-

PLE package in the pyomo.dae environment that was modified to allow for the sequential MCC then ABS parameter identification scheme described in [chapter 2](#). This section will focus more on the comparison of the two methodologies than the study result itself, which was null. We find that both methods, despite differences in observability and tradeoffs in terms of computational cost and information gained, are generally capable of identifying the model with similar results in untreated patients with CF. However, the observability and deterministic nature of the pyomo.dae model structure provide better computational performance.

#### 4.5.1 Problem Formulation

**4.5.1.1 APT-MCMC** Because the APT-MCMC algorithm is stochastic, there is no way to perform an unbiased sequential optimization routine in the same manner as the deterministic method used in [chapter 2](#). That is, there is no way to determine optimal MCC parameter ( $k_{LT}$ ,  $k_{DL}$ , FFCA) values prior to the generation of the posterior likelihoods. Only a combinatorial search involving each parameter set from the MCC posteriors could supply an unbiased basis for the ABS parameter search, and that would be far too computationally expensive. Instead we pose the following objective function for fitting whole lung clearance of TcSC and DTPA to the equations [2.3-2.7](#) for each probe simultaneously:

$$\begin{aligned}
 \min_{\underline{\theta}_F} \quad & \sum_{p=1}^P \sum_{i=1}^2 \sum_{k=0}^{46} \frac{1}{\sigma(k)^2} (\hat{y}_i(t_k, \underline{\theta}) - y_{p,i}(t_k))^2 \\
 \text{s.t.} \quad & \theta_i^L \leq \theta_i^* \leq \theta_i^U \quad \forall i \in \Theta \\
 & y_i = L_{F,i} + L_{N,i} + D_i \quad \forall i \in Y
 \end{aligned} \tag{4.4}$$

The SSE is obtained on the HS day and also the control day for P=12 matched patients over 47 time points. APT-MCMC allows for parameter bounds, which is the first constraint. Finally there is the algebraic relationship between the whole-lung clearance of TcSC and DTPA. APT-MCMC automatically performs a log-transform of the states and the data for evaluation of the objective function. The algorithm was run with 100 “walkers” on each of four chains. Walkers were allowed 25 steps before a swap was executed between chains,

and 10000 swaps were performed for each optimization attempt for a total of  $10^8$  model simulations.

**4.5.1.2 PyMPLE** The objective function in `pyomo.dae` is similar to that of APT-MCMC, with the addition of constraints related to the backward finite difference solution and the partitioning of  $\underline{\theta} = \{\underline{\theta}_{TcSC}, \underline{\theta}_{DTPA}\}$ . The deterministic nature of `pyomo.dae` allows for the minimization of the objective for TcSC first for the MCC parameters:

$$\begin{aligned}
\min_{\underline{\theta}_{TcSC}} F & \sum_p^{12} \sum_{k=0}^{46} \frac{1}{\sigma_k^2} (\hat{y}_{TcSC}(t_k, \underline{\theta}_{TcSC}) - y_{p,TcSC}(t_k))^2 \\
\text{s.t.} & \quad x_j(0) = g(0) \quad \forall j \in X \\
& \quad \frac{dx_{j,f}}{dt} = \frac{x_{j,f} - x_{j,f-1}}{\Delta x_{j,f}} \quad \forall j \in X, f \in E \\
& \quad \Delta x_f = A(\underline{\theta}_{TcSC})x_f \quad \forall j \in X, f \in E \\
& \quad \theta_{TcSC,i}^L \leq \theta_{TcSC,i}^* \leq \theta_{TcSC,i}^U \quad \forall i \in \Theta
\end{aligned}$$

The first constraint requires that the initial condition of each state is a function,  $g$ , of the dosing parameters. The second constraint is the backward finite difference constraint for every state  $j$  in  $X$  at every element  $f$  in  $E$ . The third is the difference approximation to the state equations at each element. A similar problem is then posed for the DTPA data and the ABS parameters:

$$\begin{aligned}
\min_{\underline{\theta}_{DTPA}} F & \sum_p^{12} \sum_{k=0}^{46} \frac{1}{\sigma_k^2} (\hat{y}_{DTPA}(t_k, \underline{\theta}_{DTPA}, \underline{\theta}_{TcSC}) - y_{p,DTPA}(t_k))^2 \\
\text{s.t.} & \quad x_j(0) = g(0) \quad \forall j \in X \\
& \quad \frac{dx_{j,f}}{dt} = \frac{x_{j,f} - x_{j,f-1}}{\Delta x_{j,f}} \quad \forall j \in X, f \in E \\
& \quad \Delta x_f = A(\theta_{DTPA}, \theta_{TcSC})x_f \quad \forall j \in X, f \in E \\
& \quad \theta_{DTPA,i}^L \leq \theta_{DTPA,i}^* \leq \theta_{DTPA,i}^U \quad \forall i \in \Theta
\end{aligned}$$

The difference in formulation between APT-MCMC and PyMPLE provides an interesting comparison between the performance of a global solver in an ill-posed case and a local solver under better conditions.

#### 4.5.2 Model Fit to Data

The ODE models were fit to the data and likelihoods were generated using APT-MCMC. The resulting ensembles and median trajectory for TcSC and DTPA clearance on the HS and control (Sham) days from the APT-MCMC experiments are shown in Figure 4.8.

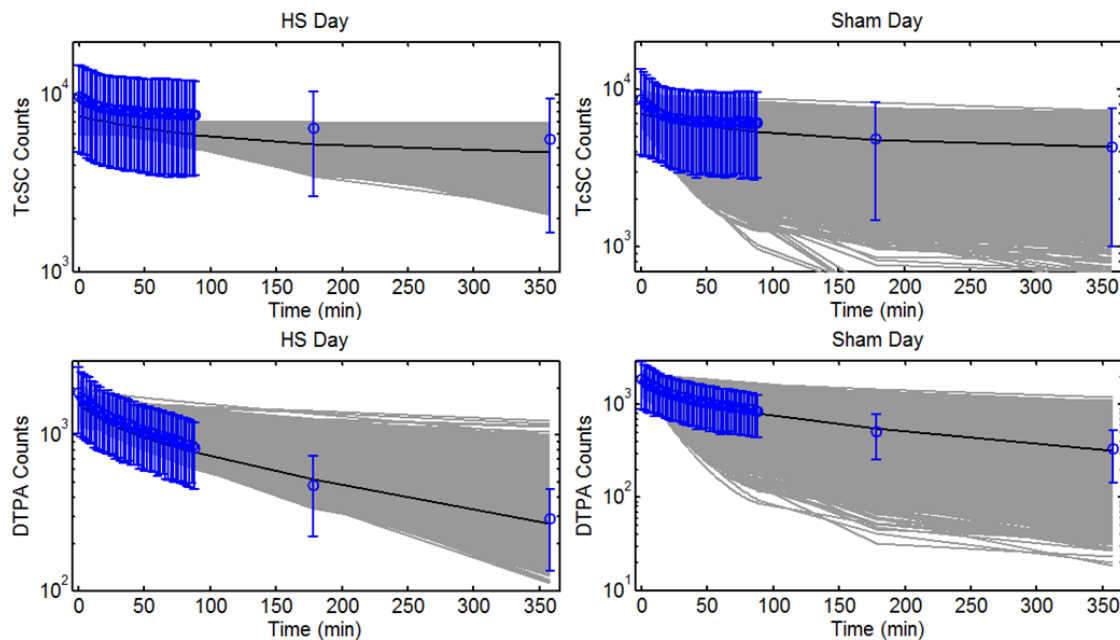


Figure 4.8: APT-MCMC ensembles of whole-lung TcSC (top) and DTPA (bottom) clearance. Model estimates capture the data and variance (mean+ SD). Ensembles are a random selection of  $10^5$  APT-MCMC simulations of  $10^6$  total post-burn-in.

Ensemble medians are in generally good agreement with the data. The low estimate for TcSC on the HS day is mostly due to one patient with high deposition. They were not excluded from the fitted data for matching purposes with the Sham day. The variance of the ensemble is in good agreement with the data except for the TcSC-HS case where the

same high-deposition patient was the only patient with a manifestly different profile than the others. Model fits via APT-MCMC are acceptable on the whole.

In accordance with the methodology outline in Figure 4.1, the model was also fit using `pyomo.dae` and the solver `ipopt` to determine a single set of optimal parameter values. Model output and fit to data are shown in Figure 4.9.

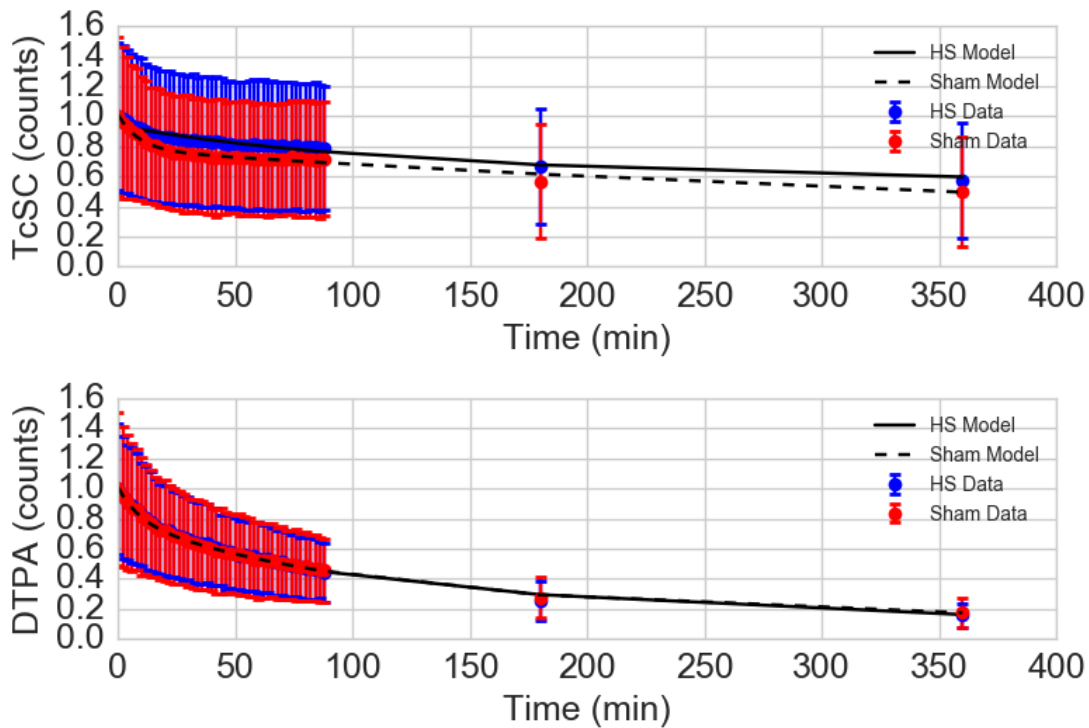


Figure 4.9: Pyomo estimates of TcSC (top) and DTPA (bottom) clearance. Model agreement with data is strong. Of note is the similarity between data sets, indicating the null result of the clinical trial.

The `pyomo.dae` fit is in strong agreement with the data on both study days. The model was not fit to normalized data, but they are presented in this manner to show the strong similarity in clearance due to both MCC and absorption on both study days. TcSC fits on the HS day produce a low estimate of initial TcSC counts for the same reason as APT-MCMC; one patient had a high deposition day that was not reflected in other patient data sets. Fits via `pyomo.dae` are also acceptable.

### 4.5.3 Comparison of Likelihood Estimates from APT-MCMC and PyMPLE

Herein the maximum likelihoods and likelihood functions calculated for each parameter in the lung clearance model are compared. APT-MCMC has the benefit of computing the entire likelihood function at the same time that it performs the parameter search. It also provides information that can be used to determine marginal distributions, which cannot be obtained from profile likelihoods. However, the profile likelihoods are typically faster to compute. Regardless, it is first useful to compare the estimated likelihoods for both methods before analysis of their computational performance. Such a comparison is given for the large airway parameters in Figure 4.10. Optimal values and algorithm performance metrics are given in Table 4.2

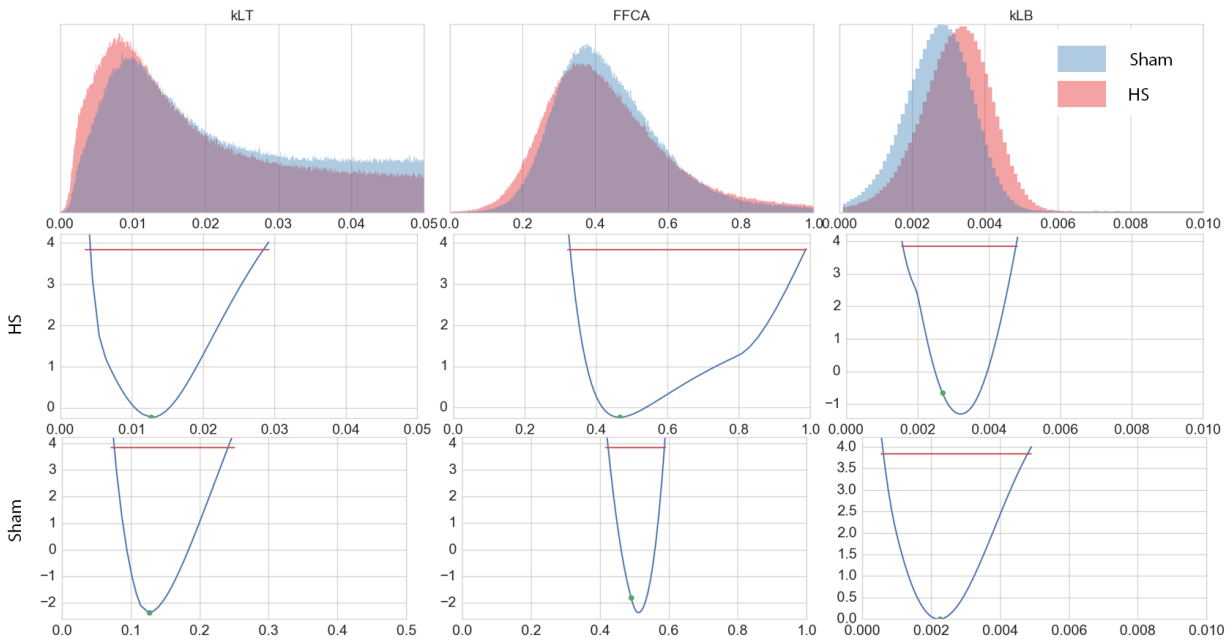


Figure 4.10: Large airway clearance parameters and their APT-MCMC distributions (top row) or profile likelihoods for HS (middle) and Sham (bottom) days. Agreement is strong in all cases for both methods except for  $k_{LT}$  on the Sham day (bottom left). This difference is likely due to a single anomalous patient that drives underestimation by APT-MCMC on the Sham day on population grounds. A lack of difference between days indicates ineffective treatment for promoting large airway clearance.

Table 4.2: Kinetic parameter estimates for MCMC and PL (as maximum likelihood) techniques. Deposition parameters were also estimated. Literature values are from Markovetz et al. [1] where trust-region-reflective estimation was used. Time to convergence is given for each method. APT-MCMC is parallelizable, but the estimations for both APT-MCMC and PL occurred on a single 2x Xeon core.

	Day Source	or	$k_{LT} \times 10^2$ ( $min^{-1}$ )	FFCA	$k_{LB} \times 10^3$ ( $min^{-1}$ )	$k_{DL} \times 10^3$ ( $min^{-1}$ )	$k_{DB} \times 10^3$ ( $min^{-1}$ )	TcSC L0/D0 (C/P)	Time (min)
MCMC	HS		0.83	0.35	3.37	2.27	1.77	1.03	299
	Sham		1	0.38	2.77	2.07	1.75	1.35	310
PL	HS		1.23	0.43	3.41	2.94	84.2	1.26	19.2
	Sham		12	0.52	2.66	4.4	7.13	0.87	13.9
Lit.	[1]		3.5	0.53	-	2.8	1.8	1.5 1.3	-

Parameters are identifiable by both methods. They also agree on nearly every estimated parameter except for  $k_{LT}$  on the Sham day, which is estimated to be an order of magnitude greater than other values for that parameter. With respect to the model dynamics and those apparent in the data, this larger value seems more reasonable (the pyomo.dae model fit to TcSC on the sham day is excellent). It may simply be, then, that one individual with much slower clearance dynamics biased the model fit on the HS day for both APT-MCMC and pyomo, resulting a lower estimated value of  $k_{LT}$ . Regardless, the high degree of overlap between most of the likelihood estimates for large airway parameters is an encouraging result.

A similar illustration is presented in Figure 4.11 for the two D parameters,  $k_{LB}$  and  $k_{DB}$ . The likelihoods for  $C_{Tc}$ , the initial TcSC counts in the central region of the imaging scan as defined in [8], are also given.

The distal airway parameters have a clear maximum likelihood as estimated by APT, but are only identifiable by PyMPLE. This is again likely due to the observability of the system. Weak identifiability of  $k_{DB}$  in the HS day is evident in the distributions and the spread of its PL. This may be due to HS producing a hydration effect in the distal lung [1] that is confounded with the relatively slow estimate of  $k_{LT}$ .  $C_{Tc}$  was bounded more tightly in the pyomo.dae (data mean $\pm$ SD) solution than in APT-MCMC. However, poor performance

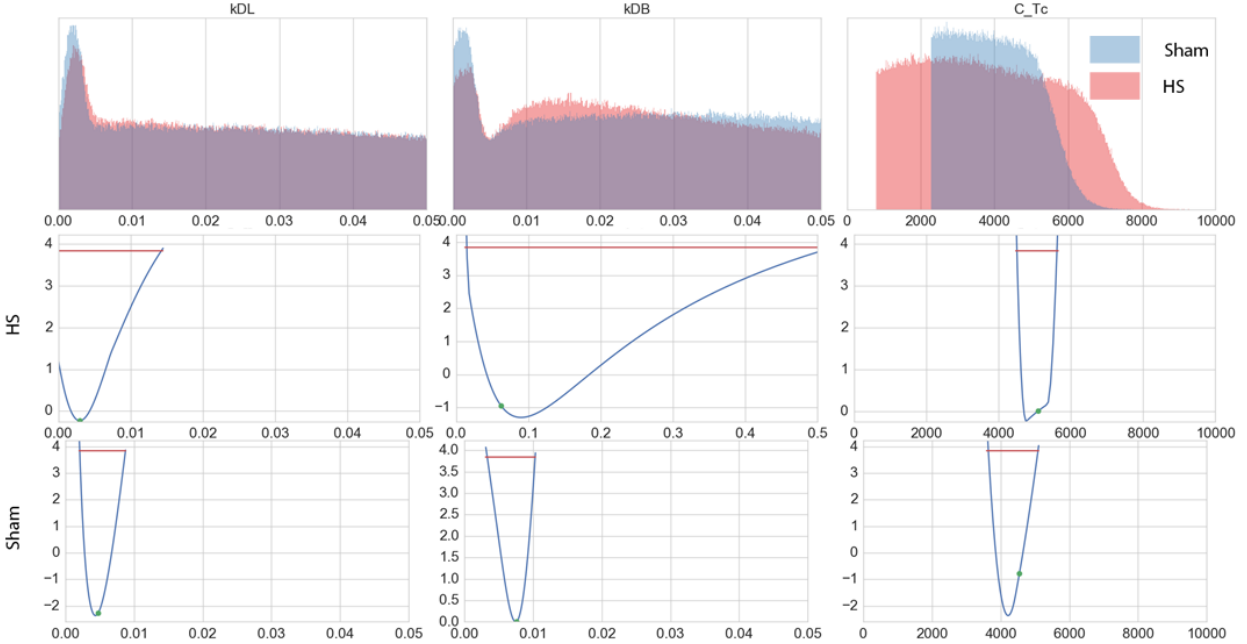


Figure 4.11: Small airway clearance parameter and initial TcSC central deposition (right column) estimates. Agreement is strong except for  $k_{DB}$  on the HS day, which is likely a compensation for the slow MCC brought about by the small values of  $k_{LT}$  estimated for HS. Distal MCC constant  $k_{DL}$  is identifiable in the Sham case using PyMPLE. Deposition estimates are much less variable using PyMPLE.

of APT-MCMC in estimating the deposition is further evidence that the observability of the PyMPLE model is beneficial, since observability is a state property. This notion would also explain the differing estimates for the deposition parameters that are illustrated in Figure 4.12.

While consensus is shared between the maximum likelihood estimates of APT-MCMC and PyMPLE, the shapes of the likelihood functions for deposition values do not agree between methods. Particularly, peripheral deposition values ( $P_{Tc}$  and  $P_{In}$ ) are practically unidentifiable in APT-MCMC case, whereas all parameters are identifiable using PyMPLE. The bimodality in  $P_{Tc}$  and the discontinuity in  $P_{In}$  profiles in the HS case are known to arise in cases with insufficient data [134]. This is a reasonable explanation in the case of initial

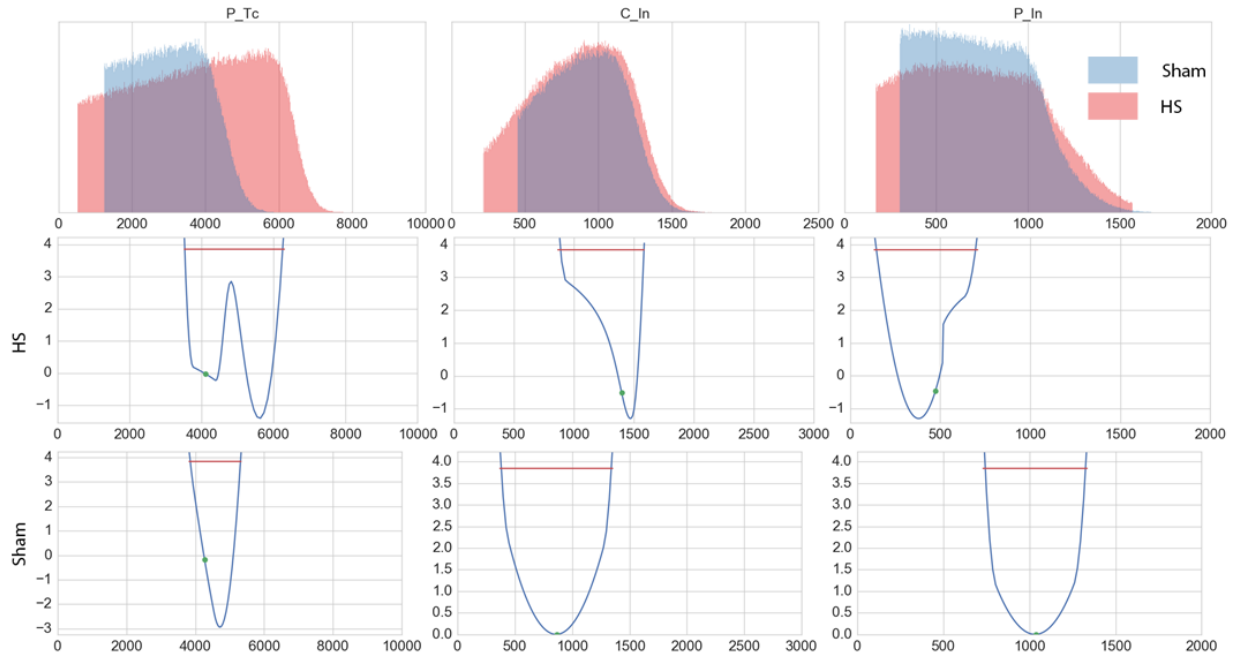


Figure 4.12: Initial TcSC peripheral (left column) and DTPA deposition estimates. Agreement is good in terms of maximum likelihood estimates, but likelihood shape agreement is varied.

conditions because of the small sample size for each study day. Even still the identifiability of these parameters is notable.

#### 4.5.4 APT-MCMC and PyMPLE Comparison

In general both methods, APT-MCMC and PyMPLE, were in agreement about optimal parameter values. However, PyMPLE outperformed APT-MCMC in terms of demonstrating the practical identifiability of clearance and deposition parameters. Admittedly, the design of the clinical trial favors PyMPLE, given that an observable model structure cannot be formulated for APT-MCMC. PyMPLE computationally outperformed APT-MCMC. This is demonstrated in Table 4.2 by order-of-magnitude improvements in terms of completion speed. It should be noted again that APT-MCMC is a highly parallelizable algorithm, but fairness in benchmarking required operation on a single core for comparison with PyMPLE.

Parallelization would obviously improve completion time for APT-MCMC, possibly reducing times to nearly identical values. However, each profiling operation in PyMPLE is independent from the others, providing an opportunity for parallelization that will be implemented in future versions of the code. Even so, the benefits of APT-MCMC include estimates of parameter-parameter correlation that can greatly aid in model reduction efforts when dealing with models of greater complexity than this parsimonious model [186].

## 4.6 SUMMARY

Overall, these case studies should demonstrate that observability is critical to identifiability. Even in the case where  $10^6$  simulations in a global solver (APT-MCMC) are performed, parameter identification is hindered by state unobservability. The global solver was outperformed by local optimization in the `pyomo.dae` environment using the `ipopt` solver (a local optimizer) and likelihood estimation via the PyMPLE package. In fairness, the marginal distributions and other meta-parametric results from MCMC methods are often useful. They provide a wealth of population based information that profile likelihoods cannot. Thus, given our findings we conclude with the following. Profile likelihoods are a useful and rapid means to assess practical identifiability and may also be useful to precondition stochastic global solution algorithms in the case that more populational information is desired. Furthermore, experimental design is critical to model performance. This is not a new concept, but we believe that our examples add emphasis to the similar statements made by others in this field, particularly those who perform optimal experimental design [185, 187, 188], which we have not covered here. Finally, we have developed an open source means of assessing both the identifiability of dynamic models. The PyMPLE package, the utility of which has been demonstrated in this chapter, is free to use for anyone.

## 5.0 SUMMARY AND FUTURE WORK

### 5.1 CONTRIBUTIONS

This dissertation presents mathematical models of airway transport processes at multiple scales and the disease that subsequently arises in the lungs of patients with Cystic Fibrosis. Particularly, these models have focused on identifying and understanding the hyperabsorption of the small-molecule probe DTPA in CF cell cultures and airways and the relationship between its hyperabsorption, airway dehydration, and MCC failure. Models of lung-scale hyperabsorption and MCC were developed and analyzed. The outcomes indicated that increases in the model parameter defining the fraction of functional ciliated area (FFCA) in the airway were associated with improvements induced by HS inhalation therapy. The need to better understand the mechanisms of DTPA hyperabsorption at the lung scale motivated the development of a cell-scale model of liquid and solute transport. This model suggests that DTPA hyperabsorption is due to increased paracellular liquid absorption in CF. It has also been used to explore modes of treatment failure and options for remediation. Finally a model parameter identification package was developed within the Pyomo modeling environment that will provide rigorous model identification and dose-schedule optimization programs within the same coded framework.

#### 5.1.1 Lung-scale Model of MCC, ABS, and Treatment Response

A number of PK models exist for inhaled therapies [101, 104, 105, 106, 107, 108, 109, 110, 111, 112], but only a few [116, 118] provide physiological detail regarding clearance differences in lung regions. The two-compartment lung model of Sakagami was successful in fitting

functional imaging data of whole-lung clearance from the study by Locke *et al.* [8] but could not be reconciled with data regarding regional specificity. A new model structure was proposed that partitioned the large airways that are the source rapid MCC dynamics into sections with and without functional MCC. This partition coefficient, FFCA, was estimated with other clearance parameters and found to allow model agreement with dynamic and regional deposition imaging data [1].

The validity of adding such a parameter was tested experimentally via a newly developed imaging algorithm in airway cell cultures. It was shown that hydration increases the FFCA observed in cell-cultures and has a saturating dose-dependency [1]. *In vivo*, the model structure best depicting the imaging outcomes included increases in FFCA associated with HS inhalation and rate constants for mucus clearance from the large airways that were otherwise similar in treated and untreated CF subjects and controls. Thus the inhalation of an osmotic treatment appears to recruit new regions of previously inactive or halted cilia rather than increasing the ciliary beat frequency. Absorption in large and distal airways was found to have an increased rate constant for all CF cohorts, but the rate constant for distal absorption,  $k_{DB}$  was decreased by HS treatment. Due to the similarity in scale between the MCC rate constant in the distal airways  $k_{DB}$  and the duration of the imaging study,  $k_{DB}$  was not identifiable as different from 0. The model itself provides a rapid method of assessing the efficacy of hydrating therapies, and the FFCA assay developed for use in cell-culture may be useful as a high-throughput marker for prospective therapies. Finally, characterizing DTPA absorption provides a potential surrogate for liquid absorption and also provides a potential estimate of the clearance of chemically similar inhaled small molecule therapeutics. The model may thus be useful as a detailed PK model structure for other inhaled compounds.

### 5.1.2 Cell-scale Model of Airway Liquid and Solute Transport

Some attention has been given to the modeling of airway transport at the cellular scale. Much of this interest is directed at the study of ion-transport in the Ussing Chamber [?, 16, 17, 87, 88, 89]. While the Ussing Chamber remains an essential experimental device in the field of epithelial transport, it requires flooding of the lumen of cultured cells [32]. For airway

epithelia this is not physiologically accurate. HBE cells transport ions and liquid in concert in order maintain a sufficient ASL volume at the air-liquid interface. Models of this “thin-film” condition have also been developed with varying degrees of detail and focus [70,96]. However, none so far have accounted for paracellular transport while accounting for multiple ions and ion transport proteins relevant to CF. The cell-scale model presented in this dissertation is meant to fill this gap in the literature.

Furthermore, the model is intended to explain in detail why DTPA is hyperabsorbed in both the CF lung [8,65] and in CF HBE cells [21]. The physiologically relevant parameterization and structure of the model revealed two transport pathways as possible culprits. First, constitutive  $\text{Cl}^-$  permeability, hence transport, is predicted to be decreased in CF cells. This result is similar to the implications that Bertrand and colleagues have made regarding SLC26A9 function in CF [3]. The second is that paracellular hydraulic permeability and liquid transport, thus solute convection, are greatly increased in CF cells. This could possibly be due to irregular interactions between CFTR and structural proteins [141,189] or inflammation [140], or a combination of the two. Exploration of how CFTR interacts, via indirect signaling, its PDZ motif, or by other means with other proteins and how those interactions affect cell structure and transport is warranted in order to better understand these predictions.

While the cell-scale model provides predictive insight regarding the origins of hyperabsorption in CF, it can also be used to study other processes that involve perturbation of the ASL. In the case of osmotic therapies, the model can be used to predict and design successful treatments as well as diagnose failure modes for unsuccessful therapies. The latter was applied to explain the most likely cause of a failed clinical trial for nasal, overnight delivery of 7% HS. Orally inhaled HS is a standard of care in CF, but has been shown to have a transient affect in improving MCC [156]. *In vitro* experiments [150,152] have shown that extended delivery periods at a slower rate provide extended hydration duration and better epithelial response. By administering HS nasally overnight, it was thought that the same effects could be achieve in patients. The study result thus required an explanation. Of all possibilities, insufficient HS deposition was found to be the most plausible explanation, including greater than predicted  $\text{Na}^+$  absorption. Possible model-predicted solutions to ad-

dress this failure mode were explored. One predicted solution required an increase in HS concentration to 14%. Modifications to delivery protocol were also suggested. By combining a priming step of rapid oral HS inhalation to prehydrate the airways with an immediately subsequent overnight treatment involving nasally administered HS, hydration is predicted to persist for the entire treatment period. The same effect can be achieved with a 20% mannitol solution, which would likely absorb more slowly from the airways potentially extending the duration of the therapeutic effect. These dose designs have not yet been optimized, but they could be posed in such a manner as to allow for optimal scheduling and dose rates.

### 5.1.3 Pyomo Model Profile Likelihood Estimation (PyMPLE) Package

Model identification is a critical aspect of systems research in general, with systems biology and medicine being no exception [134, 158, 160, 168, 175, 185]. The ability to confidently predict and bound system dynamics is vital when modeling systems as complex as those in biology. It would be otherwise impossible to design robust treatments without a characterization of system uncertainty. Assessment of the practical identification of model parameters can be performed via a number of methodologies, both deterministic [134, 168, 175] and stochastic [142, 166, 168]. Stochastic methods, such as APT-MCMC, can provide excellent characterization of globally optimal parameters and their practical identifiability. More importantly they can provide information regarding parameter-correlations. However, they are generally more computationally taxing and operate on black-box models [166]. Deterministic methods can suffer from identification inaccuracies inherent to nonlinearities in biology but have the advantage of providing a direct relationship between model structure, dynamics, and parameters [168].

This dissertation has presented a deterministic modeling tool for parameter identification. The Pyomo Model Profile Likelihood Estimation (PyMPLE) package exploits the open-source and high performance Pyomo optimization environment, particularly the recently developed `pyomo.dae` package and its utility in optimizing dynamic models. PyMPLE is implemented as a Python class object. Its identification method employs the profile likelihood [134] as a means of determining the practical identifiability of model parameters.

The method allows for the calculation of confidence intervals (from the profiles themselves) and the generation of an ensemble of model state trajectories during the profiling procedure.

The capabilities of PyMPLE were demonstrated in two case studies. In the first, reaction rate constants were profiled for the Van de Vusse reaction [181] carried out in a CSTR. The case study showed that PyMPLE is capable of accurately estimating and profiling the three parameters of the model in a well-posed case with ample data. This case also used the estimation algorithm and graphing methods in PyMPLE to illustrate the dramatic effect that a data-sparse problem can impose on the quality of the estimates of model states. The second case study compared the stochastic APT-MCMC algorithm [173] to PyMPLE for estimating and identifying the parameters of the MCC and ABS model from [1]. For this relatively compact model, PyMPLE provided faster estimates and demonstrated practical identifiability of all parameters. This includes the slow, distal-to-large airway MCC constant  $k_{DL}$  that was previously unidentifiable in patients with CF [1], though it lacks the parameter-parameter correlation information that can be obtained from APT-MCMC. These two examples combine to illustrate the utility of PyMPLE for parameter estimation in dynamic and static models in Pyomo.

## 5.2 FUTURE WORK

The above work represents the first efforts in collaboration to bring the analytical and design utility of systems biology and medicine into the field of Cystic Fibrosis research. It is intended to be a part of the groundwork for addressing the treatment of patients with CF in a rigorous, patient-specific manner. The following are suggestions for ongoing or future work in CF systems medicine.

### 5.2.1 Updates and Maintenance of PyMPLE

As an open source language, effort is expected to be made by Python users toward making software freely available to the community. For that reason, PyMPLE will ultimately be

made available on a code repository such as GitHub. Prior to distribution, a few key updates should be made to include better error checking and exception handling. Presently the `PyMPLE.get_CI` method only catches errors thrown in the solver call via a general statement that stops the current branch of the profile and moves to the next. Catching specific errors and returning information to the user should be implemented shortly. A “second-chance” method that does not immediately exit the profile branch might be useful for situations where sharp non-convexities exist in the profile that pose a difficulty for most solvers.

### 5.2.2 Additional Components in the Cell-scale Model

The parsimony of the cell-scale model presented in this dissertation is one of its appealing traits. However, ions other than  $\text{Na}^+$  and  $\text{Cl}^-$  may also play an important role in cell-volume and ASL homeostasis, particularly in other disease states. Manzanares and colleagues [51, 190] have indicated that  $\text{K}^+$  transport is an important component for ASL hydration in CF and non-CF cells. It also has implications in asthma [51] and inflammation.  $\text{K}^+$  could be added as a model state in each compartment [16, 17]. Additionally, many of the cellular ion transport pathways are pH dependent [?]. Characterization of pH would require the addition of  $\text{H}^+$  and  $\text{HCO}_3^-$  as model states. Other more specific anion channels such as TMEM16A [191], SLC26A4 (pendrin) [33], and a directed focus on SLC26A9 [3] could be useful as well. The addition of these components to the model has been attempted with success in fitting model training data. However, difficulty ensuring numerical stability (see [?, 88]) alongside physiological state dynamics and steady state concentrations was evident in simulation results that used the basic descriptions of ion transport from the cell-scale model when more species than  $\text{Na}^+$  and  $\text{Cl}^-$  are added.

More success has been achieved in adding  $\text{K}^+$  to the model when also adding complexity to the model terms describing ion transport. When using the NKCC and Na-K-ATPase terms from [53] and [54], respectively, the model is able to fit the training data, though not as well as in chapter 2. APT-MCMC was used with penalties added for severe excursions from homeostatic cell concentrations. Model fit to data with the equations are given in Appendix B.

Garcia *et al.* made considerations for feasible search spaces given electrophysiological relationships and assumptions regarding paracellular permeabilities that allowed them to avoid the numerical cost associated with the solution of the algebraic electrical relations (see [16] and its supplement). The cell model in this dissertation currently uses the Stokes-Einstein diffusion coefficients as a basis for dynamic paracellular permeabilities, so adoption of a similar approach may provide more accurate results than the penalties applied above. However, the assumption of paracellular permeabilities may be inadvisable given the implied susceptibility of the paracellular space to changes in parameter values in CF from the cell model result in this dissertation. Another approach is to solve the DAE system using `pyomo.dae` and `PyMPLE` to estimate parameters including paracellular permeabilities. These estimates could then inform a set of APT-MCMC simulations given more rigorously obtained values for paracellular permeability. Such a model could be useful for studying either Ussing Chamber or thin-film in open or short-circuit conditions.

### 5.2.3 Optimal Treatment Design at the Cell-scale

The resorption of the ASL begins as soon as an inhaled treatment is completed. Assuming that greater than minimum necessary hydration was achieved and that there is a range of ASL volumes at which MCC can occur, there will be a period of time that MCC will be improved even as ASL volume recedes. This range of ASL volumes is referred to as a therapeutic window in pharmacokinetic (PK) studies, and is useful for treatment design. The CF curve in Figure 5.1 is helpful in illustrating the therapeutic window concept using bolus additions of isosmotic Ringer’s as “treatments.”

If the SEM about the final non-CF ASL volume is taken to be the therapeutic window, then the dosing schedule in Figure 5.1 is successful in maintaining therapeutic efficacy. The model response in the CF case has not been formally optimized, but it does achieve therapeutic window maintenance in addition to a number of other quality of life improvements: there are relatively few treatments per day, which is good for patient convenience, and treatments occur no more frequently than every four hours. Because we have a mathematical model of the ASL volume regulatory system, a treatment objective, and heuristics that can

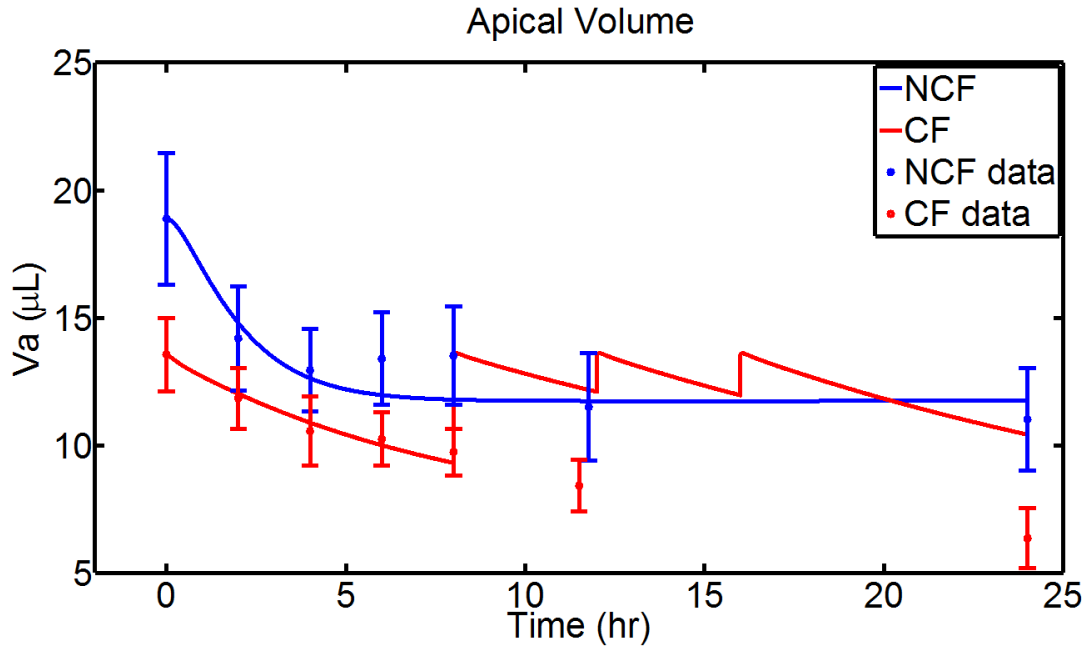


Figure 5.1: Unoptimized dosing strategy for maintaining CF ASL volumes within the SEM window about the HBE final volume. A bolus is given initially and starting at 8 hours three successive hydrating boli every four hours maintain ASL hydration above the non-CF steady state volume. Other conditions are identical to the training case of Figure 3.3

serve as formal constraints we may pose the dose scheduling problem in formal optimization language. The ODE model and its interaction with decision variables is nonlinear and the number of doses is an integer variable, making this a mixed-integer nonlinear programming (MINLP) problem. Even under the relaxed case of partial dosing (instead of at a prescribed amount), the ODE framework of the model requires that the drag variables in the paracellular space be binary, which also adds a mixed-integer component to the problem. This problem, given yet without solution, can be posed as equation 5.2.3.

$$\min_{N(k)} \sum_{k=0}^K \frac{1}{\sigma_{\epsilon(k)}^2} (\hat{V}_{A,CF}(\theta, u(t_k)) - V_{A,NCf}(\infty) + \lambda)^2 + \Gamma_D N$$

s.t.

$$\frac{dx}{dt} = Ax(t) + Bu(t, N)$$

$$y(t) = Cx(t)$$

$$Window_{lower} \leq \lambda \leq Window_{upper}$$

$$N \leq 6 \quad N = 0, \dots, 6$$

$$t_k - t_{k-1} \geq 4 \quad t \in \mathbb{R}$$

Here  $\lambda$  is a slack variable that allows for some window about the non-CF steady state volume.  $N$  is the number of treatments per day, which cannot exceed six. And the treatment at time  $k$  can be no closer to the previous  $k$  than 4 hours. The formulation is similar to the zone-control formulation of Muske and Rawlings [192]. Modeling-specific languages like Pyomo can use solvers like ipopt to solve problems of this class efficiently and rigorously.

#### 5.2.4 Individualized Patient Characterization and Treatment

While much of this work has focused on fitting models to whole samples of patient data, individual patients differ in terms of disease severity and treatment response. Part of the variability is certainly due to the variation present in the more than 2,000 known mutations in CFTR [45]. However, there is also known variation within patient subpopulations of the same genotype. This is illustrated in Figure 5.2 where the cell-model is fit to ASL volume and DTPA data in cells cultured from individual patients after lung transplant.

Model parameters were fit within a five-fold range of the nominal CF parameter set for the cell model. All patients have the most common mutation,  $\Delta F508$  ( $\Delta F$ ), on at least one allele. Homozygotes for  $\Delta F$  (left columns) are known to have significant lung disease, but the two homozygotes in Figure 5.2 have characteristically different ASL absorption dynamics from each other with similar DTPA absorption profiles. Patients with a G85E mutation are expected to have severe disease, and these patient cells are similar in ASL and DTPA dynamics to the top  $\Delta F$  patient. The patient with the often less severe G551S

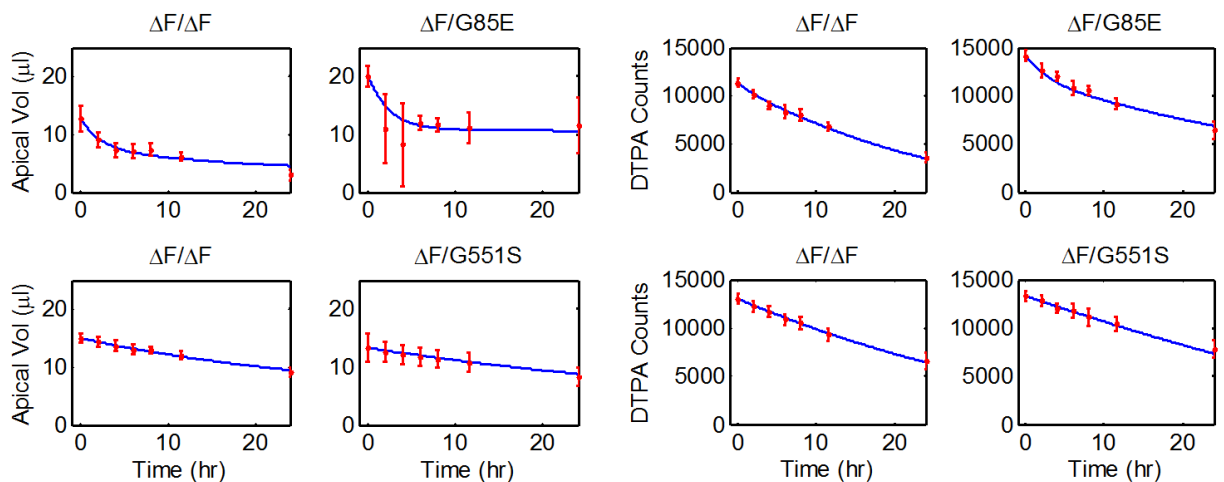


Figure 5.2: Volume absorption (left) and DTPA absorption (right) in cell cultures varies across and even within patient genotypes (panel titles as allele 1/allele 2).

mutation is similar to the other, less absorptive  $\Delta F$  patient. Ivacaftor is now available to patients with this and other gating mutations and the ivacaftor-lumacaftor combination is available to  $\Delta F$  homozygote patients [40]. However, the benefit of the osmotic therapies that have been examined in this dissertation is that they are mutation agnostic, and can be applied to any patient with a dosing schedule that could theoretically be tailored specifically to them. This gives rise to the notion that the cell-scale and lung-scale model may be used in concert to determine absorption and MCC characteristics associated with genotypes and individual-specific phenotypes.

This is the focus a recently awarded NIH grant (U01HL131046) award that used some of the modeling results presented in this dissertation as preliminary findings in support of the application. That study will use human nasal epithelial (HNE) cells from patients with CF and single-mutation biological parents of the CF subjects to inform a cell-scale model of individual absorption characteristics. HNE cells are ciliated and similar to other epithelial cell types in experimental and modeling results [17, 93]. The HNE results will be compared to functional imaging MCC and ABS measurements to determine possible bench-to-clinic correlations.

A similar comparison between HNE and imaging data and modeling will also be made using measurements obtained from a clinical trial comparing inhaled powdered mannitol to 7% HS as a therapy for CF. Mannitol has been demonstrated to increase MCC in patients with CF [136], and is an approved therapy in Europe and Australia. The cell model results have suggested that mannitol may be a more durable therapy than HS, and if that were demonstrated through *in vivo* studies it would be an important validation of the utility of the cell-scale model. However, the ultimate goal of the comparison between cell and lung-scale results is the development of a multi-scalar model-based treatment design and decision support system to personalize treatments for patients with CF. Such a decision support system would be implemented with the very same goal as the entirety of this dissertation: to provide full health and quality of life for each and every patient with Cystic Fibrosis.

## 6.0 MIXED-METHODS ANALYSIS OF THE EFFECT OF CUSTOMER VOICE ON PRODUCT DESIGN

### 6.1 INTRODUCTION

Success following graduation now requires more than just technical savvy from engineering students [193]. Engineers entering the workforce today must be more than technically proficient. They must be able to exhibit qualities similar to an entrepreneurial mindset, (i.e. the ability to work in a dynamic, creative, team-based environment while remaining aware of current and future market demands for a given class of products) [194, 195]. Purzer and colleagues [195] note that this mindset translates to an awareness of the societal value of a product within a self-efficacious and leadership focused perspective regarding the design task. Though the definition of an entrepreneurial mindset varies to some extent, each of these traits has been identified as an element of such a mindset, and regardless of definition, much focus is being directed toward instilling an entrepreneurial mindset in engineering students [193, 194, 196, 197, 198]. Companies require innovative thought, personal initiative, and market awareness from the incoming workforce to stay competitive [199]. Meeting this challenge requires creative and critical thought and adaptability to the ever-changing needs of the customer base, which are essential components of the entrepreneurial mindset [200, 201, 202]. Indeed, it is imperative that the entrepreneurial mindset be fostered in the engineering classroom [203] for either entrepreneurial or “intrapreneurial” (i.e. the entrepreneurial tendencies of an employee within a company that they do not own) purposes [204, 205]. For this reason, it is crucial to gain an understanding of how different pedagogical methods can further the development of an entrepreneurial mindset in students while still in the college environment. Byers *et al.* [193] suggest encouraging creativity, flexibility, and technical

acumen to foster entrepreneurial tendencies, whereas Kriewall and Mekemson [202] suggest that acquaintance with business principles including meeting customer needs is essential to developing entrepreneurial engineers. Bodnar, Clark, and Besterfield-Sacre [194] through a literature review were able to capture an engineering-specific definition of entrepreneurial mindset. Particular to this definition is the notion that engineers must also account for technical aspects in addition to market demands when approaching design. In the present work, the focus is on a pedagogical method of increasing awareness of customer needs at an early stage of engineering education.

The field of entrepreneurship education, specifically in engineering, is relatively young [196, 203]. However, much focus has been given to understanding the customer voice since Akao (1978) first opened the door to that concept nearly 50 years ago [206, 207, 208]. Producing a technically sound design that meets customer needs is one of the great challenges of engineering product design. Lin and colleagues [209] have stated, “Understanding customer voice and enhancing design characteristics which meet customer requirements and thus increase product competitiveness are the challenges for designers.” Furthermore, it must be understood that the map between a potential user’s mental model and the designer’s concept have to match in order for quality design to occur [210]. The ability to meet this challenge, when fostered in engineering undergraduates, will contribute to a technically savvy engineering workforce with a higher potential for creative and entrepreneurial design, per the definition of Rae [211]. Therefore, it is posited that teaching customer-focused design is beneficial for developing entrepreneurial tendencies within the minds of engineering students.

Students who are naïve to the realities of customer and marketplace demand and their importance to successful design have only preconceptions to serve as a guide, and those preconceptions may very well be incorrect [212]. These preconceptions can range from the nature of the final design to the precise meaning of design in a given field and can even include their conception of customer knowledge base. Any of these three forms of student misconceptions as suggested by Chi et al. [213], whether incorrect, inconsistent, or incompatible with the nature of customer needs and voice, pose an obstacle to effective customer focused design. However, if they are easily correctable (i.e., incorrect or inconsistent with

prior knowledge), it would be useful to know whether they can be corrected more quickly at an early stage in student progression through a degree program.

The challenge, then, is understanding how to effectively instill a customer focus in engineering students while dispelling misconceptions regarding customer desires. As it stands, engineering students in colleges today do not relate well to traditional engineering pedagogy, such as the direct transmission model, which has remained the norm for the past few centuries [214]. The current generation of students is looking for a curriculum and educational approach that uses advanced classroom technology and active learning to engage them in the learning process [214, 215]. A novel approach that can be used to engage students in the engineering product design process in a professional context are engineering epistemic games [216, 217].

Epistemic games are founded on epistemic frame theory [218]. This theory posits that the formation of “communities of practice” - groups of practitioners with similar problem-solving styles - is essential for learning to solve the most challenging problems in a discipline [218, 219]. Moreover, the concept that every community of practice has its own culture with unique skills, knowledge, values, identity, and epistemology that constitute its epistemic frame is the basis of the “epistemic frame hypothesis” [219, 220, 221].

Epistemic games are simulations that allow students to act as practitioners in a simulated real-world environment while gathering data on students’ development as practitioners within a given epistemic frame [219]. In engineering epistemic games, students role play as interns for a virtual company and are tasked with a real-world design problem to engage them in the engineering design process. Within the engineering epistemic game Nephrotex [219], students are tasked with designing a dialysis membrane for therapeutic blood ultrafiltration. The design process involves the participation of multiple students (i.e., design teammates) and a design mentor as students progress through design activities. These activities occur in stages referred to as “rooms” in which the students play through a specific task. The interns are advised by virtual employees in the company’s research and development team (either simulated or played by student volunteers) during each of these activities. The internship and product design culminate in the selection of a final design, written justification for the

selection of that design, and an oral or poster presentation of the design to other teams and the course instructor.

The implementation of Nephrotex has been shown to increase student engagement [219] and positively impact the intent of women in first-year engineering programs to persist in an engineering discipline [222]. Its utility in fostering entrepreneurial mindset was previously investigated [197]. Taking this further, we evaluate in this work the effect of the implementation of a focus group within Nephrotex for its possible effects on product performance with an emphasis on customer desired attributes. Customers can add their voice to the design process through the focus group, one of the most widely employed tools in market analysis [223]. In the context of epistemic game research, the focus group also provides a controlled environment in which to probe initial student interest in terms of focus group participant selection from a pool of customer types and ultimate student response to both internal and external stakeholder (*i.e.* customer) requests. By implementing a focus group within a virtual internship for sophomore and senior engineering students the goal is to gauge whether exposure to end-customers within the early stages of the design process yields a quantitative change in the final design specifications in terms of product performance in the marketplace and/or quality. Even though students may not specifically focus on reducing cost to meet customer needs, decreased final product cost is associated with the exposure to external stakeholders in the focus group.

## 6.2 RESEARCH QUESTIONS:

The following three research questions were investigated through quantitative analysis in this chapter:

1. Is there a direct relationship between information sought by students relevant to final design specifications during an external customer focus group and the attributes of the final design in the virtual internship Nephrotex?
2. Does the incorporation of an external customer focus group within Nephrotex influence any specific attribute of the final designs generated by student groups?

3. Does the incorporation of an external customer focus group within Nephrotex raise or lower the overall quality of student designs?

Complementing the quantitative analysis of the effect of a focus group in a virtual internship, including its effect on end customer desired attributes, is a qualitative analysis of student design process. Qualitative analysis was selected as a research methodology to better understand how and why students chose a certain design process and how it relates to customer needs. Furthermore, a qualitative description of student design process may help explain the quantitative effects observed from customer input as part of a focus group. In this work, a grounded theory framework is developed and used in order to identify themes in student responses as a starting point for analysis.

Furthermore, the differences in design conception between sophomores and more experienced seniors are also examined. Student selection of questions and responses to information gained from the focus group were evaluated across academic levels. Specifically compared were what types of customers were selected for the focus group and questions were asked of focus group members by sophomores and seniors.

The following research questions are answered by the analysis of the student responses.

- Is an external customer focus group within a virtual internship environment associated with specific product attribute or customer themes?
- Do senior engineering students have different pre-conceptions of the customer?

## **6.3 METHODS:**

### **6.3.1 Study Design**

Nephrotex was implemented in the spring semester of 2014 in two sophomore-level sections (57 students each) and one senior-level section (89 students) as part of a series of design courses in the Chemical Engineering undergraduate program at the University of Pittsburgh. One sophomore section played through a version of Nephrotex that incorporated two additional activities pertaining to a focus group that provided those students with external

stakeholder (i.e. end-customer) insight. The Nephrotex game allows for the customization of four components of each membrane design: membrane polymer, polymerization process, processing surfactant, and carbon nanotube percentage (see [219], Figure 3 for a complete description of the design space). The selections made for each of these four components are taken as inputs to the design process, and the resulting outputs are five quantified metrics of design performance: marketability (in anticipated units sold), cost (in \$), and three technical metrics – flux ( $\text{m}^3/\text{m}^2/\text{day}$ ), blood cell reactivity (BCR,  $\text{ng}/\text{mL}$ ), and reliability (hours). These output values for each final design were compared between the focus group (FG) and non-focus group (NFG) sections. Cost was considered to be a non-technical attribute, and marketability was considered as both technical and non-technical because economic and ergonomic considerations are vital for the production of a marketable product.

Lecture periods for the course utilized both direct transmission and active learning methods. The Nephrotex virtual internship took place over the course of 10 consecutive weeks in a 15-week semester. Play-through of the virtual internship occurred during the scheduled class period for one hour per week where students were assigned to one of 10 teams composed of either 5 or 6 students. Tasks assigned to the students within the internship that were not completed in the allotted time were completed outside of classroom hours. The internship culminated in the presentation of each student-group's final membrane design in poster format. Proper human subjects approval was obtained prior to the conduct of this study.

### **6.3.2 Assessment of Final Membrane Designs**

Assessments were made on the performance metrics of each final design according to the built-in design criteria of the Nephrotex software, and comparisons were made between those of the section with the added focus group and the non-focus group section, referred to as FG and NFG, respectively.

Quality of the final design was also assessed relative to thresholds for each of the five output categories based on the framework developed by Arastoopour and colleagues [224]. Four graduated thresholds per output were used. These were described to the students

in uniform detail as either suggested or required performance levels according to requests from internal Nephrotex “employees,” henceforth referred to as “internal consultants.” The designs were given a point for each threshold - minimum, medium low, medium high, and maximum - with minimum receiving one point and maximum receiving four points. Thus, a “perfect” design that met the maximum threshold (given in Table 6.1) in every output category would receive a 20 point quality score. However, the maximum possible score for any actual design in the design space was 18 due to design space constraints. Students were unaware of this quality framework during the design process, so while design requests were made by the internal consultants, the design process by which they arrived at a final design was open-ended.

Table 6.1: Thresholds for design outputs

Threshold	BCR	Flux	Cost (\$)	Marketability (Units)	Reliability (hr)
Minimum	110	10	165	250,000	1.5
Medium low	90	12	150	350,000	3
Medium high	55	13.5	100	550,000	4.7
Maximum	45	16	75	650,000	5.5

### 6.3.3 Design of Focus Group

The focus group was implemented to determine whether design input from stakeholders external to Nephrotex (*i.e.* customers) could be mapped to a resulting design output. To that end, the focus group was designed to work in concert with the existing play-through structure of the internship to ensure an otherwise equivalent (in terms of information conveyed and time required) gameplay experience for both sections. The focus group “room” of play was designed to elicit input from five simulated external stakeholders: a dialysis patient, a nephrologist, a hospital administrator, a Medicare assistant, and an industry thought leader. The questions that students could ask of each stakeholder and the subsequent stakeholder responses were pre-established within the game framework by the authors of this work. These questions and responses were sent to a practicing nephrologist independent of this work for

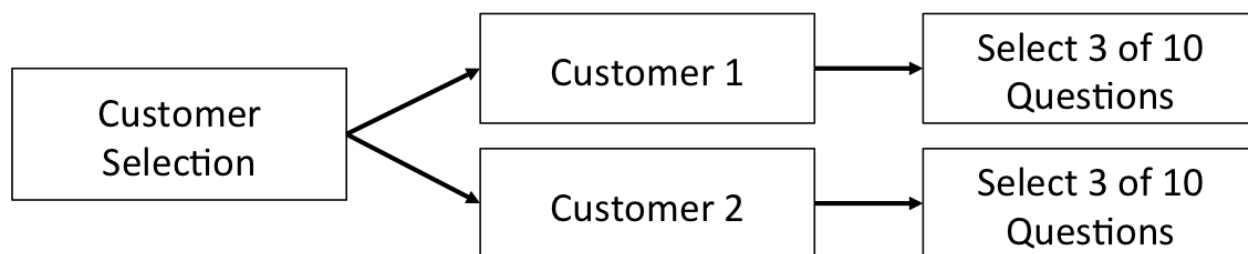


Figure 6.1: Schematic of stakeholder/customer and question selection process for the focus group interview.

review. The full set of questions and answers available to students in the focus group section is provided in [Appendix C](#).

Students in the FG section were told to select two of the five external stakeholders (i.e., end customers) to participate in their focus group and were allowed to strategize prior to the focus group within their team as to who and what questions would be best to ask. They were then allowed to ask each stakeholder three questions from a bank of ten about their opinion relating to the design of dialysis membranes (see [Figure 6.1](#)). Students discussed the focus group responses to question findings with their team members. At the completion of the virtual internship, all questions that students asked of external customers were sorted into the performance relevant categories (i.e. marketability, BCR, reliability, flux and cost).

#### 6.3.4 Assessment of Student Submissions

The qualitative work was directed toward determining differences in student design process when they are exposed to customer voice through focus groups, which may ultimately lead to differences in design output. These qualitative assessments were performed via an analysis of student notebook submissions to provided reflection questions within the virtual internship Nephrotex. Each question asked during the focus groups was also quantitatively reviewed. The number of times each customer was selected by a student design team was counted and the normalized results were compared between the sophomore and senior sections. A list of questions asked of the students is published in [Appendix D](#). Students also submitted final

designs that were assessed for quality according to the methodology in [?]. This allowed for determination of whether qualitative differences between groups resulted in quantitative differences in design performance.

### 6.3.5 Grounded Theory Framework Development

Grounded Theory was the primary analysis methodology used in this work [225]. Grounded theory frameworks are generated through iterative reduction of the set of observed themes in all analyzed responses. Recurrent or study-relevant themes are retained through subsequent iterations until a concise representation remains. In the case of this virtual internship, common themes are expected to be in line with technical terms found in dialysis. Thus, a coding scheme was generated that measures how interrelated the occurrences of specific themes are (e.g. membrane flux and customer knowledge).

Furthermore, this tool will be useful in understanding what student perceptions of the design process are regardless of academic level, and specifically between sophomores and seniors in this case. The perceptions could relate to value of information gained/to-be-gained. They could also relate to the importance of the information gained relative to patient care supply chain, whether it is regarding end-users like patients or nephrologists or intermediate stakeholders like hospital administrators, Medicare providers, or third-party industry members.

The themes (also referred to as categories) for assessing student responses within the focus group rooms as well as descriptions and quoted examples of occurrences of each theme in this study are given in Table 6.2.

Each student response from the focus group rooms was double-coded for Inter-Rater Reliability (IRR) purposes. The two coders were trained to categorize student responses according to the items in Table 6.2 by reviewing 10 randomly selected responses from the pool of 394 valid responses, reconciling differences, and retraining on another 10 responses. The remaining 374 responses were used to determine the IRR, which was found to be substantial across all responses (Cohen's  $\kappa = 0.669$ ) [23]. The frequency of each category or combination of

Table 6.2: Categories and subcategories with their notebook responses. Grammatical errors by students are denoted with [sic].

Category	Subcategory	Description	Example
Focus Group (FG)	Useful	Finds the FG useful	“The customer focus group was useful in determine [sic] what attributes are most important to the customer and therefore what we should focus on when designing the product.”
	Not Useful	Did not find the FG useful	“Our focus groups did not address too much information.”
Customer	Role	Student-perceived customer role as as end user or otherwise	“[Patient] doesn’t pay for his treatment but would love to use the best possible product.”
	Needs	Identified customer needs as price or performance constraints	“The nephrologist is on more of a budget and will not spend more than 80.”
Knowledge	High	Student believed insight could be obtained from customer	“[Patient] gave us knowledge on how often he had to have treatments. . .”
	Low	Student believed little knowledge could be gained from customer	“Half of the questions asked where [sic] outside of their expertise and was [sic] left unanswered.”
Utility	Compared	Student compares the value of responses given by two or more customers	“Depending on if we focus on the in-home or clinical patient, some of these responses may not be valuable.”
	High	Customer responses were useful to the student	“I found the industry leader more useful that [sic] the patient.”
	Low	Customer responses were not useful to the student	“From the Medicare Government Assistant, she had no useful information other than that Medicare has an \$80.00 coverage on dialysis cost.”
Attributes	Technical	Technical attributes (e.g., BCR, Flux, or Reliability) were mentioned (counted individually)	“The industry leader was concerned with a balance between reduced pain and flux.” (BCR and Flux)
	Marketability	Marketing and/or marketability were mentioned	“A low cost product may not be the best advice from a marketability perspective.”
	Cost	Cost was mentioned	“It was clear from the responses that most of the customers care about the membrane being cheap and efficient.”
Expectations	Met	Expectations of the FG or customer were met/exceeded	“This is what was expected by the internal consultants. They basically predicted each answer.”
	Not Met	Expectations of the FG or customer were not met	“My responses are rather disappointing.”

categories of interest was recorded. Differences in frequencies between sections were assessed using z-tests of proportions and/or effect sizes measured by the odds ratio (OR).

### 6.3.6 Statistical Analysis

Statistical analyses were performed in Matlab (© 2013 The MathWorks Inc., Natick, MA) using either the *ttest* (a Student’s or matched t-test), *ranksum* (Wilcoxon rank-sum), or

*corr* (determination of either the Spearman or Pearson correlation statistic) functions, using an alpha level of 0.05 for statistical significance in all cases. Due to small sample sizes, statistical tests include both parametric and non-parametric equivalents such as the Pearson and Spearman correlation coefficients as well as the t-test and Wilcoxon rank-sum test.

## 6.4 QUANTITATIVE RESULTS

This section presents the quantitative results relating to customer input in the virtual internship Nephrotex based upon each of the first three research questions. The quantitative results reflect analysis performed only on the sophomore sections.

**6.4.0.1 RQ1:** Is there a direct relationship between information relevant to final design specifications obtained from an external customer focus group and the attributes of the final design in the virtual internship Nephrotex?

Figure 6.2 shows the box-plot of the number of questions asked by each student group pertaining to each output parameter. Students asked more cost-related questions than other question-types with some overlap in the upper tail of both the flux and BCR categories.

Additionally, averaging the number of questions asked in each category over all the groups demonstrated that students ask significantly more cost-related questions versus any one technical-related question ( $p < 0.05$ ). This may indicate that cost was a highly-valued metric in the minds of students.

To determine if apparent interest had a direct relationship to design output values, the relationship between questions asked during the focus group and achievement/performance on the final design was investigated. Correlation coefficients were calculated between the number of questions asked per metric and the corresponding final design metric (e.g. BCR) value. These results are given in Table 6.3 and showed no significant correlations. This indicates that there was no correlation between the number of questions asked for any of the metrics and their associated performance level in the final team design.

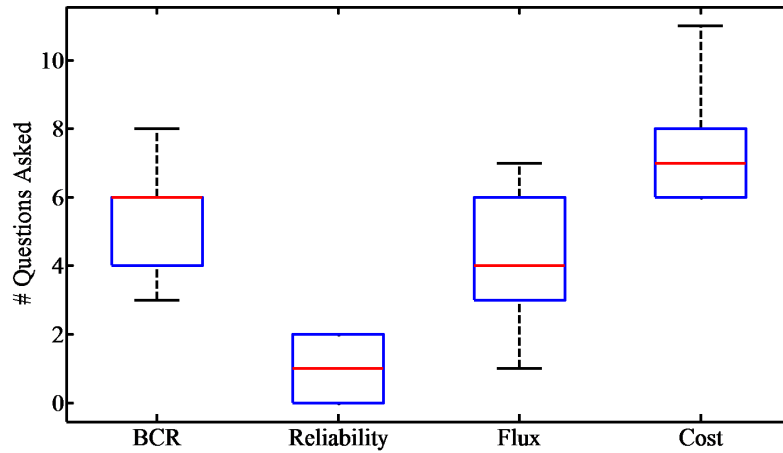


Figure 6.2: Number of cost, BCR, reliability, and flux-related questions asked by each group in FG section.

Table 6.3: Correlations for each of the four metrics of the final design versus the number of questions asked.

Value vs. #Questions	BCR	Reliability	Flux	Cost
$R^2$	0.0402	0.0192	0.0281	0.0039
p-value (Pearson)	0.579	0.703	0.643	0.863
p-value (Spearman)	0.553	0.621	0.794	0.788

**6.4.0.2 RQ2:** Does the incorporation of an external customer focus group within Nephrotex influence any specific attribute of the final designs generated by student groups?

Adding the data from the NFG section to the analysis and comparing final design metrics, including marketability, between the NFG and FG sections allowed us to investigate whether the external customer focus group within the Nephrotex virtual internship influenced any specific attribute of the final designs generated by the student groups, such as reliability or flux. The results of this comparison are given in Table 6.4.

Table 6.4: Comparison of final design metrics between FG and NFG sections.

	Marketability		Cost		Reliability		Flux		BCR	
	NFG	FG	NFG	FG	NFG	FG	NFG	FG	NFG	FG
average	7.50E+05	6.40E+05	135	114	10.7	9.7	15.6	16	42.2	47.77
std. dev.	1.35E+05	2.37E+05	10.8	15.1	2.5	1.7	1.3	1.4	16.1	14.1
p-value	0.222		0.002		0.305		0.526		0.421	

It was determined that the cost of the final design was significantly less in the section with the focus group even after adjusting for multiple comparisons using Bonferroni’s correction, and was the only metric that demonstrated any significant difference ( $p < 0.05/5$ ). In terms of effect sizes, there was a large decrease in marketability due to the focus group (Cohen’s  $d = 1.15$ ), but the impact on cost was even larger ( $d = 2.45$ ) [226].

#### 6.4.1 RQ3:

Does the incorporation of an external customer focus group within Nephrotex raise or lower the overall quality of student designs?

An overall quality score was calculated as described in the Methods by summing the number of stakeholder thresholds met for each design. The resulting score had a possible range from 0 to 18. Across all groups who produced devices, the mean overall quality score was 14.95, with a minimum of 13 and maximum of 17.

An independent samples t-test showed no significant difference ( $p > .277$ ,  $t(28) = -1.415$ ) in overall quality scores for devices chosen by the FG section (mean = 15.3, SD = 1.77) versus the NFG section (mean = 14.6, SD = 0.84).

## 6.5 DISCUSSION OF QUANTITATIVE FINDINGS

These results suggest the following:

There was not a direct relationship between questions asked in the focus group and students' priorities in device design, where priority was established according to the quantitative value of a given aspect of the final design. That is, students did not focus more on the outcomes that they asked more questions about. However, they did ask about cost more than any other issue.

Teams that were exposed to a focus group made lower cost devices than those that were not. Since there was no correlation between student interest and value of device design criteria, it may be that exposing students to customer voice is responsible, at least in part, for this difference.

The quality of devices was not different when comparing focus group and non-focus group teams. Therefore, on average, students in both sections produced equally viable designs. Given the decreased cost of designs by focus group teams, and that decreased cost meets a consumer need, the focus group may have achieved these ends by increased attunement to customer voice. Therefore, the exposure of students to customer needs via a focus group may improve the design process by preserving design quality while decreasing cost.

These results show that customer exposure through a focus group can encourage a high-quality, lower-cost design within an epistemic game environment. This result has implications for structuring engineering pedagogy to develop the entrepreneurial mindset of students at an early stage of education. As Pahl and colleagues [208] noted, "The market price and operating costs are the most important criteria for a customer when selecting between competing products and processes." Thus, the lower cost associated with the designs in the focus group section suggests that simulating interactions with external stakeholders in an educational context may help with encouraging the development of an entrepreneurial mindset. The prospect of enhancing an aspect of entrepreneurial mindset through the incorporation of end customer exposure within design experiences in the classroom is important for the future to attain the goal of creating more entrepreneurially minded engineers.

## 6.6 SUMMARY OF QUANTITATIVE FINDINGS

It was demonstrated that while students who participate as interviewers in a customer focus group show interest in both the technical and cost attributes of a product design, there is at this preliminary stage no evidence of a direct relationship between their interest level and the performance of the design in various areas, including cost and reliability, possibly because students may not ask about matters in which they already have a knowledge-base, a hypothesis that will be examined qualitatively in the next portion of this dissertation. However, students in the focus group section produced final designs that were less expensive than the designs produced in the section without a focus group. Based on this result, it may be inferred that exposing design students to end customer input processes may yield increased awareness towards customer needs, including cost. It appears that this does not sacrifice the technical performance of the final product based on analysis. This suggests the need for including elements or activities leading to increased customer focus within the design process while not sacrificing on design quality, both of which may help develop amongst students' traits inherent to an entrepreneurial mindset.

## 6.7 QUALITATIVE RESULTS

### 6.7.1 Results and Discussion

**6.7.1.1 RQ4:** is an external customer focus group within a virtual internship environment associated with specific product attribute (i.e. BCR, flux, reliability, cost, marketability) or customer themes? This research question examines only the sophomore sections, particularly the section that played through Nephrotex with a focus group (FG). First the sophomore FG notebook responses were categorized using our grounded theory framework in Table 6.2. Table 6.5 shows the total and relative frequency in descending order of percentage response for each category was mentioned during the FG module, indicating the students' focus on the particular category. The mentions of individual technical attributes (flux, BCR,

and reliability) are also reported. The percent of students with response describes how many students mentioned the category at least once.

Table 6.5: Categorized notebook responses

Code Category	Frequency	% of Students with Response (/54)
Attributes – Cost	49	78%
Customer – Needs	43	74%
Attributes - Technical	36	67%
Flux	24	44%
BCR	25	46%
Reliability	9	17%
Customer – Role	20	35%
Attributes - Marketability	9	15%

There was a nominally higher percentage of cost-related responses compared to technical (78% vs. 67%), but the difference was not significant ( $p=0.20$ , z-test) and the effect size was small ( $OR = 1.16$ ) [226]. Additionally, the cost and technical attributes were mentioned together 48% of the time as exemplified below with the appropriate code from Table 6.2 in brackets following the quote.

- “In summary, the customer focus group concluded that flux and cost are the most important values to them” [attributes – flux, attributes – cost]
- “Cost and flux were the two most important concerns cited by the customer targeting session.” [attributes – flux, attributes – cost]
- “The manufacturing engineer completely agreed with the nephrologist because he thinks that cost and reliability are most important.” [attributes – reliability, attributes – cost]

These findings that two-thirds or more of students mentioned technical or cost attributes and that responses like the ones above were given by approximately half of the students indicate that no substantive difference in student focus between cost and technical matters existed. These results demonstrate that while cost may be an important individual design

parameter to the students, it did not outweigh overall technical performance in terms of student focus.

Using data gathered from these same student sections, it was previously found that the number of questions that a given student asked about cost during the focus group had no relation to the final cost of the product, but exposure to customer voice during a focus group was associated with lower cost designs [?]. Our current finding that those same students did not have increased interest in cost relative to technical attributes coincides with our previous assessment that customer exposure alone is associated with lower cost designs. There was, however, significantly ( $p < 0.0005$ ) increased interest in cost over each individual technical metric, with medium to large effect sizes ( $OR = 1.77$  and  $OR = 1.69$ ) for flux and BCR, respectively, and very large effect size for reliability ( $OR = 4.59$ ). It was observed that there was no significant difference when balancing cost with overall technical performance however cost was prioritized over individual technical performance elements. As both cost and technical performance are known to be important factors to the customer, the number of times students mentioned either cost or technical attributes in the same submission as customer needs were also evaluated. Examples of this occurring are given for mention of customer needs alongside technical attributes, cost, and marketing, respectively below with coding for each snippet in brackets:

- “They [nephrologist] would not be happy with a lower flux because with so many patients they need a dialysis that can be completed in an efficient amount of time.” [attributes – flux, customer – needs]
- “The nephrologist said that they were willing to spend no more than \$80 per membrane.” [attributes – cost, customer – needs]
- “They also possessed [sic] no brand loyalty at all. This is very valuable data, because now we need to establish a brand name.” [attributes – marketing, utility – high, customer – needs]

Students tended to associate customer needs with both cost and technical aspects of the design more so than marketability, as presented in Table 6.6.

Table 6.6: Frequency mentions of both customer needs and a design attribute in tandem.

Combining Code	Frequency of Category	% of Students (/54)
Customer – Needs Attributes - Technical	50	61%
Customer – Needs Attributes - Cost	55	67%
Customer – Needs Attributes – Marketability	8	10%

The difference between the number of times cost or technical attributes were mentioned in combination with customer needs was not significant ( $p=0.28$ , z-test), and the effect size was small ( $OR = 1.09$ ). Students also mentioned cost or technical attributes in combination with customer needs far more than marketability and customer needs ( $OR = 6.7$  and  $6.1$ , respectively).

**6.7.1.2 RQ5:** Do senior engineering students have different pre-conceptions of the customer? The results of the analysis of focus group customer selection are given in Figure 6.3.

As demonstrated in this figure, sophomores demonstrated increased ( $p<0.05$ ) focus on end-users (i.e. patients and nephrologists) compared to seniors, as shown by the frequency of focus group questions asked. Additionally, the expected fraction of questions asked was 0.2 for each external stakeholder given the five customer types, assuming zero bias going into the focus group. However, sophomores asked a significantly different ( $p<0.05$ ) proportion of questions to each stakeholder except for the industry thought leader ( $p=0.13$ ), with the larger proportions dedicated towards the end users of the product. Seniors asked more evenly of each stakeholder, only asking the patient an increased fraction of the time ( $p= 0.02$ ). This may indicate that seniors have an increased awareness of the full scope of a product’s cus-

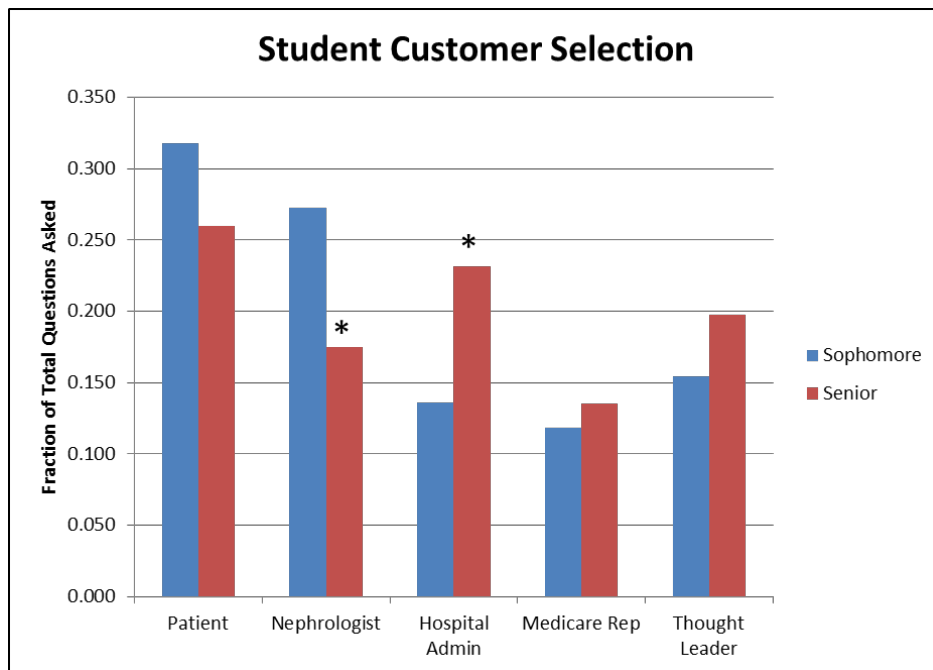


Figure 6.3: The distribution of customers interviewed. Each bar represents the fraction of times each customer was interviewed relative to the other stakeholders. Differences between sections were significant in the case of the nephrologist and hospital administrator ( $p < 0.05$ ).

customer base or supply chain. Recognizing the diversity of customer needs is important to understanding the customer and their within the design process. This finding may indicate that senior students have developed that recognition to a greater extent. Explaining what may be the source of this difference in focus could reveal a method to develop students' recognition of the entire consumer base at an earlier stage of their education. To further explore this hypothesis, senior submissions were categorized using our grounded theory framework. This allowed us to compare the design processes used by seniors and sophomores, as well as their pre-conceptions of the customer base. The frequency of occurrence of each theme that demonstrated statistically significant differences between seniors and sophomores based on a z-test for proportions is presented in Figure 6.4.

Seniors addressed important design attributes, including cost, technical, or marketability, to a greater extent than the sophomores did. Technical emphasis by seniors was primarily focused on flux, with decreased emphasis on BCR and reliability. Seniors did not, however, find the focus group or its participants as useful or as knowledgeable as the sophomores when comparing the fraction of responses that stated FG utility was high. In the case of the seniors, their expectations were not met relatively less (i.e. their preconceptions were less often wrong). For example, some responses to that end are given below:

- “The industry thought leader’s answers confirmed much of what I already knew.” [expectations – met]
- “[The focus group] was of some value but the cost could have been assumed from the beginning.” [attributes – cost, expectations – met]

This may indicate that seniors have an experiential knowledge base from which to draw when designing a product, which could have been gained either through coursework or co-op assignments or internships (hence their reduced perception of focus group utility).

It could be assumed that the seniors' relative knowledge base is more extensive and would ultimately provide an advantage in terms of final design quality and the ability to meet customer needs. However, there were no differences between final design performance of the seniors and sophomores in the FG section. The sophomore FG section had nearly equivalent cost (\$112 vs. \$111.3) and quality (15.3 vs. 15.6) as the seniors did, whereas it

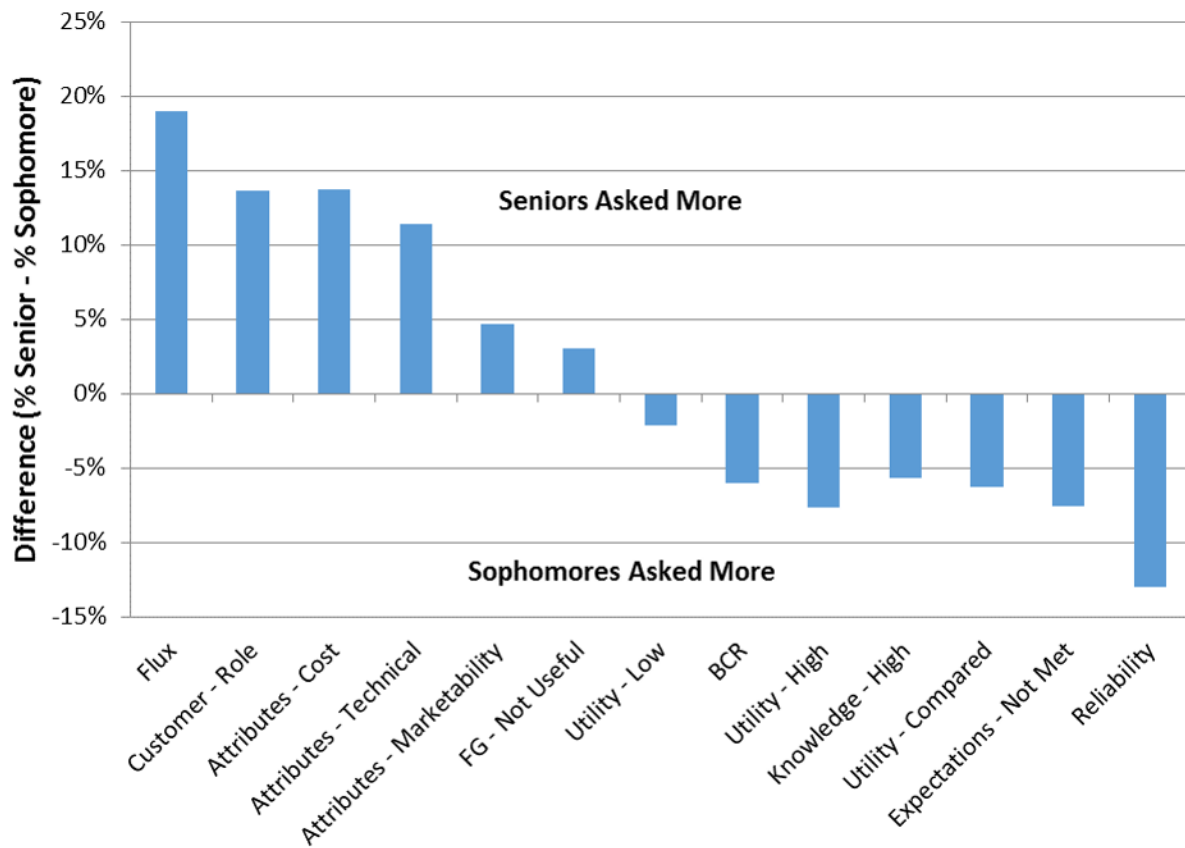


Figure 6.4: Responses that demonstrate significantly different proportions between senior and sophomore students that participated in a focus group.

has been reported above that students that did not perform a focus group have increased cost for similar quality. This may indicate that the sophomores may have experienced an informative event during their participation in the virtual internship that corrected any false preconceptions they may have had or lacked in regards to customer focused design. This could, in turn, have allowed them to achieve similar results to the seniors, who may have had an informational advantage over the sophomores prior to the course due to more experience or training. In order to test this hypothesis the sophomore FG section responses regarding their expectations of the customer types were reviewed. Sophomore expectations were met more often than not (30%, not shown in Figure 2 vs. 22%, although there was considerable mention (26% of students in both classes) of customers lacking an understanding of the technical attributes of the design. Two examples are given below. The first was in response to the in-home patient answer to the question, “What values did you have in mind when considering the flux of the membrane you use for dialysis?”

- “I noticed that the patient is unaware of the specifications and technical requirements of a membrane.” [knowledge – low]

And the second:

- “The patient did not understand what blood cell reactivity was so that was a small problem. He did say his insurance pays for it so cost is not an issue to him. Having a low blood cell reactivity will make his day more comfortable. Also he spends about 3 hours a week. That would mean he wants a decent flux and reliability.” [knowledge – low, attributes – BCR, attributes – cost, attributes – flux, attributes – reliability]

Which was a student entry in response to receiving patient answers for the questions, “Are you willing to sacrifice an efficient membrane for a membrane that reduces blood cell reactivity?” and, “Are you willing to spend over \$100 on a hemodialysis membrane?”

Based on these responses and naivety, it may be that sophomores entered the focus group lacking understanding about the design elements that are important to specific external stakeholders and which stakeholders are most appropriate to reach out to when seeking information on a proposed design element. Analysis of sophomore responses and final product design, particular in terms of the quality-cost interplay of the design, indicates that the focus

group may have increased sophomore awareness of the design space, as evidenced by the similar quality and cost between sophomore and senior final designs, hence the closing of the observed gap in end-user knowledge depicted in Figure 6.3. Moreover, it was previously reported that the focus group in Nephrotex was associated with lower cost designs for the sophomores. Now it is reported that those costs are similar to those of more experienced senior students, who achieved qualities nearing the maximum. It may then be that the similarities in terms of cost and design quality between senior and sophomore FG designs is due to information gained by exposure to the customer voice, as had previously hypothesized. A stronger validation of this claim would require a longitudinal study of the sophomore students, wherein it is tested whether the non-focus group section attains the same level of their FG peers through educational experiences within their degree program.

### 6.7.2 Study Limitations

The study presented could be hindered by sample sizes. The sophomore classes were nearly identical in size (56 and 57 students) and 54 students recorded responses in the FG section. There were 82 seniors, allowing for ten sophomore teams per section and 15 senior teams. Thus, analyses performed on team-generated results are more likely to face sample size issues with regard to statistics.

Another limitation to this work relates to the pre-constructed questions and responses built into the focus group design. The space from which students could draw questions relevant to their design was constrained in a manner that may not be reflective of what they might ask in a true industrial setting. This could be remedied by an open question format; however, this is difficult to regulate within an epistemic game environment. It would be possible to further determine student valuation of the design metrics through qualitative analysis of the notebook logs students maintained during these activities. This work is currently underway and should serve as useful feedback for future iterations of the customer focus group design as well as additional insight into the students' design processes.

This study and all analysis within was performed with chemical engineering class sections that participated in Nephrotex during the 2014 spring semester at one university. Since

no year-over-year, qualitative analysis of the impacts of focus groups on student design processes and outcomes has been performed at this point, it may be difficult to generalize these results. In order to more meaningfully characterize the differences and similarities observed between sophomores and seniors, a study tracking the state of students' mindsets would have to be performed over the duration of their engineering education. Therefore, these results obviate a need for long-term studies regarding the development of aspects of an entrepreneurial mindset. This could include research into the effects of solely classroom or industrial experiences and the two in combination. These findings provide a basis for continued research in this area.

## 6.8 SUMMARY

In this work, a mixed methods approach was used to assess quantitative and qualitative outcomes in terms of customer focused design in response to a focus group in the virtual internship Nephrotex. The quantitative results described a cost decrease without a decay in quality for a sophomore section that was exposed to a focus group vs. one that did not. In order to provide a more detailed explanation of the student design mindset that may have driven this difference, a grounded theory framework was developed to determine possible differences in design processes that occur with the introduction of a customer focus group to a virtual internship. Analysis of student responses based on this framework has shown that sophomores who engage in a focus group during the virtual internship Nephrotex showed (statistically) equal focus on cost versus technical measures of design performance during the focus group. Despite this, design cost was lower in the section that participated in a focus group, with no decrease in quality, which was described in detail in the first portion of this chapter. This indicates that customer voice may be an important factor in decreasing product cost, which provides additional support for results observed in the qualitative portion of the analysis.

In terms of other differences in the design processes that occurred with the focus group sections, sophomore students prioritized their interviewing of customers within the focus

group towards end users, such as the patient and nephrologist. Furthermore, qualitative analysis of sophomore responses demonstrated that they found utility in the focus group (30% of participants) but did not necessarily believe that the customers had useful knowledge of the relevant design attributes (17% of participants). Sophomores may have been able to use the focus group to correct any misconceptions about the important elements of customer focused design, resulting in a more customer-friendly (i.e., lower cost) product. Such realizations may have contributed to the equivalent quality and decreased costs associated with the designs of sophomores who participated in a focus group.

## APPENDIX A

### CODE FOR SIMULATING THE CELL- AND LUNG-SCALE MODELS

#### A.1 EQUATIONS OF THE CELL-SCALE MODEL

The following state equations were used for model simulations in [chapter 3](#)

Volumes:

$$\frac{dV_A}{dt} = L_{PC}A_C V_w(\pi_A - \pi_C) + L_{PP}A_{TJ}V_w(\pi_A - \pi_B) \quad (\text{A.1})$$

$$\frac{dV_B}{dt} = L_{PC}A_C V_w(\pi_B - \pi_C) - L_{PP}A_{TJ}V_w(\pi_A - \pi_B) \quad (\text{A.2})$$

$$\frac{dV_C}{dt} = -L_{PC}A_C V_w(\pi_A - \pi_C) - L_{PC}A_C V_w(\pi_B - \pi_C) \quad (\text{A.3})$$

Na<sup>+</sup>:

$$\frac{dNa_A}{dt} = \frac{-P_{ENaC}}{\frac{V_{max}}{V_A} + 1} \left( \frac{Na_A}{V_A} - \frac{Na_C}{V_C} \right) - P_{NaA,B}A_{TJ} \left( \frac{Na_A}{V_A} - \frac{Na_B}{V_B} \right) + J_{conv,Na} \quad (\text{A.4})$$

$$\frac{dNa_B}{dt} = P_{NaA,B}A_{TJ} \left( \frac{Na_A}{V_A} - \frac{Na_B}{V_B} \right) + k_{Na} \left( \frac{Na_C}{V_C} - \frac{Na_{C,\infty}}{V_{C,\infty}} \right) - J_{conv,Na} \quad (\text{A.5})$$

$$\frac{dNa_C}{dt} = \frac{P_{ENaC}}{\frac{V_{max}}{V_A} + 1} \left( \frac{Na_A}{V_A} - \frac{Na_C}{V_C} \right) - k_{Na} \left( \frac{Na_C}{V_C} - \frac{Na_{C,\infty}}{V_{C,\infty}} \right) \quad (\text{A.6})$$

Cl<sup>-</sup>:

$$\frac{dCl_A}{dt} = P_{CFTR} \left(1 - \frac{1}{\frac{V_{min}^2}{V_A} + 1}\right) \left(\frac{Cl_A}{V_A} - \frac{Cl_C}{V_C}\right) + P_{ACC} \frac{Cl_C}{V_C} - P_{Cl_{A,B}} A_{TJ} \left(\frac{Cl_A}{V_A} - \frac{Cl_B}{V_B}\right) + J_{conv,Cl} \quad (\text{A.7})$$

$$\frac{dCl_B}{dt} = k_{Cl} \left(\frac{Cl_C}{V_C} - \frac{Cl_{C,\infty}}{V_{C,\infty}}\right) + P_{Cl_{A,B}} A_{TJ} \left(\frac{Cl_A}{V_A} - \frac{Cl_B}{V_B}\right) - J_{conv,Cl} \quad (\text{A.8})$$

$$\frac{dCl_C}{dt} = -P_{CFTR} \left(1 - \frac{1}{\frac{V_{min}^2}{V_A} + 1}\right) \left(\frac{Cl_A}{V_A} - \frac{Cl_C}{V_C}\right) - P_{ACC} \frac{Cl_C}{V_C} - k_{Cl} \left(\frac{Cl_C}{V_C} - \frac{Cl_{C,\infty}}{V_{C,\infty}}\right) \quad (\text{A.9})$$

Mannitol:

$$\frac{dMl_A}{dt} = -P_{Ml_{A,B}} \left(\frac{Ml_A}{V_A} - \frac{Ml_B}{V_B}\right) + J_{conv,Ml} \quad (\text{A.10})$$

$$\frac{dMl_B}{dt} = P_{Ml_{A,B}} \left(\frac{Ml_A}{V_A} + \frac{Ml_B}{V_B}\right) - J_{conv,Ml} \quad (\text{A.11})$$

DTPA:

$$\frac{dDTPA_A}{dt} = -P_{DTPA_{A,B}} \left(\frac{DTPA_A}{V_A} - \frac{DTPA_B}{V_B}\right) + J_{conv,DTPA} \quad (\text{A.12})$$

$$\frac{dDTPA_B}{dt} = P_{DTPA_{A,B}} \left(\frac{DTPA_A}{V_A} - \frac{DTPA_B}{V_B}\right) - J_{conv,DTPA} \quad (\text{A.13})$$

## A.2 ADDITION OF POTASSIUM TO THE MODEL

The previous equations were expanded with the model addition of potassium by removing the linear basolateral regulation terms from (A.5, A.6, A.8, and A.9 and replacing them with the NaKP rate equation ( $\nu_{NaKP}$ ) of Lindenmayer and colleagues [54]:

$$\nu_{NaKP} = \nu_{pump,max} \left(\frac{Na_C}{Na_C + K_{int,Na}(1 + K_C/K_{int,K})}\right)^3 \left(\frac{K_B}{Na_B + K_{ext,K}(1 + Na_B/K_{ext,Na})}\right)^2 \quad (\text{A.14})$$

And the NKCC rate equation ( $\nu_{NKCC}$ ) of Miyamoto and colleagues [53]:

$$\begin{aligned} \nu_{NKCC} = & \nu_{NKCC,max} \left( \frac{Na_B}{Na_B + K_{Na}^{CO}} \right) \left( \frac{K_B}{K_B + K_K^{CO}} \right) \left( \frac{Cl_B}{Cl_B + K_{Cl,1}^{CO}} \right) \left( \frac{Cl_B}{Cl_B + K_{Cl,2}^{CO}} \right) \\ & - \nu_{NKCC,max} \left( \frac{Na_C}{Na_C + K_{Na}^{CO}} \right) \left( \frac{K_C}{K_C + K_K^{CO}} \right) \left( \frac{Cl_C}{Cl_C + K_{Cl,1}^{CO}} \right) \left( \frac{Cl_C}{Cl_C + K_{Cl,2}^{CO}} \right) \end{aligned} \quad (A.15)$$

And adding a calcium concentration-dependent (fixed at 0.09 mmol/ $V_C$  for the simulations) term for  $K^+$  transport through the large conductance potassium channel (BK) from [70]:

$$P_{BK} = \frac{1}{1 + \frac{K_{BK}^{1.7}}{Ca_C}} \quad (A.16)$$

The changes are reflected as follows:

Na<sup>+</sup>:

$$\frac{dNa_B}{dt} = P_{Na_{A,B}} A_{TJ} \left( \frac{Na_A}{V_A} - \frac{Na_B}{V_B} \right) - 3\nu_{NaKP} + \nu_{NKCC} - J_{conv,Na} \quad (A.17)$$

$$\frac{dNa_C}{dt} = \frac{P_{ENaC}}{\frac{V_{max}}{V_A} + 1} \left( \frac{Na_A}{V_A} - \frac{Na_C}{V_C} \right) + 3\nu_{NaKP} - \nu_{NKCC} \quad (A.18)$$

Cl<sup>-</sup>:

$$\frac{dCl_B}{dt} = k_{Cl} \left( \frac{Cl_C}{V_C} + 2\nu_{NKCC} + P_{Cl_{A,B}} A_{TJ} \left( \frac{Cl_A}{V_A} - \frac{Cl_B}{V_B} \right) - J_{conv,Cl} \right) \quad (A.19)$$

$$\frac{dCl_C}{dt} = -P_{CFTR} \left( 1 - \frac{1}{\frac{V_{min}}{V_A} + 1} \right) \left( \frac{Cl_A}{V_A} - \frac{Cl_C}{V_C} \right) - P_{ACC} \frac{Cl_C}{V_C} - k_{Cl} \left( \frac{Cl_C}{V_C} - 2\nu_{NKCC} \right) \quad (A.20)$$

K<sup>+</sup>:

$$\frac{dK_A}{dt} = P_{BK} \left( \frac{K_A}{V_A} - \frac{K_C}{V_C} \right) - P_{K_{A,B}} A_{TJ} \left( \frac{K_A}{V_A} - \frac{K_B}{V_B} \right) + J_{conv,Na} \quad (A.21)$$

$$\frac{dK_B}{dt} = P_{K_{A,B}} A_{TJ} \left( \frac{K_A}{V_A} - \frac{K_B}{V_B} \right) + 2\nu_{NaKP} + \nu_{NKCC} - J_{conv,K} \quad (A.22)$$

$$\frac{dNa_C}{dt} = -P_{BK}\left(\frac{K_A}{V_A} - \frac{K_C}{V_C}\right)P_{BK}\left(\frac{K_A}{V_A} - \frac{K_C}{V_C}\right) + 2\nu_{NaKP} - \nu_{NKCC} \quad (\text{A.23})$$

Simulation and fitting of the model equations to the same data as in [chapter 2](#) resulted in the fits in [Figure A1](#)

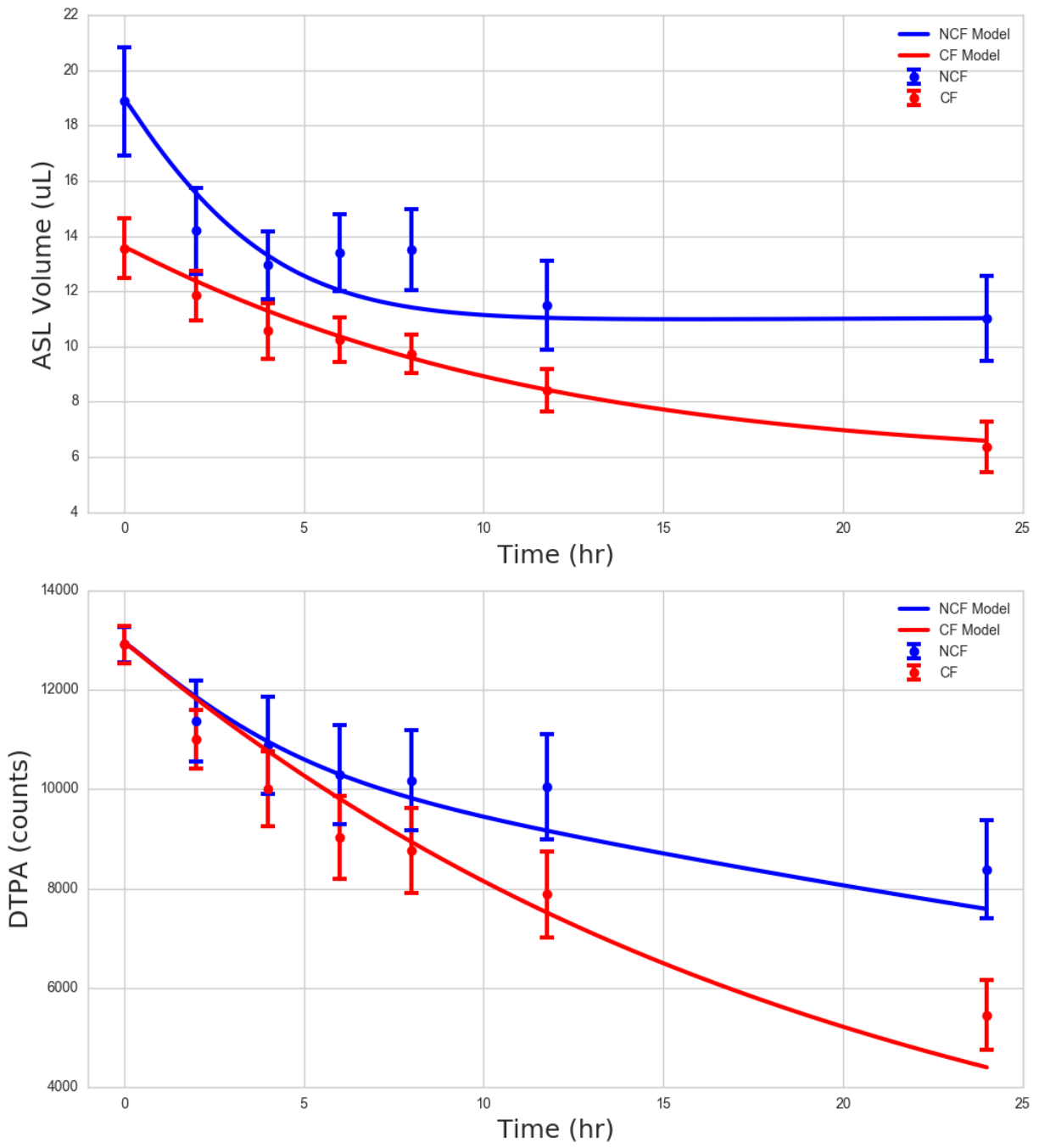


Figure A1: Model fits to ASL volume and DTPA with added  $K^+$  and more detailed transport mechanisms.

## APPENDIX B

### MODEL EQUATIONS

#### B.1 CODE FOR SIMULATING THE LUNG-SCALE MODEL

The code below will accomplish the integration of the model of [chapter 2](#) in MatLab. There is also a version written in C for MCMC simulations.

```
1 % InVivoModel – it is for the in vivo model
2 % pre_ – it comes before the plotting routine
3 % parfrac – a legacy name for models that include FFCA
4 % t – need a time vector
5 % k – need a parameter vector
6 % CR – need to provide the fraction of dose in the C region
7 % PR – need to provide the fraction of dose in the P region
8
9 function [T,In,Tc] = InVivoModelpre_parfrac(t,k,CR,PR)
10 % k many patients. Generally only one because naive pooling
11 for iter=1:length(k(:,1))
12     dose = 100; % percentaged dose could be normalized too
13     gens = 3;
14     inputs = zeros(gens+2,1);
15     f = k(iter,2); % FFCA
16     peri = PR(iter)*dose; % sets D dosage
17     cent = CR(iter)*dose; % sets P dosage
18     inputs(1) = cent*f; % L_F partition
19     inputs(2) = cent*(1-f); % L_N partition
20     inputs(3) = peri;
21     inputs(gens+1) = 10;
22     inputs(gens+2) = 0;
23     inputs(gens+3) = 0;
24
25     for n=1:1:2
26         if n==1 % Indium DTPA model
27             [T,y] = ode23s(@InVivoModelODE_parfrac, ...
28                 t, inputs, [], k(iter,:));
```

```

29     In(:, :, iter) = y;
30     else % TcSC model
31         k(iter, 3) = 0;
32         k(iter, 4) = 0;
33         [T, y] = ode23s(@InVivoModelODE_parfrac, ...
34             t, inputs, [], k(iter, :));
35         Tc(:, :, iter) = y;
36     end
37
38 end
39 end
40 function dy = InVivoModelODE_parfrac(t, y, k)
41     dy = zeros(6, 1);
42
43     kLT = k(1);
44     kDL = 0; %k(3) not identifiable
45     kLB = k(4);
46     kDB = k(3);
47     FFCA = k(2);
48
49     FL = y(1);
50     NL = y(2);
51     D = y(3);
52     T = y(4);
53     B = y(5);
54
55     dy(3) = -kDB*D -kDL*D;
56     dy(1) = -kLT*FL - kLB*FL + FFCA*kDL*FL;
57     dy(2) = -kLB*NL + (1-FFCA)*kDL*FL;
58     dy(4) = kLT*FL;
59     dy(5) = kLB*(FL + NL);
60     dy(6) = kDB*P;
61 end
62 end

```

## B.2 CODE FOR SIMULATING THE CELL-SCALE MODEL

The following C code will integrate the cell-scale model when mexed in Matlab with a helper function rhs.h.

```

1 /*
2 ** FILE: rhs.c
3 **
4 ** Requires a parameter vector with values
5 ** for all the names in the declaration
6 **/
7

```

```

8 /* math */
9 #include "math.h"
10 /* model header */
11 #include "model.h"
12 /* headers for useful mathematical functions */
13 #include "functions.h"
14
15 // #define max(a,b) ((a) >= (b) ? (a) : (b))
16
17 /* User defined RHS function */
18 int rhs_func (realtype t, N_Vector x, N_Vector xdot, void *f_data)
19 {
20     /* local variables */
21     struct function_data * data;
22     struct model_parameters * par;
23
24     /* cast f_data to 'function_data' type */
25     data = (struct function_data *)f_data;
26
27     /* get pointer to parameters, disturbance and control structures */
28     par = data->par;
29
30     /**** USER DEFINED CONTENT STARTS HERE ****/
31
32     /* Reassign parameters to things with names that don't need pointers */
33     double Oia0, OsmA0, Vb0, Nac0, Clc0, Oib0, OsmB0, Ac, Vc0, Oic0, OsmC0, Va0,
34     Atj;
35     double Lpc, Lpp, Penac, Pcftr, Vmax, Vmin, Dna, Dcl, Dml, Ddp, NCF, kna, kcl,
36     Pcacc;
37     double Vm, Pcc, Tcc, Oia, Oib, Oic, OsmA, OsmB, OsmC, Ehill, Chill, Lpb, Bcc;
38     double hc, Pna, Pcl, Pml, Pdp, AD, BD, Va, Vb, Vc, Nacss, Clcss, Tab, Tba, Tea,
39     Tcb;
40
41     /* Initial Condition Constants */
42     Oia0 = par->Oia0;
43     Nac0 = par->Nac0;
44     Clc0 = par->Clc0;
45     Oib0 = par->Oib0;
46     Ac = par->Ac;
47     Vc0 = par->Vc0;
48     Oic0 = par->Oic0;
49     Atj = par->Atj;
50
51     /* Possible to Fit Paramters */
52     Lpc = par->Lpc;
53     Lpp = par->Lpp;
54     Penac = par->Penac;
55     Pcftr = par->Pcftr;
56     Vmax = par->Vmax;
57     Vmin = par->Vmin;
58     Dna = par->Dna;
59     Dcl = par->Dcl;
60     Dml = par->Dml;
61     Ddp = par->Ddp;

```

```

59   NCF   = par->NCF;
60   kna   = par->kna;
61   kcl   = par->kcl;
62   Pcacc = par->Pcacc;
63   Lpb   = par->Lpb;
64
65   Penac = 100*Penac; /* Convert m/s to cm/s */
66   Pcftr = 100*Pcftr;
67
68   Dna = 100*Dna;
69   Dcl = 100*Dcl;
70   Dml = 100*Dml;
71   Ddp = 100*Ddp;
72
73   Lpc = 100*Lpc;
74   Lpp = 100*Lpp;
75   Lpb = 100*Lpb;
76
77   Vc0 = Vc0/1000;
78
79   OsmA= (Oia0 + (--Naa-- + --Cla-- ) + --Mla--)/(--Va--/1000); /* mOsm*/
80   OsmB= (Oib0 + (--Nab-- + --Clb-- ) + --Mlb--)/(--Vb--/1000);
81   OsmC= (Oic0 + (--Nac-- + --cCl-- ))/(--Vc--/1000);
82
83   Va = --Va--/(1000);
84   Vb = --Vb--/(1000);
85   Vc = --Vc--/(1000);
86
87   Vm = 0.018; // cm^3/mM
88   Tcc = Lpc*Ac*Vm*1000;
89   Pcc = Lpp*Atj*Vm*1000;
90   Bcc = Lpb*Ac*Vm*1000;
91
92   Ehill = 1/((Vmax/Va)+1);
93   //Ehill = hill(Va, 1, Vmax);
94   Chill = (1-1/(pow((Vmin/Va),2)+1));
95   //Chill = hill(Va, 2, Vmin);
96
97   hc = Vc/(Ac);
98
99   Pna = (Dna/hc); /* m/s Na+ paracellular permeability Interp from Li+ */
100  Pcl = (Dcl/hc); /* m/s Cl- paracellular permeability Wilke-Chang */
101  Pml = (Dml/hc); /* m/s Mannitol paracellular permeability Bashkatov */
102  Pdp = (Ddp/hc); /* m/s DTPA paracellular perm from Stokes-Einstein */
103
104  /* Determine drag directionality */
105  AD = (OsmA<OsmB?1:0);
106  BD = (OsmA>OsmB?1:0);
107
108
109  Cless = 0.044; //Clc0/Vc0;
110  Nacss = 0.023; //Nac0/Vc0;
111
112  //printf("AD is %f", OsmA);

```

```

113
114 Tca = Tcc*(OsmC-OsmA)*1e-3;
115 Tcb = Bcc*(OsmB-OsmC)*1e-3;
116 Tab = Pcc*(OsmB-OsmA)*1e-3;
117 Tba = Pcc*(OsmA-OsmB)*1e-3;
118
119 __DOT_Va__ = -Tca*1e3 - Tab*1e3;
120 __DOT_Naa__ = -Penac*Ehill*Ac*(__Naa__/Va--Nac__/Vc) - Pna*Atj*(__Naa__/Va-
    __Nab__/Vb) - __Naa__/Va*Tab*AD + __Nab__/Vb*Tba*BD;
121 __DOT_Cla__ = Pcftr*Chill*Ac*(__cCl__/Vc-Clcss)*NCF + Pcacc*Ac*__cCl__/Vc -
    Pcl*Atj*(__Cla__/Va--Clb__/Vb) - __Cla__/Va*Tab*AD + __Clb__/Vb*Tba*BD ;
122 __DOT_Mla__ = -Pml*Atj*(__Mla__/Va--Mlb__/Vb) - __Mla__/Va*Tab*AD + __Mlb__/
    Vb*Tba*BD;
123 __DOT_DTPA__ = -Pdp*Atj*(__DTPA__/Va--DTPB__/Vb) - __DTPA__/Va*Tab*AD +
    __DTPB__/Vb*Tba*BD;
124 __DOT_Mlb__ = Pml*Atj*(__Mla__/Va--Mlb__/Vb) - __Mlb__/Vb*Tba*BD + __Mla__/
    Va*Tab*AD;
125 __DOT_Vc__ = Tca*1e3 - Tcb*1e3;
126 __DOT_Nac__ = Penac*Ehill*Ac*(__Naa__/Va--Nac__/Vc) - kna*(__Nac__/Vc-Nacss)
    ;
127 __DOT_cCl__ = -Pcftr*Chill*Ac*(__cCl__/Vc-Clcss)*NCF - Pcacc*Ac*__cCl__/Vc +
    kcl*(Clcss--__cCl__/Vc);
128 __DOT_Vb__ = Tcb*1e3 + Tab*1e3;
129 __DOT_Nab__ = kna*(__Nac__/Vc-Nacss) + Pna*Atj*(__Naa__/Va--Nab__/Vb) -
    __Nab__/Vb*Tba*BD + __Naa__/Va*Tab*AD;
130 __DOT_Clb__ = Pcl*Atj*(__Cla__/Va--Clb__/Vb) - kcl*(Clcss--__cCl__/Vc) -
    __Clb__/Vb*Tba*BD + __Cla__/Va*Tab*AD;
131 __DOT_DTPB__ = Pdp*Atj*(__DTPA__/Va--DTPB__/Vb) - __DTPB__/Vb*Tba*BD +
    __DTPA__/Va*Tab*AD;
132
133 __DOT_DIFF__ = Pdp*Atj*(__DTPA__/Va--DTPB__/Vb);
134 __DOT_CONV__ = - __DTPB__/Vb*Tba*BD + __DTPA__/Va*Tab*AD;
135
136
137
138 /*** USER DEFINED CONTENT ENDS HERE ***/
139
140
141 /* All done. RHS evaluation is loaded into vector xdot. */
142 return(0);
143 }

```

## APPENDIX C

### PYMPLE CODE AND EXAMPLES

#### C.1 CODE FOR PYMPLE

The following is the code for PyMPLE as it is written on April 7, 2017.

```
1
2 # -*- coding: utf-8 -*-
3 """
4 Created on Fri Mar  4 13:36:36 2016
5
6 @author: Matthew Markovetz
7
8 This can remain unmodified if you so choose. As long as you structure your
9 model
10 module and run-file in the same format as provided in the example file , this
11 wonderful piece of code need never see the light of day.
12 """
13 import numpy as np
14 import scipy as sp
15 from pyomo.environ import *
16 from scipy.stats.distributions import chi2
17 from numpy import copy
18
19 class PyMPLE:
20     """
21     params becomes the initial parameter guess, which is the optimal solution
22     model becomes the pyomo ConcreteModel() that you are optimizing
23     objective becomes the reference objective for the likelihood ratio
24     pnames becomes the list of strings of parameter names
25     bounds is the bounds for the parameters
26
27
28
29
```

```

30
31     states becomes the list of model state or Var() names
32
33     hard tells PyMPLS if it should (True) or should not (False) profile
34     beyond the bounds of a parameter
35     """
36
37     def __init__(self, params, model, objective, pnames, bounds, states,
38                 hard=False):
39         self.popt = params
40         self.m = model
41         self.obj = objective
42         self.pkey = pnames
43         self.bounds = bounds
44         self.hard_bounds = hard
45         self.states = states
46
47     def get_CI(self, pfixed, data, maxSteps=100, stepfrac=0.01, solver='ipopt',
48               ,
49               nfe=150, alpha=0.05):
50         # Get Confidence Intervals
51         ctol = maxSteps
52         self.ctol=ctol
53
54         states_dict = dict()
55         # resultses = dict()
56
57         # Initialize
58         parup = copy(self.popt)
59         pardn = copy(self.popt)
60         parub = copy(self.popt)
61         parlb = copy(self.popt)
62         parkey = self.pkey
63         upkey = []
64         dnkey = []
65         _var_dict = dict()
66         _obj_dict = dict()
67
68         # Define Step size and the parameters to be profiled
69         def_SF = copy(stepfrac)
70         pfixCI = copy(pfixed)
71
72         _obj_CI = self.obj
73         ndat, npat = np.shape(data)
74
75         i=0
76         err = 0.0
77         pstep = 0.0
78
79         for j in range(len(pfixed)):
80             if self.hard_bounds:
81                 lower_bound = self.bounds[j][0]
82                 upper_bound = self.bounds[j][1]

```

```

83     else:
84         lower_bound = 0.0
85         upper_bound = float('Inf')
86
87     if pfixed[j]==0:# Do some first-pass initialization
88         pfixCI[j] = 1
89         df = 1.0#len(pfixed)-sum(pfixed)
90         etol = chi2.isf(alpha,df)
91         parup = copy(self.popt)
92         next_up = self.popt[j]
93
94     # Enter the upper profile arm
95     while i<ctol and err<=etol and next_up<upper_bound:
96         pstep = pstep + stepfrac[j]*self.popt[j]
97         parub[j] = self.popt[j] + pstep
98         parup[j] = self.popt[j] + pstep
99
100        itername = '_'.join([parkey[j], 'inst_up', str(i)])
101        try:
102            iterinst, iterres = self.m(data, solver, nfe, pfixCI,
103                                     parup, self.pkey,
104                                     bound=self.bounds)
105        except ValueError as e:
106            z = e
107            print(z)
108            i = ctol
109            continue
110
111        # instances[itername] = iterinst # these get very big
112        # resultses[itername] = iterres # they tend to slow things
113
114        down
115
116        states_dict[itername] = [[value(getattr(iterinst, i)[j])
117                                  for j in iterinst.t] for i in self.states]
118
119        err = 2*(log(value(iterinst.obj)) - log(_obj_CI))
120        _var_dict[itername] = [value(getattr(iterinst, parkey[i]))
121                               for i in range(len(parkey))]
122        _obj_dict[itername] = value(iterinst.obj)
123
124        #adjust step size if convergence slow
125        if i>0:
126            prevname = '_'.join([parkey[j], 'inst_up', str(i-1)])
127            d = np.abs((log(_obj_dict[prevname]) -
128                       log(_obj_dict[itername]))/log(_obj_dict[prevname]))/
129
130        stepfrac[j]
131
132        else:
133            d = err
134
135        if d<=0.01:
136            print(' '.join(['Stepsize increased from',
137                             str(stepfrac[j]), 'to',
138                             str(1.05*stepfrac[j]),
139                             'with previous p value: ', str(parup[j]
140
141 ])))]

```

```

134         stepfrac[j] = 1.05*stepfrac[j]
135     else:
136         stepfrac[j] = stepfrac[j]+def_SF[j]
137
138     print(' '.join(['finished UB iteration ', parkey[j], str(i),
139                    'with error: ', str(err),
140                    'and parameter change: ', str(pstep)]))
141     if err>etol:
142         upkey.append(itername)
143         print('Reached upper CI!')
144     elif i==ctol-1:
145         parub[j] = np.inf
146
147     next_up = self.popt[j] + pstep + stepfrac[j]*self.popt[j]
148     if next_up > upper_bound:
149         print('Reached parameter upper bound!')
150     i+=1
151     i=0
152     err=0.0
153     d=0.0
154     pstep=0.0
155     pardn = copy(self.popt)
156     stepfrac[j] = def_SF[j]
157     dneps=1e-10
158     next_down = self.popt[j]
159
160     # Enter the lower profile arm
161     while i<ctol and err<=etol and next_down>lower_bound:
162         pstep = pstep - stepfrac[j]*self.popt[j]
163         parlb[j] = self.popt[j] + pstep
164         pardn[j] = self.popt[j] + pstep
165
166         if pardn[j]<dneps:
167             pardn[j]=dneps
168             parlb[j]=dneps
169         itername = ' '.join([parkey[j], 'inst_down', str(i)])
170     try:
171         iterinst, iterres = self.m(data, solver, nfe, pfixCI,
172                                pardn, self.pkey, bound=self
173                                .bounds)
174     except ValueError as e:
175         z = e
176         print(z)
177         i = ctol
178         continue
179     #
180     instances[itername] = iterinst
181     resultses[itername] = iterres
182     states_dict[itername] = [[value(getattr(iterinst, i)[j])
183                               for j in iterinst.t] for i in self.states]
184     err = 2*(log(value(iterinst.obj)) - log(_obj_CI))
185     _var_dict[itername] = [value(getattr(iterinst, parkey[i]))
186                             for i in range(len(parkey))]
187     _obj_dict[itername] = value(iterinst.obj)

```

```

185         #adjust step size if convergence slow
186         if i>0:
187             prevname = '_' .join ([parkey[j], 'inst_down', str(i-1)])
188             d = np.abs((log(_obj_dict[prevname]) - log(_obj_dict[
itername])))/log(_obj_dict[prevname])/stepfrac[j]
189         else:
190             d = err
191
192         if d<=0.01:
193             print(' '.join(['Stepsize increased from',
194                             str(stepfrac[j]), 'to',
195                             str(1.05*stepfrac[j]),
196                             'with previous p value: ', str(pardn[j
]))))
197             stepfrac[j] = 1.05*stepfrac[j]
198         else:
199             stepfrac[j] = stepfrac[j]+def_SF[j]
200
201         print(' '.join(['finished LB iteration', parkey[j], str(i),
202                             'with error: ', str(err),
203                             'and parameter change: ', str(pstep)]))
204         if err>etol:
205             dnkey.append(itername)
206             print('Reached lower CI!')
207         elif i==ctol-1:
208             parlb[j] = -np.inf
209
210         next_down = self.popt[j] + pstep - stepfrac[j]*self.popt[j
]
211
212         if next_down < lower_bound:
213             print('Reached parameter lower bound!')
214             i+=1
215             i=0
216             err=0.0
217             pstep=0.0
218             pfixCI[j] = pfixed[j]
219             parup = [value(getattr(iterinst, parkey[i])) for i in range(len
(parkey))]
220             pardn = [value(getattr(iterinst, parkey[i])) for i in range(len
(parkey))]
221         else:
222             continue
223
224         self.parub = parub
225         self.parlb = parlb
226         self.var_dict = _var_dict
227         self.obj_dict = _obj_dict
228         self.pfix = pfixed
229         self.data = data
230         self.alpha = alpha
231         self.state_traj = states_dict
232         self.times = iterinst.t
233         # self.model_instances = instances
234         # self.model_resultses = resultses

```

```

234         return {'Lower Bound': parlb, 'Upper Bound': parub}
235
236     # Plot a simple bar plot with errorbars at the CI values
237     def ebarplots(self,):
238         import matplotlib.pyplot as plt
239         import seaborn as sns
240
241         nPars = len(self.popt)
242         sns.set(style='whitegrid')
243         plt.figure(figsize=(21,12))
244         nrow = np.floor(nPars/3)
245         ncol = np.ceil(nPars/nrow)
246         for i in range(nPars):
247             ax = plt.subplot(nrow, ncol, i+1)
248             ax.bar(1, self.popt[i], 1, color='blue')
249             pub = self.parub[i]-self.popt[i]
250             plb = self.popt[i]-self.parlb[i]
251             errs = [[plb],[pub]]
252             ax.errorbar(x=1.5,y=self.popt[i], yerr=errs, color='black')
253             plt.ylabel(self.pkey[i]+' Value')
254             plt.xlabel(self.pkey[i])
255
256         plt.tight_layout()
257         plt.show()
258
259     # Plot the profile likelihoods
260     def plot_PL(self,):
261         import matplotlib.pyplot as plt
262         import seaborn as sns
263
264         nPars = len(self.pfix) - np.count_nonzero(self.pfix)
265         sns.set(style='whitegrid')
266         PL_fig = plt.figure(figsize=(21,12))
267         nrow = np.floor(nPars/3)
268         if nrow<1:
269             nrow=1
270         ncol = np.ceil(nPars/nrow)
271         ndat, npat = np.shape(self.data)
272         j=1
273         for i, notfixed in enumerate(self.pfix):
274             if notfixed==0:
275                 dp=0.0
276                 dob=0.0
277                 k=0
278                 PLub = []
279                 OBub = []
280                 PLlb = []
281                 OBlb = []
282                 while dp<self.parub[i] and k<self.ctol:
283                     kname = '_' .join([self.pkey[i], 'inst_up', str(k)])
284                     dp = self.var_dict[kname][i]
285                     dob= log(self.obj_dict[kname])
286                     PLub.append(dp)
287                     OBub.append(2*dob)

```

```

288         k=k+1
289     k=0
290     while dp>self.parlb[i] and k<self.ctol:
291         kname = '_' .join([self.pkey[i], 'inst_down', str(k)])
292         dp = self.var_dict[kname][i]
293         dob= log(self.obj_dict[kname])
294         PLlb=np.append(dp, PLlb)
295         OBlb=np.append(2*dob, OBlb)
296         k=k+1
297     else:
298         continue
299
300     PL = np.append(PLlb, PLub)
301     OB = np.append(OBlb, OSub)
302     ax = plt.subplot(nrow, ncol, j)
303     j=j+1
304     ax.plot(PL, OB)
305     chibd = OSub[0]+chi2.isf(self.alpha, 1)
306     ax.plot(PLub[0], OSub[0], marker='o')
307     ax.plot([PLlb[0], PLub[-1]], [chibd, chibd])
308     plt.xlabel(self.pkey[i]+' Value')
309     plt.ylabel('Objective Value')
310 plt.show()
311 return PL_fig
312
313 # Plot state trajectories for the requested states
314 def plot_trajectories(self, states):
315     import matplotlib.pyplot as plt
316     import seaborn as sns
317
318     nrow = np.floor(len(states)/2)
319     if nrow<1:
320         nrow=1
321     ncol = np.ceil(len(states)/nrow)
322     sns.set(style='whitegrid')
323     traj_Fig = plt.figure(figsize=(21,12))
324     for k in self.state_traj:
325         j=1
326         for i in range(len(states)):
327             ax = plt.subplot(nrow, ncol, j)
328             j=j+1
329             ax.plot(self.times, self.state_traj[k][i])
330             plt.title(states[i])
331             plt.xlabel('Time')
332             plt.ylabel(states[i]+' Value')
333     plt.show()
334     return traj_Fig
335
336 # Return the upper and lower CI for the requested parameter names
337 def pop(self, pname, lb=True, ub=True):
338     CI_dict = dict()
339     for i in range(len(pname)):
340         plb = self.parlb[i]
341         pub = self.parub[i]

```

```

342         CI_dict[pname[i]] = (plb, pub)
343     return CI_dict

```

## C.2 VAN DE VUSSE CASE STUDY CODE

The code to run the Van de Vusse Case Study of [chapter 4](#) is below. In combination with `PyMPLE.py` in its direction the run file and the model file will generate figures similar to those in [chapter 4](#).

First is the `pyomo.dae` model:

```

1
2 # -*- coding: utf-8 -*-
3 """
4 Created on Tue Sep  1 10:13:00 2015
5
6 @author: Matthew
7 """
8
9 # -----
10 #
11 # Pyomo: Python Optimization Modeling Objects
12 # Copyright (c) 2014 Sandia Corporation.
13 # Under the terms of Contract DE-AC04-94AL85000 with Sandia Corporation,
14 # the U.S. Government retains certain rights in this software.
15 # This software is distributed under the BSD License.
16 # -----
17
18 # This import header should probably be used in every model
19
20 from pyomo.environ import *
21 from pyomo.dae import *
22 from pyomo.opt import SolverFactory
23 #from pyomo.dae.plugins.finitedifference import
24     Finite_Difference_Transformation
25 #from pyomo.dae.plugins.colloc import
26     Collocation_Discretization_Transformation
27
28 '''
29 You should set up your function to look something like this. It should have
30 all of the arguments below, but you can add whatever else you want.
31
32 data: is your data. It can be a list or ndarray, but the values have to be
33 floats if you're going to use a sum-squared error objective.
34
35 solver: any AMPL solver that is compatible with pyomo

```

```

35 nfinels: the number of finite elements that you will use for either finite
36 difference or collocation on finite elements methods.
37
38 p0: the initial parameter vector that pyomo is going to operate on.
39
40 pkey: the list of name strings for your parameters
41
42 bound: a tuple or list of tuples (prefered) containing the bounds of your
43     model
44 parameters. NOTE: this is not the profile bounds; it is the pyomo search-space
45 bounds. If you just want to search the positive reals, you can use the default
46 format given in the example function declaration below.
47
48 cp: is the number of collocation points that you will use if you elect to
49 employ collocation on finite elements to integrate your system.
50 '''
51 def VdV_model(data, solver, nfinels, pfix, p0, pkey, bound=(0.0,None), cp=3):
52     import numpy as np
53     # You should include this if and only if you are too lazy to pass your own
54     # bounds list.
55     if type(bound)==tuple:
56         mbounds = [bound for i in range(len(pfix))]
57     elif type(bound)==list:
58         mbounds = bound
59
60     # Initiliaze model as a pyomo ConcreteModel().
61     m = ConcreteModel()
62     tvals = list(data[:, -1])
63     # tvals.extend([i/10.9 for i in range(110)])
64
65     m.t = ContinuousSet(initialize=np.linspace(0,10,110))
66     m.time = Set(initialize=tvals, within=m.t, ordered=True)
67
68     rA = data[:,0]
69     rB = data[:,1]
70     rC = data[:,2]
71     rD = data[:,3]
72
73     # Set your states. This could be done automatically in a similar way to
74     # the
75     # parameters below. However, your states are independent of the profiling
76     # operation, so it might be faster to just hard code them.
77     m.A = Var(m.t)
78     m.B = Var(m.t)
79     m.C = Var(m.t)
80     m.D = Var(m.t)
81
82     for i in range(len(pfix)):
83         # This for loop has to be present in your model in order for the get_CI()
84         # method to operate for a general set of parameters specified in the run
85         # file.
86         # It accomplishes the following assignments for the VdV example case when
87         # profiling only FV and kAB.

```

```

86     # m.FV = Var(initialize=3/7)# True Value 4/7
87     # m.Caf = Param(initialize=10)
88     # m.kAB = Var(initialize=3/6)# True Value 5/6
89     # m.kBC = Param(initialize=5/3)
90     # m.kAD = Param(initialize=1/6)
91
92     if pfix[i]==0:
93         dVar = Var(initialize=float(p0[i]), bounds=mbounds[i])
94         setattr(m, pkey[i], dVar)
95         del(dVar)
96     else:
97         dPar = Param(initialize=float(p0[i]))
98         setattr(m, pkey[i], dPar)
99         del(dPar)
100
101     A0=m.Caf
102     B0=0
103     C0=0
104     D0=0
105
106     # Set your state derivatives.
107     m.dAdt = DerivativeVar(m.A, wrt=m.t)
108     m.dBdt = DerivativeVar(m.B, wrt=m.t)
109     m.dCdt = DerivativeVar(m.C, wrt=m.t)
110     m.dDdt = DerivativeVar(m.D, wrt=m.t)
111
112     # Define your model equations as constraints
113     def _A_ode(m, i):
114         if i==0:
115             return Constraint.Skip
116         return m.dAdt[i] == m.FV*(A0-m.A[i]) - m.kAB*m.A[i] - m.kAD*m.A[i]**2
117     m.A_ode = Constraint(m.t, rule=_A_ode)
118
119     def _B_ode(m, i):
120         if i==0:
121             return Constraint.Skip
122         return m.dBdt[i] == -m.FV*(m.B[i]) + m.kAB*m.A[i] - m.kBC*m.B[i]
123     m.B_ode = Constraint(m.t, rule=_B_ode)
124
125     def _C_ode(m, i):
126         if i==0:
127             return Constraint.Skip
128         return m.dCdt[i] == -m.FV*(m.C[i]) + m.kBC*m.B[i]
129     m.C_ode = Constraint(m.t, rule=_C_ode)
130
131     def _D_ode(m, i):
132         if i==0:
133             return Constraint.Skip
134         return m.dDdt[i] == -m.FV*(m.D[i]) + 1/2*m.kAD*m.A[i]**2
135     m.D_ode = Constraint(m.t, rule=_D_ode)
136
137     # Define your initial conditions
138     def _initCons(m):
139         yield m.A[0] == A0

```

```

140     yield m.B[0] == B0
141     yield m.C[0] == C0
142     yield m.D[0] == D0
143 m.initCons = ConstraintList(rule=_initCons)
144
145 # This is your objective. SSE is probably preferred, but whatever.
146 def _obj(m):
147     Asum = sum((rA[tvals.index(i)]-m.A[i])**2 for i in m.time)
148     Bsum = sum((rB[tvals.index(i)]-m.B[i])**2 for i in m.time)
149     Csum = sum((rC[tvals.index(i)]-m.C[i])**2 for i in m.time)
150     Dsum = sum((rD[tvals.index(i)]-m.D[i])**2 for i in m.time)
151     return Asum+Bsum+Csum+Dsum
152 m.obj = Objective(sense=minimize, rule=_obj)
153
154 # Discretize the problem
155 disc=TransformationFactory("dae.finite_difference")
156 disc.apply_to(m, nfe=len(m.t), wrt=m.t, scheme="BACKWARD")
157 # Solve the problem
158 opt = SolverFactory(solver)
159 opt.options['linear_solver'] = "ma97"
160 opt.options['tol'] = 1e-6
161 #model.preprocess()
162 results = opt.solve(m, tee=False)
163 #model.load(results)
164 m.solutions.load_from(results)
165
166 return m, results

```

And here is the run file:

```

1
2 # -*- coding: utf-8 -*-
3 """
4 Created on Fri Sep  9 10:57:45 2016
5
6 @author: Matthew
7 """
8
9 # This import block has basically everything you could need for calculating
10 # and graphing your results. Unused modules are left in the code for reference
11
11 from pyomo.environ import *
12 from pyomo.dae import *
13 from pyomo.opt import SolverFactory
14 import numpy as np
15 import scipy as sp
16 from scipy.stats.distributions import chi2
17 import scipy.io as sio
18 import matplotlib.pyplot as plt
19 import seaborn as sns
20 import lazytools as mrmttools
21

```

```

22 # You must import a function, here VdV_model, that solves a pyomo
    ConcreteModel
23 # and returns the solved instance and its results. See VdV_model for an
    example
24 # of that looks.
25 from VdV_module import VdV_model as model
26
27 # Import the PyMPLE class. This has everything you need for plotting and
28 # Analyzing your model response to profiling.
29 from PyMPLE import PyMPLE
30
31 div=1
32
33 # This is maybe the only example-specific line of code in here, but the data
34 # is specific to the problem. Don't use this data on your problem. Or do. YOLO
    .
35 data_struct = sio.loadmat('VdVExData.mat')
36 data = np.array([list(data_struct['C'][i,:]) for i in range(0,len(data_struct[
    'C'][: ,0]),div)])
37
38 tdata = np.linspace(0,10,110)
39 tdat = [tdata[i] for i in range(0,len(data_struct['C'][: ,0]),div)]
40 data = np.insert(data,len(data[0,:]),tdat,axis=1)
41
42 # Provide some initialization values for your pyomo model that the class can
43 # also use after the initial pyomo solution.
44 solver = 'ipopt' # your pyomo-approved solver
45
46 p0 = [4/7, 10.0, 3/6, 5/2, 2/6] # pyomo will need an initial condition vector
47 # might as well provide that here
48
49 pkey = ['FV', 'Caf', 'kAB', 'kBC', 'kAD'] # Your parameter names.
50
51 pfix = [1,1,0,0,0] # This is the vector of parameters that you don't want to
52 # profile. Ask, "Do I want to exclude this from profiling?"
53 # If yes, then enter 1 at its index location to exclude it.
54
55 nfinels = 110 # Tell pyomo (and the class) how many finite elements you want.
56
57 mstates = ['A', 'B', 'C', 'D'] # This is the names of your states for plotting
    trajectories
58
59 bds = [(0.0, None) for i in range(len(pfix))] # Your model probably has bounds.
60 # You should add them here.
61 # Solver your model to get an initial point for profiling
62 inst, mres = model(data, solver, nfinels, pfix, p0, pkey, bound=bds)
63 # Load your model solutions.
64 inst.solutions.load_from(mres)
65 # Get the reference objective value for profiling.
66 obj = value(inst.obj)
67
68 # This list comprehension auto-generates your initial parameter vector for
    profiling
69 popt = [value(getattr(inst, pkey[i])) for i in range(len(pkey))]

```

```

70
71 # Generate an instance of the PyMPLE class
72 PyMPLE_instance = PyMPLE(popt, model, obj, pkey, bds, states=mstates)
73
74 # This an exemple of how to generate a vector of the relative step-sizes you
75 # want to take when profiling each parameter.
76 sfvec = [0.005 for i in range(len(popt))]
77 nsteps = 100 # the max number of steps to take when profiling.
78
79 # Perform the profiling with this command. Returns the upper and lower bounds
80 fin = PyMPLE_instance.get_CI(pfix, data, nsteps, sfvec, solver, nfinels)
81
82 # Plot your profile likelihoods that were obtained from the get_CI method
83 PL_Fig = PyMPLE_instance.plot_PL()
84 mrmtools.setfontsize(PL_Fig,18)
85 # You can also use the ebarplots method to plot your parameters as a bar with
86 # CIs
87 PyMPLE_instance.ebarplots()
88
89 # And you can also plot each of the profiled state trajectories
90 traj_Fig = PyMPLE_instance.plot_trajectories(mstates)
91 mrmtools.setfontsize(traj_Fig,18)
92 #Obviously, you can and should pop your PyMPLE instance to get upper and lower
93 # CIs
94 PyMPLE_instance.pop(pkey)
95
96 A = []
97 B = []
98 C = []
99 D = []
100 rA= data[:,0]
101 rB= data[:,1]
102 rC = data[:,2]
103 rD = data[:,3]
104 t = []
105
106 for i in sorted(inst.t):
107     A.append(value(inst.A[i]))
108     B.append(value(inst.B[i]))
109     C.append(value(inst.C[i]))
110     D.append(value(inst.D[i]))
111     # rA.append(value(disc.rA[i]))
112     # rB.append(value(disc.rB[i]))
113     t.append(i)
114
115 fig = plt.figure()
116 ax = fig.add_subplot(1,1,1)
117 #ax.set_xlabel('Distance x')
118 #ax.set_ylabel('Time t')
119 ax.set_title('Van de Vusse!')
120 ax.plot(tdat,rA,'ob')
121 ax.plot(tdat,rB,'og')
122 ax.plot(tdat,rC,'om')
123 ax.plot(tdat,rD,'oc')

```

```

122 ax.plot(t,A)
123 ax.plot(t,B)
124 ax.plot(t,C)
125 ax.plot(t,D)
126 ax.legend(['A Data', 'B Data', 'C Data', 'D Data', 'A', 'B', 'C', 'D'])
127 #ax.plot(tvals,data,'o')
128 fig.show()
129
130
131 # add the true parameter values to the Profile Plots
132 numsp = len(pfix)-np.count_nonzero(pfix)
133 trueOpt = [5/6,5/3,1/6]
134 for i in range(numsp):
135     PL_Fig.get_axes()[i].plot(trueOpt[i],2*log(PyMPLE_instance.obj)+chi2.isf
(0.05,1),'o',markersize=8)

```

## APPENDIX D

### EXTERNAL STAKEHOLDER QUESTIONS, RESPONSES, AND CATEGORIZATIONS

#### IN-HOME PATIENT

I have recently been diagnosed with end-stage kidney disease and my nephrologist said that I only have twelve percent kidney function. After several weeks of training, I am legally allowed to have in-home dialysis. I am glad to be able to do this in my own home because I can do it more frequently and for less time each time, plus I'm more comfortable than in a clinic. All of this is important because my nephrologist said I will be doing hemodialysis for the *rest of my life*.

1. How much time do you set aside for your treatment on your dialysis days?
  1. I spend two to three hours in each of my dialysis sessions, six times per week. FLUX
2. Other than your actual dialysis sessions, how many hours a week do you set aside for your kidney disease?
  1. I have routine check-ups once a month, which last about four hours each time including meeting with my nephrologist, the nurse and the dietician. On average, I would say that I spend about 13 hours per week for my kidney disease. N/A
3. What values did you have in mind when considering the flux of the membrane you use for dialysis?
  1. I'm not sure what you mean. I am not familiar with the flux of a membrane. Therefore, I do not have any values in mind. N/A

4. Are you willing to spend over \$100 on a hemodialysis membrane?
  1. It doesn't matter to me how much it costs. Medicare and my secondary insurance pay for all of it. COST
5. How often do you plan to specifically purchase membranes for your dialyzer?
  1. My center just supplies them to me. But, membranes that don't work properly definitely cost me time and effort. RELIABILITY
6. Are you willing to sacrifice an efficient membrane for a membrane that reduces blood cell reactivity?
  1. I am not sure what blood cell reactivity is so I cannot answer this question. N/A
7. What is your pain threshold (how tolerant are you to pain)?
  1. I feel as if I can tolerate a high amount of discomfort. BCR
8. Have you seen any commercials or magazine ads for dialyzer membranes?
  1. Yes – on TV. I saw one that seemed to use really advanced technology and told my nephrologist about it. I'm not sure if we're using that one or not. MARKETABILITY
9. Would you be willing to pay more for a high-flux membrane?
  1. Like I said, I don't pay for it but if high-flux means less time for me, the answer is yes! N/A
10. For your treatment, are you performing daily (3 sessions per week), short-daily (5-7 sessions per week) or nocturnal dialysis (3-6 night sessions per week)?
  1. I am currently on a short-daily dialysis regimen about 6 times per week. N/A

## **NEPHROLOGIST**

In my practice, I care for a lot of patients with end stage renal disease. Many of them use hemodialysis. I want the most effective treatment for these patients in the shortest amount of time. I have 15 hemodialysis machines available at my clinic that are in use 8 hours a day, six days a week. These machines must be replaced after 25,000 to 40,000 hours of use and with constant monitoring. I would like to purchase membranes that are as efficient as possible and also reliable to avoid downtime.

1. Would your practice be able to use a medium-high flux through the membrane if it saved you money?
  1. As long as the membrane is able to provide the patient with the best care possible and save us money, then it would definitely be used. COST
2. Is your practice willing to purchase membranes in bulk (greater than 50 units at a time)?
  1. My clinic typically would like to purchase materials in bulk to get a volume pricing discount if possible since we have a very consistent, predictable and ongoing need. COST
3. How many patients, on average, do you have monthly?
  1. My practice has about 50 patients per month that come in for hemodialysis. N/A
4. Are you willing to use a membrane with lower flux if it means your patients will be in dialysis longer?
  1. No. We are not interested in doing so since our practice sees a lot of patients and if the treatment takes longer we would have to reduce the number of patients that we can treat. FLUX
5. Have you seen any magazine advertisements for our hemodialyzer membranes?
  1. I have seen a few membrane ads in medical magazines, but I have not seen any of yours specifically. MARKETABILITY
6. How many dialysis machines do you currently own and how many have you had to replace since your practice originally opened?
  1. My practice has 15 dialysis machines that are currently in use. I have had to replace three of them since my practice opened. N/A
7. How closely do you monitor blood cell reactivity?
  1. We try our best to minimize blood cell reactivity, as we do not want to impose any more discomfort than necessary on our patients. While we maintain the minimum legal requirement, we do not solely base our practice on the blood cell reactivity rate. BCR
8. Are you willing to pay more for a high-flux dialyzer?

1. The dialysis clinic is paid a set amount per treatment, and we have to provide care within that budget. Therefore, the cost of the membranes is very important to us. We would consider a higher cost membrane if it really improved patient care, but I'd want to really know how it improves patient outcomes. COST
9. Have you heard about any of our membranes through any other clinics or during any seminars?
  1. To be honest, I have not heard about your membranes or anything related to your company before. MARKETABILITY
10. How much is your clinic willing to pay for a membrane that has a suitable reliability?
  1. Though the membrane may have good reliability, we are still on a budget and would like to spend no more than \$80 on the membranes that we use. COST

### **HOSPITAL ADMINISTRATOR**

Nearly 175 acute and chronic kidney disease patients come into my hospital *every month*. My job is to control costs while providing the best possible care. With that said, I would like to purchase membranes that satisfy the minimal legal requirements (reliability, flux and blood cell reactivity) in bulk from you. As with all of my bulk orders, I do expect the overall price to be significantly lower than what a normal order would be due to volume discounts. I also tend to be less concerned with the reliability of the membrane since I have a large quantity in stock at the hospital.

1. Have you seen our ads for hemodialyzer membranes in any medical magazines or advertisements?
  1. What magazine did you advertise in? I have not seen any advertisements from your company before. MARKETABILITY
2. Would you be willing to have smaller, more frequent orders rather than one large bulk order?
  1. I would much rather buy the membranes in a bulk order as we go through many of them quickly. Frequent orders would mean I have to monitor membrane use much more closely and spend time ordering this item more often. Also, if I order smaller

quantities, any reliability problems could really affect the treatment of our patients.

#### RELIABILITY

3. Many patients tolerate different levels of pain. Are you willing to purchase membranes with different blood cell reactivity rates associated with the membrane in order to accommodate your patients?

1. I am not willing to order membranes based on different blood cell reactivity rates. I am interested in ordering membranes that meet the minimum legal requirements for blood cell reactivity. BCR

4. How many dialysis machines does your hospital currently have in use?

1. I currently have 15 dialysis machines in use in my hospital. N/A

5. Is your hospital willing to spend more money on a high-flux dialyzer for your patients?

1. As of right now, my hospital is not willing to spend more money in this area. We tend to use the minimum legally required membranes within our hospital, which is generally cheaper for us. COST

6. Would you ever consider making an exclusive sales contract with one company who could supply all of your dialysis membrane needs?

1. I would need to know more details before I could make this type of decision. The good part of having a large selection of vendors is that it is a competitive market which enables our hospital to get the best product at a great price point. COST

7. How important is it for your hospital to provide your patients with a comfortable setting?

1. We want our hospital to be known for patient care and overall well-being. We want our hospital to provide the maximum care for all patients and have them feel that they are comfortable. BCR

8. How does your hospital deal with the blood cell reactivity involved with the hemodialysis patients?

1. My hospital typically purchases membranes that have blood cell reactivity rates at the minimum legal requirement. BCR

9. Are you familiar with the use of carbon nanotubes within membranes?

1. I have heard of carbon nanotubes within dialysis membranes, and I do know that it makes the membrane significantly stronger. However, I do not know much more about them, or any details about the effects they have during dialysis. N/A
10. How long is a typical dialysis session at your hospital and would you be willing to accept longer or shorter sessions?
  1. A typical dialysis session in my hospital lasts for about four hours. Although shorter sessions could be advantageous if the overall treatment efficacy were the same, we wouldn't want the sessions to last any longer because it would limit the number of patients we could treat on a daily basis. FLUX

### **INDUSTRY THOUGHT LEADER**

I have been working in the field of hemodialysis for the majority of my career (greater than 30 years). My current position is Chief Medical Officer (CMO) for one of the large medical technology companies that work in the hemodialysis field. Recently, I was asked to compile my thoughts and reflections on dialysis and all the transitions the field has gone through over the course of my work in the field. Working together with other leading scientists, we have published a book that documents the history of dialysis, the changes in this field and the latest state of the art advances that we believe will lead this field into the next century.

1. Have you ever worked on the design of hemodialysis membranes?
  1. I have not specifically designed membranes although I have worked closely with biomedical engineers within my organization that have been involved in the design of these membranes. N/A
2. What specifications do you feel are most important to consider when making a hemodialysis membrane?
  1. From a pure technical standpoint, I believe that the blood cell reactivity and the flux you can achieve through the membrane are important to focus upon. FLUX and BCR
3. At your company does cost play a significant issue in design?

1. Cost always plays an issue but it is not the sole criterion. It is important that you balance cost with the overall quality of the design to create a product that customers will value. N/A
4. Have you ever seen any television or magazine ads for Nephrotex membranes?
  1. I am aware of Nephrotex and their hemodialysis membranes. As an industry leader, it is important to be aware of your competitors and what they are working on.  
MARKETABILITY
5. In the book on dialysis that you were recently involved with can you share what design parameters for membranes were discussed?
  1. We discussed all the key design parameters: membrane flux, blood cell reactivity, reliability and cost. N/A
6. In your expert position, do you feel that patients' pain threshold is an important factor in the design of hemodialysis membranes?
  1. I believe that this is a factor that needs to be considered when designing a device. However, this is not the sole criterion that needs to be accounted for. BCR
7. What are some of the state of the art advances that were discussed in the dialysis book?
  1. We discussed developments in the field overall but didn't examine specifically innovations related to the design of hemodialysis membranes, so unfortunately I cannot help you in this regard. N/A
8. As an industry leader, what compromises do you observe being made in the design of hemodialysis membranes?
  1. I believe that each company makes its own decisions; I wouldn't necessarily call these compromises, in order to provide the best possible product to their target customer.  
N/A
9. When deciding on the target flux for a membrane, are there any specific questions you seek answers for?
  1. We seek to determine what is important for our target customer and then utilize that information in the design of our membranes. N/A

10. What are your thoughts on the use of carbon nanotubes in a hemodialysis membrane?

1. I have read that they have extremely smooth walls which will allow for increased flow of fluids and gases through them. I believe that for this reason, they are an interesting possibility to consider in hemodialysis membrane design. FLUX

### **MEDICARE GOVERNMENT ASSISTANT**

As of 1972, the United States government extended Medicare coverage to all people of any age with end-stage renal disease. We cover up to 80 percent of the costs for the treatment of end-stage renal diseases, which includes both in-home and on-site patients. However, over the past few years, we have seen an increase in the average cost of treatment per individual with kidney disease. As of 2012, the average cost of treatment, dialysis, supplies and aide per person was roughly \$88,000. While we want every one of our customers to have the best treatment possible, we recognize that we do need to cut down on some areas of coverage for our customers due to the increasing costs. Our analysts have decided that one area we can cut down on costs is through limiting the selection of membranes used during the hemodialysis process for which we will cover costs. We would like to limit our coverage to a lower cost membrane while still providing our customers the best possible care.

1. What is the maximum price range you will cover for customers' membranes?

1. Medicare will cover up to \$80.00 for customers' membranes. COST

2. What percent of the total costs will you cover if your customers do in fact use a high priced membrane?

1. After the \$80.00 coverage, the customer will have to cover the cost. This is most often through a secondary insurance company but could be as an individual co-pay. COST

3. How important is it to you for your customers to be comfortable during the hemodialysis process?

1. We want our customers to be as comfortable as possible throughout their hemodialysis treatment. Additional pain and suffering would likely increase patient care costs long-term. BCR

4. How important is blood cell reactivity to the Medicare program?
  1. I will have to double check with our analysts before I can answer this question. Medicare wants to provide the most efficacious, efficient and comfortable treatment for each patient that we can finically support in a responsible, sustainable way. BCR
5. Are you willing to cover a membrane that is shown to be successful in waste removal in a smaller amount of time for the customer?
  1. Medicare would like to cover as efficient a membrane as possible for our customers; that is, one that reduces treatment times the most. As long as the membrane falls within our coverage limit, Medicare will cover the cost of a more efficient membrane. FLUX
6. Are you willing to cover a membrane that is associated with a small amount blood cell reactivity during a hemodialysis session?
  1. I will have to check my resources before I can answer any questions regarding blood cell reactivity. N/A
7. Will you cover more expensive membranes if it is proven that lower priced membranes did not sufficiently remove enough waste from the patients?
  1. I have to check my resources before I answer any questions about the waste removal rate. I do know that up until now, the membranes that Medicare has covered meet the minimum legal requirements for all aspects of dialyzers. N/A
8. How often do you see our membrane advertisements in medical magazines?
  1. As an agent for Medicare, I have not personally read or seen any magazines related to hemodialysis membranes. Medicare analysts are always up to date, however, so I would have to double check with them for this question. MARKETABILITY
9. Does your coverage fluctuate for the in-home or on-site patients?
  1. Medicare's coverage does not fluctuate between in-home and on-site patients. There is an 80 percent coverage for approved fees for customers. A private insurance company or a co-pay is required for the other 20 percent of the fees. N/A
10. How efficient of a membrane will Medicare cover?

1. Medicare will cover up to \$80.00 for any membrane that meets the minimal legal requirements. The efficiency of the membrane is not a consideration. COST

That's it. To God be the glory!

## BIBLIOGRAPHY

- [1] Markovetz MR, Corcoran TE, Locke LW, Myerburg MM, Pilewski JM, et al. (2014) A Physiologically-Motivated Compartment-Based Model of the Effect of Inhaled Hypertonic Saline on Mucociliary Clearance and Liquid Transport in Cystic Fibrosis. *PLoS ONE* 9: e111972.
- [2] Stutts MJ, Canessa CM, Olsen JC, Hamrick M, Cohn Ja, et al. (1995) CFTR as a cAMP-dependent regulator of sodium channels. *Science (New York, NY)* 269: 847–850.
- [3] Bertrand Ca, Zhang R, Pilewski JM, Frizzell Ra (2009) SLC26A9 is a constitutively active, CFTR-regulated anion conductance in human bronchial epithelia. *The Journal of general physiology* 133: 421–438.
- [4] Boucher RC (1994) Human Airway Ion Transport. *American journal of respiratory and critical care medicine* 150: 581–593.
- [5] Matsui H, Grubb BR, Tarran R, Randell SH, Gatzky JT, et al. (1998) Evidence for periciliary liquid layer depletion, not abnormal ion composition, in the pathogenesis of cystic fibrosis airways disease. *Cell* 95: 1005–1015.
- [6] Trimble AT, Donaldson SH (2015) Cftr modulator therapies for cystic fibrosis. *Pediatric Allergy, Immunology, and Pulmonology* 28: 230–236.
- [7] Bertrand C, Durand DM, Saidel GM, Laboissee C, Hopfer U (1998) System for dynamic measurements of membrane capacitance in intact epithelial monolayers. *Biophysical journal* 75: 2743–2756.
- [8] Locke LW, Myerburg MM, Markovetz MR, Parker RS, Weber L, et al. (2014) Quantitative imaging of airway liquid absorption in cystic fibrosis. *The European respiratory journal* : 1–10.
- [9] Matsui H, Davis CW, Tarran R, Boucher RC (2000) Osmotic water permeabilities of cultured, well-differentiated normal and cystic fibrosis airway epithelia. *Journal of Clinical Investigation* 105: 1419–1427.

- [10] Sood N, Bennett WD, Zeman K, Brown J, Foy C, et al. (2003) Increasing concentration of inhaled saline with or without amiloride: effect on mucociliary clearance in normal subjects. *American journal of respiratory and critical care medicine* 167: 158–163.
- [11] Boon M, Verleden SE, Bosch B, Lammertyn EJ, McDonough JE, et al. (2016) Morphometric analysis of explant lungs in cystic fibrosis. *American journal of respiratory and critical care medicine* 193: 516–526.
- [12] Tarran R, Grubb BR, Gatzky JT, Davis CW, Boucher RC (2001) The relative roles of passive surface forces and active ion transport in the modulation of airway surface liquid volume and composition. *The Journal of general physiology* 118: 223–36.
- [13] Myerburg MM, Harvey PR, Heidrich EM, Pilewski JM, Butterworth MB (2010) Acute regulation of the epithelial sodium channel in airway epithelia by proteases and trafficking. *American journal of respiratory cell and molecular biology* 43: 712–9.
- [14] Castellani S, Favia M, Guerra L, Carbone A, Abbattiscianni A, et al. (2016) Emerging relationship between cfr, actin and tight junction organization in cystic fibrosis airway epithelium. *Histology and histopathology* : 11842.
- [15] Palmer LG (1982) Ion selectivity of the apical membrane Na channel in the toad urinary bladder. *The Journal of Membrane Biology* 67: 91–98.
- [16] Garcia GJM, Boucher RC, Elston TC (2013) Biophysical model of ion transport across human respiratory epithelia allows quantification of ion permeabilities. *Biophysical journal* 104: 716–26.
- [17] O’Donoghue DL, Dua V, Moss GWJ, Vergani P (2013) Increased apical Na<sup>+</sup> permeability in cystic fibrosis is supported by a quantitative model of epithelial ion transport. *The Journal of physiology* 591: 3681–92.
- [18] Button B, Cai L, Ehre C, Kesimer M (2012) A periciliary brush promotes the lung health by separating the mucus layer from airway epithelia. *Science* 937.
- [19] Regnis Ja, Robinson M, Bailey DL, Cook P, Hooper P, et al. (1994) Mucociliary clearance in patients with cystic fibrosis and in normal subjects. *American journal of respiratory and critical care medicine* 150: 66–71.
- [20] Mauroy B, Fausser C, Pelca D, Merckx J, Flaud P (2011) Toward the modeling of mucus draining from the human lung: role of the geometry of the airway tree. *Physical biology* 8: 056006.
- [21] Corcoran TE, Thomas KM, Myerburg MM, Muthukrishnan a, Weber L, et al. (2010) Absorptive clearance of DTPA as an aerosol-based biomarker in the cystic fibrosis airway. *The European respiratory journal* 35: 781–6.

- [22] Donaldson SH, Bennett WD, Zeman KL, Knowles MR, Tarran R, et al. (2006) Mucus clearance and lung function in cystic fibrosis with hypertonic saline. *The New England journal of medicine* 354: 241–50.
- [23] Goralski JL, Boucher RC, Button B (2010) Osmolytes and ion transport modulators : new strategies for airway surface rehydration. *Current Opinion in Pharmacology* 10: 294–299.
- [24] Tarran R, Button B, Picher M, Paradiso AM, Ribeiro CM, et al. (2005) Normal and cystic fibrosis airway surface liquid homeostasis the effects of phasic shear stress and viral infections. *Journal of Biological Chemistry* 280: 35751–35759.
- [25] Chen JH, Stoltz DA, Karp PH, Ernst SE, Pezzulo AA, et al. (2010) Loss of anion transport without increased sodium absorption characterizes newborn porcine cystic fibrosis airway epithelia. *Cell* 143: 911–23.
- [26] Läuger P (1984) Thermodynamic and kinetic properties of electrogenic ion pumps. *Biochimica et Biophysica Acta (BBA)-Reviews on Biomembranes* 779: 307–341.
- [27] Goldman DE (1943) Potential, impedance, and rectification in membranes. *The Journal of General Physiology* 27: 37–60.
- [28] Fromter E, Diamond J (1972) Route of passive ion permeation in epithelia. *Nat New Biol* 235: 9–13.
- [29] House CR (1974) *Water transport in cells and tissues*. E. Arnold.
- [30] Ussing HH, Zerahn K (1951) Active transport of sodium as the source of electric current in the short-circuited isolated frog skin. *Acta physiologica Scandinavica* 23: 110–127.
- [31] Levi H, Ussing HH (1949) Resting potential and ion movements in the frog skin. *Nature* 164: 928–928.
- [32] Li H, Sheppard DN, Hug MJ (2004) Transepithelial electrical measurements with the Ussing chamber. *Journal of Cystic Fibrosis* 3: 123–126.
- [33] Frizzell RA, Hanrahan JW (2012) Physiology of epithelial chloride and fluid secretion. *Cold Spring Harbor perspectives in medicine* 2: a009563.
- [34] Anderson J, Van Itallie C (1995) Tight junctions and the molecular basis for regulation of paracellular permeability. *American Journal of Physiology-Gastrointestinal and Liver Physiology* 269: G467–G475.
- [35] Fronius M, Rehn M, Eckstein-Ludwig U, Clauss W (2001) Inhibitory non-genomic effects of progesterone on  $Na^+$  absorption in epithelial cells from xenopus kidney (a6). *Journal of Comparative Physiology B* 171: 377–386.

- [36] Bosch B, De Boeck K (2016) Searching for a cure for cystic fibrosis. a 25-year quest in a nutshell. *European journal of pediatrics* 175: 1–8.
- [37] Van Goor F, Hadida S, Grootenhuis PDJ, Burton B, Cao D, et al. (2009) Rescue of CF airway epithelial cell function in vitro by a CFTR potentiator, VX-770. *Proceedings of the National Academy of Sciences of the United States of America* 106: 18825–18830.
- [38] Kerem E, Konstan MW, De Boeck K, Accurso FJ, Sermet-Gaudelus I, et al. (2014) Ataluren for the treatment of nonsense-mutation cystic fibrosis: a randomised, double-blind, placebo-controlled phase 3 trial. *The Lancet Respiratory Medicine* 2: 539–547.
- [39] Brodlie M, Haq IJ, Roberts K, Elborn JS (2015) Targeted therapies to improve cftr function in cystic fibrosis. *Genome medicine* 7: 1.
- [40] Wainwright CE, Elborn JS, Ramsey BW, Marigowda G, Huang X, et al. (2015) Lumacaftor–ivacaftor in patients with cystic fibrosis homozygous for phe508del cftr. *New England Journal of Medicine* 373: 220–231.
- [41] Accurso F, Rowe S (2010) Effect of VX-770 in persons with cystic fibrosis and the G551D-CFTR mutation. . . . *England Journal of . . .*: 1991–2003.
- [42] Van Goor F, Hadida S, Grootenhuis PDJ, Burton B, Stack JH, et al. (2011) Correction of the F508del-CFTR protein processing defect in vitro by the investigational drug VX-809. *Proceedings of the National Academy of Sciences of the United States of America* 108: 18843–8.
- [43] Pilewski J, Cooke J, Lekstrom-Himes J, Donaldson S, et al. (2015) Ws01. 4 vx-661 in combination with ivacaftor in patients with cystic fibrosis and the f508del-cftr mutation. *Journal of Cystic Fibrosis* 14: S1.
- [44] Jones AM, Barry PJ (2015) Lumacaftor/ivacaftor for patients homozygous for phe508del-cftr: should we curb our enthusiasm? *Thorax* 70: 615–616.
- [45] for Sick Children H (2011). Cftr mutations database. URL <http://www.genet.sickkids.on.ca/StatisticsPage.html>.
- [46] Joyner MJ, Paneth N (2015) Seven questions for personalized medicine. *Jama* 314: 999–1000.
- [47] Stutts MJ, Rossier BC, Boucher RC (1997) Cystic fibrosis transmembrane conductance regulator inverts protein kinase a-mediated regulation of epithelial sodium channel single channel kinetics. *Journal of Biological Chemistry* 272: 14037–14040.
- [48] Dorwart MR, Shcheynikov N, Yang D, Muallem S (2008) The solute carrier 26 family of proteins in epithelial ion transport. *Physiology* 23: 104–114.
- [49] Tarran R, Button B, Boucher RC (2006) Regulation of normal and cystic fibrosis airway surface liquid volume by phasic shear stress. *Annual review of physiology* 68: 543–561.

- [50] Caputo A, Caci E, Ferrera L, Pedemonte N, Barsanti C, et al. (2008) Tmem16a, a membrane protein associated with calcium-dependent chloride channel activity. *Science* 322: 590–594.
- [51] Manzanares D, Gonzalez C, Ivonnet P, Chen RS, Valencia-Gattas M, et al. (2011) Functional apical large conductance,  $Ca^{2+}$ -activated, and voltage-dependent  $K^{+}$  channels are required for maintenance of airway surface liquid volume. *Journal of Biological Chemistry* 286: 19830–19839.
- [52] Schreiber R, Nitschke R, Greger R, Kunzelmann K (1999) The cystic fibrosis transmembrane conductance regulator activates aquaporin 3 in airway epithelial cells. *The Journal of biological chemistry* 274: 11811–11816.
- [53] Miyamoto H, Ikehara T, Yamaguchi H, Hosokawa K, Yonezu T, et al. (1986) Kinetic mechanism of  $Na^{+}$ ,  $K^{+}$ ,  $Cl^{-}$ -cotransport as studied by  $Rb^{+}$  influx into hela cells: effects of extracellular monovalent ions. *The Journal of membrane biology* 92: 135–150.
- [54] Lindenmayer GE, Schwartz A, Thompson HK (1974) A kinetic description for sodium and potassium effects on  $(Na^{+} + K^{+})$ -adenosine triphosphatase: a model for a two-nonequivalent site potassium activation and an analysis of multiequivalent site models for sodium activation. *The Journal of physiology* 236: 1–28.
- [55] Falkenberg CV, Jakobsson E (2010) A biophysical model for integration of electrical, osmotic, and pH regulation in the human bronchial epithelium. *Biophysical journal* 98: 1476–85.
- [56] Willumsen NJ, Boucher RC (1991) Sodium transport and intracellular sodium activity in cultured human nasal epithelium. *American Journal of Physiology-Cell Physiology* 261: C319–C331.
- [57] Shachar-Hill B, Hill A (1993) Convective fluid flow through the paracellular system of necturus gall-bladder epithelium as revealed by dextran probes. *The Journal of physiology* 468: 463.
- [58] Hill AE, Shachar-Hill Y (2013) Response to “what do aquaporin knockout studies tell us about fluid transport in epithelia?” *maclaren oj, sneyd j, crampin ej (2013) j membr biol* 246:297–305. *The Journal of Membrane Biology* 246: 665–667.
- [59] Fischbarg J, Diecke FPJ, Iserovich P, Rubashkin a (2006) The role of the tight junction in paracellular fluid transport across corneal endothelium. Electro-osmosis as a driving force. *Journal of Membrane Biology* 210: 117–130.
- [60] Fischbarg J (2010) Fluid transport across leaky epithelia: central role of the tight junction and supporting role of aquaporins. *Physiological reviews* 90: 1271–1290.
- [61] Reuss L (2009) Water transport by epithelia. *eLS* .

- [62] Maclaren OJ, Sneyd J, Crampin EJ (2013) What do aquaporin knockout studies tell us about fluid transport in epithelia? *The Journal of Membrane Biology* 246: 297–305.
- [63] Kovbasnjuk O, Leader JP, Weinstein AM, Spring KR (1998) Water does not flow across the tight junctions of mdck cell epithelium. *Proceedings of the National Academy of Sciences* 95: 6526–6530.
- [64] Spring KR (1998) Routes and mechanism of fluid transport by epithelia 1. *Annual Review of Physiology* 60: 105–119.
- [65] Corcoran TE, Thomas KM, Brown S, Myerburg MM, Locke LW, et al. (2013) Liquid hyper-absorption as a cause of increased DTPA clearance in the cystic fibrosis airway. *EJNMMI research* 3: 14.
- [66] Kitano H (2002) Systems biology: a brief overview. *Science* 295: 1662–1664.
- [67] Bard J (2013) Systems biology — the broader perspective. *Cells* 2: 414.
- [68] Smith N, Crampin E (2004) Development of models of active ion transport for whole-cell modelling: cardiac sodium–potassium pump as a case study. *Progress in biophysics and molecular biology* 85: 387–405.
- [69] Benjamin B, Johnson E (1997) A quantitative description of the na-k-2cl cotransporter and its conformity to experimental data. *American Journal of Physiology-Renal Physiology* 273: F473–F482.
- [70] Warren NJ, Tawhai MH, Crampin EJ (2009) A mathematical model of calcium-induced fluid secretion in airway epithelium. *Journal of Theoretical Biology* 259: 837–849.
- [71] Federoff HJ, Gostin LO (2009) Evolving from reductionism to holism: is there a future for systems medicine? *JAMA* 302: 994–996.
- [72] Ledzewicz U, Schättler H (2002) Optimal Bang-Bang Controls for a Two-Compartment Model in Cancer Chemotherapy. *J Optimization Theory Appl* 114: 609–637.
- [73] Friberg LE, Henningson A, Maas H, et al (2002) Model of Chemotherapy-induced Myelosuppression with Parameter Consistency Across Drugs. *Cancer Res* 20: 523–527.
- [74] Harrold JM, Eiseman JL, Joseph E, Strychor S, Zamboni WC, et al. (2005) Control-relevant modeling of the antitumor effects of 9-nitrocamptothecin in SCID mice bearing HT29 human colon xenografts. *Journal of pharmacokinetics and pharmacodynamics* 32: 65–83.
- [75] Florian Ja, Eiseman JL, Parker RS (2008) Nonlinear model predictive control for dosing daily anticancer agents using a novel saturating-rate cell-cycle model. *Computers in biology and medicine* 38: 339–47.

- [76] Ho T, Clermont G, Parker RS (2013) A model of neutrophil dynamics in response to inflammatory and cancer chemotherapy challenges. *Computers & Chemical Engineering* 51: 187–196.
- [77] Parker RS, Doyle FJ, Peppas NA (1999) A model-based algorithm for blood glucose control in type i diabetic patients. *IEEE Transactions on biomedical engineering* 46: 148–157.
- [78] Kitano H, Oda K, Kimura T, Matsuoka Y, Csete M, et al. (2004) Metabolic syndrome and robustness tradeoffs. *Diabetes* 53 Suppl 3: S6–S15.
- [79] Roy A, Parker RS (2006) Dynamic modeling of free fatty acid, glucose, and insulin: An extended” minimal model”. *Diabetes technology & therapeutics* 8: 617–626.
- [80] Lin J, Razak NN, Pretty CG, Le Compte A, Docherty P, et al. (2011) A physiological intensive control insulin-nutrition-glucose (icing) model validated in critically ill patients. *Computer methods and programs in biomedicine* 102: 192–205.
- [81] Vilkhovoy M, Pritchard-Bell A, Clermont G, Parker RS (2014) A control-relevant model of subcutaneous insulin absorption. *IFAC Proceedings Volumes* 47: 10988–10993.
- [82] Knab TD, Clermont G, Parker RS (2015) Zone model predictive control and moving horizon estimation for the regulation of blood glucose in critical care patients. *IFAC-PapersOnLine* 48: 1002–1007.
- [83] Dick TE, Molkov YI, Nieman G, Hsieh YH, Jacono FJ, et al. (2012) Linking inflammation, cardiorespiratory variability, and neural control in acute inflammation via computational modeling. *Frontiers in Physiology* 3 JUL.
- [84] Zhang LA, Parker RS, Swigon D, Banerjee I, Bahrami S, et al. (2016) A one-nearest-neighbor approach to identify the original time of infection using censored baboon sepsis data. *Critical care medicine* 44: e432–e442.
- [85] Perelson AS, Neumann AU, Markowitz M, Leonard JM, Ho DD (1996) Hiv-1 dynamics in vivo: virion clearance rate, infected cell life-span, and viral generation time. *Science* 271: 1582.
- [86] Oda K, Matsuoka Y, Funahashi A, Kitano H (2005) A comprehensive pathway map of epidermal growth factor receptor signaling. *Molecular systems biology* 1.
- [87] Hartmann T, Verkman aS (1990) Model of ion transport regulation in chloride-secreting airway epithelial cells. Integrated description of electrical, chemical, and fluorescence measurements. *Biophysical journal* 58: 391–401.
- [88] Novotny JA, Jakobsson E (1996) Computational studies of ion-water flux coupling in the airway epithelium. i. construction of model. *American Journal of Physiology-Cell Physiology* 270: C1751–C1763.

- [89] Novotny JA, Jakobsson E (1996) Computational studies of ion-water flux coupling in the airway epithelium. ii. role of specific transport mechanisms. *American Journal of Physiology-Cell Physiology* 270: C1764–C1772.
- [90] Fischbarg J, Diecke FPJ (2005) A mathematical model of electrolyte and fluid transport across corneal endothelium. *The Journal of membrane biology* 203: 41–56.
- [91] Zhu H, Chauhan A (2007) Tear dynamics model. *Current eye research* 32: 177–97.
- [92] Terashima K, Takeuchi a, Sarai N, Matsuoka S, Shim EB, et al. (2006) Modelling Cl<sup>-</sup> homeostasis and volume regulation of the cardiac cell. *Philosophical transactions Series A, Mathematical, physical, and engineering sciences* 364: 1245–1265.
- [93] Willumsen NJ, Boucher RC (1991) Transcellular sodium transport in cultured cystic fibrosis human nasal epithelium. *American Journal of Physiology-Cell Physiology* 261: C332–C341.
- [94] Knowles MR, Robinson JM, Wood RE, Pue CA, Mentz WM, et al. (1997) Ion composition of airway surface liquid of patients with cystic fibrosis as compared with normal and disease-control subjects. *Journal of Clinical Investigation* 100: 2588.
- [95] Okada SF, Nicholas RA, Kreda SM, Lazarowski ER, Boucher RC (2006) Physiological regulation of atp release at the apical surface of human airway epithelia. *Journal of Biological Chemistry* 281: 22992–23002.
- [96] Herschlag G, Garcia GJM, Button B, Tarran R, Lindley B, et al. (2013) A mechanochemical model for auto-regulation of lung airway surface layer volume. *Journal of theoretical biology* 325: 42–51.
- [97] Harvey PR, Tarran R, Garoff S, Myerburg MM (2011) Measurement of the airway surface liquid volume with simple light refraction microscopy. *American journal of respiratory cell and molecular biology* 45: 592–9.
- [98] Liu L, Shastry S, Byan-Parker S, Houser G, K Chu K, et al. (2014) An Autoregulatory Mechanism Governing Mucociliary Transport Is Sensitive to Mucus Load. *American Journal of Respiratory Cell and Molecular Biology* 51: 485–493.
- [99] Bennett WD, Laube BL, Corcoran T, Zeman K, Sharpless G, et al. (2013) Multisite comparison of mucociliary and cough clearance measures using standardized methods. *Journal of aerosol medicine and pulmonary drug delivery* 26: 157–64.
- [100] Rocci ML, Jusko WJ (1983) Lagran program for area and moments in pharmacokinetic analysis. *Computer programs in biomedicine* 16: 203–216.
- [101] Geller DE, Pitlick WH, Nardella PA, Tracewell WG, Ramsey BW (2002) Pharmacokinetics and bioavailability of aerosolized tobramycin in cystic fibrosis. *CHEST Journal* 122: 219–226.

- [102] Burness CB, Keating GM (2012) Mannitol Dry Powder for Inhalation. *Drugs* 72: 1411–1421.
- [103] Wilkinson PK, Sedman AJ, Sakmar E, Kay DR, Wagner JG (1977) Pharmacokinetics of ethanol after oral administration in the fasting state. *Journal of pharmacokinetics and biopharmaceutics* 5: 207–224.
- [104] Li J, Coulthard K, Milne R, Nation RL, Conway S, et al. (2003) Steady-state pharmacokinetics of intravenous colistin methanesulphonate in patients with cystic fibrosis. *Journal of Antimicrobial Chemotherapy* 52: 987–992.
- [105] Geller DE, Konstan MW, Smith J, Noonberg SB, Conrad C (2007) Novel tobramycin inhalation powder in cystic fibrosis subjects: pharmacokinetics and safety. *Pediatric pulmonology* 42: 307–313.
- [106] Vic P, Ategbro S, Turck D, Husson M, Launay V, et al. (1998) Efficacy, tolerance, and pharmacokinetics of once daily tobramycin for pseudomonas exacerbations in cystic fibrosis. *Archives of disease in childhood* 78: 536–539.
- [107] Yaffe SJ, Gerbracht LM, Mosovich LL, Mattar ME, Danish M, et al. (1977) Pharmacokinetics of methicillin in patients with cystic fibrosis. *Journal of Infectious Diseases* 135: 828–831.
- [108] Ratjen F, Rietschel E, Kasel D, Schwiertz R, Starke K, et al. (2006) Pharmacokinetics of inhaled colistin in patients with cystic fibrosis. *Journal of Antimicrobial Chemotherapy* 57: 306–311.
- [109] Monogue ML, Pettit RS, Muhlebach M, Cies JJ, Nicolau DP, et al. (2016) Population pharmacokinetics and safety of ceftolozane/tazobactam in adult cystic fibrosis patients admitted with acute pulmonary exacerbation. *Antimicrobial Agents and Chemotherapy* : AAC–01566.
- [110] Xu H, Zhou W, Zhou D, Li J, Al-Huniti N (2016) Evaluation of aztreonam dosing regimens in patients with normal and impaired renal function: A population pharmacokinetic modeling and monte carlo simulation analysis. *The Journal of Clinical Pharmacology* .
- [111] Costabile G, d’Angelo I, di Villa Bianca Rd, Mitidieri E, Pompili B, et al. (2016) Development of inhalable hyaluronan/mannitol composite dry powders for flucytosine repositioning in local therapy of lung infections. *Journal of Controlled Release* 238: 80–91.
- [112] Devereux G, Steele S, Griffiths K, Devlin E, Fraser-Pitt D, et al. (2016) An open-label investigation of the pharmacokinetics and tolerability of oral cysteamine in adults with cystic fibrosis. *Clinical drug investigation* : 1–8.

- [113] Le Brun P, De Boer A, Mannes G, De Fraiture D, Brimicombe R, et al. (2002) Dry powder inhalation of antibiotics in cystic fibrosis therapy: part 2: inhalation of a novel colistin dry powder formulation: a feasibility study in healthy volunteers and patients. *European Journal of Pharmaceutics and Biopharmaceutics* 54: 25–32.
- [114] Gibson RL, Retsch-Bogart GZ, Oermann C, Milla C, Pilewski J, et al. (2006) Microbiology, safety, and pharmacokinetics of aztreonam lysinate for inhalation in patients with cystic fibrosis. *Pediatric pulmonology* 41: 656–665.
- [115] Geller DE, Flume PA, Griffith DC, Morgan E, White D, et al. (2011) Pharmacokinetics and safety of mp-376 (levofloxacin inhalation solution) in cystic fibrosis subjects. *Antimicrobial agents and chemotherapy* 55: 2636–2640.
- [116] Sakagami M (2006) In vivo, in vitro and ex vivo models to assess pulmonary absorption and disposition of inhaled therapeutics for systemic delivery. *Advanced drug delivery reviews* 58: 1030–60.
- [117] Sakagami M, Byron PR, Venitz J, Rypacek F (2002) Solute disposition in the rat lung in vivo and in vitro: determining regional absorption kinetics in the presence of mucociliary escalator. *Journal of pharmaceutical sciences* 91: 594–604.
- [118] Weber B, Hochhaus G (2013) A pharmacokinetic simulation tool for inhaled corticosteroids. *The AAPS journal* 15: 159–71.
- [119] O’Reilly R, Elphick HE (2013) Development, clinical utility, and place of ivacaftor in the treatment of cystic fibrosis. *Drug design, development and therapy* 7: 929–37.
- [120] Boucher RC (2007) Cystic fibrosis: a disease of vulnerability to airway surface dehydration. *Trends in molecular medicine* 13: 231–40.
- [121] Elkins MR, Sc MH, Robinson M, Ph D, Rose BR, et al. (2006) new england journal. *New England Journal of ...* 354: 229–240.
- [122] Bennett WD, Ilowite JS (1989) Dual pathway clearance of 99mtc-dtpa from the bronchial mucosa<sup>1</sup> 3. *The American review of respiratory disease* 139: 1132.
- [123] Ilowite JS, Bennett WD, Sheetz MS, Groth ML, Nierman DM (1989) Permeability of the bronchial mucosa to 99mtc-dtpa in asthma. *American Review of Respiratory Disease* 139: 1139–1143.
- [124] Eckford PDW, Li C, Ramjeesingh M, Bear CE (2012) Cystic fibrosis transmembrane conductance regulator (CFTR) potentiator VX-770 (ivacaftor) opens the defective channel gate of mutant CFTR in a phosphorylation-dependent but ATP-independent manner. *The Journal of biological chemistry* 287: 36639–49.
- [125] Corcoran T, Niven R, Verret W, Dilly S, Johnson B (2014) Lung deposition and pharmacokinetics of nebulized cyclosporine in lung transplant patients. *Journal of aerosol medicine and pulmonary drug delivery* 27: 178–184.

- [126] BYRON P, PATTON J (1994) Drug delivery via the respiratory tract. *Journal of Aerosol medicine* 7: 49–75.
- [127] Sturm R (2012) An advanced stochastic model for mucociliary particle clearance in cystic fibrosis lungs. *Journal of Thoracic Disease* 4: 48–57.
- [128] Akaike H (1974) A new look at the statistical model identification. *Automatic Control, IEEE Transactions on* .
- [129] Yamaoka K, Nakagawa T, Uno T (1978) Application of Akaike’s information criterion (AIC) in the evaluation of linear pharmacokinetic equations. *Journal of pharmacokinetics and biopharmaceutics* 6: 165–75.
- [130] Biddiscombe MF, Meah SN, Underwood SR, Usmani OS (2011) Comparing lung regions of interest in gamma scintigraphy for assessing inhaled therapeutic aerosol deposition. *Journal of aerosol medicine and pulmonary drug delivery* 24: 165–173.
- [131] Donaldson SH, Corcoran TE, Laube BL, Bennett WD (2007) Mucociliary clearance as an outcome measure for cystic fibrosis clinical research. *Proceedings of the American Thoracic Society* 4: 399–405.
- [132] Locke LW, Myerburg MM, Weiner DJ, Markovetz MR, Parker RS, et al. (2016) Pseudomonas infection and mucociliary and absorptive clearance in the cystic fibrosis lung. *European Respiratory Journal* : ERJ-01880.
- [133] Newman S, Bennett WD, Biddiscombe M, Devadason SG, Dolovich MB, et al. (2012) Standardization of techniques for using planar (2D) imaging for aerosol deposition assessment of orally inhaled products. *J Aerosol Med Pulm Drug Deliv* 25 Suppl 1: S10–28.
- [134] Raue a, Kreutz C, Maiwald T, Bachmann J, Schilling M, et al. (2009) Structural and practical identifiability analysis of partially observed dynamical models by exploiting the profile likelihood. *Bioinformatics (Oxford, England)* 25: 1923–9.
- [135] Hoegger MJ, Awadalla M, Namati E, Itani Oa, Fischer AJ, et al. (2014) Assessing mucociliary transport of single particles in vivo shows variable speed and preference for the ventral trachea in newborn pigs. *Proceedings of the National Academy of Sciences of the United States of America* 111: 2355–60.
- [136] Robinson M, Daviskas E, Eberl S, Baker J, Chan HK, et al. (1999) The effect of inhaled mannitol on bronchial mucus clearance in cystic fibrosis patients: A pilot study. *European Respiratory Journal* 14: 678–685.
- [137] Birket DSE, Chu DKK, Liu DL, Houser DGH, Diephuis MBJ, et al. (2014) A Functional Anatomic Defect of the Cystic Fibrosis Airway 190: 421–432.

- [138] Vázquez E, Nobles M, Valverde Ma (2001) Defective regulatory volume decrease in human cystic fibrosis tracheal cells because of altered regulation of intermediate conductance  $\text{Ca}^{2+}$ -dependent potassium channels. *Proceedings of the National Academy of Sciences of the United States of America* 98: 5329–5334.
- [139] Chanson M, Scerri I, Suter S (1999) Defective regulation of gap junctional coupling in cystic fibrosis pancreatic duct cells. *The Journal of clinical investigation* 103: 1677–84.
- [140] Coyne CB, Vanhook MK, Gambling TM, Carson JL, Boucher RC, et al. (2002) Regulation of airway tight junctions by proinflammatory cytokines. *Molecular biology of the cell* 13: 3218–3234.
- [141] Molina SA, Stauffer B, Moriarty HK, Kim AH, McCarty NA, et al. (2015) Junctional abnormalities in human airway epithelial cells expressing delF508 CFTR. *American journal of physiology Lung cellular and molecular physiology* : ajplung.00060.2015.
- [142] Hogg JS (2013) Advances in rule-based modeling: compartments, energy, and hybrid simulation, with application to sepsis and cell signaling. Ph.D. thesis, University of Pittsburgh.
- [143] Boucher RC (1994) Human Airway Ion Transport. *American journal of respiratory and critical care medicine* 150: 271–281.
- [144] Fischbarg J, Kuang KY, Vera JC, Arant S, Silverstein SC, et al. (1990) Glucose transporters serve as water channels. *Proceedings of the National Academy of Sciences of the United States of America* 87: 3244–7.
- [145] Farinas J, Simanek V, Verkman aS (1995) Cell volume measured by total internal reflection microfluorimetry: application to water and solute transport in cells transfected with water channel homologs. *Biophysical journal* 68: 1613–1620.
- [146] Farinas J, Verkman aS (1996) Cell volume and plasma membrane osmotic water permeability in epithelial cell layers measured by interferometry. *Biophysical journal* 71: 3511–3522.
- [147] Ballard DH (1981) Generalizing the hough transform to detect arbitrary shapes. *Pattern recognition* 13: 111–122.
- [148] Lennernäs H (1995) Does fluid flow across the intestinal mucosa affect quantitative oral drug absorption? Is it time for a reevaluation? *Pharmaceutical research* .
- [149] Schnermann J, Chou CL, Ma T, Traynor T, Knepper Ma, et al. (1998) Defective proximal tubular fluid reabsorption in transgenic aquaporin-1 null mice. *Proceedings of the National Academy of Sciences of the United States of America* 95: 9660–9664.
- [150] Goralski J, Button B (2013) Faster is not always better: relationship between hypertonic saline aerosolization rate, airway hydration, and cell volume. In: *PEDIATRIC*

PULMONOLOGY. WILEY-BLACKWELL 111 RIVER ST, HOBOKEN 07030-5774, NJ USA, volume 48, pp. 243–243.

- [151] Patton JS, Brain JD, Davies LA, Fiegel J, Gumbleton M, et al. (2010) The particle has landed—characterizing the fate of inhaled pharmaceuticals. *Journal of Aerosol Medicine and Pulmonary Drug Delivery* 23: S–71.
- [152] ParionSciences (2013) INVESTIGATOR BROCHURE - tPAD trans-Nasal Pulmonary Aerosol Delivery of Hypertonic Saline : 1–61.
- [153] Weibel E (1965) Morphometry of the human lung. *Anesthesiology* .
- [154] Martonen T (1993) Mathematical model for the selective deposition of inhaled pharmaceuticals. *Journal of pharmaceutical sciences* 82: 1191–1199.
- [155] Gerrity TR, Lee PS, Hass FJ, Marinelli A, Werner P, et al. (1979) Calculated deposition of inhaled particles in the airway generations of normal subjects. *Journal of Applied Physiology* 47: 867–873.
- [156] Bennett WD, Wu J, Fuller F, Balcazar JR, Zeman KL, et al. (2015) Duration of action of hypertonic saline on mucociliary clearance in the normal lung. *Journal of Applied Physiology* : jap-00404.
- [157] Itani Oa, Chen Jh, Karp PH, Ernst S, Keshavjee S, et al. (2011) Human cystic fibrosis airway epithelia have reduced Cl<sup>-</sup> conductance but not increased Na<sup>+</sup> conductance. *Proceedings of the National Academy of Sciences of the United States of America* 108: 10260–5.
- [158] Cobelli C, Distefano JJ, Distefano JJ, Parameter III (2013) Parameter and structural identifiability concepts and ambiguities : a critical review and analysis Parameter and structural identifiability concepts and ambiguities : a critical review and analysis .
- [159] Rooney WC, Biegler LT (2001) Design for Model Parameter Uncertainty Using Non-linear Confidence Regions. *AIChE Journal* 47.
- [160] Raue A, Becker V, Klingmüller U, Timmer J (2010) Identifiability and observability analysis for experimental design in nonlinear dynamical models. *Chaos: An Interdisciplinary Journal of Nonlinear Science* 20: 045105.
- [161] Cobelli C, Lepschy A, Jacur GR (1979) Identifiability of compartmental systems and related structural properties. *Mathematical Biosciences* 44: 1–18.
- [162] Kalman RE (1963) Mathematical description of linear dynamical systems. *Journal of the Society for Industrial and Applied Mathematics, Series A: Control* 1: 152–192.
- [163] Hermann R, Krener A (1977) Nonlinear controllability and observability. *IEEE Transactions on automatic control* 22: 728–740.

- [164] Whalen AJ, Brennan SN, Sauer TD, Schiff SJ (2015) Observability and controllability of nonlinear networks: The role of symmetry. *Physical Review X* 5: 011005.
- [165] Wächter A, Biegler LT (2006) On the implementation of an interior-point filter line-search algorithm for large-scale nonlinear programming. *Mathematical Programming* 106: 25–57.
- [166] Moles CG, Mendes P, Banga JR (2003) Parameter estimation in biochemical pathways: a comparison of global optimization methods. *Genome research* 13: 2467–2474.
- [167] Hirmajer T, Balsa-Canto E, Banga JR (2009) Dotcvpsb, a software toolbox for dynamic optimization in systems biology. *BMC bioinformatics* 10: 1.
- [168] Raue A, Schilling M, Bachmann J, Matteson A, Schelker M, et al. (2013) Lessons learned from quantitative dynamical modeling in systems biology. *PloS one* 8: e74335.
- [169] Sahinidis NV (1996) Baron: A general purpose global optimization software package. *Journal of global optimization* 8: 201–205.
- [170] Byrd RH, Nocedal J, Waltz RA (2006) Knitro: An integrated package for nonlinear optimization. In: *Large-scale nonlinear optimization*, Springer. pp. 35–59.
- [171] Runarsson TP, Yao X (2000) Stochastic ranking for constrained evolutionary optimization. *IEEE Transactions on evolutionary computation* 4: 284–294.
- [172] Szu H, Hartley R (1987) Fast simulated annealing. *Physics letters A* 122: 157–162.
- [173] Zhang LA, Parker RS, Clermont G Apt-mcmc. In Preparation .
- [174] Landaw E, DiStefano JJ (1984) Multiexponential, multicompartmental, and noncompartmental modeling. ii. data analysis and statistical considerations. *American Journal of Physiology-Regulatory, Integrative and Comparative Physiology* 246: R665–R677.
- [175] Word DP, Young JK, Cummings DA, Iamsirithaworn S, Laird CD (2013) Interior-point methods for estimating seasonal parameters in discrete-time infectious disease models. *PloS one* 8: e74208.
- [176] Gallant AR (1987) *Nonlinear statistical models*, volume 310. John Wiley & Sons.
- [177] Hart WE, Laird C, Watson JP, Woodruff DL (2012) *Pyomo—optimization modeling in python*, volume 67. Springer Science & Business Media.
- [178] Fourer R, Gay D, Kernighan B (1993) *Ampl*, volume 117. Boyd & Fraser Danvers, MA.
- [179] Nicholson B, Sirola JD, Watson JP, Zavala VM, Biegler LT pyomo. dae: A modeling and automatic discretization framework for optimization with differential and algebraic equations .

- [180] Esposito WR, Floudas CA (2000) Global optimization for the parameter estimation of differential-algebraic systems. *Industrial & Engineering Chemistry Research* 39: 1291–1310.
- [181] Van de Vusse J (1964) Plug-flow type reactor versus tank reactor. *Chemical Engineering Science* 19: 994–996.
- [182] Doyle III FJ, Ogunnaike BA, Pearson RK (1995) Nonlinear Model-based Control Using Second-order Volterra Models. *Automatica* 31: 697–714.
- [183] Feinberg M, Hildebrandt D (1997) Optimal reactor design from a geometric viewpoint—i. universal properties of the attainable region. *Chemical Engineering Science* 52: 1637–1665.
- [184] Sistu PB, Bequette BW (1995) Model predictive control of processes with input multiplicities. *Chemical engineering science* 50: 921–936.
- [185] Gadkar KG, Gunawan R, Doyle FJ (2005) Iterative approach to model identification of biological networks. *BMC bioinformatics* 6: 1.
- [186] Daun S, Rubin J, Vodovotz Y, Roy A, Parker R, et al. (2008) An ensemble of models of the acute inflammatory response to bacterial lipopolysaccharide in rats: results from parameter space reduction. *Journal of theoretical biology* 253: 843–53.
- [187] Kremling A, Fischer S, Gadkar K, Doyle FJ, Sauter T, et al. (2004) A benchmark for methods in reverse engineering and model discrimination: problem formulation and solutions. *Genome Research* 14: 1773–1785.
- [188] Faller D, Klingmüller U, Timmer J (2003) Simulation methods for optimal experimental design in systems biology. *Simulation* 79: 717–725.
- [189] Rymut SM, Ivy T, Corey DA, Cotton CU, Burgess JD, et al. (2015) Role of exchange protein activated by camp 1 in regulating rates of microtubule formation in cystic fibrosis epithelial cells. *American journal of respiratory cell and molecular biology* 53: 853–862.
- [190] Manzanares D, Krick S, Baumlin N, Dennis JS, Tyrrell J, et al. (2015) Airway surface dehydration by transforming growth factor  $\beta$  (tgf- $\beta$ ) in cystic fibrosis is due to decreased function of a voltage-dependent potassium channel and can be rescued by the drug pirfenidone. *Journal of Biological Chemistry* 290: 25710–25716.
- [191] Accurso FJ, Moss RB, Wilmott RW, Anbar RD, Schaberg AE, et al. (2011) Denufosal tetrasodium in patients with cystic fibrosis and normal to mildly impaired lung function. *American journal of respiratory and critical care medicine* 183: 627–634.
- [192] Muske KR, Rawlings JB (1993) Model Predictive Control with Linear Models. *AIChE J* 39: 262–287.

- [193] Byers T, Seelig T, Sheppard S, Weilerstein P (2013) The Bridge - Summer 2013 - v43n2. The Bridge 43.
- [194] Bodnar CA, Clark RM, Besterfield-Sacre M (2015) Lessons Learned through Sequential Offerings of an Innovation and Entrepreneurship Boot Camp for Sophomore Engineering Students. *Journal of Engineering Entrepreneurship* 6: 52–67.
- [195] Purzer S, Fila N, Nataraja K (2016) Evaluation of current assessment methods in engineering entrepreneurship education. *Advances in Engineering Education* 5: n1.
- [196] Täks M, Tynjälä P, Toding M, Kukemelk H, Venesaar U (2014) Engineering students' experiences in studying entrepreneurship. *Journal of Engineering Education* 103: 573–598.
- [197] Rogy KM (2010) Examining the Entrepreneurial Mindset of Senior Chemical Engineering Students as a Result of Exposure to the Epistemic Game "Nephrotex" Examining the Entrepreneurial Mindset of Senior Chemical Engineering Students as a Result of Exposure to the Epistemic .
- [198] Schar M, Sheppard S, Brunhaver S, Cuson M, Grau MM (2014) Bending moments to business models: Integrating an entrepreneurship case study as part of core mechanical engineering curriculum. *The Journal of Engineering Entrepreneurship* 5: 1–18.
- [199] Litzinger T, Lattuca LR, Hadgraft R, Newstetter W (2011) Engineering Education and the Development of Expertise. *Journal of Engineering Education* 100: 123–150.
- [200] Gibb A (2002) In pursuit of a new 'enterprise' and 'entrepreneurship' paradigm for learning: creative destruction, new values, new ways of doing things and new combinations of knowledge. *International Journal of Management Reviews* 4: 233.
- [201] Ramsey E, Smith K, Martin L, Gibb A (2011) Concepts into practice: meeting the challenge of development of entrepreneurship educators around an innovative paradigm: The case of the international entrepreneurship educators' programme (ieep). *International Journal of Entrepreneurial Behavior & Research* 17: 146–165.
- [202] Kriewall, Timothy J, Mekemson K (2010) Instilling the Entrepreneurial Mindset Into Engineering. *The Journal Of engineering entrepreneurship* 1: 5–19.
- [203] Ortiz-Medina, Leovigilda, Fernández-Ahumada E, Lara-Vélez P, Garrido-Varo A, Pérez-Marín D, Guerrero-Ginel JE (2014) Assessing an Entrepreneurship Education Project in Engineering Studies by Means of Participatory Techniques. *Advances in Engineering Education* : 1–30.
- [204] Damon W, Lerner R (2008) Entrepreneurship across the life span: A developmental analysis and review of key findings. Kansas City: Kauffman Foundation .
- [205] Antoncic B, Hisrich RD (2003) Clarifying the intrapreneurship concept. *Journal of Small Business and Enterprise Development* 10: 7–24.

- [206] Akao Y (2004) Quality function deployment .
- [207] Woodruff RB (1997) Customer value: The next source for competitive advantage. *Journal of the Academy of Marketing Science* 25: 139–153.
- [208] Pahl G, Beitz W, Feldhusen J, Grote KH, Approach aS (2007) Engineering design: a systematic approach. doi:10.1007/978-1-84628-319-2.
- [209] Lin MC, Wang CC, Chen MS, Chang CA (2008) Using AHP and TOPSIS approaches in customer-driven product design process. *Computers in Industry* 59: 17–31.
- [210] Norman DA (2013) *The Design of Everyday Things, Revised and Expanded Edition*. Currency-Doubleday.
- [211] Rae D (2003) Opportunity centred learning: an innovation in enterprise education? *Education + Training* 45: 542–549.
- [212] Newstetter, Wendy, McCracken M (2001) Novice conceptions of design: Implications for the design of learning environments. In: *Design Knowing and Learning: Cognition in Design Education*. pp. 63–77.
- [213] Chi, MT, Glaser, R FM (1998) *The nature of expertise*. Hillsdale, NJ: Lawrence Erlbaum Assoc., Inc.
- [214] Freeman S, Eddy SL, McDonough M, Smith MK, Okoroafor N, et al. (2014) Active learning increases student performance in science, engineering, and mathematics. *Proceedings of the National Academy of Sciences* 111: 8410–8415.
- [215] Mina M, Gerdes RM (2006) The pedantic 21st century freshman engineering student. *European journal of engineering education* 31: 509–516.
- [216] Hatfield D, Shaffer DW (2006) Press play: Designing an epistemic game engine for journalism. In: *Proceedings of the 7th international conference on Learning sciences*. International Society of the Learning Sciences, pp. 236–242.
- [217] Svarovsky GN, Shaffer DW (2007) Sodaconstructing knowledge through exploratoids. *Journal of Research in Science Teaching* 44: 133–153.
- [218] Shaffer DW (2004) Epistemic frames and islands of expertise: Learning from infusion experiences. In: *Proceedings of the 6th international conference on Learning sciences*. International Society of the Learning Sciences, pp. 473–480.
- [219] Chesler NC, Arastoopour G, D’Angelo CM, Bagley EA, Shaffer DW (2013) Design of a professional practice simulator for educating and motivating first-year engineering students. *Advances in Engineering Education* 3: 1–29.
- [220] Rohde M, Shaffer DW (2003) Us, ourselves, and we: Thoughts about social (self-) categorization. *ACM SIGGROUP Bulletin* 24: 19–24.

- [221] Shaffer DW (2006) Epistemic frames for epistemic games. *Computers & education* 46: 223–234.
- [222] Arastoopour G, Chesler NC, Shaffer DW (2014) Epistemic persistence: A simulation-based approach to increasing participation of women in engineering. *Journal of Women and Minorities in Science and Engineering* 20.
- [223] Langford J, McDonagh D (2003) *Focus groups: supporting effective product development*. CRC press.
- [224] Arastoopour G, Collier W, Chesler NC, Linderoth J, Shaffer DW (2015) Measuring the complexity of simulated engineering design problems. *American Society for Engineering Education* .
- [225] Neuendorf KA (2002) *The content analysis guidebook*. Sage.
- [226] Sullivan GM, Feinn R (2012) Using Effect Size - or Why the P Value Is Not Enough. *Journal of graduate medical education* 4: 279–82.